Modelling wind-driven inter-ocean exchange in the greater Agulhas with the Regional Ocean Modelling System

Benjamin R. Loveday

February 2014

Thesis presented for the Degree of

DOCTOR OF PHILOSOPHY

in the Department of Oceanography

UNIVERSITY OF CAPE TOWN

This work has been supervised by the following:

*__Supervisor 1__
Prof. Chris Reason
Department of Oceanography, University of Cape Town, 7700 Rondebosch, Cape Town, South Africa

*__Supervisor 2__
Dr. Pierrick Penven
Laboratoire de Physique des Oceans - UBO, UMR6523, IFREMER, IRD, CNRS, Plouzané, France

*Signatures are on file in the Science Faculty

Publications based on this work, in whole or in part:

- **Chapter 5**; Loveday, B. R., Durgadoo, J., Reason, C. J. C., Biastoch, A. and Penven, P. Decoupling of the Agulhas leakage from the Agulhas Current. *(accepted; J. Phys. Oceanogr.)*
- **Chapter 6**; Durgadoo, J., Loveday, B. R., Reason, C. J. C., Penven, P., and Biastoch, A. (2013). Agulhas leakage predominantly responds to the Southern Hemisphere Westerlies. *J. Phys. Oceanogr.*, **43**, 2113-2131.

Abstracts for these papers are included in the appendices.

Abstract

Two Regional Ocean Modelling System configurations, AGIO and ARC112, are developed to investigate (1) the structure of the Agulhas leakage, (2) the dynamical link between the leakage and the Agulhas Current, and (3) the sensitivity of this link to changes in the regional wind field. Both configurations span the Indian Ocean and South East Atlantic Ocean (29°W - 115°E, 48.25°S - 7.5°N) at 1/4° resolution. ARC112 includes a two-way, AGRIF nested, 1/12° child domain, encapsulating the Agulhas retroflection (0°E - 40°E, 45.5°S - 29.5°S).

Model evaluation shows that the basin-scale circulation patterns of the South Indian Ocean are appropriately captured. Western boundary transports match those derived from *in situ* hydrography, though source region fluxes exceed those observed. Both configurations exhibit inertially governed retroflections and produce Agulhas rings with eddy kinetic energy patterns consistent with those derived from altimetry. Improved topography in ARC112 yields a retroflection position and leakage value closer to observations. Dominant regional water masses are captured, but discrepancies in their distributions remain, especially in highly turbulent areas. The interannual variability of upper ocean heat content is well captured, and Indian Ocean dipole modes are appropriately expressed.

Leakage is shown to be confined to the top 1500 m. Flux estimates, derived using complementary Eulerian passive tracer and Lagrangian virtual float techniques, converge where retroflection position is more accurate. Eddy flux, isolated using an Okubo-Weiss parameterisation, contributes only 1/3 to the total flux at the GoodHope line, with a 2:1 anticyclone to cyclone ratio. The remaining intra-ring flux occurs due to mixing between rings in the Cape Basin thermocline, which contains up to 50% Indian Ocean waters. Using a hybrid-criteria eddy-tracking scheme, ARC112i is shown to represent all three recently identified eddy paths, producing an accurate number of rings and cyclones with trajectories and radii that mirror observations, despite higher simulated speeds. A multi-decadal strengthening of the eddy component of Agulhas leakage is ascribed to increases in anti-cyclone speed and cyclone size.

Linear changes in trade wind intensity, imposed through a series of idealised wind stress anomalies, concomitantly modulate Agulhas Current transport. The leakage flux response to changing western boundary current inertia is minimal, decreasing with higher resolution. Large changes in eddy kinetic energy are associated with small leakage anomalies, suggesting that the former is a poor leakage proxy. Initially, the leakage responds linearly to increasing westerly wind intensity, but increased mixing between the Agulhas Return Current and Antarctic Circumpolar Current reduces inter-basin flux as the latter adjusts. Consequently, it is suggested that Agulhas Current and leakage magnitude may, to a degree, vary independently, and that multi-decadal trends in the region may be a function of the wind forcing used. Equatorward shifts in the zero line of wind-stress curl drive a small leakage increase, counter to proposed palaeoceanographic mechanism where leakage is implied to reduce under these conditions.

Declaration

The present work has been originally written by me, with the full support of my supervisors: Dr. Pierrick Penven at the Institut de Recherche pour le Développement (IRD), France, and Prof. Chris Reason at the Department of Oceanography, University of Cape Town, South Africa. Beyond this, important contributions on the approach used in this study are clearly acknowledged through referencing within the text.

Contents

Acknowledgements

This work would not have been possible without the guidance and expertise of my two supervisors: Prof. Chris Reason and Dr Pierrick Penven. Chris, your critical eye has improved this work no end, and I am most grateful for the teaching opportunities that you afforded me. Pierrick, the exceptional scope of your knowledge, your imagination and your enthusiasm has been nothing short of inspiring, while your constructive and honest feedback (especially with regard to manuscript drafts!) has been invaluable.

I would like to thank my collaborators, Dr. Lydiane Mattio (UCT), Dr. Jens Zinke (University of Western Australia), Margit Simon (Cardiff University) and most notably, Prof. Arne Biastoch and Dr. Jonathan Durgadoo at the GEOMAR Helmholtz Centre for Ocean Research, Kiel. Their ambition and vision has been essential in broadening the interdisciplinary scope of this research. Within UCT, scientific discussions with Dr. Julie Deshayes, Dr. Bjorn Backeberg, Dr. Stephen Herbette, Dr. Jenny Veitch and Dr. Issufo Halo, have undoubtedly enhanced the quality of this work. I am extremely grateful to all of them for patiently sharing their expertise and for tolerating my constant barrage of questions.

I gratefully acknowledge the European Community's Seventh Framework Programme FP7/2007-2013-Marie-Curie ITN GATEWAYS project and ICE-MASA for funding this research, and the MARE-BASICS programme for additional travel support. In particular I would like to thank Dr. Francis Marsac for the efforts he has made to secure funds on my behalf. All simulations were performed at the Centre for High Performance Computing (CHPC) or on Climate Systems Analysis Group (CSAG) CORE cluster, and I am indebted to both for allowing access to substantial resources and for their technical support. Eric Mbele, Dr. Chris Jack, Rodger Duffet, Philip Mukwena and Jerome Guiet all deserve a special mention for the latter. Thanks also to Claire Khai, Emlyn Balarin and Helen King for helping me keep the wheels turning.

My sincere thanks also go to the following people. To my parents and brother, for propelling me forward with their unconditional support and unwavering belief in my success. To Lauren, Ross, Brett, Bjorn, Ffion, Janine, Sarah, Penny and Hazel for dragging me kicking and screaming away from my screen and reminding me of the glittering, musical world of Cape Town beyond the office. To Emily, for graciously putting up with a grumpy old man over two years of emotional turmoil. And, finally, to Hayley, who has been largely responsible for preserving my sanity, at considerable cost to her own; without your unerring encouragement, inexhaustible patience and sublime poached eggs, I would never have made it this far. Thanks for everything, H.

List of Figures

List of Tables

List of Symbols

β	-	change of Coriolis with latitude
ϵ	-	the longwave emissivity of the ccean
ζ	-	sea-surface displacement
θ_b, θ_s	-	s-coordinate stretching parameters
κ	-	von Karman constant
ξ	-	vertical component of relative vorticity
$\triangle\xi$	-	change in eddy relative vorticity
ξ_o	-	characteristic relative vorticity
ρ	-	sea water density
ρ_o	-	reference density of sea water
ρ_a	-	air density
σ	-	the Stefan-Boltzmann constant
$\tau_s^x, \tau_s^y, \tau_b^x, \tau_b^y$	-	surface wind and bottom boundary stresses
$\Phi_{e1,e2}$	-	non-dimensional distance between eddies
A_h, A_v	-	horizontal, vertical viscosity
AC_E	-	Eulerian Agulhas Current flux
AC_L	-	Lagrangian Agulhas Current flux
AL_E	-	Eulerian Agulhas leakage flux
AL_L	-	Lagrangian Agulhas leakage flux
AL_{crit}	-	tracer limited Agulhas leakage flux
C_{d_b}	-	quadratic bottom friction coefficient
C_p	-	specific heat capacity of water
C_{pa}	-	specific heat capacity of air
C_h, C_e, C_d	-	dimensionless transfer coefficients for sensible heat, latent heat and momentum (drag)
E	-	Ekman number
f	-	Coriolis parameter
g	-	acceleration due to gravity
h	-	ocean bathymetry depth
$horcon$	-	Smagorinsky selective damping co-efficient

H	-	layer depth
K_{M_v}, K_{M_h}	-	vertical and horizontal viscosity coefficients
$K_{T_v}, K_{T_h}, K_{S_v}, K_{S_h}$	-	vertical and horizontal tracer diffusivity coefficients.
L_e	-	latent heat of vaporisation
O_W	-	Okubo-Weiss parameter
P	-	pressure
q, q_s	-	specific humidity and saturation at T = Ts
Q_{net}	-	net surface heat flux
Q_{lw}	-	outgoing black-body radiation
Q_{sh}	-	sensible heat flux
Q_{lh}	-	latent heat flux
$\triangle R$	-	change in eddy diameter
R_o	-	characteristic eddy radius
Rad_{sw}, Rad_{lw}	-	prescribed downwelling short and long-wave radiations
r_o	-	characteristic length scale
S	-	salinity
S_n	-	normal strain tensor term
S_s	-	shear strain sensor term
T	-	potential temperature
T_a	-	potential ar temperature
T_s	-	surface temperature
t	-	time
u, v, w	-	Three-dimensional (x, y, z) velocity components
$\|\overline{u_{10}}\|$	-	average wind speed relative to the surface at 10 m
$u_{i_{10}}$	-	horizontal wind components relative to a fixed earth at 10 m
$u_{i_{si}}$	-	surface current (ms-1)
U_{Ek}, V_{Ek}	-	depth integrated horizontal Ekman transports
$\triangle X$	-	change in eddy position
X_o	-	characteristic eddy length scale
x, y, z	-	Cartesian co-ordinate directions
Z_{Ekman}	-	Ekman depth
z_r	-	rugosity scale

List of Acronyms

AABW	-	Antarctic Bottom Water
AAIW	-	Antarctic Intermediate Water
AAMW	-	Antarctic Mode Water
AC	-	Agulhas Current
ACC	-	Antarctic Circumpolar Current
ACT	-	Agulhas Current Time Series (mooring array)
AGIO	-	1/4° AGulhas Indian Ocean model (ROMS)
AGRIF	-	Adaptive Grid Refinement in Fortran
AL	-	Agulhas leakage
AMOC	-	Atlantic Meridional Overturning Circulation
ARC	-	Agulhas Return Current
ARC112	-	1/12° Agulhas Regional Configuration (ROMS)
AS	-	Arabian Sea
ASLOW	-	Arabian Sea Low Oxygen Water
ASW	-	Arabian Sea Water
BB	-	Bay of Bengal
CDW	-	Circumpolar Deep Water
CFC	-	chlorofluorocarbons
CORE	-	Common Ocean-Ice Reference Experiment surface forcing variables, made available by GFDL
EACC	-	East African Coastal Current
EKE	-	Eddy kinetic energy
EMC	-	East Madagascar Current
ENSO	-	El Niño Southern Oscillation
EQW	-	Equatorial waters
GEBCO	-	General Bathymetric Chart of the Oceans
GFDL	-	Geophysical Fluid Dynamics Laboratory
ICW	-	Indian Central Water
IDW	-	Indian Deep Water
IEW	-	Indian Equatorial Water

ITF	-	Indonesian Throughflow
IOD	-	Tropical Indian Ocean dipole mode
LADCP	-	lowered acoustic doppler current profiler
LC	-	Leeuwin Current
MKE	-	Mean kinetic energy
MZC	-	Mozambique Channel
NADW	-	North Atlantic Deep Water
NCEP	-	National Centres for Environmental Prediction
NEMC	-	North East Madagascar Current
OGCM	-	Ocean general circulation model
PGF	-	pressure gradient force
PGW	-	Persian Gulf Water
ROMS	-	the Regional Ocean Modelling System
RSW	-	Red Sea Water
SACW	-	South Atlantic Central Water
SAMW	-	Sub-Antarctic Mode Water
SC	-	Somali Current
SEISAMW	-	Southeast Indian Sub-Antarctic Mode Water
SICC	-	South Indian Current
SICW	-	South Indian Central Water
SICC	-	South Indian Counter Current
SEC	-	South Equatorial Current
SECC	-	South Equatorial Counter Current
SEMC	-	South East Madagascar Current
SSH	-	Sea surface height
SHW	-	southern hemisphere westerlies
SSS	-	Sea surface salinity
SST	-	Sea surface temperature
STF	-	Subtropical front
STSW	-	Subtropical Surface Waters
STIOD	-	Subtropical Indian Ocean dipole mode
SWIO	-	South West Indian Ocean
TCHP	-	Tropical cyclone heat potential
TSW	-	Tropical Surface Waters
WOCE	-	World Ocean Circulation Experiment
XBT	-	Expendable bathythermograph

Chapter 1

What drives the greater Agulhas system? An overview of the salient features, dynamics and climatic role of the South West Indian Ocean.

1.1 Introduction

Understanding the causes of past climate variability is essential when attempting to accurately predict future climatic scenarios. The meridional overturning circulation, the mechanism via which the oceans globally distribute heat and salt, is one of the predominant ocean systems that govern this variability, and plays a defining role in determining the extent and phase of glaciation events (Blunier et al., 1998; Ganopolski and Rahmstorf, 2001; Epica Community Members, 2006). Increasingly, evidence suggests that changes in the mesoscale dynamics of inter-ocean "gateways" (e.g. the Drake Passage, the Indonesian Throughflow) can have a notable impact on this global thermohaline circulation (Toggweiler and Samuels, 1995; Godfrey, 1996). The greater Agulhas system, which acts to mediate buoyancy transfer in the "warm-water route" between the Indian and Atlantic Ocean thermocline layers, is a significant example of such a feature (de Ruijter et al., 1999a; Beal et al., 2011; Gordon, 1986).

The Agulhas Current (AC) is the major western boundary current of the Indian Ocean, drawing its water from the turbulent upstream regions, the Mozambique Channel (MZC) and East Madagascar Current (EMC), and via recirculation in the South West Indian Ocean (SWIO) subgyre. Typically, western boundary currents, such as the Gulf Stream and Kuroshio Current, break from their respective continental shelves due to interplay between inertia, topography and the effects of the large-scale wind field (Veronis, 1973; Özgökmen et al., 1997). In contrast, the sudden termination of the African continent causes the Agulhas to break from the shelf around Port Elizabeth at 35^{o}S, continuing south-westward into the open ocean without the

steering effect of topography. Due to the balance between the inertia and vorticity, and the proximity of the zero-line of wind stress curl, this jet "retroflects" sharply eastwards (Ou and de Ruijter, 1986; Boudra and Chassignet, 1988; Lutjeharms and van Ballegooyen, 1988). Most Agulhas waters negotiate this retroflection, and are returned to the Indian Ocean basin via the meandering Agulhas Return Current (ARC) (de Ruijter et al., 1999a; Lutjeharms and Ansorge, 2001; Boebel et al., 2003b). Only a small component of thermocline water is shed from the retroflecting jet, subsequently entering the Atlantic via the highly turbulent Cape Basin in the form of Agulhas Rings (Gordon, 1986), filaments (Lutjeharms and Cooper, 1996) and the Good Hope Jet (Gordon et al., 1995). This inter-basin flux, termed the Agulhas leakage (AL) and estimated at $\backsim$15 Sv (Richardson, 2007) in the top 1000 m (where 1 Sv = 1×10^6 m^3s^{-1}), contributes heat and salt to the upper branch of the Atlantic Meridional Overturning Circulation (AMOC), forming the upper thermohaline connection between the Indian and Atlantic Oceans (Weijer et al., 1999).

The key climatic role played by the greater Agulhas system is possibly most evident in palaeoclimatic records. Significant millennial scale variability in leakage magnitude, derived from core based counts of tropical fauna in the Cape Basin, suggests that severe reductions in inter-basin flux accompanied glacial phases (Peeters et al., 2004). In addition, ejections of large pulses of Indian Ocean waters into the South Atlantic are associated with glacial terminations T1 to T5 (*ibid*). These warm, saline water pulses are suggested to instigate a resumption and strengthening of the AMOC in both ocean-only (Knorr and Lohmann, 2003) and coupled-climate models (Weijer et al., 2001, 2002). Bard and Rickaby (2009) suggest that the magnitude of inter-basin flux may be modulated by the latitude of the Sub-Tropical Front (STF), which bounds the leakage corridor to the south. However, although Graham et al. (2012) show that the latitude of the STF is determined by the latitude of the westerly wind belt, the location of this belt during glacials remains poorly defined (Sime et al., 2013). Additionally, although some coupled climate studies suggest that northward migration of the westerly winds would result in a reduced leakage (Sijp and England, 2008), high-resolution ocean-only simulations show that an equatorward shift may actually enhance leakage on the decadal scale (Durgadoo et al., 2013).

Historically, efforts to map the Agulhas Current began as early as the mid 1800s (Rennell, 1832), driven by the establishment of maritime trading routes around the southern tip of Africa. Hydrographic observations followed soon after (van Gogh, 1857), but periods of sustained monitoring were largely absent until the mid 20^{th} century. More recently *in situ* observations have been gathered from numerous oceanographic cruises, beginning in the 1960s with the International Indian Ocean Expeditions (Wust, 1960; Wyrtki, 1971) and Combined Agulhas Cruise (Bang, 1970). In addition, the installation of mooring stations such as the Agulhas Current Time-series (ACT) and Indian-Atlantic Exchange in Present and Past Climate (INATEX) arrays and the introduction of the satellite-based remote sensing platforms have helped to define the greater Agulhas as a highly complex, turbulent system. However, whilst observational efforts to obtain longer time series for the modern AC and associated leakage are underway (via the ACT array

and hydrographic cruises along the GoodHope Line (Swart et al., 2008), respectively), many of the processes that appear to define the behaviour of the system remain sparsely sampled.

In support of observations, theoretical and numerical models have been used to extensively investigate the dynamics of the greater Agulhas. Many of these studies underline the key role the basin-scale winds play in determining the behaviour of the system (de Ruijter, 1982; de Ruijter et al., 1999a; Biastoch and Böning, 2013; Biastoch et al., 2009b; Rouault et al., 2009). However, while hindcast simulations suggest that increases in Agulhas leakage occur concurrently with the intensification and southward migration of the southern hemisphere westerlies (*ibid*), possibly driven by anthropogenic influences (Thompson and Solomon, 2002; Gillett and Thompson, 2003; Seidel et al., 2008), they fail to find a consensus on the long term trend in Agulhas Current transport; a point of some debate. While the paucity of observations make it impossible to validate the leakage trend, coupled ocean-ice models further suggest that the rise in heat flux associated with a larger injection of Indian Ocean waters is largely responsible for the observed increase in 20^{th} century Atlantic Ocean heat content (Lee et al., 2011). Further, expansion of the trend into future projections appear to reinforce the anthropogenic link (Biastoch and Böning, 2013). More conceptually, it has been suggested that increases in the salinity of the upper branch of the AMOC, driven by a larger leakage, could potentially oppose the effects of the freshening northern Atlantic that is associated with increased, climate-change driven, ice melt (Stammer, 2008; Gregory et al., 2005).

Recent observation suggest that the Indian Ocean trade winds are intensifying (Backeberg et al., 2012) and southern hemisphere westerlies may be strengthening and progressing southwards (Swart and Fyfe, 2012; Thompson and Solomon, 2002; Gillett and Thompson, 2003). Theory suggests that the stronger trade winds may effect the Agulhas leakage as the inertia of the incoming Agulhas Current is increased. Concurrently, changes in the westerly wind system may effect the leakage through modification of the sub-gyre and supergyre (Cai, 2006; Durgadoo et al., 2013). This superposition of signals makes it difficult to attribute the changes seen in hindcast models to specific mechanisms, and therefore to extrapolate conclusions into the palaeoceanographic context. In addition, while modern hindcast models typically quantify leakage in terms of volume flux, salinity flux may be a more useful diagnostic when considering palaeoclimatic signals and the effect on the AMOC. With these factors in mind, this introductory chapter presents an overview of the salient features of the Indian Ocean and the dynamics of the greater Agulhas system, culminating in key questions that need to be addressed.

1.2 The Indian Ocean: A general overview

Historically, the Indian Ocean, the third largest[1] of the world's oceans at 68.5 x 10^6 km^3, has been somewhat overlooked in terms of its effects on global climate (Schott et al., 2009). Prior to the identification of the dipole modes (Saji et al., 1999; Behera and Yamagata, 2001), its climatic

[1] https://www.cia.gov/library/publications/the-world-factbook/geos/xo.html

role, other than through the monsoon, was considered to be somewhat passive; a slave to Pacific El Niño Southern Oscillation (ENSO) signals (Latif and Barnett, 1995). However, Indian Ocean sea-surface temperature (SST) signals are increasingly being shown to have a substantial impact on both regional and global climate (Bader, 2003; Saji and Yamagata, 2003; Yang et al., 2007; Reason, 2002). In addition, the wind field across the Indian Ocean gives rise to one of the most energetic western boundary systems in the global ocean; the greater Agulhas Current system. The high latent heat flux and evaporation associated with the warm western boundary current has a notable effect on southern African climate, influencing regional rainfall (Jury et al., 1993), atmospheric circulation (Reason, 2001) and the occurrence of extreme flooding events (Rouault et al., 2002).

The Agulhas Current also exerts a substantial influence on the global climate system (Beal et al., 2011). The AMOC describes the northward flow of warm waters in the surface ocean, and southward return transport of cold waters at depth; transports substantial amounts of heat northward, and playing a defining role in determining global climate. The upper branch of the AMOC draws waters form two sources; intermediate waters through the 'cold-water' route originating in the Drake Passage, and thermocline waters derived from the 'warm-water' route originating in the Indian Ocean. The Agulhas system mediates the flux through this latter route, partially determining the AMOC strength (Weijer et al., 1999) and by extension, plays a key role in determining global climate variability on multi-decadal (Biastoch et al., 2008b; Lee et al., 2011), centennial (Weijer et al., 2002), and glacial-interglacial timescales (Peeters et al., 2004).

The Indian Ocean spans the tropical and southern mid-latitude wind systems, and is bounded by land on three sides. In the north, the Red Sea, Persian Gulf, Arabian Sea and Bay of Bengal, collectively termed the marginal seas, lie adjacent to the Asian continent. In the South, the basin is open to the Southern Ocean, but is bounded by the STF. In the east, the maritime continent and Australia form a semi-continuous barrier to the Pacific Ocean, broken only by the Indonesian Seas equatorward of 40°S. Continental Africa separates the Indian Ocean from the Atlantic Ocean along the entire western boundary to the shelf at Cape Agulhas at 35°S. Poleward of this, the Atlantic and Indian Oceans lie adjacent to each other around 20°E. As a result of the semi-enclosed nature of the basin, the circulation is highly dependant on the regional wind field, exchanges across the STF, and the balance between the influx of Pacific waters and volume loss to the Atlantic Ocean south of Africa. As the wind driven Agulhas system mediates the inter-ocean exchange at this latter confluence, it plays a defining role in the oceanography of the South West Indian Ocean region.

1.2.1 Seasonal to decadal wind variability

The large-scale circulation of the Indian Ocean is, to the first order, determined by the wind field. Typically, tropical oceans display constant easterly winds along the equator, but the Indian Ocean is anomalous in this respect. The seasonal monsoon cycle, which prevails over the

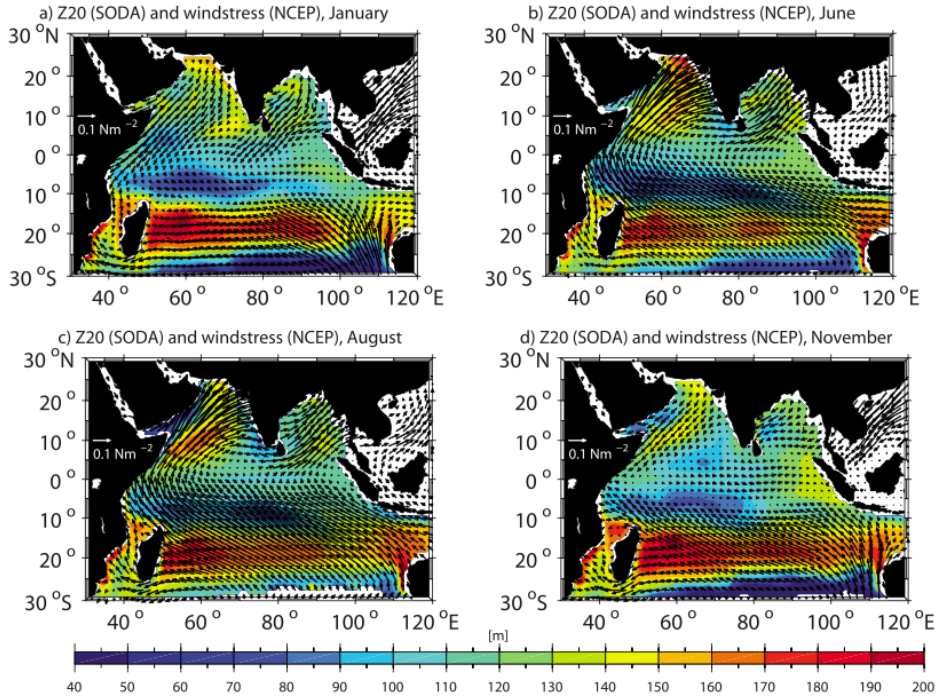

Figure 1.1: Monsoon wind stress fields from the 1990-1998 National Center for Environmental Prediction (NCEP) climatology (vectors) (Kalnay et al., 1996) and depths of 20°C isotherm (Z20) from Simple Ocean Data Assimilation (SODA) (mean for 1992-2001, colour shaded) for (a) January, (b) June, (c) August, and (d) November. [After Schott et al. (2009)]

low latitudes north of 10°S, is characterised by sharp reversals in the wind direction prominent during the inter-monsoon periods (Schott et al., 2009) (Fig. 1.1). Consequently, the wind stresses in the equatorial Indian Ocean are firstly, weak, and secondly, westerly in the annual mean (Xie et al., 2002).

In contrast, the winds further south are much more stable, and are dominated by two belts; the southeast trade winds between 10°S and 32°S, and the southern hemisphere westerlies (SHW) between 32°S and 60°S. Negative wind stress curl contributes cyclonic vorticity to the ocean between the equator and 17°S. Positive wind stress curl drives the anticyclonic flow of the subtropical gyre between 17°S and 47°S (Marshall and Plumb, 2007). The extension of this positive vorticity regime poleward of the African continent (35°S) is critical to the behaviour of the Agulhas system.

In response to the monsoon, there is a small seasonal migration of the northern edge of the wind field northwards during the austral winter (Schott et al., 2009). This seasonal modulation of the subtropical wind field during March and September causes the subtropical gyre to extend further south to a mean position of 43°S and intensify during these periods (Ffield et al., 1997). The converse situation occurs in July and December, when the gyre shifts north to 38°S.

While the monsoon-driven seasonal cycle of the Indian Ocean represents the strongest mode of variability, interannual signals, such as those associated with ENSO also exert a considerable influence on regional ocean-atmosphere dynamics. Modification of the Walker circulation during

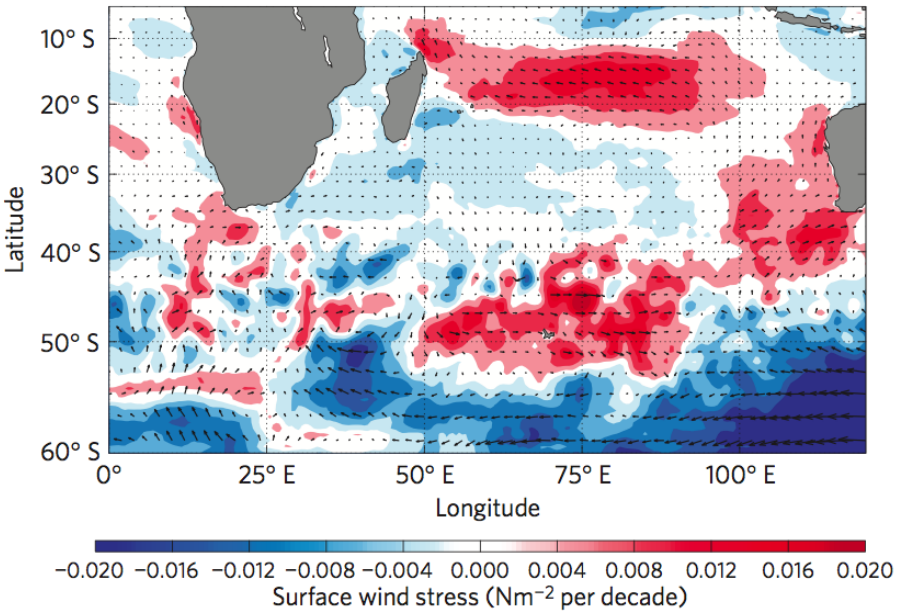

Figure 1.2: Decadal trends of the surface wind stress of the subtropical Indian Ocean. Decadal trend of the surface wind-stress magnitude for 1993-2009 from the CFSR reanalysis data. The vectors indicate the direction and magnitude of the trend [After Backeberg et al. (2012)].

ENSO events, produces anomalous easterly wind bursts, inducing downwelling Rossby waves in the ocean (Reason et al., 2000; Jury and Huang, 2004). In addition, sea-surface temperature (SST) dipole patterns occur in both the tropics and subtropics; the tropical Indian Ocean Dipole Mode (IOD) (Saji et al., 1999; Webster et al., 1999) and subtropical Indian Ocean Dipole mode (STIOD) (Behera and Yamagata, 2001), respectively. In its positive phase, the IOD is expressed through the formation of a warm (cold) pool in the tropical eastern (western) basins. It is associated with anomalous easterly wind stresses at the equator, suggesting a large degree of ocean-atmosphere coupling here (Ashok et al., 2001; Yu and Lau, 2005). Further south, a positive STIOD state, defined as an anomalously cool pool off of Australia and warm pool south of Madagascar, results in a more intense, southward shifted sub-tropical high, and stronger attendant winds (Behera and Yamagata, 2001).

Western boundary currents, such as the Agulhas, are to some extent functions of their adjacent wind-driven gyres, from where they derive their water mass properties and volume flux (de Ruijter et al., 1999a). As such, it is feasible to assume that they will respond to the seasonal and interannual wind variability described above. However, while Krug and Tournadre (2012) derive an annual cycle in the Agulhas Current transport from altimetry, they do not link it to any basin scale climatic mode. Schouten et al. (2002a) note that, in general, incoming Rossby waves can be associated with western boundary eddy variability, and suggest in a later study that this process may be subject to ENSO/IOD driven variability (Schouten et al., 2002b). However, evidence that Agulhas Current transport retains an interannual component consistent with ENSO/IOD phases remains elusive.

Analysis of satellite era reanalysis winds across Indian Ocean winds since 1993, suggests substantial decadal variability (Backeberg et al., 2012) (Fig. 1.2). In the subtropics, increases in trade wind intensity (Han et al., 2010) have driven increasing turbulence in the Agulhas source regions west and south of Madagascar. Further south, an intensification (Swart and Fyfe, 2012) and poleward migration (Thompson and Solomon, 2002; Gillett and Thompson, 2003) of the southern hemisphere westerlies (SHW) has been associated with an increased Agulhas leakage (Biastoch et al., 2009b; Rouault et al., 2009; Durgadoo et al., 2013). Intensification of the SHW, projected under intensified greenhouse forcing, implies that leakage may increase yet further in the future (Biastoch and Böning, 2013).

1.2.2 Inter-ocean connections

Warm, fresh, waters from the Pacific enter the eastern tropical Indian Ocean via the complex channels of the Indonesian Throughflow (ITF) (Gordon and McClean, 1999). Transports inferred from hydrography suggest an ITF flux of 10 ± 10 Sv (Macdonald, 1998), consistent with directly observed values Gordon and McClean (1999). Lee et al. (2002) considered the simulated effects of reducing and blocking ITF, and established a link between it and the flow of the South Equatorial Current (SEC), which weakens as ITF flux is constricted. Downstream, this in turn affects the magnitude of the Agulhas Current transport. A blocked ITF also weakens (strengthens) the seasonal (interannual) variation in the eastern thermocline, suggesting that it represents a critical path via which the Pacific ENSO signal can be transmitted to the south Indian Ocean. Ocean general circulation model (OGCM) simulations suggest that the Pacific and Indian oceans are also connected by a secondary path south of Australia; the Tasman Leakage. Observations (Sokolov and Rintoul, 2009) and inverse modelling studies (Ganachaud and Wunsch, 2000) show that the westward transport between Tasmania and the Subtropical Front can exceed can exceed 30 Sv; 26 ± 4 Sv as AAIW and 13 ± 3 Sv as SAMW. The local contribution of these waters into the Indian Ocean at 115°E are inferred to be 10 ± 3 Sv and 3.7 ± 2.5 Sv, respectively (Ganachaud and Wunsch, 2000). Speich et al. (2002) and Speich et al. (2007) considered the fate of the Tasman leakage waters in GCMs, determining that 3.2 Sv reaches the North Atlantic.

The African continent terminates at ∽35°S, equatorward of the zero line of wind-stress curl at around 42°S. At the southern shelf tip, the Agulhas Current overshoots the continental margin, heading southward as an inertial jet. The majority of the current turns back into the the Indian Ocean through the Agulhas retroflection (Lutjeharms and van Ballegooyen, 1988), but some incoming flux is ejected from into the Atlantic as the Agulhas leakage. Estimates from limited observations suggest that, in the upper ocean, the export of Indian Ocean waters is between 2 Sv and 15 Sv (Richardson, 2007; Gordon et al., 1992; de Ruijter et al., 1999a), with far-reaching consequences for the evolution of the AMOC (Gordon, 1986; de Ruijter et al., 1999a; Biastoch et al., 2008b). However, the magnitude of this exchange is largely determined by the dynamics of the Agulhas retroflection (Lutjeharms, 2006b), the complexities of which are a primary focus

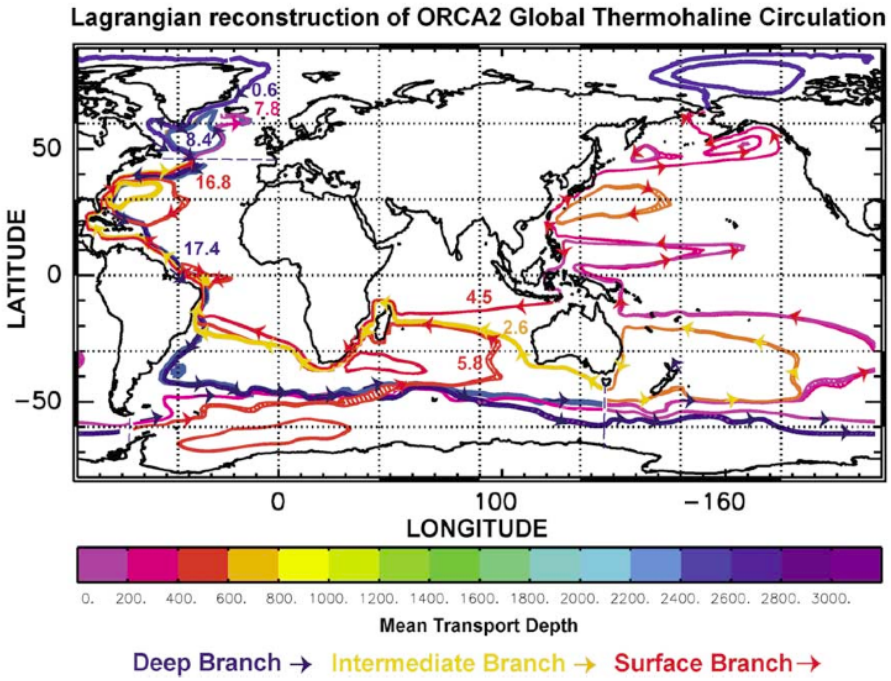

Figure 1.3: Lagrangian pathways of water parcels in a global model simulation. Colours indicate depths, and numbers are transports (in Sv). [After Speich et al. (2007)].

of this review. Retroflection features and dynamics will be discussed fully in sections 1.3.3and 1.4.2.

Recent observations (Ridgway and Dunn, 2007) and global model simulations (Tilburg et al., 2001; Speich et al., 2007) show the existence of a "supergyre" connecting the South Atlantic, South Indian and South Pacific ocean basins. The southern supergyre branch is expressed through eastward flow in the surface and deep waters north of the STF (figure 1.3). Without inertial separation, the entire Agulhas Current would flow around the southern tip of Africa and into the Atlantic Ocean (Ou and de Ruijter, 1986), forming the continuous northern supergyre branch. While Veronis (1973) were first to suggest this possibility, he concedes that it has never been observed. In reality the inertia of the Agulhas Current serves to chokes the inter-ocean link (de Ruijter, 1982). This choking somewhat severs the northern branch, and inter-basin flux is reduced to discrete bursts of Indian Ocean water in Agulhas rings. Recent observations suggest that the supergyre has recently intensified and migrated poleward, due to the modification of the SHW, driven by the depletion of Antarctic Ozone (Cai, 2006).

The Agulhas leakage connects the Indian Ocean to South Atlantic Ocean. The circulation and water masses of the South Atlantic Ocean are comprehensively described in Peterson and Stramma (1991) and Stramma and England (1999). The circulation of the South Atlantic is dominated by the anticyclonic wind-driven sub-tropical gyre (Peterson and Stramma, 1991). However, while the upper ocean in the subtropical gyre consists predominantly of South Atlantic Central Water (SACW) of Atlantic origin, the SACW found in the tropical gyre further north arrives from the South Indian Ocean Stramma and England (1999). Beneath this, two forms

of Antarctic Intermediate Water (AAIW) predominate. One type is formed in the circumpolar region of the Drake passage (Stramma and England, 1999), the other arrives from the Indian Ocean through the Agulhas leakage (Rusciano et al., 2012). Contributions from the Indian Ocean are transmitted across the South Atlantic basin through Agulhas Rings, which steadily decay forming a transient component of the Benguela Current (Garzoli, 1999).

Recently, LADCP measurements taken during the 1995 R. R. S. Discovery cruise identified the presence of an Agulhas Undercurrent. This lies underneath the Agulhas Current with a core at around 1200 m, and transports North Atlantic Deep Water (NADW) east into the Indian Ocean (Beal and Bryden, 1997). Its path remains somewhat unclear. However, simulations suggest that the Agulhas Undercurrent does not appear to connect to deep currents in the MZC due to topographic barriers (Biastoch et al., 2009a). In consequence, the undercurrent fails to ventilate the wider Indian Ocean basin below 3000 m, and has little effect beyond the Natal Valley (Biastoch et al., 2009a; Beal et al., 2006). Nevertheless, it may play a role in determining water mass properties in the Agulhas Current (Biastoch et al., 2009a), and has ramifications for the calculation of western boundary transport.

The Southern Ocean lies at the poleward boundary of the Indian Ocean. Analysis of CFC tracers shows that waters of southern origin play a role in the ventilation of the south Indian Ocean, with concentrations in the thermocline, intermediate and bottom waters decreasing towards the north (Fine et al., 2008). Although the ITF and northern marginal seas are significant sources of low and high salinity waters, respectively, their contribution to ocean ventilation is less important than that of the Antarctic Intermediate Water (AAIW) and Sub-Antarctic Mode Water (SAMW). Fine et al. (2008) suggest that the AAIW enters the intermediate levels of the Indian Ocean via a north flowing boundary current in the southwest, which subsequently passes east of Madagascar. The geostrophic study of Reid (2003) suggests that the bottom waters take a similar path forming a deep western boundary current that traverses the eastern edge of the Central and South Indian Ridges.

1.2.3 Basin-scale circulation

In the top 2000 m, the geostrophic flow of the south Indian Ocean is described by two basin-wide gyres; cyclonic in the tropics and anti-cyclonic in the sub-tropics (Stramma and Lutjeharms, 1997; Reid, 2003) (figure 1.4). The tropical gyre extending from the equator to 10°S, and subtropical gyre, extending from 17°S to 42°S and intensifying towards the southwest (Stramma and Lutjeharms, 1997; Davis, 2005; Reid, 2003), are separated by westward flow in the SEC. There are, however, some distinct differences between the depth integrated flow and that at the surface. A schematic representation of the major current systems in the upper Indian Ocean is shown in Fig. 1.5.

The SEC, augmented by transport contributions from the Pacific via the Indonesian Throughflow (ITF), flows westward between 12°S and 25° (Lutjeharms, 2006b) with a negligible meridional component to the flow (Hastenrath and Greischar, 1991). While predominantly

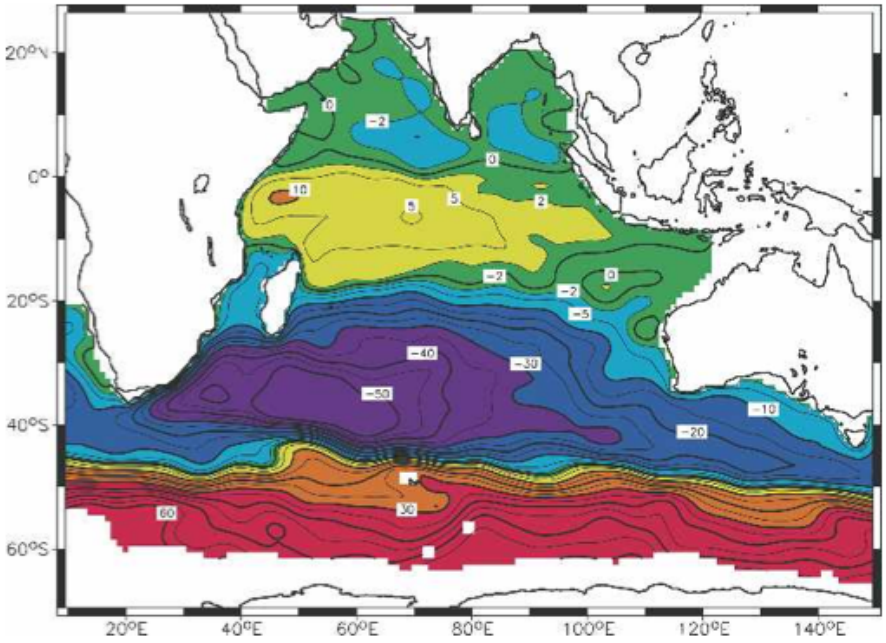

Figure 1.4: Streamfunction for Indian Ocean mean circulation at 900 m. Contours are labeled in units of 1000 m^2s^{-1} with an interval of 5000 m^2s^{-1} plus contours at $\pm$2000 m^2 s^{-1}. [After Davis (2005)]

a geostrophic current, the zonal flow during the austral winter is dominated by a wind-induced Ekman component (Hastenrath and Greischar, 1991). Geostrophic estimates (Schott and McCreary, 2001) ascribe the SEC a transport of 39 Sv (where 1 Sv = 10^6 m^3s^{-1}). Earlier geostrophic measurements by Hastenrath and Greischar (1991) estimates the volume transport at 13 Sv. The SEC bifurcates at the Madagascar coast (at $\sim$17°S), splitting into the Northeast and East Madagascar currents (referred to here as the NEMC and EMC, respectively) (Chapman et al., 2003).

In the northern branch of the bifurcation, The NEMC transports $\sim$30 Sv northwards along the coast around Cape Amber. Here, the flow splits again, dividing into a southern branch, which is incorporated into the eddy rich Mozambique Channel (MZC), and a northern branch which joins the East African Coastal Current (EACC). Westward pulses in the SEC directly influence the formation of mesoscale eddies in the MZC (Backeberg and Reason, 2010), one of the source regions of the Agulhas Current. The northward flowing EACC and southward flowing Somali Jet meet at the northward extremity of the tropical gyre, where surface flow is dominated by the eastward-flowing South Equatorial Counter Current (SECC). During the winter monsoon season this current deviates into the southern hemisphere and weakens as the geostrophic eastward flow is counterbalanced by the wind driven zonal Ekman transport (Hastenrath and Greischar, 1991). In the southern branch, the EMC transports an estimated $\backsim$20.6 $\pm$ 6 Sv (Schott and McCreary, 2001) southward along the coast of Madagascar until it splits at the southern tip of the island, shedding dipole vortices. Here, the current makes a sporadic but sudden westward turn, connecting to the recently discovered, but poorly observed, South Indian Ocean Countercurrent

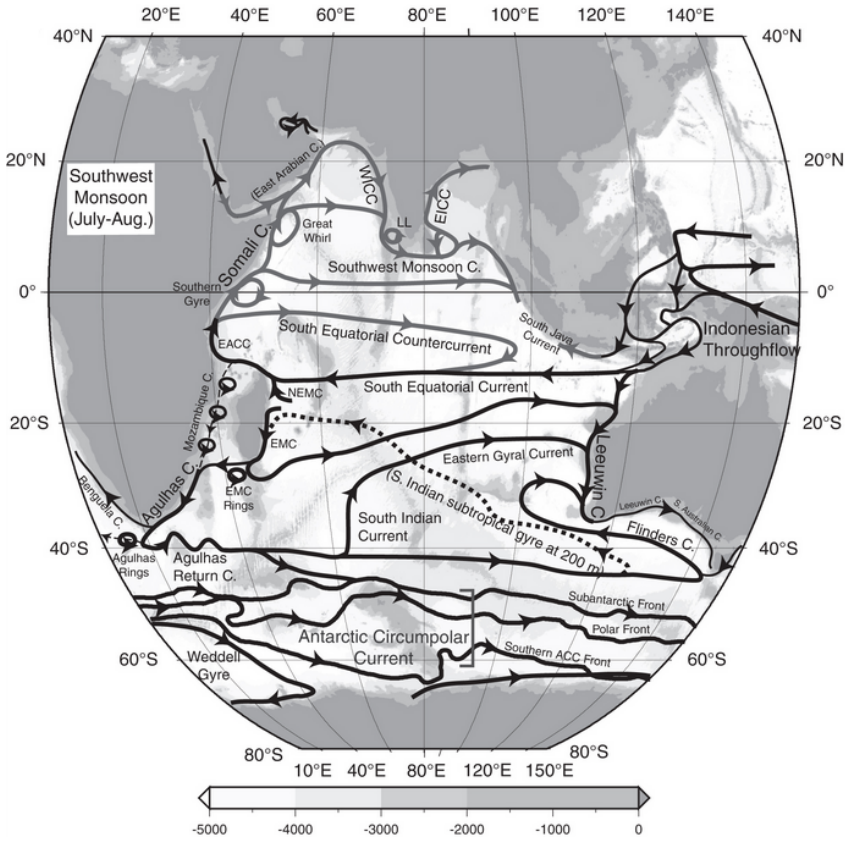

Figure 1.5: Indian Ocean schematic surface circulation. Black: mean flows without seasonal reversals. Grey: monsoonally reversing circulation [After (Schott and McCreary, 2001)]: (a) Southwest Monsoon (July-August). The ACC fronts are taken directly from Orsi et al. (1995). The subtropical gyre in the Southern Hemisphere just 200 m below the sea surface differs significantly from the surface circulation, as indicated by the dashed curve. Acronyms: EACC, East African Coastal Current; EICC, East Indian Coastal Current; EMC, East Madagascar Current; LH and LL, Lakshadweep high and low; NEC, North Equatorial Current; NEMC, Northeast Madagascar Current; and WICC, West Indian Coastal Current. [After Talley et al. (2011)]

(SICC) (Siedler et al., 2006, 2009), which proceeds westward across the sub-tropical basin.

Typically, the zonally integrated wind stress curl over the basin would produce a continuous western boundary current at the continental margin. However, the mean circulation along the East African coast cannot be treated so simply due to the disruptive presence of Madagascar. Consequently, the flow in the MZC and in the extensions of the EMC is observed to be turbulent and eddy-rich (de Ruijter et al., 2002). As such, the Agulhas Current only forms as a coherent western boundary current polewards of the southern point of Madagascar. The mesoscale variability of the upstream source regions of the Agulhas provides a first indication of the non-linearity which is a defining characteristic of the greater Agulhas system. The basin-scale wind field at 31°S suggests a Sverdup solution of 28 to 48 Sv at the western boundary (Saunders et al., 1999) (Josey et al., 2002). This solution is much less than the observed Agulhas Current transport of 70 Sv (Bryden et al., 2005; Donohue and Toole, 2003) at this latitude. The shortfall is accounted for by contributions from the Pacific, and as a consequence of local recirculation and eddy-mean interaction. The Agulhas Current and it's source regions will be discussed in

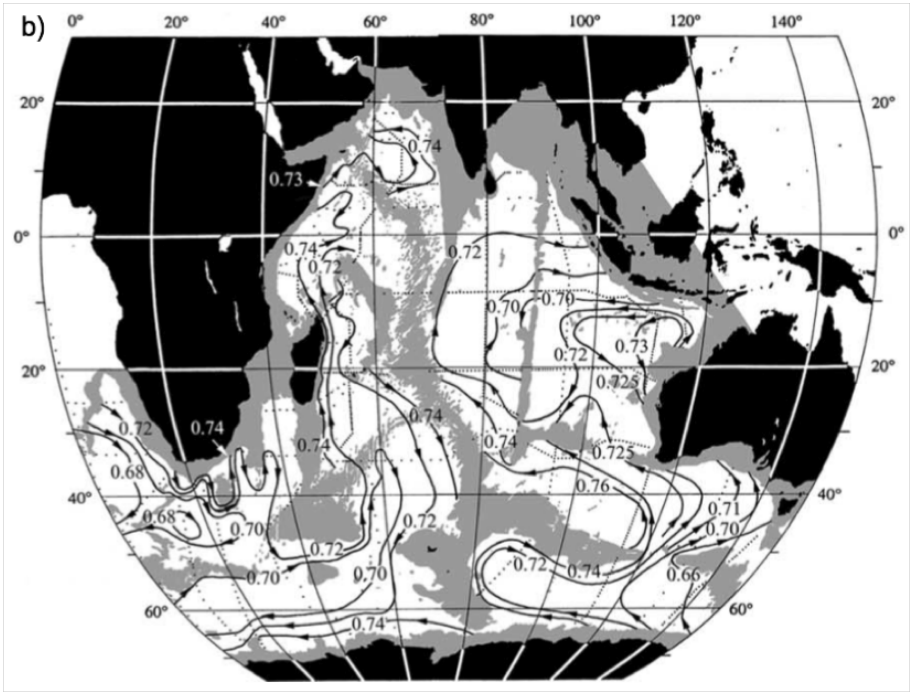

Figure 1.6: Adjusted steric height at 3500 db (measured in 10 m^2s^{-2} or 10 Jkg^{-1}). Depths less than 3500 m are shaded (Reid, 2003).

detail in the section 1.3.

At the southern tip of Africa, the Agulhas Current overshoots the continental shelf, returning sharply eastward. This hairpin-turn, termed the retroflection (Lutjeharms and van Ballegooyen, 1988), recycles the majority of western boundary waters back into the Indian Ocean, via the Agulhas Return Current (ARC). The ARC forms a bridge between the South Atlantic and South Indian Current (SIC) (Stramma, 1991; Lutjeharms and Ansorge, 2001), which flow eastward along the northern edge of the Subtropical Front (STF). The STF forms the nominal southern boundary of the Indian Ocean with the Antarctic Circumpolar Current. Historically, it has been asserted that the STF occurs at the zero-line of wind-stress curl, however, recent studies suggest that the two fail to coincide away from the western extrema of ocean basins, and that the latitude of the STF is also determined by the dynamics of the ACC and topographical influences (Graham et al., 2012)

Reid (2003) offers a comprehensive analysis of the geostrophic transports of the Indian Ocean. The westward flowing South Equatorial Current (SEC) and the subtropical anticyclonic gyre are shown to penetrate into the deep ocean, though surface flows are stronger. The tropical gyre is more confined to the surface. In the deep ocean the bathymetric configuration begins to play a significant role in circulation dynamics at a steric height of 2500 db (figure 1.6).

1.2.4 Bathymetry

Meridional ridges in the wider south Indian Ocean subdivide the basin into eastern, central and western sub-basins (figure 1.7). These ridges, exerting a control on the circulation of the Indian

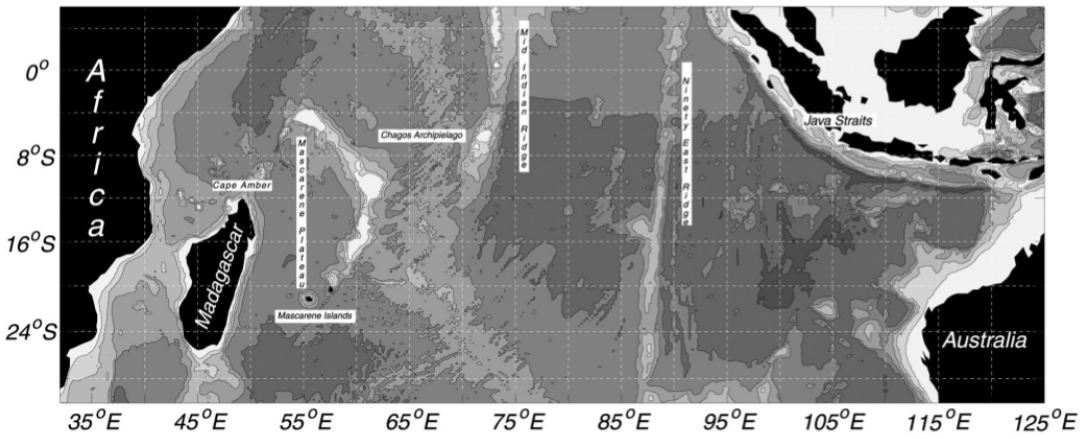

Figure 1.7: Bottom topography of the south Indian Ocean. [After Matano et al. (2002)].

Ocean (figure 1.6) and serve to topographically insulate the southwest Indian Ocean from the variations in the wider wind field (Matano et al., 1999). Numerical simulations show that this insulation occurs through the suppression of the fast barotropic modes of seasonal adjustment Kindle (1991); Matano et al. (1999). Ffield et al. (1997) note that, despite strong seasonal variation in the basin-scale wind pattern, there is no analogous signal in the western boundary. The lack of a linear Sverdrupian response in the Agulhas Current is, in part, ascribed to this scattering of the more energetic barotropic modes into slower baroclinic components (Ffield et al., 1997).

Although predominantly baroclinic, the barotropic component of the ITF may be similarly inhibited by topography as it travels westward (Kindle, 1991). Further, Wang et al. (2001) identify the Chagos Archipelago as a region in which the baroclinic Rossby wave signal breaks down. However, a mechanism where the interference between the local, wind-forced, and remote, ITF-forced, signals is used to explain this pattern. In a later sensitivity study, the effect of the regional bathymetry of the Mascerene Plateau on the Rossby wave modulation of the Seychelles-Chagos Thermocline Ridge was shown to be small (Hermes and Reason, 2009).

1.2.5 Hydrography

Strong zonal imbalances in the tropical evaporation and precipitation rates, the seasonal reversal of the monsoon circulation and the impacts of the adjacent shelf seas give rise to a complex hydrography (Wyrtki, 1971; Schott and McCreary, 2001; Gordon and McClean, 1999; Beal et al., 2000). The major water masses of the Indian Ocean are presented in Fig. 1.8 and Fig. 1.9. Broadly, they can be separated into three classes; those formed within the basin through open ocean subduction, those formed through mixing, and those derived from external sources (Schott and McCreary, 2001). Here they are discussed in relation to their distribution in the water column, beginning with the surface and thermocline water masses (0 - 500 m depth) and latterly discussing the constituents of the intermediate (500 - 1500 m) and deep and abyssal

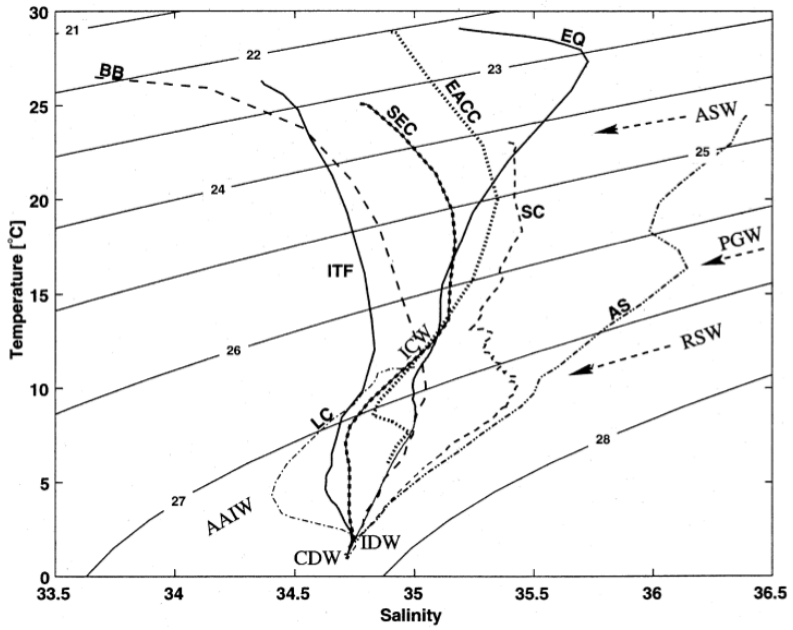

Figure 1.8: Climatological temperature-salinity diagram of Indian Ocean water masses taken from the Bay of Bengal (BB), northern Arabian Sea (AS), equatorial region of western basin (EQ), South Equatorial Current (SEC), western exit of Indonesian Throughflow (ITF/AAMW), and Leeuwin Current (LC). The Somali Current (SC) curve is from August 1993 measurements in northern upwelling wedge. Core water masses indicated are Circumpolar Deep Water (CDW), Indian Deep Water (IDW), Antarctic Intermediate Water (AAIW), Indian Central Water (ICW), Red Sea Water (RSW), Persian Gulf Water (PGW), and Arabian Sea Water (ASW). Profiles are for respective winter seasons in each hemisphere. [After Levitus and Boyer (1994a), Levitus and Boyer (1994b) and Schott and McCreary (2001)].

layers (1500 m to the ocean floor). An additional focus is placed on the SWIO and greater Agulhas Current system.

In the northern Indian Ocean, the upper thermocline waters predominantly consist of water masses formed in the Arabian Sea, Persian Gulf and Bay of Bengal. Arabian Sea Water (ASW), formed seasonally in response to the northeast monsoon, subducts and spreads across the region as a sub-surface salinity maximum (Schott and McCreary, 2001; Morrison, 1997; Schott and Fischer, 2000). Similar to ASW in formation, but distinct in properties is the Persian Gulf Water (PGW). This also forms a near salinity minimum, but its influence is constrained to the northern Arabian Sea (Schott and McCreary, 2001). Latterly, the combined effects of river run-off and increased precipitation in the Bay of Bengal (BB) give rise to a comparatively fresh surface layer.

In the south-west Indian Ocean, Tropical Surface Waters (TSW) and Subtropical Surface Waters (STSW) contribute to the surface and thermocline layers Fig. 1.9. The light, low-salinity TSW is formed in the central Indian Ocean basin, near the equator (Jackett and MacDougall, 1997; Beal et al., 2006). The comparative freshness is the result of excess precipitation in the tropics and mixing with North Pacific waters, arriving through the ITF.

While Pacific waters are comparatively saline east of the Indonesian Archipelago, strong vertical mixing in the shelf seas causes them to be expressed as a salinity minimum in the

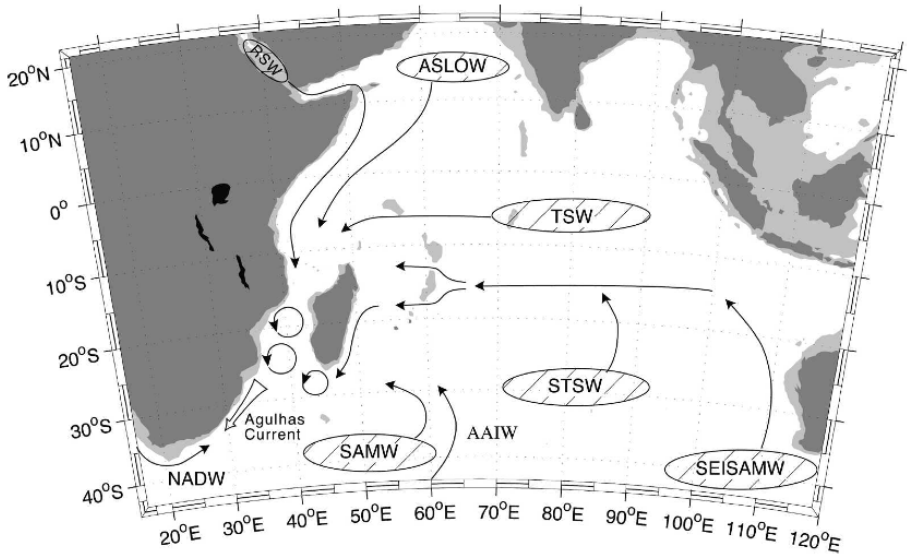

Figure 1.9: A cartoon of the source regions and pathways of water masses that converge into the Agulhas Current. Waters which are formed within the Indian Ocean are shown circled. Waters imported from outside the Indian Ocean are not circled. Water masses are defined as follows: Red Sea Water (RSW), ASLOW, Tropical Surface Water (TSW), Subtropical Surface Water (STSW), Southeast Indian Sub-Antarctic Mode Water (SEISAMW), Sub-Antarctic Mode Water (SAMW), North Atlantic Deep Water (NADW), Antarctic Intermediate Water (AAIW) [After Beal et al. (2006)].

eastern Indian Ocean basin (Field and Gordon, 1992). The TSW, carried westwards in the SEC, is predominantly advected into the subtropics through the MZC (Beal et al., 2006; Swallow et al., 1988), though some studies note its presence in the boundary currents east of Madagascar (Swallow et al., 1988; Schott et al., 1988; Donohue and Toole, 2003).

The STSW forms in the eastern Indian Ocean (Wyrtki, 1971) between 25°S and 35°S (Tomczak and Godfrey, 1994; DiMarco et al., 2002). Equatorward of 28°S, it underlies the TSW (Donohue and Toole, 2003), occupying depths between 200 m and 500 m. The STSW forms a sub-surface salinity maximum at 200 m, and forms due to subduction driven by high evaporation west of 90°E. It is advected northward by the subtropical gyre and, like its tropical counterpart is carried westward in the SEC, shallowing to 100 m in the western basin (Swallow et al., 1988). However, unlike the TSW, which tends to be transported through the MZC at the western boundary, the STSW predominantly re-enters the subtropics in the EMC (Beal et al., 2006).

In the lower thermocline, the various subtropical water masses around 300 m are collectively termed the Indian Ocean Central Water (ICW) (Beal et al., 2006). Of particular note are the Southeast Indian Sub-Antarctic Mode Water (SEISAMW) (Wyrtki, 1971; Hanawa and L.D.Talley, 2001) and Sub-Antarctic Mode Water (SAMW) (Fine, 1993; Donohue and Toole, 2003). Both water masses enter the Indian Ocean between 300 m and 500 m, after being formed at convection sites along the STF. SAMW forms between 46°E and 62°E and SEISAMW east of 80°E. ICW is incorporated into the subtropical gyre (Toole and Warren, 1993), spreading westward in the SEC (Schott and McCreary, 2001), and eventually comprises the dominant

mode waters of the Agulhas Current (Beal et al., 2006).

The intermediate levels are predominantly defined by the south-eastern input of fresh Antarctic Intermediate Waters (AAIW) (Fine, 1993) and northern input of high salinity Red Sea Water (RSW) (Beal et al., 2000). The AAIW, formed in the south Pacific (McCartney, 1977) and advected eastward by the ACC south of the STF, enters the Indian Ocean near 60°E and propagates northwards in the subtropical gyre to 10°S, where it is blocked by the equatorial systems (Tomczak and Godfrey, 1994; Fine, 1993; Beal et al., 2006). The saline RSW forms in the Red Sea basin, sinking in response to excess evaporation at the surface and spreading south into the Arabian Sea. Although RSW flux has been estimated at only $\backsim$0.5 Sv Murray and Johns (1997), its very high salinity allows it to be traced through the MZC and into the Agulhas Current (Beal et al., 2006). Beal et al. (2006) also characterise a high-salinity Arabian Sea Low Oxygen Water (ASLOW), formed through the mixing of ASW and water masses from the Bay of Bengal.

The bottom layers are characterised by Lower Circumpolar Deep Water / Antarctic Bottom Water (CDW / AABW), which forms in the Southern Ocean (Emery, 2001). It enters the Indian Ocean through the Madagascan and West Australian basins (Toole and Warren, 1993), but is prevented from entering the central Indian Ocean basin by topography. Above this, the deep waters are characterised by the high-salinity Indian Ocean Deep Water (IDW) (Mantalya and Reid, 1995; Schott and McCreary, 2001), which forms either through deep upwelling of CDW and subsequent mixing with the intermediate waters (Schott and McCreary, 2001), or as a result of incomplete intermediate water formation in the Atlantic (Tomczak and Godfrey, 1994).

In the south west extreme of the basin, North Atlantic Deep Water (NADW) enters the

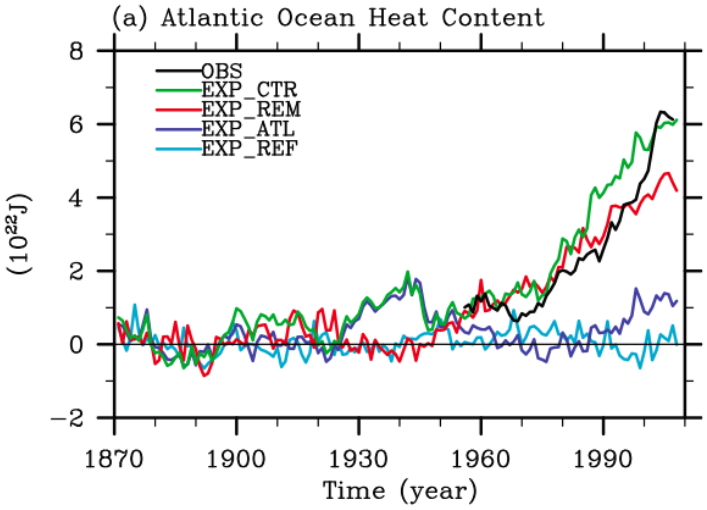

Figure 1.10: Simulated Atlantic Ocean heat content change in the upper 700 m in reference to the 1871 to 1900 baseline period obtained from the four model experiments. The EXP-CTR experiment is the most realistically forced. The EXP-REM experiment highlights the contribution of increased Agulhas leakage to observed Atlantic warming. The thick black line is the observed heat content of the Atlantic Ocean, recomputed from (Levitus et al., 2009) for the Atlantic basin from 30°S to 75°N. [After Lee et al. (2011)].

Water Mass	Temperature [^{o}C]	Salinity	Neutral density [kg.m^{-3}]	Depth [m]
TSW	24.7-26.3	34.9-35.3	25.5-26.5	0-200
STSW	8.0-25.0	>35.5	25.8	200-500
ITF	8.0-25.0	34.4-35.0	26.5 - 26.7	300-500
ICW	7.0-15.0	34.6-35.8	26.6-26.8	300 -500
RSW	7.0-23.0	34.8-40.0	27.3-27.7	500-1500
AAIW	2.0-10.0	33.8-34.6	27.2-27.4	800-1200
IDW	4.0-7.0	34.7-34.8	27.1-27.7	1500-4000
AABW	1.0-2.0	34.6-34.7	27.5-27.7	>3500
NADW	<2.0	34.8	28.0-28.1	>2500

Table 1.1: Characteristics of the major water masses of the SWIO. Acronyms are described in the text. Values are drawn from Beal et al. (2006), You (1997), and Donohue and Toole (2003).

Indian Ocean through the Agulhas Undercurrent (Beal et al., 2006). Due to the constraining effects of topography in the Natal Valley, the NADW is recirculates south at this point. However, the portion of NADW that lies above 3000 m is able to escape the valley across through breaks in the Mozambique Plateau (Beal et al., 2006). A summary of the properties of the Indian Ocean water masses discussed in this section is given in table 1.1.

Anthropogenic forcing has driven a substantial increase in upper ocean heat content in recent decades (Levitus et al., 2001; Barnett et al., 2001, 2005; Levitus et al., 2009). The Indian Ocean is no exception, with substantial warming evident in the southern hemisphere. Further to this, Alory et al. (2007) note that this warming signal is particularly strong in the top 800 m of the subtropical Indian Ocean south of 40^{o}S; a signal that they attribute to changes in dynamical forcing and a latitudinal shift of the subtropical gyre. A warming signal has also been observed in the Agulhas Current (Rouault et al., 2009), though its origin is somewhat unclear.

Since the mid-20th century, the surface layers of the South Atlantic have warmed more than the South Indian and Pacific oceans combined (Levitus et al., 2009). Lee et al. (2011) examined this warming signal and attribute much of the signal to the effects of the increased heat and mass flux through the Agulhas leakage (Fig. 1.10). The CCSM model used in the simulations performed by Lee et al. (2011) is not sufficient to resolve retroflection eddy-processes, and potentially overestimates the magnitude of the Agulhas leakage. However, it is clear from Lee et al. (2011) that any modification of the Agulhas leakage has substantial downstream effects in the South Atlantic, and potentially on the AMOC as a whole (Weijer et al., 1999). With this in mind, a specific focus is now given to the greater Agulhas system.

1.3 The greater Agulhas system: Observations and kinematics

The Agulhas Current, which flows along the coast of southern Africa from 27^{o}S to 35^{o}S, arises due to the western intensification of the predominantly wind-driven south Indian Ocean subtropical gyre (de Ruijter et al., 1999a). As such, western boundary responses are, to some extent, a function of the behaviour of the gyre as a whole. However, the Agulhas Current is defined by

substantial mesoscale variability in its source regions and at its retroflection at the southern tip of Africa, making it impractical to discuss the western boundary responses without reference to these components.

From a global perspective, the Agulhas leakage forms the key climatic feature of the western boundary system (Beal et al., 2011); comprising those waters that are ejected from the Indian Ocean, and are incorporated into the upper branch of the AMOC. The division of Agulhas Current waters into leakage, and those retained by the Indian Ocean is determined by the non-linear dynamics of the Agulhas retroflection. The retained waters are subsequently recirculated back into the upstream Agulhas Current through the Agulhas Return Current and South West Indian Ocean subgyre, forming a feedback loop with the source regions.

Considering the above, the greater Agulhas system is defined as incorporating the following: the Agulhas source regions, the western boundary Agulhas Current (AC; section 1.3.2), its associated Agulhas Undercurrent, the Agulhas retroflection (section 1.3.3), the Agulhas Return Current (ARC; section 1.3.5) and the Agulhas leakage (AL; section 1.3.4). With regard to the source regions; the Agulhas Current is supplied by contributions from three locations; the Mozambique Channel (MZC; section 1.3.1.1), the East Madagascar Current (EMC; section 1.3.1.2) and re-circulated in the South West Indian Ocean subgyre (section 1.3.1.3). Beginning with the source regions, each facet of the greater Agulhas system will be discussed in turn.

1.3.1 Source regions

1.3.1.1 The Mozambique Channel

Fig. 1.11 shows a schematic representation of the upstream source regions of the greater Agulhas system. Driven by the trade winds, zonal flow in the tropical South Indian Ocean is characterised by the South Equatorial Current (SEC), which flows westward in a broad band between the subtropical gyre and the tropical monsoon system to the north (Schott and McCreary, 2001). On encountering the east coast of Madagascar, the SEC splits into two branches around 17°S (Chapman et al., 2003; Siedler et al., 2006); the northward flowing North East Madagascar Current (NEMC) and the southward flowing East or South East Madagascar Current (EMC or SEMC; the former term is adopted, throughout). On reaching Cape Amber, the NEMC travels west towards the coast of Mozambique, where it bifurcates again. The southward fraction enters the MZC; the remainder becomes the northward flowing East African Coastal Current (EACC).

Moored current measurements place the transport at the northern point of Madagascar at 26.9 ± 9.4 Sv (Schott et al., 1988), consistent with geostrophic estimates of 29.1 Sv (Swallow et al., 1991). (Schott et al., 1988) noted substantial intra-seasonal variability in the flow, but only a weak seasonal cycle. However, subsequent analysis of altimetry have determined a pronounced semi-annual cycle (Backeberg and Reason, 2010). Analysis of ALACE drifters released in the intermediate waters east of Madagascar highlight the presence of a gyre system in the north of the channel, with many drifters sequestered around the Comores for months before exiting to the north or south (Chapman et al., 2003). During this period the drifters recorded low

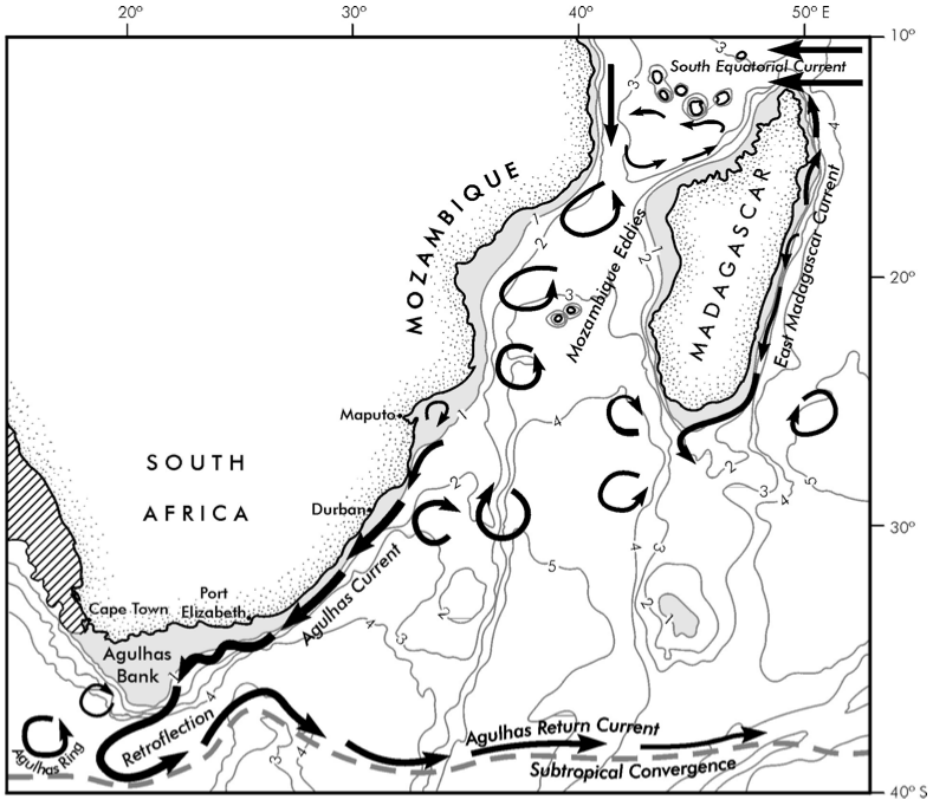

Figure 1.11: A conceptual portrayal of the flow patterns in the greater Agulhas Current. [After Lutjeharms (2006c)]

speeds, typically 5 cm.s^{-1}, less than half the 11 cm.s^{-1} recorded at Cape Amber during the same experiment.

Historically, the Mozambique Channel was considered to contain a continuous western boundary current, carrying a constant flux of warm surface waters southward. Simulations of the South West Indian Ocean imply that this would be the case in the absence of Madagascar (Penven et al., 2006c). However, recent observations and model experiments show that this description is invalid in the realistic case. Analysis of the *in situ* measurements collected during the ASCEX cruise found no evidence of a western boundary current in the channel, instead characterising the flow through a series of anticyclonic vortices, >300 km in diameter, which move steadily poleward (de Ruijter et al., 2002) (Fig. 1.11). The eddies themselves are surface intensified, but reach through the entire water column (de Ruijter et al., 2002), and contain water masses that are markedly different to their surrounds, with heat and salt transport anomalies standing at 1.3×10^{20} J and 6.9×10^{12} kg, respectively (Swart et al., 2010).

Transport estimates for the Mozambique Channel suggest a net poleward transport of $\backsim$16.7 Sv (van der Werf et al., 2010) across the narrowest point of the channel, though this value may fluctuate from 20 Sv northwards to 60 Sv southwards as the anticyclonic eddies pass (Ridderinkhof and de Ruijter, 2003; van der Werf et al., 2010). From hydrographic observations, Ridderinkhof and de Ruijter (2003); Quartly and Srokosz (2004); van der Werf et al. (2010)

shows that this transport predominantly occurs through anti-cyclonic eddies, which form at a rate of $\backsim$4 year^{-1}, with no observed seasonal signal. However, comparing ADCP transport measurements with altimetry products, Schouten and de Ruijter (2003) note that the formation rate in the northern channel is higher (7 year^{-1}), ascribing the difference to modification by incoming Rossby waves. Further, there is some evidence that eddy formation in the north of the channel exhibits interannual and seasonal variability, related to Rossby waves associated with Indian Ocean dipole modes (Palastanga et al., 2006), and transport pulses in the SEC (Backeberg and Reason, 2010). van der Werf et al. (2010) also note that although no seasonal signal can be extracted from observations in the southern channel, it is prevalent in many models, possibly due to an under-representation of signals at other spectral frequencies and, potentially, an incorrect eddy generation mechanism and position in the north of the channel.

In the intermediate and deep waters, a northward flowing Mozambique Undercurrent is observed to flow along the continental slope. ADCP measurements show the current to have two cores at 1000 m and 2400 m, respectively carrying AAIW and NADW north with a total transport of $\sim$5 Sv (de Ruijter et al., 2002). The intermediate waters are subsequently entrained in the southward propagating eddies, returning to the Agulhas retroflection.

1.3.1.2 The East Madagascar Current

On the east coast of Madagascar, the EMC flows south along the continental shelf to Cape Saint-Marie at 25.5^{o}S. Employing the same tandem ship/mooring approach as above, Schott et al. (1988) and Swallow et al. (1991) converged on a transport estimate of 20.6$\pm$6 Sv for the EMC, a value echoed by a later synoptic survey of Donohue and Toole (2003). Little seasonal variability was observed in the transport. Early comparisons of AVHRR derived sea-surface temperature and drifter track data suggested that south of Madagascar, the EMC breaks from the shelf and, much like the Agulhas, retroflects (Lutjeharms, 1988a,b). However, unlike in the Agulhas, the background flow at this point is westerly, leading Quartly et al. (2006) to conclude that a permanent retroflection was unlikely given the lack of an eastward flowing current between 25^{o}S and 30^{o}S to connect to. In contrast, de Ruijter et al. (2005) suggested that, for it to be a permanent feature, the retroflection must necessarily be confined to the boundary layer.

This latter conclusion is supported by the ALACE drifter study of Chapman et al. (2003), who found a near ubiquitous western flow in the subsurface, with little deviation northward into the Mozambique Channel. However, earlier analysis of drift trajectories proved inconsistent suggesting that both westward and southward drift tracks were of importance (Lutjeharms et al., 1981; Lutjeharms, 1988a). Direct current measurements gathered during the ACEX cruise appeared to reconcile the observations, highlighting the presence of a dipole vortex system, consisting of a central jet with counter-rotating lobes on each side (de Ruijter et al., 2004). Subsequent analysis of the TOPEX/POSEIDON altimetry products confirmed the presence of the jet, with opposing anticyclonic and cyclonic eddies, $\backsim$250 km in diameter, formed at regular intervals (de Ruijter et al., 2004). Further hydrographic studies show that only the westward

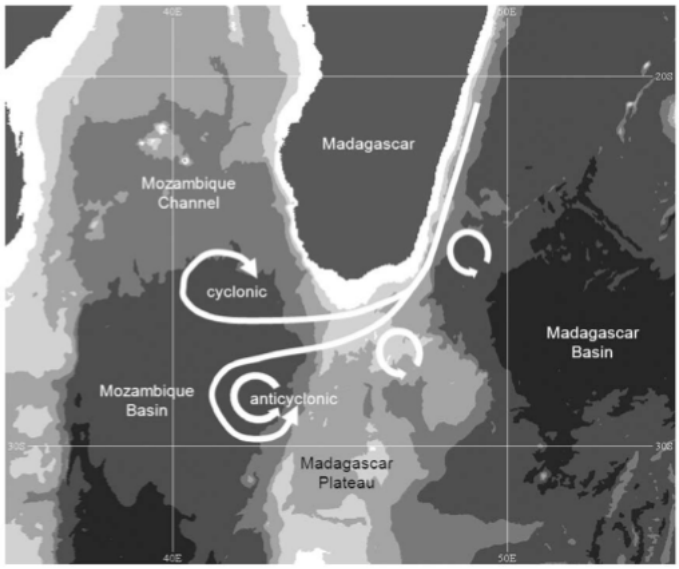

Figure 1.12: Schematic representation describing the modes of the EMC extension. The shading indicates isobaths with 1000 m separation where greater depths correspond to darker shading. [After Siedler et al. (2009)]

travelling anticyclonic eddies retain the water mass properties of the central jet (de Ruijter et al., 2005). The cyclonic, lee eddies, which form during separation from the shelf, adopt a more south-westward trajectory. As a consequence of vortex pair interaction, the mesoscale flow regime in the Mozambique Basin is particularly irregular (de Ruijter et al., 2005).

Recent comparisons of high-resolution model data and satellite observations suggest that in fact the retroflection of the EMC is a more permanent feature, joining with a recently identified South Indian Ocean Countercurrent (SICC) (Siedler et al., 2006). A later study by Siedler et al. (2009) concluded that the EMC has two modes of extension; a branch penetrating into the Mozambique Basin and a branch which retroflects. Cyclonic and anticyclonic eddies are spawned when the former of these two branches is in the appropriate configuration (Fig. 1.12). Siedler et al. (2009) assert that 40% of the SEMC is retroflected, with half carried westward as anticyclonic eddies and the remaining 10% south-westward as cyclonic eddies. Time series analysis of the dipole vortex highlighted significant interannual variability in the formation rate. de Ruijter et al. (2004) established a significant link between the formation of clusters of vortex pairs and the occurrence of negative phases of the IOD and ENSO, related to the anomalously strong flow of the EMC during these episodes.

1.3.1.3 Subgyre recirculation

Observations from moored current meters place Agulhas Current transport at 69.7 Sv (Bryden et al., 2005). Together, the MZC and EMC contribute $\backsim$30 Sv to this flux. The remaining 35 Sv is derived from waters recirculated in the south west Indian Ocean subgyre, which recirculates south of Madagascar (Fig. 1.3.1.3), making it the largest contributor to western boundary flux

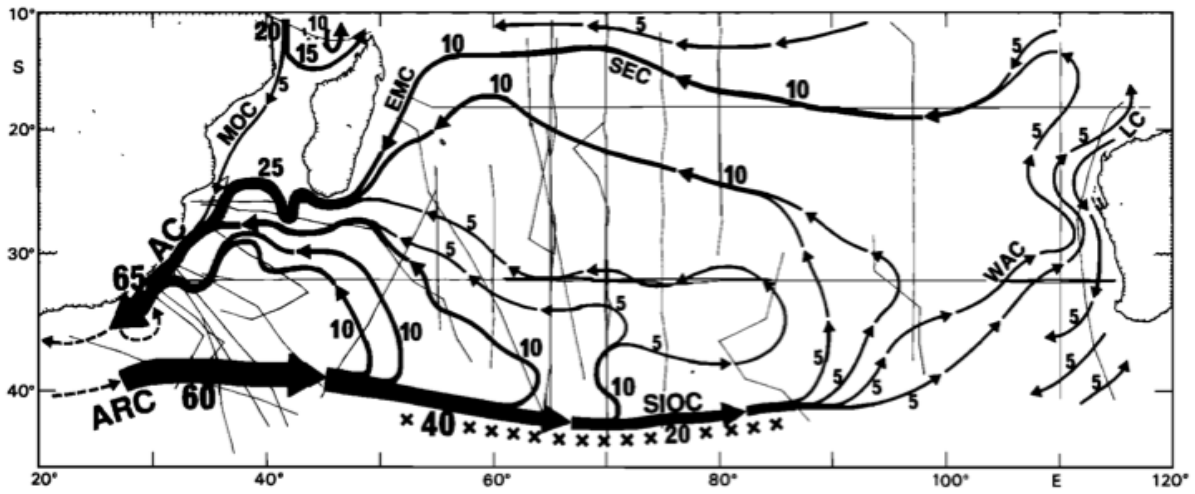

Figure 1.13: Schematic illustration of the flow field in the South Indian Ocean. The transports for the upper 1000 m are given by the numbers in 5 Sv steps. [After Stramma and Lutjeharms (1997)]

(Stramma and Lutjeharms, 1997; Wyrtki, 1971). Approximately 85% of the total recirculated waters are derived from the Agulhas Return Current (Lutjeharms, 2006b). These waters, which consist of retroflected Indian Ocean waters, augmented by some Atlantic contributions, are gradually shed by the Return Current west of 70°E (Lutjeharms and Ansorge, 2001).

1.3.2 The Agulhas Current

The Agulhas Current is the western boundary current of the South Indian Ocean. To the first order, its poleward flow balances the equatorward transport of the subtropical gyre. It can be considered as consisting of two distinct parts; a coherent northern section, which flows along the western boundary between 28°S and Port Elizabeth at 33.5°S, and a more turbulent southern section, poleward and westward of this (Harris et al., 1978; Lutjeharms, 1981). The behaviour of the current in each zone is quite distinctive, and will be discussed separately, beginning in the north.

Flow in the northern Agulhas is defined by narrow boundary flow along the shelf edge, clearly evident from satellite SST products (Lutjeharms, 2006b) (Fig. 1.15, left panel). From hydrographic surveys, Grundlingh (1983) determined the core of the current to be represented by the intersection of the 10°C isotherm with the 200 m isobath (Fig. 1.15, right panel), with surface temperatures and speeds around 22°C and 1.3 ± 0.3 m.s^{-1} (Grundlingh, 1980). From moored current arrays, Bryden et al. (2005) determined that the current extends to ∽200 km offshore and down to 2200 m depth.

Data from the World Ocean Circulation Experiment (WOCE) cruise finds that the current extends from 2300 m to full depth offshore (Donohue et al., 2000). LADCP profiles describe a V-shaped profile, with the Agulhas Undercurrent confined below 800 m on the inshore edge (Beal and Bryden, 1999) (Fig. 1.14). The undercurrent carries ∽6 Sv northwards at speeds of 30 - 40 cm.s^{-1} (Donohue and Toole, 2003; Donohue et al., 2000). While the undercurrent does

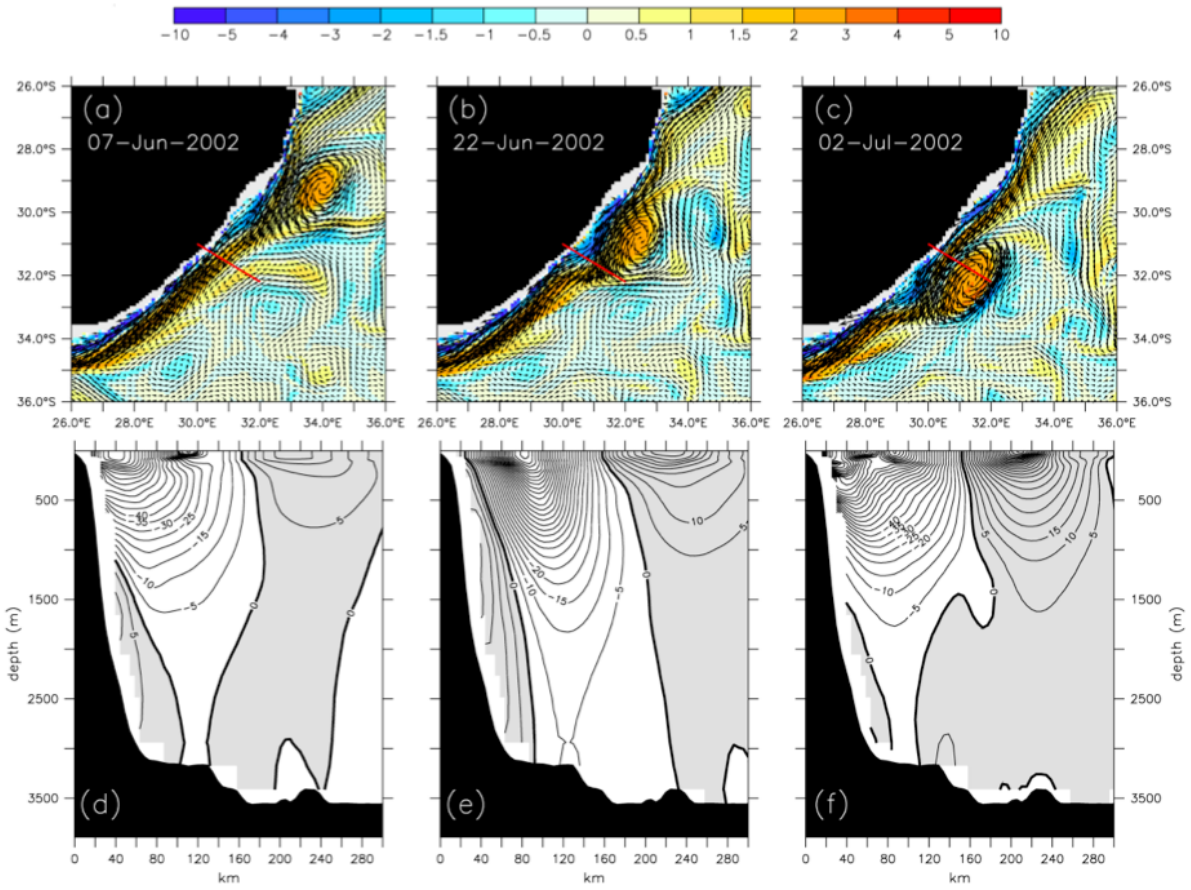

Figure 1.14: Model derived sample snapshots (5-day averages) (a and d) before and during the transition of a (b and e) Natal Pulse and consecutive (c and f) Mozambique eddy: (a-c) showing vorticity (colour, in $10^{-5}s^{-1}$, blue = cyclonic, red = anticyclonic) and velocity (every 2nd vector) at 100 m depth, (d-f) showing simultaneous speeds in a section off Port Shepstone (similar to Fig. 2).. [After Biastoch et al. (2009a)]

carry some modified RSW northward again, the bulk of the undercurrent consists of NADW (Bryden and Beal, 2001).

Unlike other western boundary currents (e.g. the Gulf Stream and Kuroshio), which typically exhibit large scale meanders in their upper reaches, the flow structure in the northern Agulhas is coherent and well defined. de Ruijter et al. (1999b) suggest that the stability of the northern Agulhas Current is a direct consequence of the steep continental slope against which it flows. The exception to this stability occurs around the Natal Bight around 29.5°S, where the slope gradient relaxes generating a large solitary meander; the Natal Pulse (Grundlingh, 1979), discussed more fully below. Grundlingh (1983) estimates that, in the absence of this meander, the current deviates from its mean position by only ±15 km.

Agulhas Current transport estimates in this region, vary greatly from 9 Sv to 90 Sv (Bryden et al., 2005). In general, the more recent 5-daily transport estimate of 69.7 ± 21.5 Sv (Bryden et al., 2005; Beal and Bryden, 1999) (± 4.3 Sv standard error) is considered the most accurate estimate. This value is frequently used as a target for model validation (e.g. Biastoch et al. (2009a)).

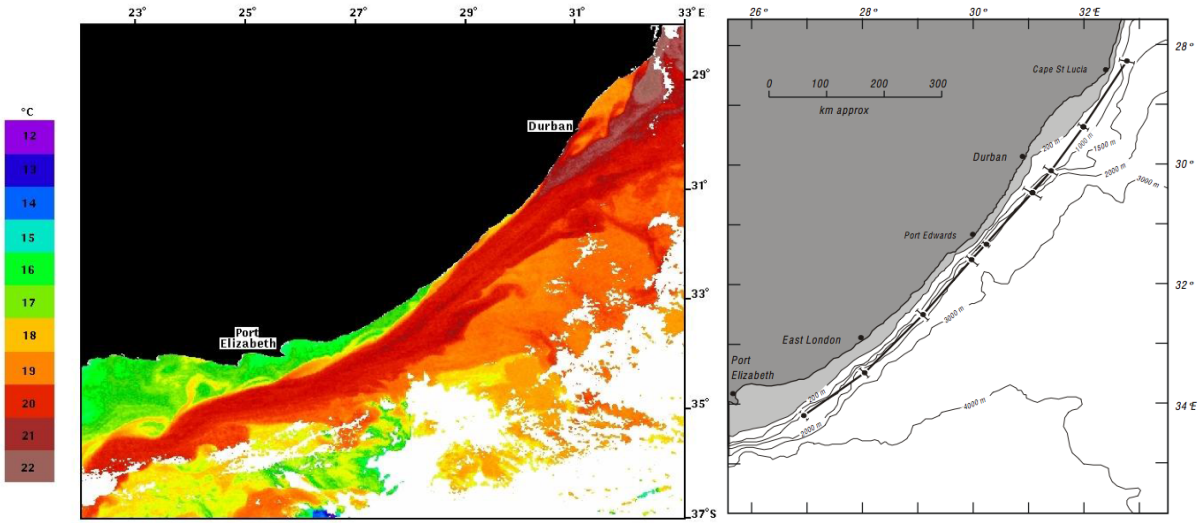

Figure 1.15: Left: Sea surface temperature picture of the northern Agulhas Current as gathered from the NOAA 9 satellite for 26 August 1985 [After Lutjeharms (2006b)]. Right: Location of the core of the northern Agulhas Current. Error bars show the standard deviation at each section, superimposed on the bathymetry. The wider part of the continental shelf between Durban and Cape St. Lucia is termed the Natal Bight [After Grundlingh (1983)].

Beal et al. (2006) note that the water masses inshore of the Agulhas core differ markedly from those offshore. Inshore, water mass properties are consistent with those derived from the Arabian Sea (ASW), Red Sea (RSW) and Indian Ocean equatorial waters (TSW). Offshore, the waters are derived from Atlantic, Southern Ocean and subtropical Indian Ocean waters (STSW). At the surface, and in the intermediate waters, the inshore water masses are separated by a strong a strong cross frontal potential vorticity gradient and kinematic steering (Beal et al., 2006). However, below the steering level, deep waters are able to mix freely. This steering level rises when Natal Pulses pass (*ibid*).

The Natal Pulse is a sporadically occurring solitary meander in the northern Agulhas Current (Grundlingh, 1979). It is generated in the region of the Natal Bight, a section of coastline north of Durban that is defined by a notably wider continental shelf. Estimates of pulse generation frequency around the bight are put at 50-240 days (de Ruijter et al., 1999b) and 4-6 year^{-1} (Lutjeharms, 2006a; Bryden et al., 2005). The pulse travels southwards at a speed of $\backsim$20 km.day^{-1}, steadily growing in size (van der Vaart and de Ruijter, 2001), spawning secondary meanders in the main perturbation (Rouault and Penven, 2011). A synthesis of ASAR and AVISO altimetry data products clearly associates the largest perturbations in the upstream Agulhas Current with the passage of Natal Pulses (Rouault et al., 2010).

At Cape St Lucia, the northern coastal extremity of the bight, the Agulhas Current is forced away from the coast and an upwelling cell consequently develops on its inshore side (Lutjeharms et al., 2000). In addition, deviation of the current jet at this point introduces a barotropic instability, giving rise to the fledgling meander. Lutjeharms (2006b) suggests that pulse generation is a result of topographic changes associated with the widening shelf, as the shelf slope is much less steep at this point. This conclusion is echoed by de Ruijter et al. (1999b) who

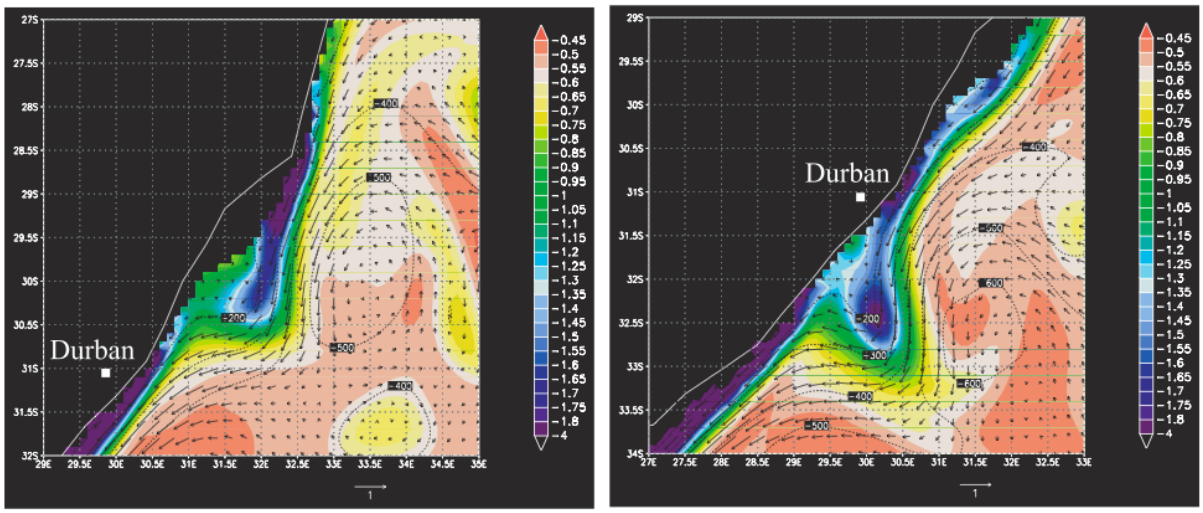

Figure 1.16: Potential vorticity (10^{-6}m^{-1}s^{-1}) of the layer between σ_θ 26.4 and 26.6, when (left) the anticyclonic eddy is off the Natal Bight and (right) the eddy moves in the downstream of the Natal Bight [After Tsugawa and Hasumi (2010)].

note that shallow slope gradient at this point also provides favourable conditions for meander growth. However, the previous authors also note, that pulse generation is accompanied by an anticyclonic eddy which sits to the east of Durban, originating in the southern Mozambique Channel (or further east). Recent model simulations by Tsugawa and Hasumi (2010) suggest that it is the interaction of the core of the Agulhas Current with this eddy that causes the Natal Pulse, with the the topography being somewhat incidental (Fig. 1.16). A parallel experiment from the same authors, in which a modified Natal Bight still generates a pulse appears to support this latter argument, although the simulations in general appear to over-estimate the rate of pulse generation. Between the Natal Bight and Port Edward, remote SST signals suggest that secondary meanders develop behind the primary perturbation (Rouault and Penven, 2011). The authors suggest that formation of these secondary features causes a possible cascade of energy to smaller scales, dampening the meanders such that, by Port Elizabeth, only 1.6 pass per year.

At Port Elizabeth, the continental shelf widens into the Agulhas Bank, signifying the start of the southern Agulhas Current. Changes in the steepness of the continental slope, drive a notable change in Agulhas behaviour (de Ruijter et al., 1999b). In contrast to the comparatively stable northern current, the shallower gradient in the south allows for more freedom of lateral movement. The flow here begins to develop meanders, which grow as they move downstream (Lutjeharms, 2006b). As meanders move downstream, cyclonic eddies form on the landward side of the current core, formed by the contrast between fast moving current water and slow moving shelf water (Lutjeharms et al., 1989). These eddies are theorised to draw current waters onto the shelf in the form of warm plumes, which are subsequently able to spread across the bank. High-resolution ocean models support this hypothesis, suggesting that as eddies become trapped against the Agulhas Bank shelf bight they spawn smaller cyclonic features at intervals

of ∼20 days (Lutjeharms et al., 2003). These eddies propagate downstream at speeds 8 km day^{-1} (*ibid*).

As it proceeds westwards, the Agulhas Current overshoots the edge of the continental shelf around 35°S and flows into the open-ocean as a free inertial-jet (de Ruijter, 1982). Estimates of current speeds here are as high as 2 ms^{-1}, with a total transport of 125 Sv, suggesting a gain of 6 Sv for every 100 km travelled past the shelf (Jacobs and Georgi, 1977). Hydrographic measurements by place the surface temperature at 23°C to 26°C and salinity at 35.4, similar to the northern Agulhas (Gordon, 1986).

1.3.3 The Agulhas Retroflection

Once away from the shelf, the Agulhas Current makes a sharp eastward bend, the Agulhas Retroflection (Lutjeharms et al., 1989), and returns into the Indian Ocean directly to the north of the STF via the eastward flowing Agulhas Return Current (Lutjeharms and Ansorge, 2001). The retroflection is highly turbulent and substantial eddy variability contributes to the highest eddy kinetic energy signal in the global ocean. While the vast majority (>75%) of the incoming mass flux negotiates this bend (Gordon, 1985; Gordon et al., 1987; Lutjeharms and van Ballegooyen, 1988), the remainder is lost to the Atlantic Ocean through the Agulhas leakage (Gordon et al., 1992), and, possibly southward across the discontinuous subtropical front (Dencausse et al., 2011). The Agulhas leakage (section 1.3.4) forms the thermocline connection between the Indian Ocean and upper branch of the AMOC, and is of key importance to global climate. As the magnitude and nature of the leakage is determined by the dynamics of the retroflection, it has been the focus of substantial amounts of theoretical research, numerical modelling and observational programmes. Here, only the latter component is discussed. The current understanding of the physics governing the retroflection is discussed in section 1.4.2.

Despite the dramatic alteration to the course of the flow, the current maintains a constant width and depth throughout the retroflection, penetrating to around 4000 m (Gordon et al., 1987; Schmitz, 1996). Current speeds here mirror those of the Southern Agulhas Current, and are up to 2 ms^{-1} (Lutjeharms, 2006b). The retroflection loop itself has a diameter of 300 - 400 km (Lutjeharms and van Ballegooyen, 1988), but its position is far from static (Lutjeharms and Gordon, 1987). Instead, the retroflection loop continuously progrades into the South Atlantic until an Agulhas Ring is occluded, and the loop is short-circuited, re-establishing itself in a more easterly position (Lutjeharms and Gordon, 1987).

Deriving the retroflection position from absolute SSH data, Dencausse et al. (2010b) place its mean position between 18°E and 20°E, with a defined annual signal (Fig. 1.17). There is no apparent shift in the mean retroflection position between 1992 and 2005 (Dencausse et al., 2010b; Backeberg et al., 2012). Of particular note is the upstream event of 2000/2001 during which the retroflection was temporarily confined behind the Agulhas Plateau far to the east, resulting in a change in seasonal phasing (Dencausse et al., 2010b). de Ruijter et al. (2004) assert that this upstream event was triggered by the influx of a train of unusually coherent dipoles,

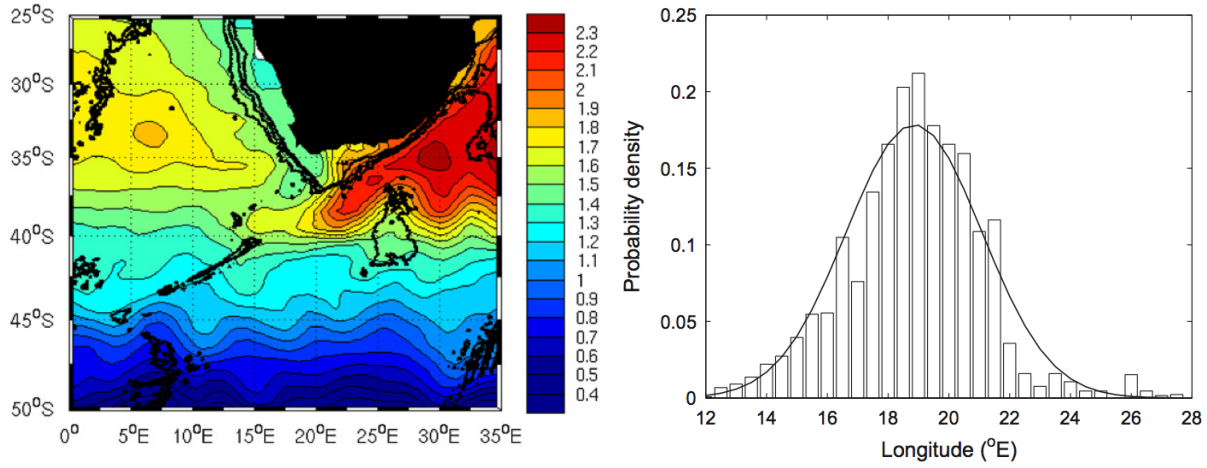

Figure 1.17: Left: Averaged field of SSH (m) for the period 12 October 1992-18 May 2005. Contour interval is 0.1 m. Right: Density of probability of the longitude of the retroflection point between 1992 and 2005 [After Dencausse et al. (2010b)].

produced in the extension of the EMC between late-1999 and mid-2000. During this period, there was a hiatus in the production of Agulhas Rings (Dencausse et al., 2010b), leading to a surmised reduction in leakage (van Sebille et al., 2009a).

Given the apparent relationship between retroflection position and Agulhas Ring occlusion, attempts have been made to use the former as a proxy for Agulhas leakage. van Sebille et al. (2009a) found that leakage and retroflection extent were significantly correlated in an eddy-resolving model, and applied the derived linear regression to an altimetry derived signal. While this approach suggested an implied leakage value of 13.2 Sv, consistent with observations, and captured the 2000/2001 upstream event, in general the wide confidence intervals made the relationship somewhat impractical for predictive purposes.

Numerous studies have linked the production of Natal Pulses with the subsequent occlusion of Agulhas Rings (van Leeuwen et al., 2000; Lutjeharms and Boebel, 2003; Schouten et al., 2002a). However, ring production has also been observed to occur in the absence of such upstream perturbations (Dencausse et al., 2010b). Further, more recent studies of Natal Pulse propagation (Rouault and Penven, 2011) suggest that they alone are unable to account for observed ring occlusion rates. This apparent 'disconnect', and link between ring occlusion and upstream perturbations is revisited in section 1.4.3.

1.3.4 Agulhas leakage

The term Agulhas leakage collectively refers to those Indian Ocean waters that are ejected from the retroflection and persist into the Atlantic Ocean, where they are retained. It represents the thermohaline link between the Indian Ocean and Atlantic Ocean, connecting the western boundary Agulhas system with the upper branch of the AMOC through the "warm-water" route (Beal et al., 2011; Gordon, 1986). As such, it is of particular relevance to global climate, and its variability has been associated with interdecadal AMOC strength (Weijer et al., 2002; Biastoch

et al., 2008b), and glacial terminations (Peeters et al., 2004).

Due to the turbulence of the Cape Basin, measuring the leakage through *in situ* observations has proven to be extremely challenging. The partial expression of leakage through sporadically forming Agulhas Rings complicates deriving estimate of inter-ocean flux from ship based measurements, due to timing concerns. In addition, the leakage occurs over a wide region, making monitoring with moored instrumentation impractical. While satellite altimetry is able to resolve the signal of Cape Basin eddies, it is unable to determine the depth of these features, or determine the portion of advected waters that are of Indian Ocean origin. As such, estimates of leakage magnitude are somewhat broad. Estimates derived from geostrophy, heat and salt fluxes, and ring profiling place the leakage between 2 Sv and 10 Sv (de Ruijter et al., 1999a). Later, drifter-derived, Lagrangian estimates place the leakage at 15 Sv in the top 1000 m (Richardson, 2007). This latter value is generally considered the most accurate, however it was determined from only a small number of drifters, leading the authors to note that it may have a substantial error attached. Thus far, four leakage mechanisms have been identified: through rings, via filaments, as direct leakage and as a coastal jet.

Agulhas Rings are large, anticyclonic eddies, occluded from the retroflection at a rate of $\backsim 5 \pm 1$ year^{-1} (Schouten et al., 2002a) (Fig. 1.18). They have a strong barotropic signal, and are characterised by an annulus of warm (up to 26°C) surface water, up to 240 ± 40 km in diameter, which migrates westward at 5 - 8 km.day^{-1} (Olson et al., 1992) with rotation speeds of 0.29 - 0.90 ms^{-1} (Duncombe Rae, 1991). Initially, the eddy retains the water mass characteristics of the parent Agulhas current, but are modified as they release their heat and salt content to the surrounds (de Steur, 2004; Doglioli et al., 2006). Further, substantial heat loss to the atmosphere drives convection and overturning, modifying vertical structure (Olson et al., 1992; Walker and Mey, 1988). A census of ring characteristics suggests that they exhibit a broad spectrum of characteristics, showing marked deviations from the mean values for size, surface temperature and rotational speed; deviations which become more apparent once the rings have left the retroflection zone (Schmid et al., 2003) and are dependant on the season of formation, time spent in the Cape Basin (Arhan et al., 1999) and their route into the South Atlantic (Dencausse et al., 2010a). The processes governing Agulhas Ring formation are discussed in section 1.4.3.

Estimates of the contribution of Agulhas Rings to total leakage vary from 5 Sv to 15 Sv (Richardson, 2007; Gordon, 1985; Gordon et al., 1987; Byrne et al., 1995; van Ballegooyen et al., 1994), with most studies placing it as the dominant contributor to total inter-basin flux. The rings remain coherent and detectable as far as the mid-Atlantic (Arhan et al., 1999), remaining poleward of 20°S (Byrne et al., 1995). As they head westward, they are subject to modification by topography at the Walvis Ridge (Richardson and Garzoli, 2003). Schouten and de Ruijter (2000) show that the rings lose 70% of their kinetic energy in the first 5 months of their lifetime; a loss that is partially attributable to interaction with other eddy features in the Cape Basin., during which there is substantial exchange of intermediate water masses (Boebel et al., 2003a).

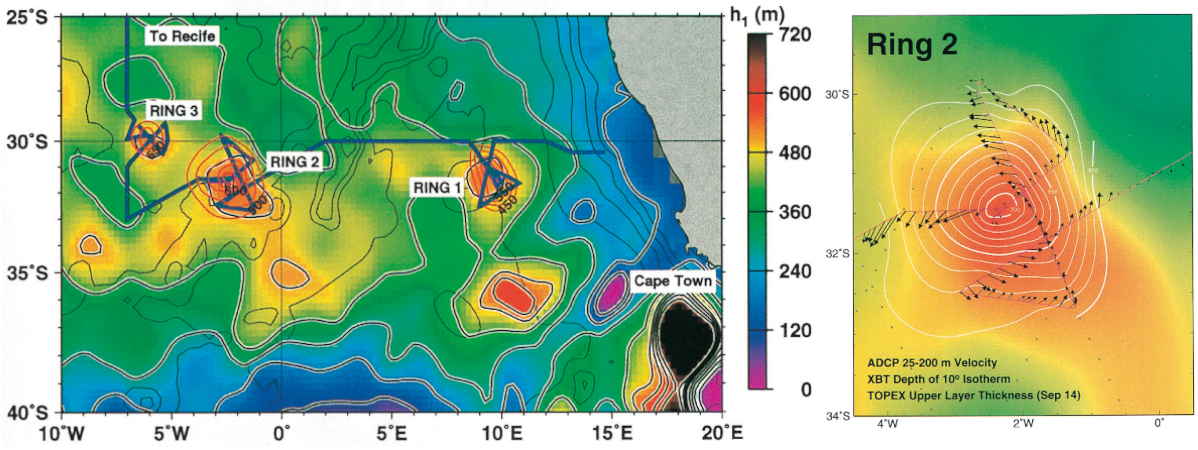

Figure 1.18: Left: Locations of the three rings as depicted by the altimeter upper layer thickness map corresponding to September 16, 1997. Also shown are the cruise tracks (blue line), hydrography-derived depths (meters) of the 10°C isotherm (red contours), and bathymetry (black contours). Right: Vectors are acoustic Doppler current profiler (ADCP) upper ocean velocity averaged between 25 and 200 m along the cruise track. The upper layer thickness from TOPEX/POSEIDON altimetry is depicted in the coloured background images. Red shades correspond to greater thickness, green shades to lesser thickness. The locations of the TOPEX/POSEIDON data points are indicated by small circles. The 10°C isotherm depth determined from the expendable bathythermograph (XBT) surveys is contoured in white. [Adapted from Garzoli (1999)].

Boebel et al. (2003a) also note the occurrence of small cyclonic features near the retroflection. Penven et al. (2001) show that these occur as lee eddies, a response to the interaction between the current jet and the shelf, but that, while these may modify Agulhas Rings, they occur *in situ* and are devoid of Indian Ocean water, themselves.

Lutjeharms and Cooper (1996) show that inter-ocean exchange may occur through spindle-like filaments, which split off from the northern edge of the retroflection loop. These filaments, present approximately half the time, are only 50 km in width and penetrate to 50m depth (*ibid*). Although their heat content is quickly dissipated by atmospheric exchange, the salt content (1-5 $\times$ 10^{11} kg) is notable, making a substantial contribution to inter-ocean leakage (Lutjeharms and Cooper, 1996). However, as the filaments are not as long lived as Agulhas Rings they do not have as extensive an impact in the Southern Atlantic (van Sebille et al., 2010b; Treguier et al., 2003).

A final contribution to the inter-ocean exchange is made by direct leakage. Gordon et al. (1987) calculate this volume flux to be up to $\backsim$10 Sv. However, Lutjeharms (2006b) suggest that, at the upper bound, this estimate is exceptionally high given a total observed leakage of up to 15 Sv (Richardson, 2007). This flow may partially occur through an intense frontal jet along the African Coast (Bang and Andrews, 1974), however, it is not well investigated.

1.3.5 The Agulhas Return Current

The southern branches of the subtropical gyres are expressed through the eastward flowing South Atlantic and South Indian Currents in their respective basins. Between 12°E and $\backsim$70°E, these

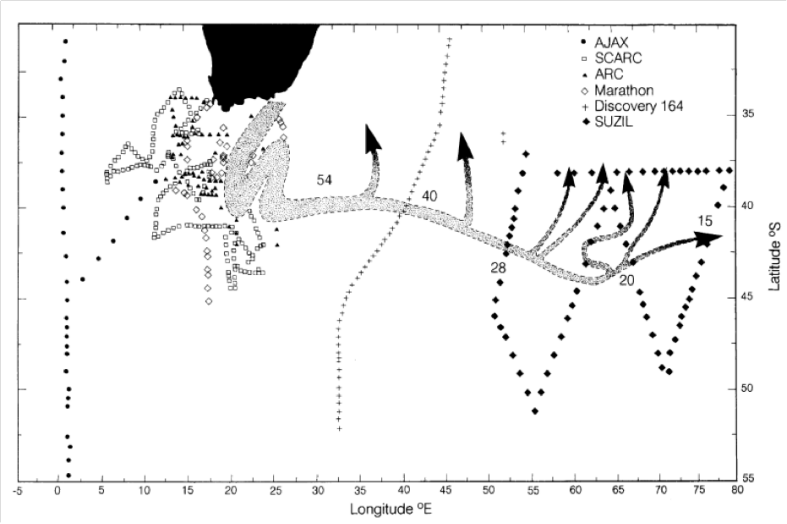

Figure 1.19: The volume transport (in Sv) of the Agulhas Return Current system along its full length, suggesting the locations of major leakage from the current. These locations are inferred from the reduced volume transport values between adjacent sections [After Lutjeharms and Ansorge (2001)].

two systems are connected by the Agulhas Return Current, forming the southern branch of the super-gyre (Lutjeharms and Ansorge, 2001). As discussed above, the Agulhas Return Current (ARC) is predominantly formed from the retroflected waters of the Agulhas Current, and, in the western basin, flows eastwards immediately to the north of the Subtropical Front (STF).

A synthesis of available hydrographic data by Lutjeharms and Ansorge (2001) shows a reduction in geostrophic speed relative to 1500 m along the current path; values of 75 cm.s^{-1} are recorded post retroflection, dropping to 13 cm.s^{-1} at 76°E. Analysing data from the 1997-1999 KAPEX programme, Boebel et al. (2003b) place surface speeds at up to 2.1ms^{-1} at the retroflection, and at 1.1ms^{-1} around 32°E, broadly consistent with previous estimates (Lutjeharms and Ansorge, 2001). The two studies also present convergent transport estimates for the 70 km wide current core; Boebel et al. (2003b) calculates an average transport along the current of 44 $\pm$ 5 Sv in the top 1000 m, while Lutjeharms and Ansorge (2001) record western and eastern (76°E) values of 15 Sv and 54 Sv, respective to a 1500 m reference level (Fig. 1.19). The transport reduction reflects the loss of volume flux into the Indian Ocean subgyre to the north (Park et al., 1993; Stramma and Lutjeharms, 1997) (Fig. 1.19). Post retroflection, ARC waters masses are notably different from those upstream. Due to lateral mixing and atmospheric interaction at the retroflection, no trace of the previously present TSW remains (Lutjeharms and Ansorge, 2001). Additionally, the intermediate depths are freshened by the inclusion of Atlantic waters.

The ARC, which exhibits very high mesoscale variability, is characterised by the presence of extensive meridional meanders, extending up to 2°N (Lutjeharms and Ansorge, 2001). The most westward of these meanders (typically referred to as the first meander), is partially meridionally constrained by the presence of the Agulhas Plateau, which the return current tends to traverse to the north of (Lutjeharms and Valentine, 1988). Subsequent, more eastward meanders are less topographically constrained, and are, therefore, more able to freely migrate westward along

the current itself (Lutjeharms and Ansorge, 2001). In concert, extreme northward migrations in these meanders and southward deviations in the Agulhas Current may cause a short circuit that leads to Agulhas Ring occlusion and an early retroflection (Boebel et al., 2003a; Dencausse et al., 2010b).

As a result of shear instability between the ARC and subtropical convergence, cold core eddies are periodically shed from the northward side of the ARC, with the strongest cyclonic features most common in austral autumn (Boebel et al., 2003b). These subsequently move westwards and are re-absorbed by the next meander they encounter. Similarly, Lutjeharms and van Ballegooyen (1988) suggest that warm water eddies that form on the pole-ward side of the ARC may be similarly re-incorporated into meanders when they don't dissipate *in-situ*.

1.4 The greater Agulhas system: Numerical modelling and dynamics

One does not simply model the Agulhas. Biases in the representation of the western boundary current, retroflection position and ring path are well catalogued. Inappropriate numerical choices may cause the Agulhas Current to be represented as a train of eddies, as opposed to a continuous stream (Barnier et al., 2006; Backeberg et al., 2009). Numerous models exhibit high levels of eddy-kinetic energy east of the retroflection, indicating erroneous upstream recirculations (Wallcraft et al., 2003). In extreme cases, the retroflection itself occurs far to the east of the observed position Sasaki et al. (2005). Consequently, while altimetry suggests that rings take multiple paths across the Cape Basin and spread substantially across the South Atlantic, biases in retroflection position may produce rings that follow an overly specific path. This is typically evident in a strong eddy kinetic energy signal expressed in a narrow eddy-corridor across the Cape Basin (Maltrud and McClean, 2005).

Equatorward flow in the ocean interior, driven by the wind stress curl must, at some point, be balanced by the poleward flow in the western boundary. However, in the Agulhas, two factors that warrant specific consideration. Firstly, the presence of Madagascar induces substantial eddy variability in the upstream western boundary. Secondly, the African continent terminates equatorward of the zero-line of wind stress curl, but the resulting free jet is choked by the inertia of the Agulhas Current (de Ruijter, 1982). As the link between the South Indian and South Atlantic Ocean is of key importance to the global meridional overturning circulation, it is critical to understand why this choking effect occurs. In consequence, the greater Agulhas system, its retroflection dynamics, and its associated inter-basin flux have been extensively studied using numerical simulations. With continuing increases in computational capability, these simulations reach ever-finer scales, allowing for the explicit representation of the mesoscale field, often in the context of realistically forced hindcast simulations. These latter experiments have raised further questions about the link between western boundary transport and Agulhas leakage specifics under changing winds.

1.4.1 Western boundary non-linearity

Sverdrup dynamics dictate that the poleward transport of a western boundary current can be determined from the wind stress curl across the adjacent gyre. However, recent hindcast experiments differ with regard to how closely the Agulhas Current conforms to this regime. Rouault et al. (2009) suggest that the Agulhas Current is Sverdrupian on a decadal basis, showing similar trends in the measured and theoretically inferred transport. However, the signals are inconsistent on an interannual basis, and the Sverdrup relationship is integrated across the basin from 33°S to 21°S. Conversely, from interannually forced OGCM simulations, Biastoch et al. (2009b) found a distinct discrepancy between between the transport expected through the Sverdrup relationship at 32°S and those modelled numerically. The authors ascribe the disparity to non-linear eddy-mean interactions and topographical shielding. Currently, the degree to which the Agulhas Current transport responds linearly to the winds remains ambiguous.

Eddy-mean interactions are prevalent in all western boundary currents, however, in the case of the Agulhas, the effect is enhanced by the presence of Madagascar, which induces substantial eddy variability upstream, and the Agulhas Undercurrent (Biastoch et al., 2009a). Penven et al. (2006c) underline this effect, performing experiments in which the island is excised. Here, a continuous western boundary current forms along the African coast from $\backsim$15°S. Further south this results in notable changes to the transport spectra at Port Elizabeth (25.5°S). However, while the timing of Agulhas Rings was altered, suggesting a link between the upstream eddy field and the rate of downstream ring generation, the leakage magnitude was not significantly affected. This link between upstream eddy formation and downstream ring shedding echoes the observations of Schouten et al. (2002a). In addition, Biastoch et al. (1999) suggest that the eddies in the Mozambique Channel also play a key role in determining the seasonality of the Agulhas Current; a signal only recently confirmed through along-track altimetry (Krug and Tournadre, 2012). Further highlighting this point, Biastoch et al. (2009b) compare the Agulhas Current transport time series for simulations with an eddy-resolved and coarse resolution Mozambique Channel, noting substantial differences in western boundary volume fluctuations between the two, changes in Agulhas Ring timing and path, but no change in leakage.

Agulhas non-linearity also occurs due to topographical insulation of the western boundary. At lower latitudes, Rossby waves associated with basin scale adjustment are less sensitive to bottom topography (Biastoch et al., 1999). However, in two related studies Matano et al. (1999) and Matano et al. (2002) modelled the seasonal cycle of the south Indian Ocean, noting that, in the subtropics, the western boundary is strongly shielded by the topography to the east.

1.4.2 Retroflection dynamics

The Agulhas retroflection is a defining component of the regional circulation. Its dynamics determine the division of waters into those retained by the Indian Ocean and those exported into the South Atlantic. Theory and numerical modelling studies suggest that its behaviour is governed by five factors: inertia and planetary vorticity advection (the β-effect), vortex stretching,

coastline geometry, bottom topography, and the wind field structure over the higher latitudes of the Indian Ocean (de Ruijter et al., 1999a).

Using a weakly non-linear, one-layer model de Ruijter (1982) shows that the inertia of the Agulhas Current, which allows it to overshoot a highly-idealised continental shelf as a free-jet, is critical in establishing the retroflection. The Agulhas Return Current subsequently arises due to the accumulation of negative vorticity as the jet flows poleward. In this model, the decrease in wind stress curl across the inertial boundary layer region south of Africa, determines how much transport the Agulhas Current can unload in the Sverdrup transport regime to the east via the Agulhas Return Current (*ibid*). Consequently, a more severe decrease in wind stress curl results in a larger separation between the Atlantic and Indian sub-gyres, resulting in a stronger Agulhas Return Current, and by extension, a weaker leakage; a process termed 'inertial-choking' (de Ruijter et al., 1999a). de Ruijter and Boudra (1985), Boudra and de Ruijter (1986) and Boudra and Chassignet (1988) confirmed this inertial relationship in a series of barotropic and baroclinic cases, using highly idealised basin geometry throughout. Analysis of the vorticity balance showed that decreases in planetary vorticity are compensated for by an increase in anticyclonic relative vorticity. As such, the Agulhas retroflection is in part driven by the β-effect. Further, vortex stretching in the upper layers of the Agulhas Current generates positive relative vorticity once it separates from the coast. In tandem with the β-effect, this encourages flow to return in an anticyclonic loop (Boudra and Chassignet, 1988).

Retroflections are also possible in high-friction cases (Boudra and Chassignet, 1988; Chassignet and Boudra, 1988). However, Dijkstra and de Ruijter (2001) show that only those governed by inertia are valid, as high-friction may produce a non-physical barrier to inter-ocean transport due to viscous choking. In addition to the inertial and viscous retroflection regimes, Le Bars et al. (2012) describe a third case. Here, the Agulhas leakage reaches an asymptotic maximum at high wind stress due to an increase in turbulent cross frontal mixing in the Agulhas Return Current and a southward loss of Indian Ocean waters.

Although it is not the sole determinant, the viscosity of a configuration is in part dependant on the spatial resolution employed. At low resolutions, numerical viscosity is typically high. Dijkstra and de Ruijter (2001) suggest that $1/6^{o}$ is necessary to capture an inertial retroflection, while Beal et al. (2011) suggest $1/10^{o}$ is required. However, these numbers are largely unqualified, and, as viscosity is also a function of the numerical scheme employed, are somewhat misleading. Despite this caveat, as hindcast simulations and projections performed with coupled climate models typically employ an ocean circulation model with resolution of 1^{o} or coarser (Meehl et al., 2005), it is likely they exhibit viscous retroflection regimes, resulting in potentially unrealistic behaviour associated with an over-expressed Agulhas Leakage (Dijkstra and de Ruijter, 2001).

In general, early studies investigated the behaviour of the Agulhas in a highly idealised basin, with the African continent represented by a rectangular of triangular landmass. Ou and de Ruijter (1986) considered the separation of the Agulhas Current from a curved coastline

geometry. They found that an increasingly curved coastline causes an earlier coastal separation and a more eastward retroflection position. This earlier separation is driven by a shoaling of the upper ocean layers caused by the accumulation of anticyclonic shear in the current. Further, their idealised system was highly sensitive to Agulhas Current transport, suggesting that an increase in incoming volume flux results in an earlier (more eastward) retroflection position. In the converse case, a reduction of 10% of the volume flux was enough to cause the entire Agulhas Current to flow into the South Atlantic, a configuration which remains undocumented in observations. However, Ou and de Ruijter (1986) make no mention of leakage in their study, which also produced no Agulhas rings.

In most cases the idealised experiments described above feature a flat bottom. Matano (1996) compared the circulation of a flat bottom 15-layer model, to the same configuration with realistic bathymetry. The latter case showed a strong, realistic retroflection, while the former showed almost no retroflection, suggesting that bathymetry may play a key role in the retroflection behaviour. However, the flat bottom experiments performed by Boudra and de Ruijter (1986) and Chassignet and Boudra (1988) show substantial retroflections, suggesting an apparent inconsistency. Performing a parameter space analysis, Dijkstra and de Ruijter (2001) suggest that the retroflection described by Matano (1996) may not be inertially governed. However, as yet, no analytical study has specifically focussed on the role of bathymetry in the inertial regime.

Speich et al. (2006) considered the role of bathymetry in Agulhas Current behaviour using a $1/6^{o}$ regional primitive equation model. They show that coastal bathymetry plays a key role in determining current path. Removal of the Agulhas Bank enhances inter-ocean flux substantially, as does smoothing of the continental shelf. When the Agulhas Plateau is removed, meridional meanders in the Agulhas Return Current move steadily westward.

1.4.3 Agulhas ring shedding

Agulhas rings are the predominant pathway through which the Agulhas Current exports its water masses to the Atlantic Ocean, forming a turbulent link in the global thermohaline conveyor. Locally, isopycnic models suggest that ring generation occurs as a result of mixed barotropic-baroclinic instabilities in the sheer zone of the retroflection loop (Chassignet and Boudra, 1988). Ring formation is additionally dependant on continental configuration, with a triangular landmass producing more rings than its rectangular counterpart (Chassignet and Boudra, 1988).

Pichevin et al. (1999) and Nof and Pichevin (1996) considered the effects of the integrated balances on ring formation processes. Under a series of quite specific conditions, they determined that, in a non-linear gravity model, the retroflection loop can have no integrated momentum flux balance; the 'retroflection paradox' (Nof and Pichevin, 1996). The shedding of rings solves this apparent problem, provided that the inertial flow is uniform, conserves potential vorticity and leaves the region as parallel geostrophic flow. Relaxation of these conditions suggested that retroflection regimes may occur with and without eddy shedding, with coastal geometry and the

retroflection latitude as the controlling parameters (Pichevin et al., 2009).

Using a one-and-a-half layer model, Zharkov and Nof (2008b) and Zharkov et al. (2010) specifically considered the effect of coastline geometry on ring occlusion. They determined that, if the retroflection is pushed northwards (e.g. during a northward migration of the zero line of wind stress curl, potentially associated with glacial phases), the near north-south orientation of the African coast would preclude ring formation. Only where the angle is below a critical value of 60^o will rings successfully break from the current and escape westwards, a result echoed by Pichevin et al. (2009). Ring occlusion is stimulated by the growth of downstream meanders, driven westward by the β-effect. In consequence, rings may only occur when the continent terminates, allowing meanders to drift westward unimpeded, or when the continental angle is sufficient to allow along coast drift to separate rings from the main current (Pichevin et al., 2009). In addition, Nof et al. (2011) show that in the case of increased westerly wind stress, the progress of occluded eddies may be sufficiently retarded so as to prevent their escape.

Upstream perturbations may also play a role in the ring occlusion process. The protrusion of the Natal bight causes the sporadic generation of large meanders in the Agulhas Current (Harris et al., 1978; Lutjeharms and Roberts, 1988). In their reduced gravity model, Pichevin et al. (1999) considered the role these perturbations may play in ring occlusion. Their analysis determined that offshore meanders have little effect on the frequency of ring occlusion, but that transport pulses may contribute to ring formation. Observations from altimetry echo this point, showing a disparity between Natal Pulse occurrence in the Southern Agulhas and ring occlusion rate (Rouault and Penven, 2011).

In a series of idealised numerical experiments performed with a coarse resolution ocean model, Fetter et al. (2007) determined that the winds across the subtropical Atlantic contribute substantially to the annual signal of Agulhas Current transport. However, given the 1/2^o resolution of the model used in this study, the authors were unable to draw any conclusions with regard to the sensitivity of the Agulhas leakage to this forcing.

1.5 Multi-decadal signals and climatic role

Reanalysis forced hindcasts, performed with high-resolution ocean models, suggest that, post-1970, changes in the Indian Ocean wind field have driven a substantial increase in the Agulhas leakage (Biastoch et al., 2009b; Rouault et al., 2009). Although these differ in their numerics and atmospheric forcing, both studies record a warming of the Agulhas during this period, consistent with the satellite derived SST trend. This increase in leakage, projected to continue under further intensified westerlies (Biastoch and Böning, 2013), is expected to further salinity (*ibid*) and temperature (Lee et al., 2011) in the South Atlantic. However, while Biastoch et al. (2009b) show a weakening Agulhas Current during this 1980-2007 period, Rouault et al. (2009) record a strengthening.

As discussed previously, idealised numerical experiments (de Ruijter, 1982; de Ruijter and Boudra, 1985; Boudra and Chassignet, 1988) find that a stronger Agulhas Current is associated with a weaker leakage. van Sebille et al. (2009b) extend these dynamical arguments to the realistic case, suggesting that the anti-correlation between the current and leakage expressed in Biastoch et al. (2009b) has a dynamical basis (section 1.4.2). Latterly, van Sebille et al. (2010a) infer that Rouault et al. (2009) lacks the necessary resolution to simulate an inertial retroflection; a problem outlined by Dijkstra and de Ruijter (2001). However, this inference has been suggested to be incorrect, as the SAfE configuration used by Rouault et al. (2009) has sufficient effective resolution and zero explicit viscosity (*P. Penven; Comment on "Sea surface slope as a proxy for Agulhas Current strength" and pers. comms.*). Further, the trends in Rouault et al. (2009) are consistent with an eddy-resolving Hybrid Coordinate Ocean Model hindcast (Backeberg, 2010). As such, arguments centering on resolution do not appear to give an adequate answer with regard to this ambiguity and it remains unclear as to whether the simulated signals are driven by local inertial processes, or are the result of long term trends in the prevailing wind fields.

Retroflection separation studies (Ou and de Ruijter, 1986) imply that a weakening (strengthening) Agulhas Current should be associated with a westward (eastward) shift in mean retroflection position. However, no such shift has been observed in the modern paradigm (Dencausse et al., 2010b; Backeberg et al., 2012), despite substantial modification of the Indian Ocean winds in the past two decades (Backeberg et al., 2012; Swart and Fyfe, 2012; Gillett and Thompson, 2003). van Sebille et al. (2009a) did find a statistically significant link between retroflection position and Agulhas leakage on shorter timescales, with the latter decreasing as the retroflection proceeds westwards. However, attempts to apply the model-derived linear relationship between the retroflection position and leakage to altimetry were largely unsuccessful, due to the wide, $\backsim$15 Sv confidence interval surrounding any prediction. Franzese et al. (2009) also raise the possibility that the retroflection retained its modern position at the Last Glacial Maximum (LGM), despite the possibility of substantial changes in the winds compared to recent observations (Kohfeld et al., 2013).

On climatic timescales, the changes in Agulhas leakage have been implicated in the termination of glacial phases (Peeters et al., 2004) and subsequent increase of AMOC strength (Knorr and Lohmann, 2003). In the glacial state, leakage is hypothesised to be greatly reduced due to the northward migration of the STF, driven by a northward shift in the SHW winds (Bard and Rickaby, 2009). However, recent research underlines substantial uncertainty in the state of the westerly winds during the LGM (Kohfeld et al., 2013). In addition, there is evidence that the frontal systems north of the Southern Ocean are not as intimately linked with the winds as palaeoceanographic studies assert (Graham et al., 2012).

1.6 Conclusions

The greater Agulhas is a complex, highly non-linear system that dominates the oceanography of the South West Indian Ocean. It plays a key role in modulating the strength of the AMOC and, by extension, global climate on multi-decadal to glacial-interglacial timescales. It is clear that the behaviour of the Agulhas system is highly dependant on the winds across the Indian Ocean basin; which are divided into the easterly trades and southern hemisphere westerlies. Understanding how the system responds to variability in these wind belts is essential when attempting to extrapolate and simulate its behaviour under various palaeoclimatic and future scenarios.

While substantial efforts have been made to isolate the processes that govern the retroflection, idealised approaches, by definition, sacrifice some complexity. On the other hand, interannually forced hindcast simulations seek to reproduce a realistic Agulhas, retaining as many processes as possible. However, the reanalysis products used in these simulations contain a complex superposition of wind signals, and, in consequence, disentangling the various responses becomes a significant challenge. An approach is needed where the dynamical insight offered by idealised scenarios can be balanced against the realism offered by the realistic circulation within primitive equation models. Regardless of the model approach adopted, horizontal resolution, and by extension the balance between inertia and viscosity, appears to be critical to the behaviour of the Agulhas system (Dijkstra and de Ruijter, 2001).

Modern observations suggest that both the trade and westerly wind systems are intensifying, with the latter also moving southward (Backeberg et al., 2012; Swart and Fyfe, 2012; Gillett and Thompson, 2003; Thompson and Solomon, 2002). Inertial arguments, drawn from numerical experiments, suggest that increased trades may drive greater western boundary transport, and a decreased leakage. But is this the case in the realistic ocean? Current hindcast experiments do not appear to reach a consensus, and ambiguity remains.

Of more potential relevance to palaeoceanography is the role of the westerlies. Modification of the SHW and attendant responses on the STF are frequently invoked as a driving force through which the Agulhas gateway, and its attendant leakage, can be constricted (Bard and Rickaby, 2009). From a modern perspective, this appears feasible, as hindcasts unanimously suggest a leakage increase as the STF and supergyre are driven south by anthropogenic forcing and ozone depletion (Cai, 2006; Biastoch et al., 2009b; Biastoch and Böning, 2013). However, it is unclear if this increased leakage is driven by the widening of the Agulhas gateway, or the strengthening of the winds.

This leaves palaeoceanographic assertions about the response of the Agulhas during potential LGM states somewhat ambiguous, especially given the lack of consensus about the wind state and latitude of the STF (Kohfeld et al., 2013; Sime et al., 2013) at that time.

Here, a proposed framework is developed, which allows the effects of variations in the trade and westerly wind systems can be considered separately. The aim is to address the following:

Outstanding questions:

- What is the structure and magnitude of the Agulhas leakage, and how has this changed in recent times?
- How do the source regions of the Agulhas Current respond to changes in the trade wind pattern across the Indian Ocean?
- How do these changes propagate downstream in the western boundary, and what is the effect on the Agulhas leakage?
- What effect do the westerly wind changes have on the Agulhas leakage?
- Can separation of the wind fields into the trade and westerly wind systems provide an insight into the interannual trends in the Agulhas Current and leakage?

To realise these goals, a new suite of eddy-permitting and eddy-resolving configurations has been developed using the Regional Ocean Modelling System (ROMS). The outcome of this research enhances the understanding of the dynamics of the Agulhas system, its role in the climate system and the interpretation of recent trends.

This manuscript will proceed as follows: **Chapter 2** and **Chapter 3** present an introduction to the regional model configurations used in this study and an assessment of their performance with respect to obervations. **Chapter 4** compares and contrasts methodologies used to quantify the Agulhas leakage and determine its structure. **Chapter 5** discusses the effect that climatic changes in the Indian Ocean trade-wind pattern has on the nature of the flow in the greater Agulhas system and ramifications for the leakage. **Chapter 6** focusses on the response of the greater Agulhas system to idealised changes in the westerly winds, including a discussion on the interannual signals seen in previous hindcasts. Finally, **Chapter 7** summarises the conclusions of this work and presents avenues that warrant further investigation.

Chapter 2

Contructing a basin-scale model of the greater Agulhas Current system

2.1 Introduction

Western boundary currents play a key role in the global ocean circulation, carrying large quantities of tropical heat poleward and influencing local and global climate variability on interannual to millennial timescales (Kwon et al., 2010; Beal et al., 2011; Peeters et al., 2004). Although predominantly wind-driven, turbulence associated with eddy-mean interactions induces a degree of non-linearity, exacerbated by the complex topographical interactions associated with flow along continental margins (Biastoch et al., 2009a; Speich et al., 2006; Matano, 1996). As such, they present significant challenges to the development of regional model configurations that seek to accurately simulate their dynamics, and, subsequently the large-scale consequences of their behaviour.

As the major western boundary current of the Indian Ocean, the Agulhas Current is no exception, but there are a number of factors that make it unique. Firstly, although all western boundary current shed rings (Richardson, 1983; Li et al., 1998), in the Agulhas system these represent a significant climatic link in the global meridional overturning circulation (Gordon, 1986). Secondly, the Agulhas Current retroflects south of Africa, returning most of its constituent waters to the Indian Ocean (Lutjeharms and van Ballegooyen, 1988). Thirdly, the proximity of the southern tip of the African continent to both the sub-tropical front and line of zero wind-stress curl presents a viable mechanism under which the width of the Agulhas 'Gateway', and the magnitude of inter-basin flux through it, can be modulated by climatic events, both palaeoclimatic (Bard and Rickaby, 2009; Peeters et al., 2004) and, potentially, anthropogenic (Biastoch and Böning, 2013). Lastly, the connection between the Agulhas Current and the basin scale adjustment of the Indian Ocean is interrupted by the presence of Madagascar (Penven et al., 2006c); inducing upstream variability that exerts an effect on the flow pattern further south (Biastoch et al., 1999).

As a result of these complexities, numerical modelling of the Agulhas requires special con-

sideration. Previous studies have shown that, in turbulent systems, model solutions can be highly sensitive to numerical choices (Backeberg et al., 2009; Barnier et al., 2006). Further, the simulated behaviour of the Agulhas retroflection depends on the horizontal resolution of the configuration used (Dijkstra and de Ruijter, 2001), the representation of bathymetry (Speich et al., 2006), the effects of bottom bottom topography (Matano, 1996), and possibly the parameterisation of horizontal viscosity (see Chassignet and Garraffo (2001) for an analogous description for the Gulf Stream). In addition, the choice of surface and boundary forcing may play a role in determining long term trends. As such, constructing a successful regional model of the greater Agulhas system requires that all of these factors be considered.

In this chapter two model configurations designed to address these concerns are introduced, commencing with a comprehensive presentation of the model used. Building on this, the development of an Indian Ocean and greater Agulhas configurations is discussed, and the choices made are justified in the context of the current understanding of Agulhas dynamics, as presented in section 1.4. Assessment of the performance of the configurations is performed in the chapter 3.

2.1.1 Motivation for using ROMS

The Regional Ocean Modelling System (ROMS) has shown previous ability in simulating the Agulhas Current. The South African Experiment (SAfE) configuration (Penven et al., 2006a) is an eddy-permitting configuration the captures the greater Agulhas region at $1/4^{o}$ resolution. It has been used extensively to investigate the consequences of the presence of Madagascar (Penven et al., 2006c), the dynamical link between the Agulhas Current and leakage, and decadal changes in the greater Agulhas system (Rouault et al., 2009). Variations of the configuration have also been used to investigate the role of bathymetry (Speich et al., 2006) and the production of cyclonic eddies in the lee of the Agulhas Bank (Penven et al., 2001).

ROMS employs higher order numerics, allowing for increased precision at a given resolution. As a result, steep gradients are well preserved. In addition, the vertical sigma co-ordinate of the model should capture topographical interactions effectively. Although the SAfE configuration has shown previous success in capturing the variability of the Agulhas Current on a variety of spatial and temporal scales, the experimental approach proposed requires additional capability. Here, using SAfE as a developmental start point, two new configurations are developed to suit these needs; AGIO and ARC112.

2.2 The Regional Ocean Modelling System

2.2.1 General description

ROMS is a split-explicit, free-surface, ocean-only model discretised in coastline and terrain-following curvilinear co-ordinates (Shchepetkin and McWilliams, 2003, 2005, 2008). In separating the solutions to the barotropic and baroclinic modes of the momentum equations, the

split-explicit approach reduces the number of time-stepping operations required (Shchepetkin and McWilliams, 2005). The associated gain in computational efficiency allows for simulations to be performed at higher resolution, advantageous for studies that focus on the mesoscale.

ROMS currently exists in three configurations; with respective ongoing development at UCLA, Rutgers University and at the Institut de recherche pour le développement (IRD) and the Institut national de recherche en informatique et en automatique (INRIA). As it has already been successfully applied to studies of the greater Agulhas system (Penven et al., 2006c; Rouault et al., 2009) and allows for the inclusion of nested high resolution domains, v.2.1 of the IRD/INRIA ROMS_AGRIF implementation (Debreu et al., 2012; Penven et al., 2006b) is used here. The numerical components inherent to the model are presented in the following sections.

ROMS solves the incompressible primitive equations under the Boussinesq and hydrostatic approximations. The former specifies that density variations that do not pertain to buoyancy forcing are neglected. The latter negates vertical acceleration and the effect of Coriolis on vertical velocity; the vertical pressure gradient is balanced solely by buoyancy forcing in this case. Under these approximations, the horizontal (Eq. 2.1 and Eq. 2.2) and hydrostatic vertical momentum (Eq. 2.3) equations take the following form in cartesian coordinates:

$$\frac{\partial u}{\partial t} + \vec{u}.\nabla u - fv = -\frac{1}{\rho_0}\frac{\partial P}{\partial x} + \nabla_h(K_{M_h}.\nabla_h u) + \frac{\partial}{\partial z}(K_{M_v}\frac{\partial u}{\partial z}) \tag{2.1}$$

$$\frac{\partial v}{\partial t} + \vec{u}.\nabla v + fu = -\frac{1}{\rho_0}\frac{\partial P}{\partial y} + \nabla_h(K_{M_h}.\nabla_h v) + \frac{\partial}{\partial z}(K_{M_v}\frac{\partial v}{\partial z}) \tag{2.2}$$

$$0 = -\frac{\partial P}{\partial z} - \rho g \tag{2.3}$$

where:

- x, y are the horizontal and z the vertical coordinate in a cartesian reference frame (m)
- u, v are the horizontal and w the vertical velocity components in x, y and z, respectively (ms^{-1})
- t is the time (s)
- $\vec{u}$ is a velocity vector
- f is the Coriolis parameter (s^{-1})
- g is the accelaration due to gravity (ms^{-2})
- ρ_0 is the reference density of sea-water (1025 kgm^{-3})
- P is pressure (Nm^{-2})
- $\nabla_h(K_{M_h}.\nabla_h v)$ and $\nabla_h(K_{M_h}.\nabla_h v)$ are the lateral momentum dissipation terms

- K_{M_v} is the vertical viscosity parameter (m^2s^{-1})

In addition, three further equations govern the advective/diffusive evolution of tracer properties (Eq. 2.5 and Eq. 2.6) and the conservation of mass in an incompressible fluid (Eq. 2.4). Finally, these are coupled with a non-linear equation of state (Eq. 2.7) (Jacket and MacDougall, 1995).

$$0 = \frac{\partial u}{\partial x} + \frac{\partial v}{\partial y} + \frac{\partial w}{\partial z} \tag{2.4}$$

$$\frac{\partial T}{\partial t} + \vec{u}.\nabla T = \nabla_h(K_{T_h}.\nabla_h T) + \frac{\partial}{\partial z}(K_{T_v}\frac{\partial T}{\partial z}) \tag{2.5}$$

$$\frac{\partial S}{\partial t} + \vec{u}.\nabla S = \nabla_h(K_{S_h}.\nabla_h S) + \frac{\partial}{\partial z}(K_{S_v}\frac{\partial S}{\partial z}) \tag{2.6}$$

$$\rho = \rho(S, T, P) \tag{2.7}$$

where, in addition to the variables described above:

- T is the potential temperature (°C)
- S is the salinity
- K_{T_h} and K_{S_h} are the horizontal tracer diffusion terms (m^2s^{-1})
- K_{T_v} and K_{S_v} are the vertical diffusivity (m^2s^{-1})
- ρ is density (kgm^{-3})

ROMS calculates the following prognostic variables; u,v,T,S and ζ, where ζ is the sea-surface displacement in metres . These are calculated from the diagnostic variables (w,P,ρ) and parameters (K_{T_h},K_{S_h},K_{T_v},K_{S_v},K_{M_u},K_{M_v}). A full description of the ROMS numerical implementation of the above equations can be found in Shchepetkin and McWilliams (2005) and Shchepetkin and McWilliams (2003).

2.2.2 Boundary condition schemes

As a regional model, ROMS requires boundary information at each of its external faces; the free-surface, bottom and, (typically) four lateral boundaries, where it may connect to an external solution. The effects of external forcing at the surface and ocean floor are achieved by the modification of vertical viscosity and diffusivity in the free-surface and bottom boundary layers. At the free-surface (z=$\zeta(x,y,t)$), heat (Eq. 2.8), salt (Eq. 2.9) and wind-driven momentum fluxes (Eq. 2.10 and Eq. 2.11) are introduced as follows.

$$K_{T_v}\frac{\partial T}{\partial z} = \frac{Q}{\rho_0 C_p} \tag{2.8}$$

$$K_{S_v}\frac{\partial S}{\partial z} = \frac{S(E-P)}{\rho_0} \tag{2.9}$$

$$K_{M_v}\frac{\partial u}{\partial z} = \frac{\tau_x^s}{\rho_0} \tag{2.10}$$

$$K_{M_v}\frac{\partial v}{\partial z} = \frac{\tau_y^s}{\rho_0} \tag{2.11}$$

$$\frac{\partial \zeta}{\partial t} = w \tag{2.12}$$

Similarly, in the bottom boundary later (z=-$h(x,y)$):

$$K_{T_v}\frac{\partial T}{\partial z} = 0 \tag{2.13}$$

$$K_{S_v}\frac{\partial S}{\partial z} = 0 \tag{2.14}$$

$$K_{M_v}\frac{\partial u}{\partial z} = \frac{\tau_x^b}{\rho_0} \tag{2.15}$$

$$K_{M_v}\frac{\partial v}{\partial z} = \frac{\tau_y^b}{\rho_0} \tag{2.16}$$

$$\vec{u}.\nabla(-h) = w \tag{2.17}$$

where, in addition to the previous;

- ζ is the sea-surface height (m)
- h is the depth of the bottom boundary (m)
- τ_s^x / τ_s^y are the zonal (x) / meridional (y) surface wind stresses ($\mathrm{Nm^{-2}}$)
- τ_b^x / τ_b^y are the zonal / meridional bottom stresses ($\mathrm{Nm^{-2}}$)
- Q is the surface heat flux ($\mathrm{Wm^{-2}}$)
- $E-P$ is the surface fresh water balance (evaporation minus precipitation)
- c_p is the specific heat capacity of water ($\mathrm{Jkg^{-1}K^{-1}}$)

Stresses in the bottom boundary layer are determined using a quadratic friction expression with a variable coefficient, C_d, determined by a Von Kármán log layer (Eq. 2.18 and Eq. 2.19). These stresses are calculated as:

$$(\tau_b^x, \tau_b^y) = -\rho C_{d_b} \sqrt{(u_b^2 + v_b^2)}(u_b, v_b) \tag{2.18}$$

$$C_{d_b} = (\frac{\kappa}{log[\triangle z_b / z_r]})^2; C_{d_b}^{min} < C_{d_b} < C_{d_b}^{max} \tag{2.19}$$

where;

- κ is the von Karman constant, equal to 0.41
- z_r is the Rugosity scale (m)
- $\triangle z_b$ is the thickness of the bottom layer (m)
- C_{d_b} is the quadratic bottom friction coefficient

In large model domains, it is often advantageous to damp the sea surface temperate and salinity signal to a climatological value to prevent model drift. However, this approach may lead to an overly constrained system, especially when considering experiments that are designed to deviate substantially from the climatological mean state. Here, to minimise this constraint, atmospheric interaction is governed by the bulk flux routines described by Fairall et al. (1996). Under this formulation, surface heat, freshwater and momentum fluxes are free to evolve according to the atmospheric and oceanic bulk variables, although sea surface temperature does remain damped to the prescribed air temperature value.

Heat flux can be divided into components that are associated with a change in temperature (sensible heat) and those that are not (latent heat). The net surface heat flux (Eq. 2.20) is therefore calculated from the balance between incident radiation, outgoing black-body radiation (Eq. 2.21) and the sensible (Eq. 2.22) and latent heat fluxes (Eq. 2.23). The latter two components are calculated simultaneously and as a function of surface roughness parameters, in tandem with momentum flux (Eq. 2.24). The transfer coefficients, C_h, C_e and C_d, which are again related to surface roughness lengths, are calculated via an iterative method according to their Monin-Obukhov similarity scales (Fairall et al., 1996). The evaporative component of the fresh water flux (Eq. 2.8) is calculated from Eq. 2.25

$$Q_{net} = Rad_{sw} - Q_{lw} - Q_{sh} - Q_{lh} \tag{2.20}$$

$$Q_{lw} = -Rad_{lw} + \epsilon\sigma T_s^4 \tag{2.21}$$

$$Q_{sh} = \rho_a C_{pa} C_h |\overline{u_{10}}|(T_s - T_a) \tag{2.22}$$

$$Q_{lh} = \rho_a L_e C_e |\overline{u_{10}}|(q_s - q) \tag{2.23}$$

$$\tau_i = \rho_a C_d |\overline{u_{10}}| (u_{i_s} - u_{i_{10}}) \tag{2.24}$$

$$E = -C_p (\frac{Q_{lh}}{L_e}) \tag{2.25}$$

where;

- Rad_{sw} and Rad_{lw} are the prescribed downwelling short and long-wave radiations (Wm^{-2})
- ϵ is the longwave emissivity of the ccean
- σ is the Stefan-Boltzmann constant; 5.6697x10^{-8} m^2K^{-4}
- ρ_a is the air density (kgm^{-3})
- C_{pa} is the specific heat capacity of air ($Jkg^{-1}K^{-1}$)
- C_h, C_e and C_d are the dimensionless transfer coefficients for sensible heat, latent heat and momentum (drag), respectively
- $|\overline{u_{10}}|$ is the average wind speed relative to the surface at 10 m (ms^{-1})
- q and q_s are the specific humidity and saturation at $T = T_s$, respectively ($g.kg^{-1}$).
- T_s is the sea surface temperature (K)
- T_a is the potential air temperature (K)
- $u_{i_{10}}$ is one of the horizontal wind components relative to a fixed earth at 10 m (ms^{-1})
- $u_{i_{si}}$ is the surface ocean current (ms^{-1}). In ROMS this is set to zero.
- L_e is the latent heat of vaporisation (K)

Lateral boundaries may either be closed, in the case of land-masking, or open, where they connect to an external solution. In the case of masking, prognostic variables (*T, S, u, v,* ζ) are set to zero. However, velocities at the closed boundary edge are modified, according to imposed free-slip conditions (Hedström, 1997).

Open boundaries require special consideration. The scheme imposed must allow external information to be communicated into the regional domain and disperse outgoing signals without detriment to the internal signal. In ROMS, this exchange is managed through a two-way active radiation scheme (Marchesiello et al., 2001), in which the signals are separated. Outgoing information is weakly nudged to external conditions ($\tau \approx 180$ days), and dispersed through an oblique radiation scheme. To accommodate the external solution, ROMS employs an adaptive-nudging scheme, which strongly constrains the incoming signal to the external solution ($\tau \approx 1$ day). Lateral viscosity, zero in the model interior, is increased in a sponge layer at the open

boundary, smoothing out model-boundary inconsistencies. The scheme, which guarantees a reasonable equilibrium solution, imposes a barotropic mode based volume constraint, improving long term model stability.

2.2.3 Temporal and spatial discretisation

The computational efficiency of ROMS allows it to be used at mesoscale and sub-mesoscale resolutions. To facilitate this capability, it uses a staggered Arakawa-C type grid, which promotes accuracy in models that capture the first Rossby radius of deformation (Arakawa and Lamb, 1977). Here, ρ, h, f and Ω are defined in the centre of the grid cell, while u and v are defined in centres of the the respective east/west and north/south cell boundaries, offset from the centre by half a grid cell (Fig. 2.1). Trace properties (T,S) and sea-surface height, ζ, are defined at ρ points. Vertical levels are also staggered, as shown in Fig. 2.2.

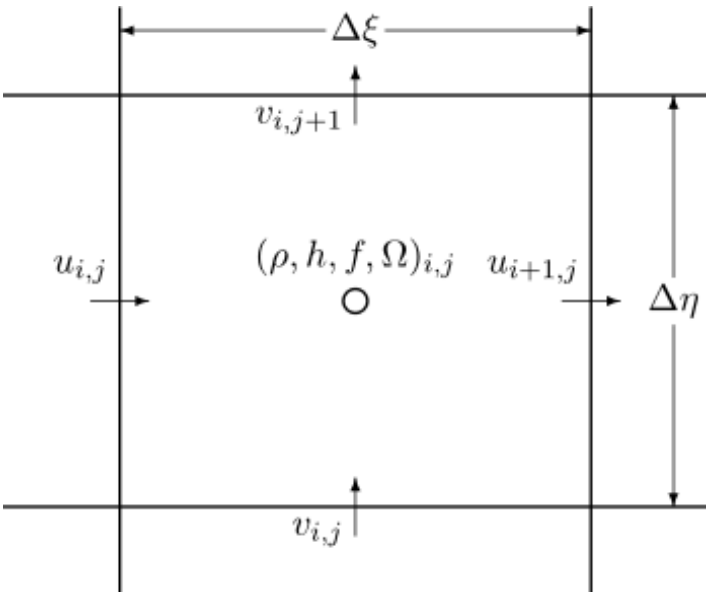

Figure 2.1: Horizontal distribution of variable points on a staggered Arakawa C-grid (after Hedström (1997)).

In the vertical, ROMS uses a stretched, terrain-following, σ-coordinate, which improves the interaction of flow with topography and allows for increase vertical resolution at the continental shelf (Marchesiello et al., 1998). Use of this co-ordinate system implies that ocean depth at all points can be transformed such that:

$$z = z(x, y, \sigma) \tag{2.26}$$

Here z is the ocean depth and σ is the fractional depth of the water column. Under this system, the depth level extremes, -h $\leq$ z $\leq$ ζ, where -h is ocean depth and ζ is the free-surface, are represented by -1 $\leq$ σ $\leq$ 0. The vertical levels are non-linearly distributed throughout the water

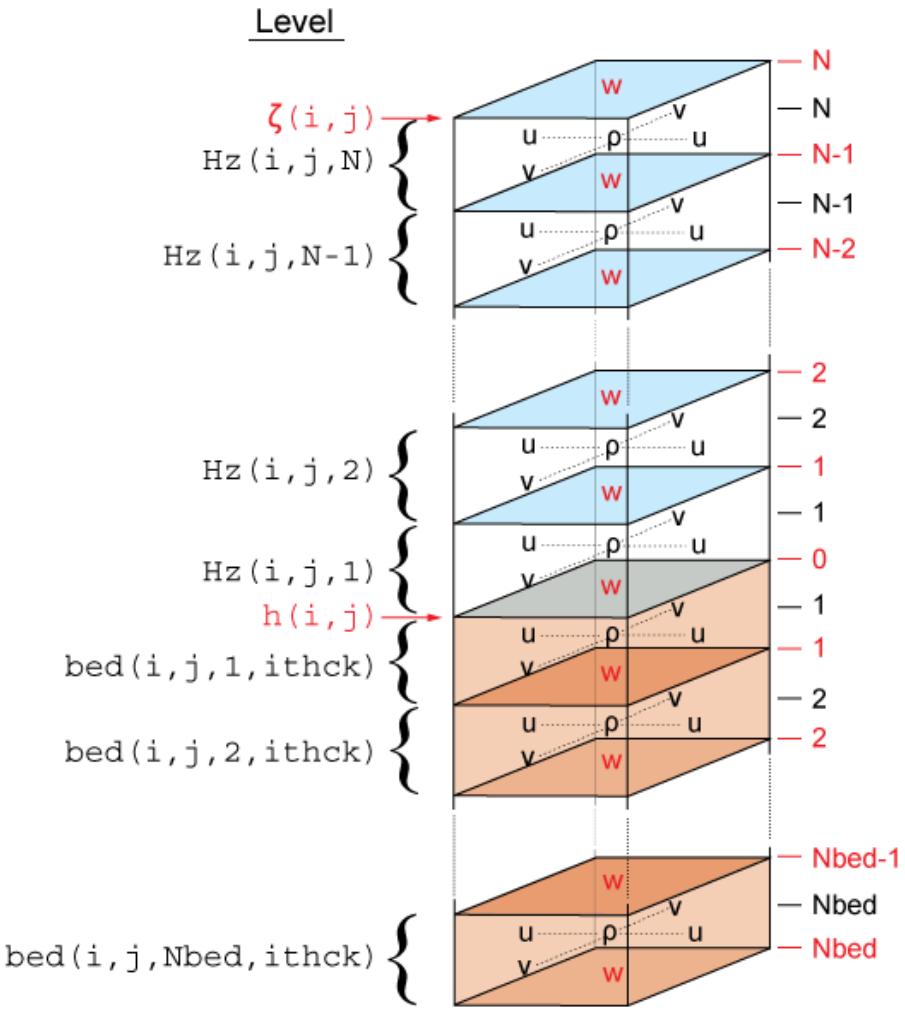

Figure 2.2: Vertical distribution of variable points on a staggered Arakawa C-grid (sourced from *www.myroms.org*).

column, following the methodology described in Song and Haidvogel (1994). The distribution of the levels depends can be stretched to favour level-density increases near the surface and at the bottom through changes to the θ_b and θ_s parameters (*ibid*). For the configurations presented here, θ_b and θ_s are set to 0 and 6, respectively.

The calculation of baroclinic pressure gradient force (PGF) across sharp topography can lead to truncations errors, arising from hydrostatic inconsistency in the transformation of the horizontal component to σ-coordinates (Shchepetkin and McWilliams, 2003). This effect, which can introduce spurious geostrophically balanced flows, has been addressed by (Shchepetkin and McWilliams, 2003), who introduced a new, more accurate formulation for the PGF. However, errors may still occur at steep topography gradients. To reduce this effect, bathymetry is selectively smoothed according to a non-linear filter (Eq. 2.27), where h represents the bathymetry (Fig. 2.3). The smoothing effect becomes more pronounced as resolution decreases.

$$r = \triangle h/h \geq 0.2 \tag{2.27}$$

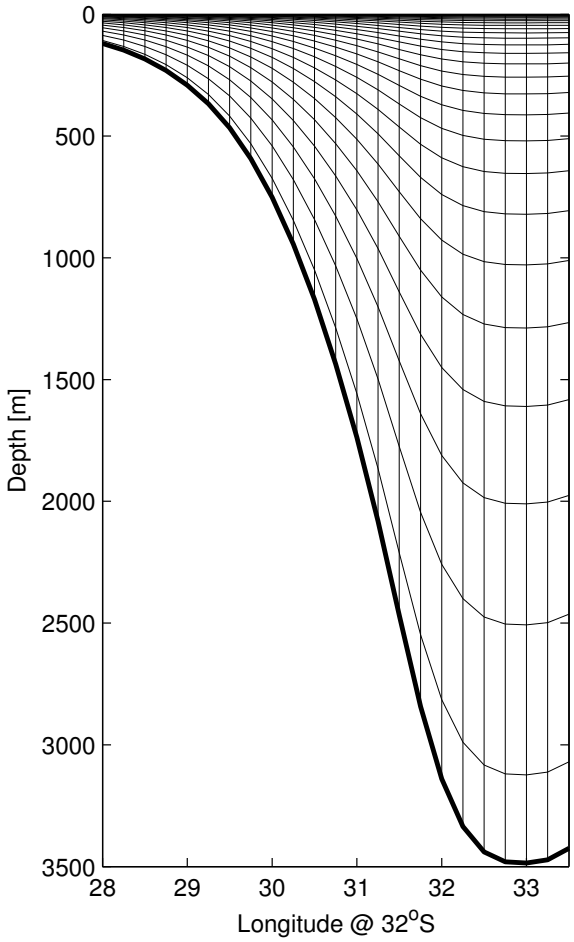

Figure 2.3: Terrain following stretched sigma co-ordinates over the African continental shelf at 32°S, $\theta_b = 0$ $\theta_s = 6$, r=0.2.

Time stepping in ROMS is performed using a 3$^{\text{rd}}$-order leap-frog / Adams-Moulton (predictor / corrector) routine (Shchepetkin and McWilliams, 2005). The separation of barotropic and baroclinic momentum modes allows the former fast mode to be advanced by multiple short time-steps during the longer time-step baroclinic calculation. Advantageously, this allows for calculation of the free-surface, and immediate access to velocity components for use in the tracer diffusion/advection calculations. Possible instabilities arising from mode splitting errors are avoided by applying a specific time-averaging filter across the barotropic sub-cycle. This reduces the risk of aliasing and guarantees exact conservation of tracer properties. Additionally, the enhanced numerical stability of the forward-backward time-stepping scheme allows for longer time-steps, increasing computational efficiency.

2.2.4 Advection and diffusion

ROMS uses a 3$^{\text{rd}}$-order, upstream biased advection scheme, which reduces dispersion (Shchepetkin and McWilliams, 1998). This scheme allows for the preservation of steep gradients and enhances precision for given resolution. To reduce spurious diapycnal mixing, which of-

ten attends higher-order diffusion-advection schemes, diffusion and advection are split and the former is represented by a rotated biharmonic operator, with flow-dependent hyperdiffusivity (the RSUP3 scheme (Marchesiello et al., 2009)).

2.2.5 Turbulent closure

Unresolved vertical mixing processes, which occur at the subgrid-scale, are parameterised in a non-local K-Profile Parameterisation (KPP) scheme (Large et al., 1994). The scheme provides specific parameterisations for mixing in both the ocean interior and in the boundary layers. The depth of the surface boundary layer, hbl, is determined through the parameterisation of turbulent process via the bulk Richardson number. Boundary layer turbulence, representative of stable or wind-driven unstable conditions is communicated through into the ocean interior via expression for diffusivity and non-local transport. Mixing processes in the interior, such as double diffusion and shear instability, are parameterised via the Richardson number.

2.2.6 Regional nesting: adaptive grid refinement

Regional nesting allows for an arbitrary number of high-resolution areas, termed 'child' grids, to be embedded in the coarser resolution 'parent' grid. ROMS achieves this through the use of the Adaptive Grid Refinement in Fortran routines (AGRIF, Debreu et al. (2008)). The AGRIF approach facilitates two-way information exchange between the parent and child grid, allowing the high-resolution signal in the nest to be communicated to the wider domain. Typically, child grids are refined by a factor of three.

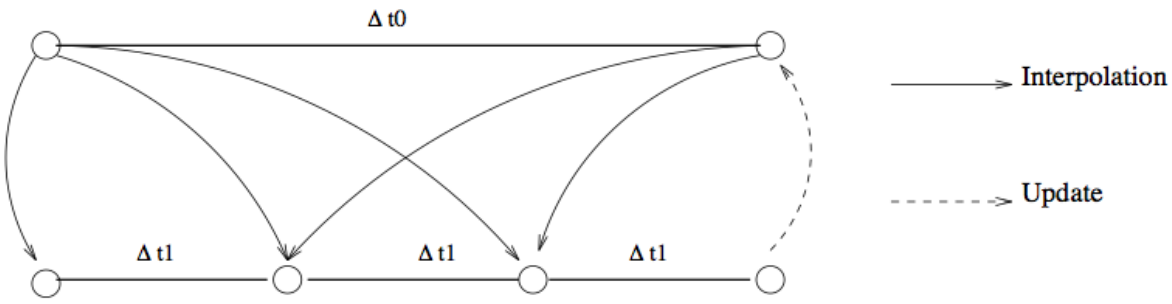

Figure 2.4: Baroclinic time-step coupling between a parent $\triangle t0$ and a child grid $\triangle t1$, for a refinement factor of 3

In order to satisfy the CFL (Courant-Friedrichs-Lewy) criteria in the refined grid, the parent grid is advanced a single step to provide boundary conditions for the child. The child is subsequently updated by the number of time steps necessary to match the parents' advancement (Fig. 2.4). The parent is then updated using the spatially averaged values from the child grid. The shorter time-step required by grid refinement raises computational cost, but, due to a minimisation of grid-points, the approach is substantially more efficient than developing a high-resolution grid alone.

2.3 The AGulhas-Indian-Ocean (AGIO) configuration

The experimental approach outlined in the introduction requires that the model used can satisfy a number of criteria, listed below:

- First and foremost, as testing the western boundary response to changes in the Indian Ocean wind field is proposed, it is necessary that the southern basin is captured in its entirety.
- The basin must be captured at sufficient resolution to capture the mesoscale dynamics of both the Agulhas source regions and the retroflection; one of the most energetic locations in the global ocean. Resolution requirements must be weighted against experimental flexibility and computational cost.
- The domain must extend far enough into the South Atlantic Ocean that Agulhas leakage changes can be quantified and that boundary conditions do not contaminate the signal.
- The interplay between the Antarctic Circumpolar Current (ACC) is poorly understood, so it is prudent to have a well established northern branch of the ACC in the domain.
- The bulk flux algorithms must allow adaptation of the wind fields to accommodate sensitivity experiments.

The model specifics are discussed in the remainder of this section, with a focus on how they address the requirements outlined above. Climatological and interannual reference runs are performed with both the configurations introduced below. A synopsis of the nomenclature used to refer to these simulations can be found in table 2.1.

2.3.1 Domain specifics

AGIO is an extension of the SAfE configuration (Penven et al., 2006a), constructed using ROMSTOOLS v. 2.1 (Penven et al., 2008). The domain spans the entire southern Indian Ocean, and extends from 29°W to 115°E and 48.25°S to 7.5°N. The southern extent of the domain allows the northern branch of the ACC to be captured. To prevent spurious boundary effects, care has been taken to keep the western boundary away from the mid-Atlantic Ridge. The configuration has a resolution of 1/4°, and is designed to capture the prominent features of the Indian Ocean basin and the mesoscale variability of the greater Agulhas system. Grid spacing at the latitude of the southern Aguhas Current is $\backsim$23 km (Fig. 2.5). AGIO is considered eddy-permitting as this spatial scale is comparable to the first Rossby radius of deformation at this latitude, $\backsim$30 km (Chelton et al., 1998). Vertical resolution in AGIO is described by 32 σ-coordinate levels, distributed according to $\theta_b = 0$ and $\theta_s = 6$, resulting in an increased concentration in the surface layers.

The masking applied is consistent with coastal geometry at this resolution, with two exceptions. Firstly, it is highly desirable to maintain the eastern Indian ocean in the domain to allow

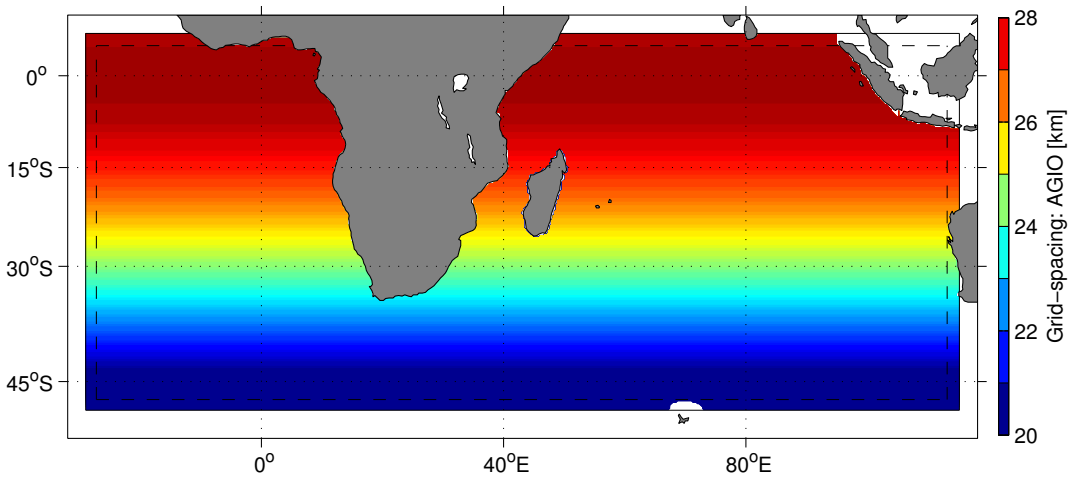

Figure 2.5: The extent and resolution of the AGIO domain at 1/4° resolution. The solid line shows the domain extent. The dashed line shows the extent of the sponge layer. White areas in the Indonesian Archipelago and around Kerguelin Island indicate masking. The average resolution over the greater Agulhas region is ∽23 km.

for full basin scale adjustment and a more accurate transport from the Pacific through the ITF. However, smoothing of the bathymetry results in the partial closing of the minor tributaries of the Indonesian Archipelago (e.g. the Sunda and Lombok Straits). This leads to isolated basins and model instability. To counteract this, much of the Indonesian Archipelago is masked out. The majority of ITF transport occurs through the Timor Sea. As the Sunda Strait and Lombok Strait transport only 0.32 (Potemra et al., 1997) and 0.15 Sv (Susanto et al., 2007) respectively, the loss of transport as a result of this masking is minimal.

Secondly, the shelf around Kerguelen Island forces the terrain following sigma co-ordinate to bunch together as the bathymetry shallows. Here, due the reduced spacing of the vertical levels, complications arising from the transition between the diffusivity in the model interior and that imposed in the sponge layer cause the solution to become unstable. To counteract this issue, the Kerguelen shelf is masked out. This masking occurs in the sponge layer and has a minimal effect on the internal solution. Typically σ-coordinate models do not need to parameterise side wall friction, as no such contact exists. However, this is not true where the model solution encounters the mask. A free-slip condition is applied where this occurs (Hedström, 1997).

Experiment	*Forcing/Anomaly*	*Boundary Conditions*
AGIOr	CNY	ORCA05 monthly climatology
AGIOi	CI	ORCA05 interannual 1948-2007
ARC112r	CNY	ORCA05 monthly climatology
ARC112i	CI	ORCA05 interannual 1948-2007

Table 2.1: Summary of experiments performed with AGIO and ARC112. CNY refers to the Core v.2b normal year forcing fields (Large and Yeager, 2009), CI to the analogous 1948-2007 annually varying fields (Large and Yeager, 2004)(discussed in section 2.3.3). ORCA05 refers to model from which boundary conditions are drawn (discussed in section 2.3.2)

Bathymetry is derived from the 1' General Bathymetric Chart of the Oceans (GEBCO)[1] global topography data set, and bilinearly interpolated onto the grid. As mentioned in the previous section, pressure gradient errors are reduced by smoothing the bathymetry such that the smoothing parameter, r, is less than a critical value of 0.2 (Haidvogel and Beckmann, 1999). As shelf dynamics are not accurately represented at this resolution, the minimum depth at the shore is set to 50 m. In addition, to prevent the establishment of large coastal walls, the maximum depth at the shore is set to 500 m. A selective filter is applied to reduce isolated deep-ocean seamounts, the source of potential PGF errors. Finally, to remove spurious 2D noise, the bathymetry is twice passed through a Hanning filter.

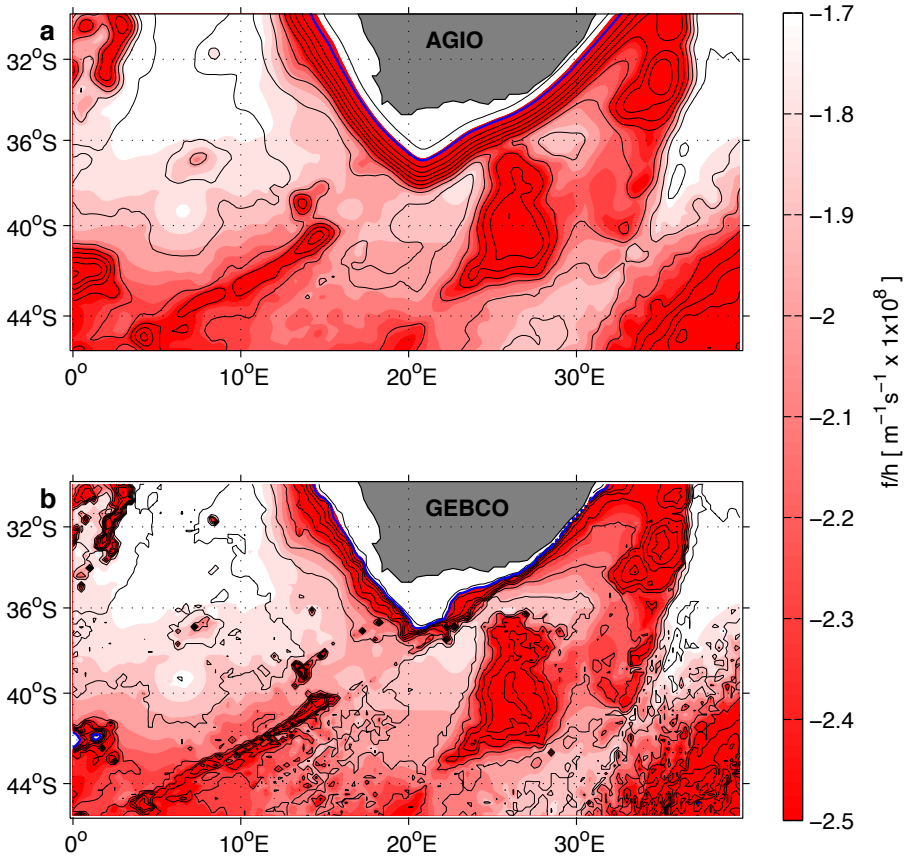

Figure 2.6: Comparison of the GEBCO derived bathymetry (contours) and f/h values (shading) in (a) the AGIO domain with (b) the raw GEBCO bathymetry values. Bathymetry is shown in contours every 500 m, with the 1000 m contour shown in blue. Note the break in f/h values between the African continent and Agulhas Plateau.

From Fig. 2.6, it is clear that there are notable differences between the raw and interpolated bathymetry. There is a widening of the shelf east of Africa, and a reduction in shelf gradient. In addition, the concave 'divot' north east of the Agulhas Bank is reduced in the top 2000 m. Further, smoothing at depth has resulted in a shallower connecting ridge between the continental landmass and the Agulhas Plateau, severing the f/h contours between the two. As highly

[1]; http://www.gebco.net

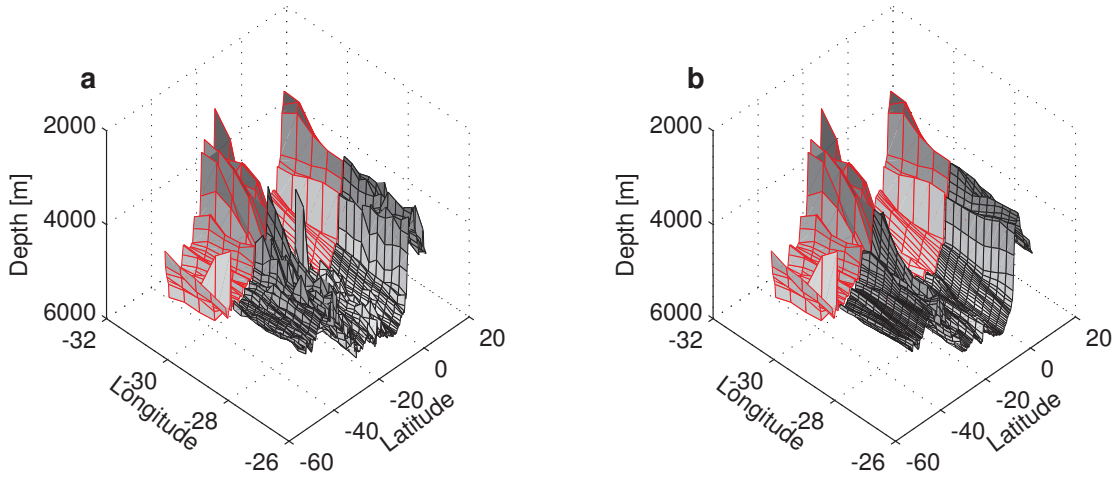

Figure 2.7: Internal (black polygons) and external (red polygons) bathymetry at the domain boundary (a) before smoothing and (b) after smoothing. The connection at the western boundary is shown. Bathymetric smoothing does not extend beyond the sponge layer.

barotropic currents tend to follow f/h contours (Schulman, 1975), this raises the possibility that the bathymetry in AGIO could induce early retroflections by steering the Agulhas Current offshore too early. However, (Beal and Bryden, 1999) observe that the core of the Agulhas is highly baroclinic at this point, reducing this effect.

The western boundary of any large-scale regional domain is typically energetic, and the southern boundary of AGIO lies within the highly barotropic ACC. Bathymetric discontinuities at these locations have the potential to cause boundary exchange problems. To reduce these discontinuities, bathymetry at the domain boundaries are smoothed such that it matches that of the external solution. To achieve this, a linear smoothing parameter, α averages the bathymetry determined by ROMSTOOLS and that provided by the external solution (h_{ext}) in the final 100 km of the sponge layer (Eq. 2.28). A comparison of the pre- and post-smoothed bathymetry is shown in Fig. 2.7. In the bottom boundary layer, the variable friction coefficient, C_d is determined according to a Von Kármán log layer (Eq. 2.18 and Eq. 2.19). For AGIO, the boundary layer roughness parameter $z_b = 0.01$ m and C_d is clipped such that $C_{d_b}^{min} = 0.0025$ and $C_{d_b}^{max} = 0.02$.

$$h(x) = \alpha(x).h_{ext}(x) + (1 - \alpha(x)).h_{roms}(x)\Big|_{\alpha=(x-100)/100,\ 0\leq x<100\ km}^{\alpha=0,\ x\geq 100\ km} \tag{2.28}$$

2.3.2 Lateral boundary conditions

AGIO has open boundaries at all four lateral faces. Velocity and tracer conditions at these faces are derived from the global ORCA05 model (Biastoch et al., 2008a). ORCA05 is a global 0.5° ocean-only model that appropriately simulates the large-scale circulation of the Indian Ocean, Atlantic Ocean and Southern Ocean. Boundary conditions are extracted from two ORCA05

simulations; a 60 year climatology and a 1948-2007 interannual simulations (Biastoch et al., 2008a). Both simulations start form a pre-spun state initialised with values from Levitus World Ocean Atlas 1998[2] and the Polar Science Centre Hydrographic Climatology (Steele et al., 2001).

In the climatological case, AGIO boundary conditions are extracted from the monthly mean of year 1 to 60 of the ORCA05 climatological simulation. Monthly values are linearly interpolated in time towards the preceding and following month, enabling a smooth transition between months. For the climatological case, December values are interpolated onto the following January, and vice versa, removing edge-effect discontinuities from the end of the year.

ROMS provides two approaches for providing boundary conditions. Boundary values can be made available at the boundary edge only, or alternatively can be made available for use in the sponge layer nudging schemes. Here latter approach is used. The sponge layer, shown in Fig. 2.5, extends 200 km, with a linear ramping of viscosity from 0 m^2s^{-1} in the model interior to 1200 m^2s^{-1} at the domain border.

Within the sponge layer, tracer and momentum outflow are weakly nudged to the external solution with coefficients of $\tau_{T_{out}}$ and $\tau_{M_{out}} = 6.430\text{x}10^{-7}$ s^{-1}. For inflow, nudging coefficients of $\tau_{T_{in}}$ and $\tau_{M_{in}} = 1.157\text{x}10^{-5}$ s^{-1} are applied to the tracer and momentum fields.

2.3.3 Surface forcing

Surface heat, freshwater and momentum fluxes are derived from v. 2b of the Common Ocean-Ice Reference Experiments (CORE) reanalysis products, provided by the Geophysical Fluid Dynamics Laboratory[3] (GFDL) (Hereafter referred to as CORE). The global flux fields are available as a corrected "Normal Year" climatology or corrected interannual, spanning the 1948-2007 period. A full description of the normal year forcing can be found in Large and Yeager (2009), while Large and Yeager (2004) describes the interannually varying data set. The CORE data set provides the following fields at T62 ($\backsim 2^o$ x 2^o) gridded resolution:

- 6-hourly scatterometry corrected NCEP zonal and meridional winds (ms^{-1})
- 6-hourly NCEP air temperature (K)
- 6-hourly NCEP specific humidity ($kg.kg^{-1}$)
- Daily satellite derived short and longwave radiation fluxes (Wm^{-2})
- Monthly satellite derived precipitation rate ($kg.m^{-2}.s^{-1}$)

The above fields are bilinearly interpolated onto the AGIO grid at a common daily resolution. Objective analysis is used to fill missing grid points, lost under the coarse resolution T62 land-sea mask. Daily averages are taken in the case of the 6-hourly fields. To allow the ocean state to evolve more freely, AGIO incorporates surface fluxes via the bulk forcing described in Fairall

[2]http://www.esrl.noaa.gov/psd/
[3]http://data1.gfdl.noaa.gov/nomads/forms/core/COREv2.html

et al. (1996). This formulation calls for relative humidity, while the CORE data set provides specific humidity. However, the specific humidity is calculated from the relative humidity early in the bulk routine, so the algorithm was adapted to take the CORE prescribed value.

Sensitivity testing requires the adaptation of the basin scale wind field. To necessitate this, the bulk forcing algorithm has been adapted to incorporate an anomaly field. This field, applied to the zonal wind stress, is linearly increased during year 31 of the experiment ($t_1 = 9.447408 \times 10^8$ s, $t_2 = 9.762768 \times 10^8$ s), so equation 2.24 becomes equation 2.29. The anomaly, $\tau_{x_{anom}}$, is applied after drag coefficient calculation. In the case of the reference experiments, this anomaly field is set to zero across the domain.

$$\tau_x = \rho_a C_d |\overline{u_{10}}| u_{10} + \begin{cases} \tau_{x_{anom}} & \text{for } t \geq t_2 \\ \tau_{x_{anom}} \cdot \frac{(t-t_1)}{(t_2-t_1)} & \text{for } t_2 > t > t_1 \\ 0 & \text{for } t \leq t_1 \end{cases} \tag{2.29}$$

2.3.4 Applying the RSUP3 scheme

To reduce spurious diapycnal mixing v. 2.1 of ROMS introduced the new RSUP3 advection/diffusion scheme, described in section 2.2.4 and fully described in Marchesiello et al. (2009). Crucially, Marchesiello et al. (2009) note that it is incorrect to assume that the mixing problem is reduced with increasing resolution, and may in fact reach a maximum value when eddy-driven lateral mixing begins to becomes explicitly resolved, i.e. under the eddy-permitting regime that AGIO operates in. The RSUP3 scheme is activated in all of the simulations performed. Fig. 2.9 shows the effect that this numerical scheme has on the preservation of waters masses at selected points in the domain, shown by Fig. 2.8.

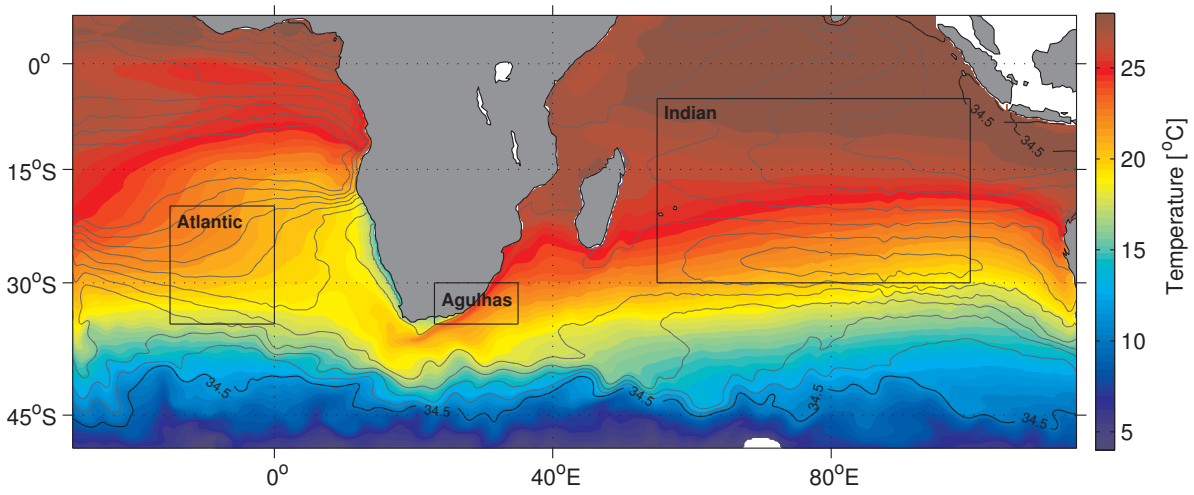

Figure 2.8: Mean sea-surface temperature (shading) and salinity (contours) for AGIOr. The black boxes show domains over which water mass properties are compared in Fig. 2.9 and Fig. 3.4.

Activation of the RSUP3 scheme leads to a substantial improvement in water mass properties

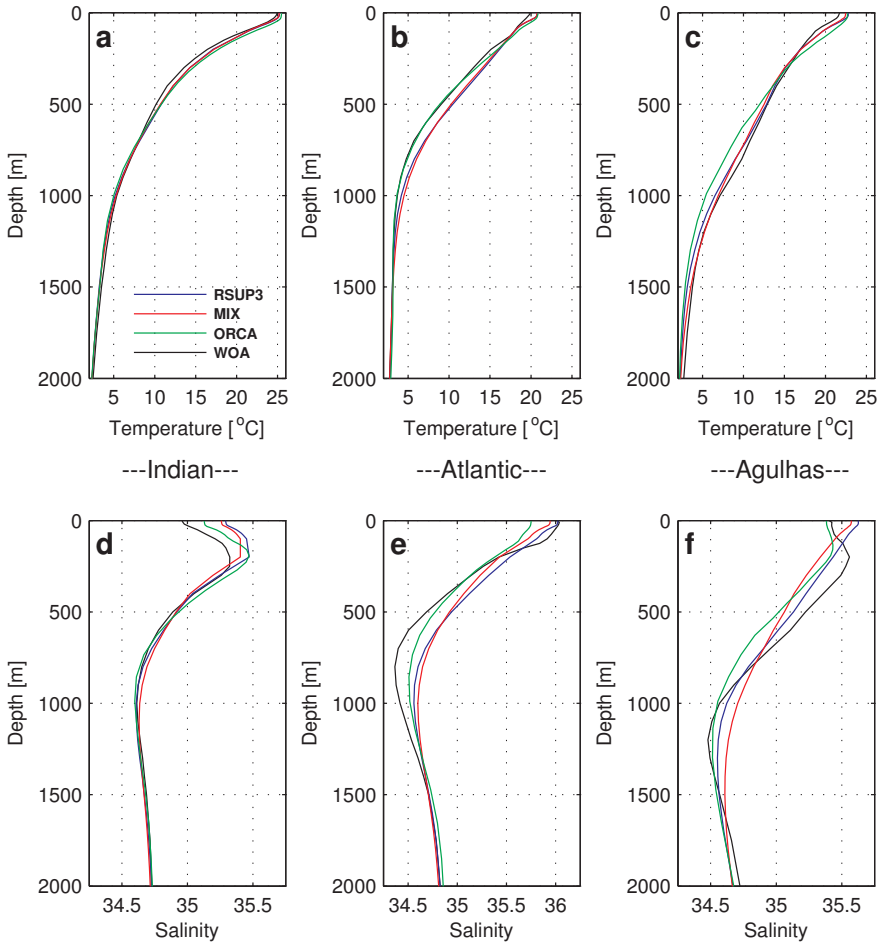

Figure 2.9: Effects of implementing the RSUP3 scheme. Red (MIX) lines show the old tracer advection scheme, blue the RSUP3 scheme. Comparisons of mean temperature, (a) to (c), and salinity, (d) to (f), are shown for the boxes in Fig. 2.8. Mean water mass properties for years 11 to 15 are compared with WOA2009 (in black) temperature (Locarnini et al., 2010) and salinity (Antonov et al., 2010) and mean tracer conditions for ORCA05 (in green); used to provide boundary conditions.

across the domain (Fig. 2.9, red (MIX) and blue (RSUP3) lines) The boundary conditions signals, provided by ORCA05 (Fig. 2.9 green traces), are retained more strongly in the RSUP3 case, as compared to the older MIX case, where diapycnal mixing is over-expressed. This is most evident in the salinity distribution, shown in Fig. 2.9 panel (e - f). In particular, the scheme appears to markedly improve the preservation of the halocline in the Agulhas region. The increase in stratification has significant consequences for the Agulhas, resulting in an increase in upstream recirculation. The changes in the Agulhas salinity profile in the MIX and RSUP3 experiments are echoed in the water mass properties measured in the Atlantic, suggesting that the stratification of the Agulhas may have a substantial downstream effect. However, increased salinity in the Atlantic sector intermediate layers ($\backsim$700 m) suggests that the properties of the Antarctic Intermediate Water (AAIW) are being eroded. In all simulations a horizontal Laplacian mixing coefficient of 100 m^2s^{-1} is applied across the AGIO domain.

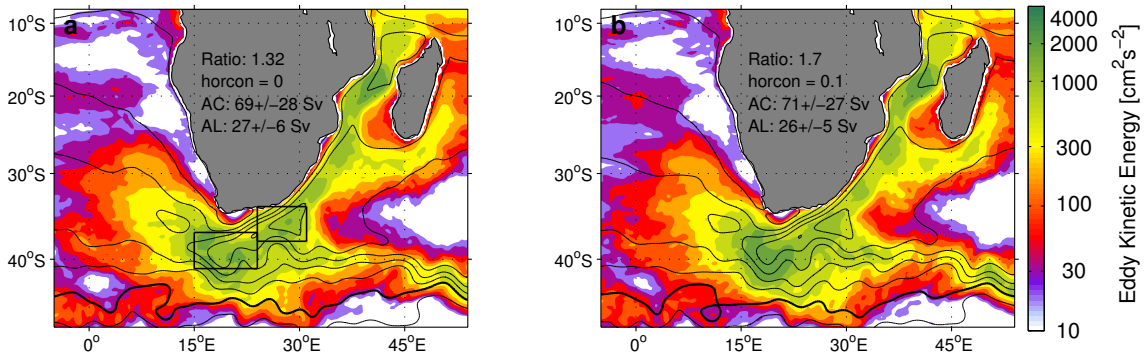

Figure 2.10: Effects of Smagorinsky parameterisation (Smagorinsky, 1963) on Agulhas Current variability. EKE is shown for year 21-25 of the the AGIO climatology with a *horcon* of (a) 0.0, and (b) 0.1. The EKE ratio is derived from the spatial average across the black boxes shown in (a).

2.3.5 Parameterising western boundary viscosity

To correct an unrealistically high level of variability in the western boundary, the horizontal viscosity, A_h, is parameterised as shown in equation 2.30 and discussed in Penven et al. (2006c).

$$A_h = horcon \times \frac{\Delta x \Delta y}{2} \times |\text{deformation tensor}| \tag{2.30}$$

Here Δx and Δy are the zonal and meridional spatial scales, . The deformation tensor describes the spatial gradient of the velocity fields. Fig. 2.10 shows the effect that this parameterisation has on the Agulhas Current. The prevalence of upstream recirculation is quantified through the ratio of eddy kinetic energy (EKE) in the downstream retroflection region, to that upstream around 30°E. EKE values for each section are calculated as spatial averages across the boxes shown in Fig. 2.10. With $horcon = 0$ (no parameterisation), there is increased upstream recirculation north east of the Agulhas Plateau (Fig. 2.10a), as shown in the ratio of 1.32 between the upstream and downstream variability. This recirculation dissipates as *horcon* increases, and the ratio of variability reaches 1.7 at $horcon = 0.1$.

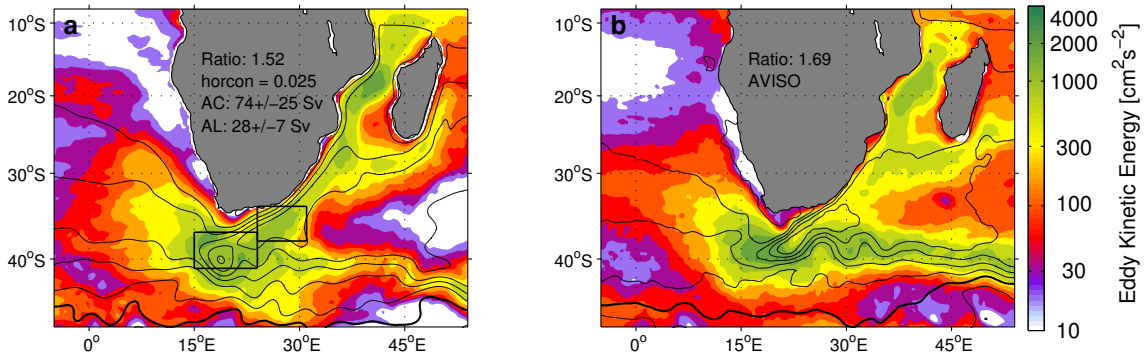

Figure 2.11: As in Fig. 2.10, but for (a) AGIOi with $horcon = 0.025$, and (b) AVISO 7-daily altimetry. Both panels show the 1992-2007 period.

As viscosity increases, the mean position of the retroflection moves westward. At a *horcon* = 0.025 the retroflection position and EKE pattern most closely resemble altimetry. Fig. 2.11 shows the comparison of EKE for 1992-2007 derived from altimetry with AGIOi at this *horcon* value.

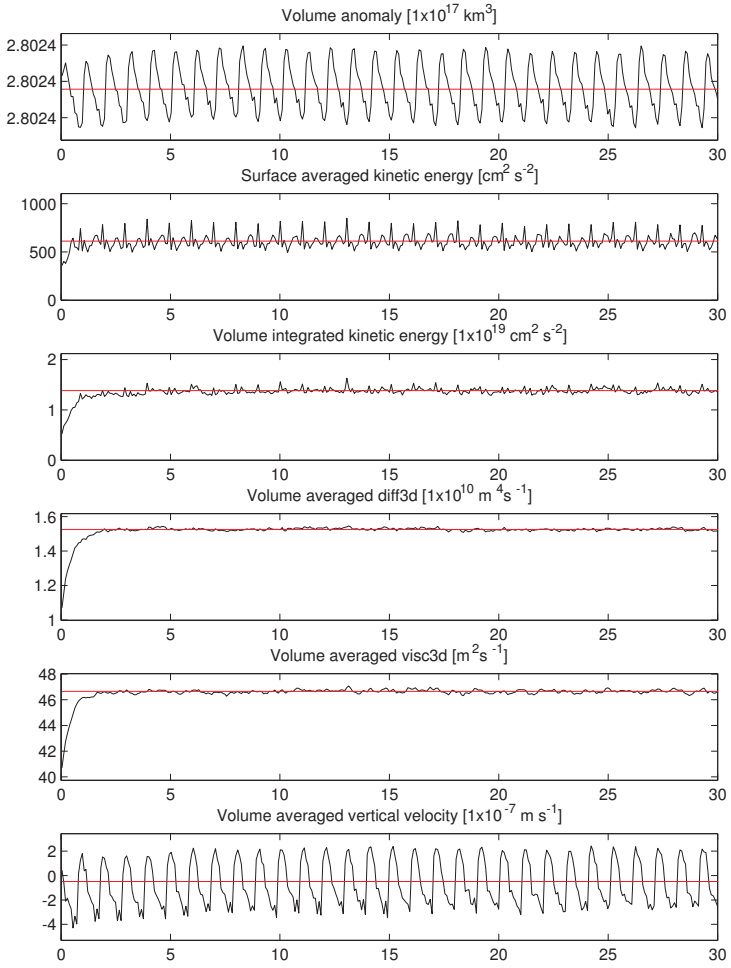

Figure 2.12: Evolution of diagnostic properties during the initial spin-up period

2.3.6 Initialisation and primary spin-up

AGIOr is initialised from January of the ORCA05 and CORE climatologies and is spun for 30 years. Kinetic equilibrium is reached following a rapid 2 year adjustment period (Fig. 2.12). However, it requires ∽15 years for the tracer fields to reach quasi-equilibrium, such that there is no long term trend in the surface ocean water mass properties (Fig. 2.13). The interannual simulation, AGIOi, is initialised from January 1948, and spun for 30 years using the 1948 fields. Subsequent to this, the full 1948-2007 period is analysed at 5-daily resolution.

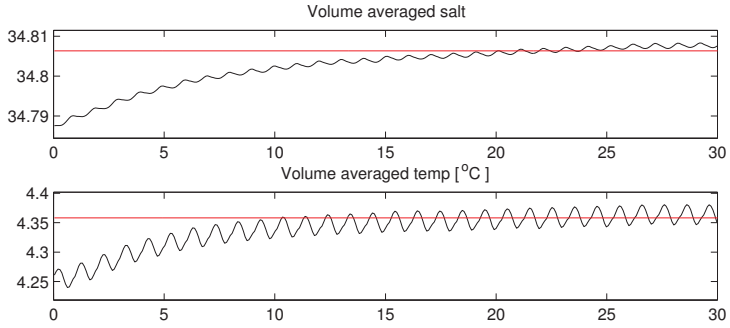

Figure 2.13: Evolution of trace properties during the initial spin-up period

2.4 The Agulhas Regionally nested Configuration (ARC112)

The higher order numerics employed by ROMS allows for significant eddy variability to be captured at eddy-permitting resolutions (Fig. 2.10) (Rouault et al., 2009; Penven et al., 2006c). However, the full range of mesoscale processes that determine the coastal detachment of the Agulhas Current, and the dynamics of the retroflection are likely best captured in eddy-resolving configurations.

Higher resolutions ROMS configurations have previously shown to be capable of simulating a leakage comparable to that observed. For example, the $1/10^{o}$ configuration described by Doglioli et al. (2006) captured a leakage of 14 Sv. However the configuration used is highly regionalised and excludes upstream variability. The mesoscale dynamics of the Agulhas source regions, and their connection to the wider Indian Ocean basin exerts an influence on the timing and path of Agulhas rings (Biastoch et al., 2008c; Schouten et al., 2002a). However, the development of a basin-scale eddy-resolving configuration is infeasible, due to the prohibitively expensive computational cost. The inclusion of AGRIF capability in ROMS v. 2.1 (Debreu et al., 2008) allows high-resolution grids to be deployed locally as regionally nested configurations. This approach allows for areas of specific interest to be rendered with high precision without incurring greatly increased integration times. The Agulhas Regional Configuration (ARC112) is an adaptation of the AGIO configuration, which uses this approach. A regional nest, designed to capture the variability of the southern Agulhas Current, retroflection and Agulhas Leakage at eddy-resolving resolutions, is embedded within the previously described AGIO domain. The eddy-permitting nature of the AGIO configuration allows the connections to the upstream mesoscale variability of the Agulhas source regions and the basin-scale variability to be maintained.

2.4.1 Domain specifics

The ARC112 nest extends from 0^{o}E to 40^{o}E, 45.5^{o}S to 29.5^{o}S at a resolution of $1/12^{o}$, a refinement factor of 3 over the original AGIO parent grid (Fig. 2.5). The child domain is connected to the parent solution through a 50 km sponge layer in which viscosity is linearly ramped up to 200 m $^{2}s^{-1}$. Coefficients for horizontal mixing and viscosity are both set to zero.

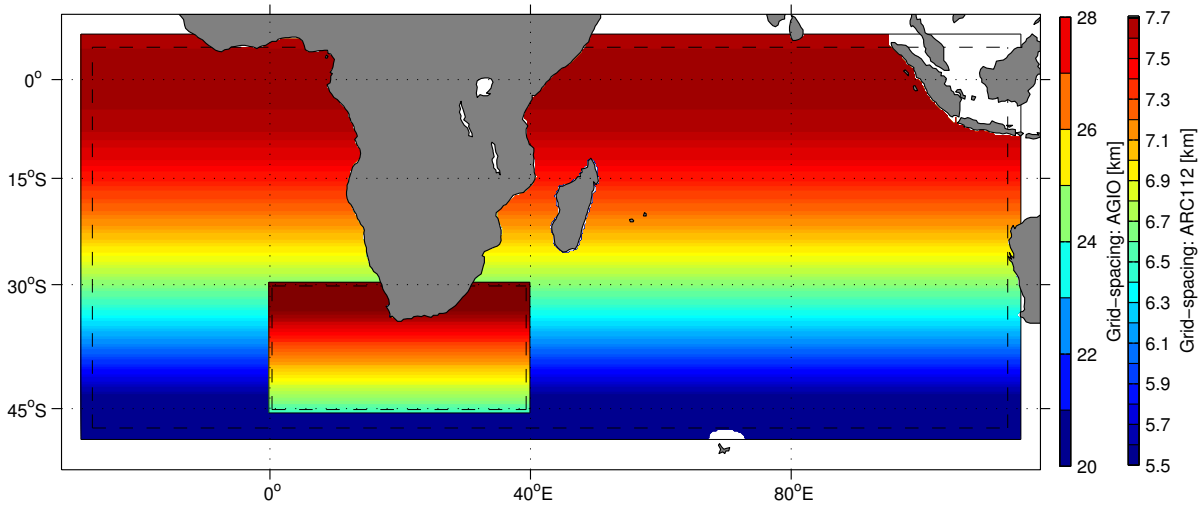

Figure 2.14: The extent and resolution of the AGIO and ARC112 domains at 1/4° and 1/12° resolution, respectively. The solid line shows the domain extent. The dashed lines shows the extent of the respective sponge layers.

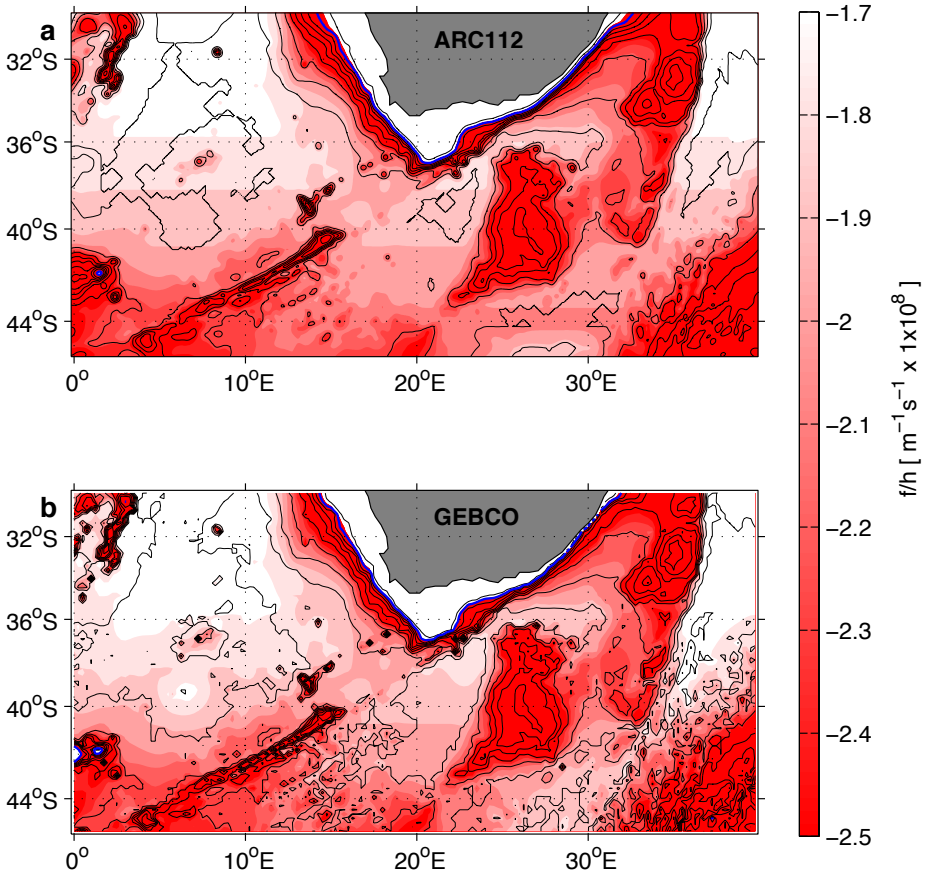

Figure 2.15: Comparison of the GEBCO derived bathymetry (contours) and f/h values (shading) in (a) the ARC112 nest with (b) the raw GEBCO bathymetry values. Bathymetry is shown in contours every 500 m, with the 1000 m contour shown in blue. Note the constant f/h values between the African continent and Agulhas Plateau.

Interpolation of the nested bathymetry is preformed using the same approach as that described for AGIO (section 2.3.1). Fig. 2.15 shows a comparison between the GEBCO bathymetry as interpolated onto the ARC112 grid (Fig. 2.15a) and the raw GEBCO bathymetry (Fig. 2.15b). The new bathymetry does not display the widening of the continental shelf, minimisation of Agulhas Bank relief and severing of the f/h contours between the Agulhas Bank and continental margin that are present in the $1/4^{o}$ interpolation.

2.5 Retroflection behaviour

Simulated retroflections may occur under two regimes; an erroneous high-viscosity case and an inertial case (Dijkstra and de Ruijter, 2001). As viscosity is in part determined by grid spacing, the horizontal resolution of a model is critical in determining the extent to which the retroflection is inertially governed. Dijkstra and de Ruijter (2001) suggest a grid-spacing surpassing $1/6^{o}$ is required to attain the inertial case. However, effective resolution is not a function of grid-spacing alone (Winther et al., 2007).

Attempts have been made to re-configure the AGIO domain at $1/6^{o}$ resolution. However, this did not yield satisfactory results, producing a leakage of $\backsim$40 Sv, comparable with that of Speich et al. (2006), and reducing the flexibility of the configuration. More recently, Beal et al. (2011) suggest that a resolution of $1/10^{o}$ is required to accurately simulate the coastal detachment of the Agulhas current, though no physical reason for this number is given. Simulations of Gulf Stream detachment by Chassignet and Garraffo (2001), show that even at $1/10^{o}$, numerical choices, and the parameterisation of viscosity, still play a key role in both the detachment of a western boundary current and the behaviour of the free jet.

2.5.1 Effective resolution and numerical viscosity

The effective resolution of a model configuration is dependant on the numerical schemes employed (Winther et al., 2007), and not simply a function of grid spacing. ROMS employs a 3^{rd}-order upstream biased advection scheme and a 3^{rd}-order leap-frog / Adams-Moulton (predictor / corrector) algorithm for the time stepping. These higher-order numerics allow for a greater effective resolution, attributable to the increased accuracy in the momentum scheme (Shchepetkin and McWilliams, 1998).

At the western boundary the Agulhas Current is selectively damped, based on the parameterisation of horizontal viscosity (Smagorinsky, 1963) (described in Eq. 2.30), a common practice for western boundary currents (Chassignet and Garraffo, 2001). However, the Laplacian viscosity coefficient, A_H, remains small throughout, with an average value of 95 m^2s^{-1} in AGIO and 35 m^2s^{-1} in ARC112. Both values are substantially less than the 330 m^2s^{-1} used in Boudra and Chassignet (1988) and considered as low by Dijkstra and de Ruijter (2001).

$$E = \frac{A_H}{r_o^2 f} \tag{2.31}$$

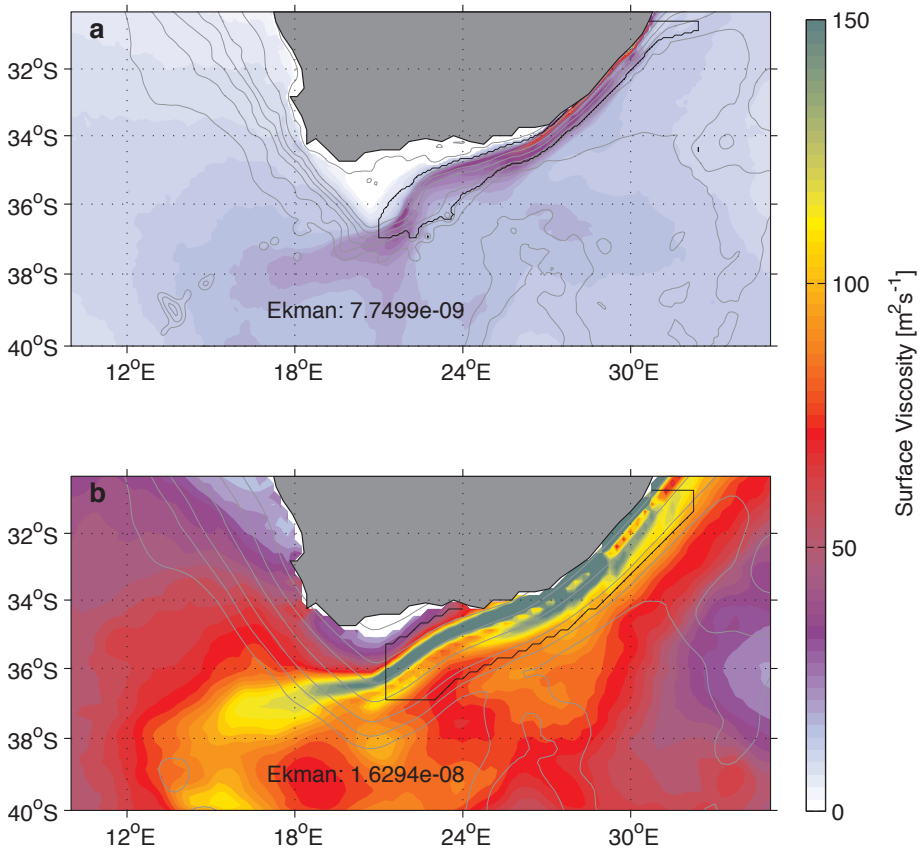

Figure 2.16: Comparison of surface viscosity in (a) the ARC112r and (b) the AGIOr configurations, with Ekman numbers for each calculated in the top 1500 m over the Agulhas box, shown in black.

The Ekman number, E, is a function of the horizontal viscosity (Eq. 2.31). Here, r is the characteristic length scale, and f is the Coriolis frequency. Fig. 2.16 shows the average horizontal viscosity in the top 1500 m for the AGIOr and ARC112r simulations. Calculating the Ekman number across the Agulhas Current yields respective values of 1.63 x 10^{-8} and 7.75 x 10^{-9}, suggesting that both should reside in the inertial regime Dijkstra and de Ruijter (2001), an assertion explicitly tested in the following section.

2.5.2 The vorticity balance

The processes governing the behaviour of the retroflection, and the contributions of viscosity and inertia can be quantified through the vorticity terms. To calculate these, the horizontal momentum equation tendency terms, extracted from AGIOr and ARC112r are averaged for five years. Taking the curl, and integrating over depth H, the vertical average of the equation for the vertical component of vorticity is derived (Eq. 2.32).

$$
\begin{aligned}
0 = \quad & \underbrace{-\frac{1}{H}\int_{-H}^{0} \nabla_h \times \overline{\mathbf{u} \cdot \nabla \mathbf{u_h}}\, dz}_{\nabla\times\text{Advection (ADV)}} \quad \underbrace{-\frac{1}{H}\int_{-H}^{0} \nabla_h \times \overline{f\mathbf{k} \times \mathbf{u_h}}\, dz}_{\nabla\times\text{Coriolis}} \\
& \underbrace{+\frac{1}{H}\int_{-H}^{0} \nabla_h \times \overline{\frac{\partial}{\partial z} A_v \frac{\partial \mathbf{u_h}}{\partial z}}\, dz}_{\nabla\times\text{Vertical Mixing (VMIX)}} \quad \underbrace{+\frac{1}{H}\int_{-H}^{0} \nabla_h \times \overline{\nabla_h A_h \nabla_h \mathbf{u_h}}\, dz}_{\nabla\times\text{Horizontal Mixing (HMIX)}}
\end{aligned} \tag{2.32}
$$

Here, $\mathbf{u}$ ($\mathbf{u_h}$) is the (horizontal) velocity vector, z and w the vertical coordinate and velocity, f the Coriolis parameter, $\mathbf{k}$ the vertical unity vector and A_v/A_h the vertical/horizontal turbulent mixing coefficients. Due to the vertical integral, VMIX is the difference between the wind stress curl and the vertical mixing flux at the bottom of the layer, which should be small at 300 m. The $\nabla\times$ Coriolis term is separated into planetary advection (Eq. 2.33) and vortex stretching (Eq. 2.34) contributions. For precision, the latter is diagnosed from the difference between the β-effect and $\nabla\times$ Coriolis terms. The ADV and HMIX terms represents relative vorticity advection and viscous stress curl, respectively.

$$
\frac{-\beta}{H}\int_{H}^{0} v.dz \quad \text{(BETAV)} \tag{2.33}
$$

$$
\frac{f}{H}\int_{H}^{0} \frac{\partial w}{\partial z}.dz \quad \text{(VSTR)} \tag{2.34}
$$

Fig. 2.17 shows the retroflection vorticity balance for the top 300 m of ARC112 and AGIO. In the current core, high meridional velocity produces a strong β-effect. In general, this and vortex stretching are balanced by advection. The viscous stress term is small throughout, but increases at the western boundary due to steep topography and the Smagorinsky parameterisation (Smagorinsky, 1963). However, even here, HMIX (Fig. 2.17 second row from the top) is dominated by ADV, VSTR and BETAV terms in both AGIO and ARC112. Small positive values of HMIX inshore of the current at the shelf break (35°S) in ARC112 are indicative of an inertial overshoot, consistent with Boudra and Chassignet (1988) experiment E11. Positive vortex stretching inshore of the current in both configurations is characteristic of the isopycnal shoaling associated with this overshoot (Boudra and Chassignet, 1988).

The retroflection loop itself is predominantly governed by advection and vortex stretching, with the β-effect playing a small role in the return current meanders (de Ruijter et al., 1999a). The well defined VSTR and ADV patterns around the Agulhas Plateau at 26°E strengthen with current transport, indicating a potentially strong topographical control downstream of the retroflection (Matano, 1996; Speich et al., 2006). In general the β-effect, advection and stretching terms are stronger in the ARC112 return current than in its lower resolution counterpart, but a consistent pattern is retained between the two models.

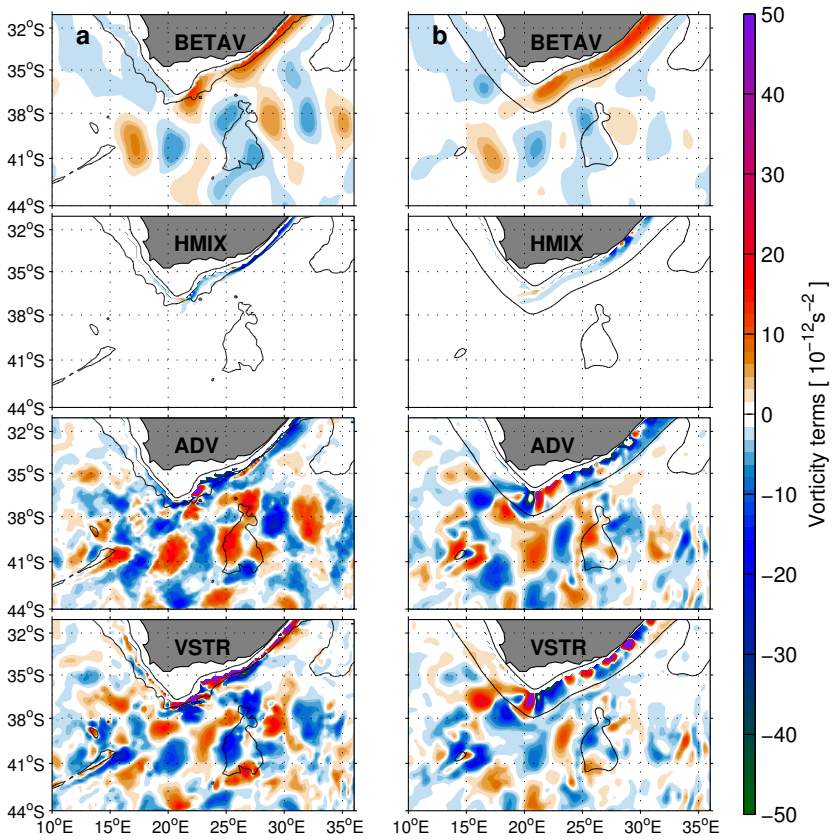

Figure 2.17: Depth integrated vorticity balance terms for the top 300 m for a) ARC112 and b) AGIO, derived via Eq. 2.32 to Eq. 2.34.

2.6 Conclusions

Like all western boundary currents, the greater Agulhas is predominantly a wind driven system. However, numerical modelling of the Agulhas system underlines the decisive role that inertia, viscosity, eddy-mean interaction and bathymetry all play in the behaviour of the western boundary current, the dynamics of the retroflection and specifics of ring shedding (section 1.4). As such, any simulation that hopes to capture these processes in a realistic configuration must possess low numerical viscosity, facilitate eddy variability and accurately represent interaction with topography. ROMS satisfies all these constraints, providing a numerical architecture that is computationally efficient, numerically precise and, from an experimental perspective, highly flexible (section 2.2).

Here, two complimentary ROMS configurations, AGIO and ARC112, are developed, making geographic and numerical choices that are intended to maximise the accuracy of the regional circulation and mesoscale variability of the Indian Ocean basin and western boundary. Further, the implementation of the ARC112 improves the representation of the mesoscale variability at the retroflection and the magnitude of inter-basin flux south of Africa. These improvements are fully discussed in the following chapter, where the behaviour of both configurations is compared to observations.

Chapter 3

Assessing the AGIO and ARC112 configurations

3.1 Introduction

In order to make inferences about reality from models, it is necessary to assess their behaviour through variables that can be directly compared with observational data. Western boundary responses are intrinsically linked to the large-scale behaviour of the adjacent subtropical gyre. In the Agulhas this is coupled with a substantial mesoscale signature and therefore requires variability to be considered on various spatial and temporal scales. Chapter 2 presents the development of two regional configurations, AGIO and ARC112, designed to explore the regional response to changes in the large-scale Indian Ocean wind field. In this chapter, to evaluate the performance of these configurations, model behaviour is compared with *in situ* observations, remote sensing data products, and published transport values.

Here, the two configurations are assessed under three broad headings; tracer distribution, basin-scale circulation and mesoscale features. The heat and salt flux associated with the Agulhas leakage exerts a controlling influence over the multi-decadal variability of the AMOC (Weijer et al., 1999, 2002; Biastoch et al., 2008a). However, the thermocline water masses of the Agulhas system, from where the leakage derives its properties, are determined in the tropical and subtropical gyres of the Indian Ocean basin. Consequently, any characterisation of leakage through heat and salt flux necessitates that Indian Ocean water masses (described in section 1.2.5) are correctly represented. In the first instance, water mass properties are compared to climatological values. To assess interannual variability in the surface ocean, sea-surface temperature fields are compared to observations using Tropical and Subtropical Indian Ocean dipole indices as a diagnostic. This approach also allows us assess the response of the surface ocean to the bulk forcing routines employed, giving a measure of how well upper ocean processes are captured.

The primary concern of this work is the relationship between the Agulhas Current transport and the Agulhas leakage magnitude under changing wind conditions. It is, therefore, essential to establish to what extent the regional transports and basin scale circulation patterns match

observed values. Lastly, as presented in chapter 1, the mesoscale variability of the Agulhas Current plays a defining role in determining its behaviour. Upstream eddies in the source regions and transport pulses associated with the Natal Pulse meander may exert an influence on the timing of ring shedding at the retroflection (Schouten et al., 2002a; Penven et al., 2006c; Biastoch et al., 2008c; Pichevin et al., 1999). Altimetry suggests that these rings subsequently take multiple paths across the Cape Basin (Dencausse et al., 2010a). However, as previously mentioned, in many cases models exhibit substantial biases in ring path, and fail to reproduce this spread (Maltrud and McClean, 2005). Often, this bias is associated with unrealistically high levels of upstream recirculation (Wallcraft et al., 2003), erroneous retroflection positions Sasaki et al. (2005), or an Agulhas Current that is expressed through a discontinuous 'eddy train' (Barnier et al., 2006; Backeberg et al., 2009). For HYCOM, these discrepancies are ably summarised by Thoppil et al. (2011). It should be noted that these model maladies occur irrespective of resolution, and it is false to assume that decreasing grid spacing automatically delivers an improvement in model performance. In consequence, assessing the performance of both configurations in the retroflection region is of paramount importance.

With these factors in mind, the AGIO and ARC112 configurations are assessed against the following requirements:

- The water mass properties of the Indian Ocean and Agulhas region are well represented.
- Interannual variability associated with the Tropical and Subtropical Indian Ocean dipole modes is captured.
- Basin scale circulation and regional transports are consistent with those observed.
- Key mesoscale features, such as MZC eddies, EMC dipoles, Natal Pulses are represented.
- The mesoscale variability associated with these features is consistent with observed mean and eddy kinetic energy distributions.
- The position of the Agulhas Retroflection compares well with that derived from altimetry
- The magnitude of the Agulhas leakage approximates drifter based estimates.
- The various Agulhas Leakage mechanisms are present; and the Agulhas ring path is not overly biased

3.2 Data sets and methods

3.2.1 World Ocean Atlas, 2005

Water mass properties for the model solutions and boundary conditions are compared with those derived from WOA05[1], provided by the National Oceanographic Data Center (NODC). WOA05

[1] http://www.nodc.noaa.gov/

consists of a gridded climatology of objectively analysed temperature (Locarnini et al., 2010) and salinity (Antonov et al., 2010) measurements at 1° x 1° horizontal resolution, spread over 33 depth levels from Z = 0 m to Z = 5500 m.

3.2.2 SODA v. 2.1.6

Climatological hydrographic measurements allow for verification of the mean tracer distribution across the domain. However, it is additionally useful to confirm that interannual signals are represented. The Simple Ocean Data Assimilation forecast product (SODA[2])(Carton and Giese, 2008) uses an OGCM forced with era-40 winds to predict the ocean climate state, subject to continuous correction through assimilation of observations. SODA v.2.1.6 spans the 1958-2008 period at monthly mean resolution, assimilating virtually all hydrographic data for the period. Data are provided on a 0.5° x 0.5° x 40 z-level grid.

3.2.3 Expendable Bathythermograph (XBT) and Argo float profiles

Although SODA assimilates XBT and Argo data, it is a reanalysis product and not direct observations. Uncorrected, observed level, XBT data for the Indian Ocean were sourced from the NODC World Ocean Database. As XBT use in the Indian Ocean decreases significantly in the 1990s, quality controlled, delayed-mode, Argo float profiles are also included in the analysis. These are sourced from the US GODAE project[3].

3.2.4 Satellite altimetry products

Due to its extent and turbulent nature, observations of the greater Agulhas system are somewhat sparse. However, the mesoscale variability of the system can be assessed through its sea-surface height variability, which can be derived from gridded from altimetry products. Here, the gridded Ssalto/Duacs synthesis product, distributed by AVISO[4], is used. Sea level anomalies, derived from the Jason-1, Envisat, GFO, ERS-1, ERS-2 and Topex-Poseidon platforms, are merged with the corrected Rio09 mean dynamic topography (Rio et al., 2011). The delayed-time altimetry products are provided on a regular 1/4° x 1/4° grid, and are available from October 1992 to present at 7-daily resolution.

3.2.5 Comparing climatological tracer fields

Although ORCA05 and WOA05 tracer fields are discretised in the vertical by a z-coordinate, spatial averaging of the regional σ-coordinate fields requires some interpolation, due to variation in the level depths. Here, depth slices are extracted from the AGIOr and ARC112r fields at discrete Z-levels and spatially averaged across the averaging boxes (shown in Fig. 2.8).

[2]http://apdrc.soest.hawaii.edu/datadoc/
[3]http://www.usgodae.org/index.html
[4]http://www.aviso.oceanobs.com/

3.2.6 Indian Ocean climate indices

To assess the interannual evolution of the sea-surface state, interannual time series of SST in the tropical and sub-tropical Indian Ocean are compared with climate indices for the tropical and sub-tropical Indian Ocean dipole modes. For the tropical dipole mode (DMI), an SST anomaly between spatial averages across a western (50°E to 70°E, 10°S to 8°N) box and eastern (90°E to 110°E, 10°S to 0°N) box is constructed, consistent with Saji et al. (1999). To remove decadal and intra-annual variability, the detrended anomaly time-series is smoothed with a 5-month window, before normalisation by the standard deviation. For the subtropical mode (STIOD) the same methodology is applied but using a western box spanning 55°E to 60°E, 37°S to 27°S and eastern box spanning 90°E to 110°E, 28°S to 18°S, as described in Behera and Yamagata (2001).

3.2.7 Upper ocean properties: tropical cyclone heat potential (TCHP)

Although dipole indices give an indication of how well surface fluxes translate to the ocean surface, they do not provide any information on the communication of this signal into the thermocline. During the development of the model, the output was used in an associated study investigating the effects of upper ocean heat content on the generation of tropical storms (Malan et al., 2013). As it is directly comparable with observations, TCHP is used as a diagnostic to assess the interannual variability of the simulated tropical Indian Ocean thermocline. TCHP is defined as the ocean heat content above the 26° isotherm (3.1) (Leipper and Volgenau, 1972).

$$TCHP = \rho.C_p \int_{z_{26^oC}}^{0} (T - 26)\delta z \tag{3.1}$$

where, T is the temperature, ρ is the density and C_p is the specific heat capacity of sea-water. While ρ is dependant on depth, the change in the upper ocean is minimal, justifying moving it outside of the integral.

TCHP time series for AGIOi and SODA are constructed from the spatially averaged values across a box spanning 50°E to 70°E, 12°S to 8°S, as described in Xie et al. (2002). Monthly mean values are then averaged across the November-April cyclone season, resulting in an average TCHP value for each year. An observational TCHP record is reconstructed from XBT and Argo float data in a similar fashion. All float data for the defined box across the cyclone season is averaged for each year. The number of profiles used in each averaging process is noted on Fig. 3.8.

3.2.8 Agulhas diagnostics: Mesoscale variability

Values for EKE and MKE are calculated from the 5-daily model SSH, and 7-daily AVISO mean sea-level anomaly (MSLA) fields. Geostrophic velocities, are calculated from the SSH fields according to equations 3.2 and 3.3. MKE and EKE are subsequently calculated using equations 3.4 and 3.5.

$$u = -\frac{g}{f}\zeta_y \tag{3.2}$$

$$v = \frac{g}{f}\zeta_x \tag{3.3}$$

$$EKE = \frac{u'^2 + v'^2}{2} \tag{3.4}$$

$$MKE = \frac{\bar{u}^2 + \bar{v}^2}{2} \tag{3.5}$$

where g is the acceleration due to gravity, f is the Coriolis parameter, and ζ is SSH. Velocity anomalies $u' = u - \bar{u}$ and $v' = v - \bar{v}$, where $\bar{u}$ and $\bar{v}$ represent the annual mean velocities centred about u and v, respectively.

3.2.9 Agulhas diagnostics: Retroflection position

Retroflection extent is derived via a sea-surface height (SSH) contour, tracked through the 5-daily fields (following Backeberg et al. (2012)). The contour value is determined from the mean SSH spanning 30°S-32.5°S, 28°E-32.5°E, capturing the upstream Agulhas Current where the flow is less turbulent (Fig. 3.18). To capture the inshore current edge, the mean value is considered where 200 m < h < 1500 m. The westernmost contour value is taken as maximum loop extent. Retroflection positions are spatially binned into 1/2° longitudinal boxes, producing a zonal probability density function for each experiment.

3.3 Comparison with observations

3.3.1 Hydrography: Surface tracer properties

The distribution of tracer properties is governed by three mechanisms; the incorporation of surface fluxes, the incoming signal form the lateral boundary conditions, and internal physical processes. As such, while the sea surface state may be largely driven by the atmosphere, the underlying thermocline properties are in part determined by the ORCA05 values used at the boundary. For this reason, the ORCA05 tracer fields will be shown along-side the regional distributions and those derived from observations.

Comparison with observations shows that AGIOr and ARC112r exhibit a realistic SST pattern across the domain (Fig. 3.1 a, b, d). The warming in the eastern tropical Indian Ocean is indicative of the influx of warm Pacific waters via the ITF. Further south, the sharp SST gradient poleward of ∽40°S represent the frontal zones that form the northern edge of the ACC. Here, there is evidence of more turbulence in the simulated SST, a consequence of the higher resolution employed in the regional configurations. South of this frontal zone, cold SSTs indicate the ACC proper.

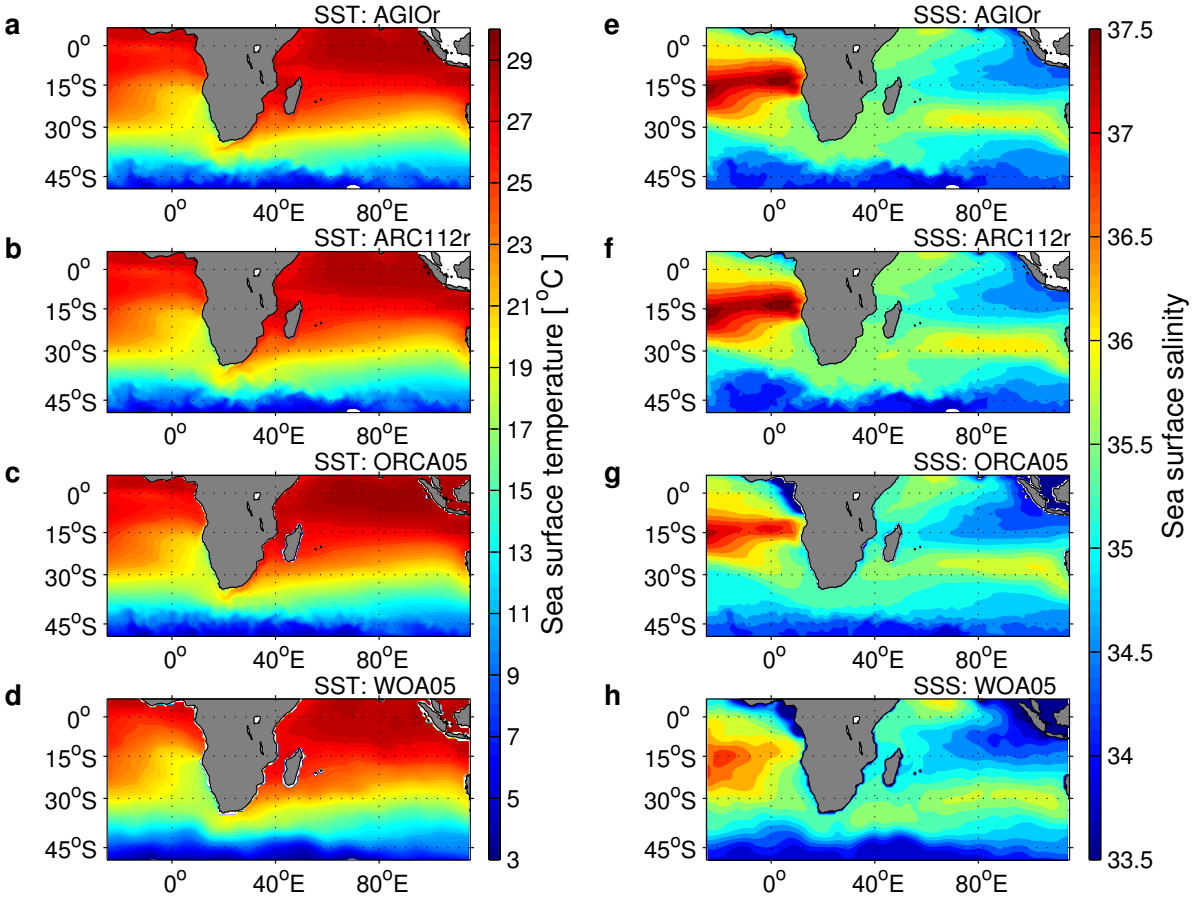

Figure 3.1: Sea-surface variables for AGIOr, ARC112r and WOA05. Panels a through d show climatological mean SST for AGIOr, ARC112r, ORCA05 and WOA05, respectively, with panels d through f showing the analogous SSS fields.

In the south east Atlantic, cooler temperatures toward the African coast are indicative of the Benguela Upwelling System, which appears slightly cooler in AGIOr and ARC112r than it does in ORCA05 (Fig. 3.1 a, b, c). The Agulhas Current is more clearly realised in the regional simulations, a result the increased definition of the western boundary at higher resolutions. In AGIOr, the thermal imprint of the Agulhas Current appears to extend further into the Cape Basin than in ARC112r.

SST anomalies show that ARC112r is warmer than observations in the subtropical Indian Ocean, although the discrepancy is less than 1°C (Fig. 3.2 a). Increased SST along the Indonesian and Australian coast is likely due to the incorporation of the boundary condition values. Fig. 3.2b indicates that ORCA05 is also substantially warmer than the regional fields throughout the tropical eastern Indian Ocean.

Larger anomalies of $\backsim$1.5°C occur in the tropical Atlantic Ocean. Here again, regional behaviour echoes that of the boundary conditions, suggesting that part of this signal may be inherited from bias in the large scale solution. SST anomalies in the sub-tropical Atlantic are slightly lower in ARC112r than they are in AGIOr (not shown), suggesting an increased

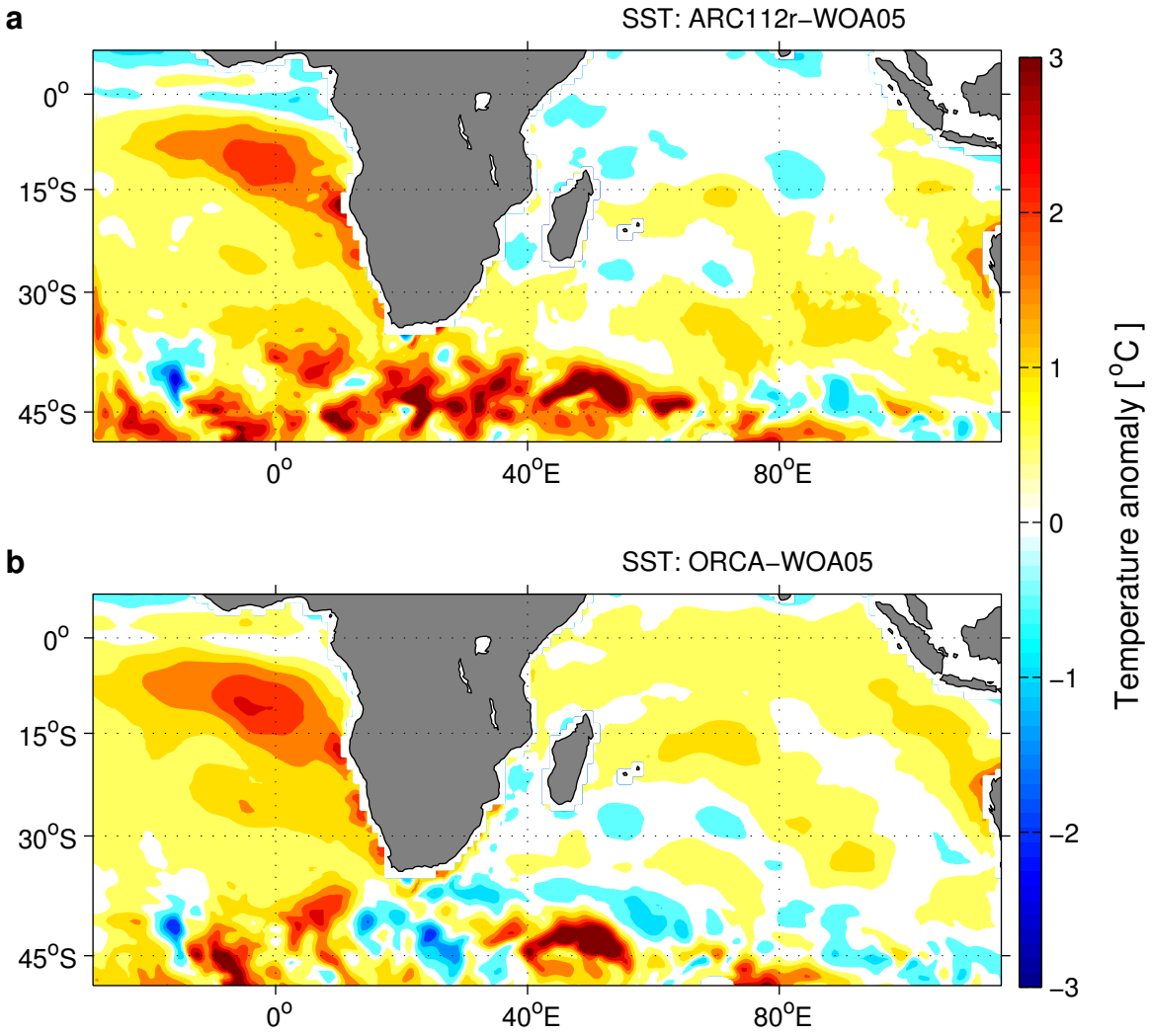

Figure 3.2: Climatological a) ARC112r and b) ORCA05 sea-surface temperature (SST) anomalies from WOA05 fields.

Agulhas leakage in the latter. Substantial anomalies of both signs also occur along the sub-tropical front. However, given the turbulent nature of this feature and the lack of an eddy-field in either ORCA05 or WOA05, this is perhaps unsurprising. In ARC112r, the SST directly south of the STF south of Africa is also high, suggesting a possible over-expression of cross frontal mixing in this region.

The distinct signal of the ITF and ACC are also evident in the SSS signal (Fig. 3.1 e, f), however, from the anomalies it is clear that both are more saline than observed (Fig. 3.3a). The abnormally warm and saline ACC is potentially inherited from the large-scale solution, lying, as it does, along the southern boundary of the regional domain (Fig. 3.3b). Comparing Fig. 3.1 e and h, it appears that the large anomalies around the Indonesian archipelago may be indicative of the masking used, reducing the input of fresh pacific waters through the Lombok Strait.

By far the largest anomalies occur in the tropical Atlantic Ocean, where all simulations are substantially more saline than observations (Fig. 3.3). However, while ORCA05 shows some bias

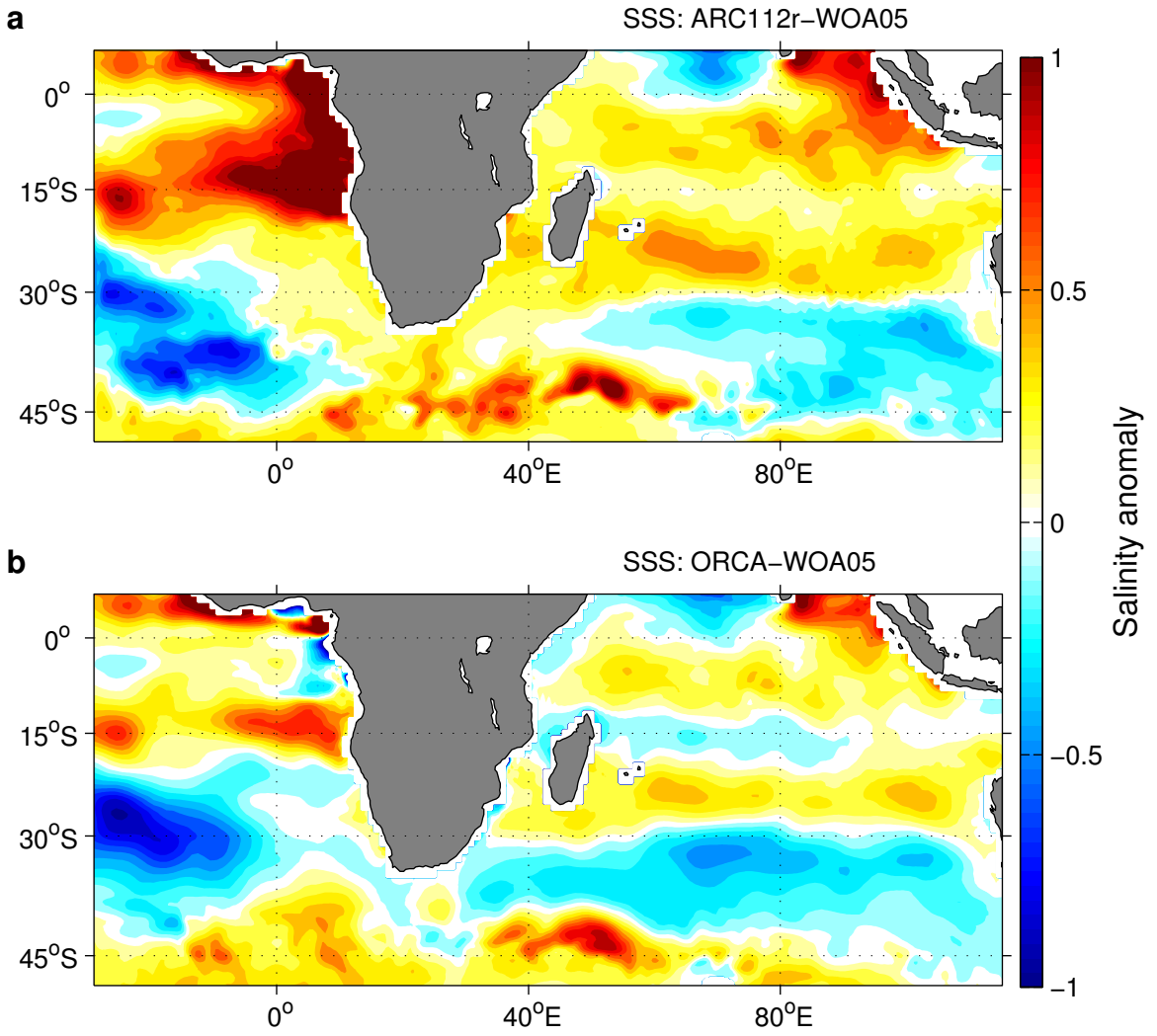

Figure 3.3: As in Fig. 3.2 but for sea surface salinity (SSS).

in SSS in this location, the situation is worse in ARC112r (and AGIOr), which show an increase of $\backsim$1. In the Gulf of Guinea, this large anomaly, is likely in part attributable to the lack of a regional river run-off scheme. The missing Congo River may exacerbate an already unrealistically saline tropical Atlantic, partially prescribed by the ORCA05 conditions. Alternatively, it may be that severing the Atlantic gyre prevents basin scale adjustment processes, resulting in unrealistic Atlantic tropical dynamics in the regional simulations. Further south, these anomalies become less severe, but, excepting the subtropical gyre, the entire south Atlantic is more saline than observed at the surface, consistent with ORCA05.

3.3.2 Hydrography: Sub-surface tracer distribution

Fig. 3.4 shows a comparison of sub-surface tracer distributions in AGIOr, ARC112r, ORCA05 and WOA05. The thermocline is quite accurately represented in both AGIOr and ARC112r (Fig. 3.4 a to c), although it is deeper than expected in the Atlantic sector (Fig. 3.4b). The thermal

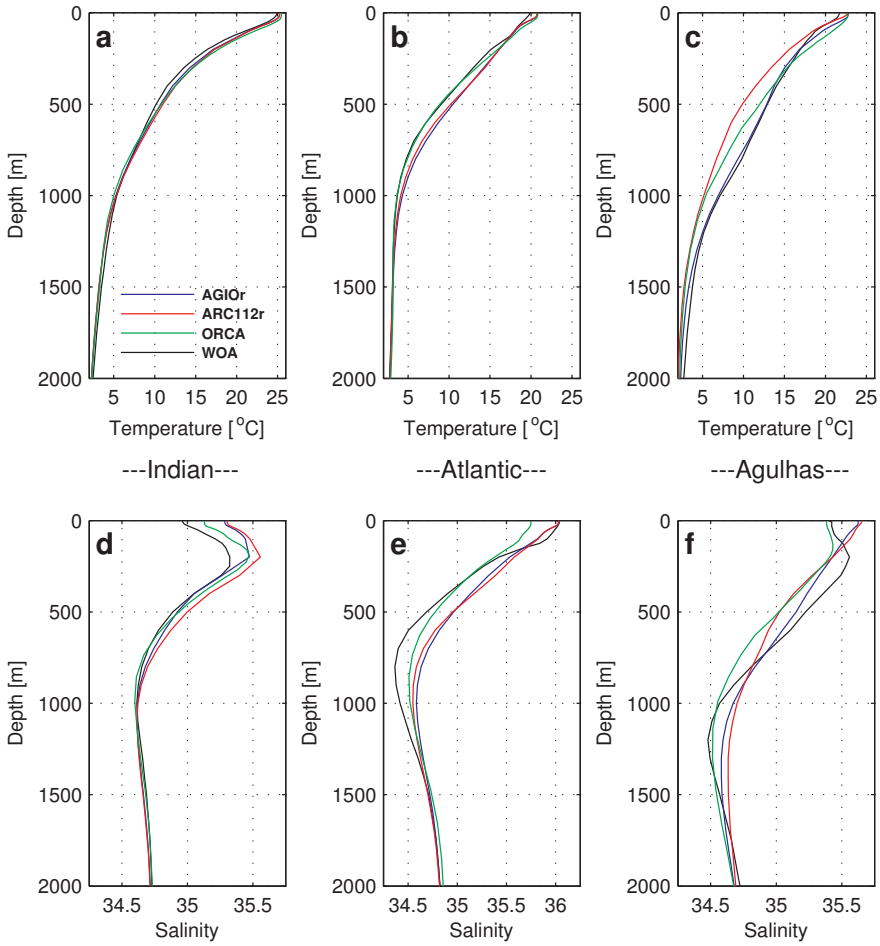

Figure 3.4: Tracer distributions with depth for AGIOr (blue), ARC112r (red), ORCA05 (green) and WOA05 (black). Panels show temperature in the top 2000 m for (a) the Indian Ocean, (b) Atlantic Ocean (c) Agulhas Current boxes shown in Fig. 2.8. Panels (d) to (f) show the analogous salinity fields.

structure of the Agulhas is accurately represented in AGIOr, which closely approximates the WOA05 data (Fig. 3.4c). However, in ARC112r it is much shallower suggesting that the level of eddy-variability plays a role in determining the thermocline depth in the western boundary.

Variations in salinity profiles in the Indian, Atlantic and Agulhas sections are much greater than their temperature counterparts (Fig. 3.4 d to f). Although the halocline depth in the Indian ocean is well preserved, there is a distinct bias in near-surface salinity in this basin. However, in part this bias may be inherited from the ORCA05 boundary conditions, which shows the same signal, though less pronounced (possibly due to the SSS restoring employed in the OGCM (Biastoch et al., 2008a)). The Atlantic halocline is somewhat eroded, though the near surface values coincide. Above 1500 m, there are substantial discrepancies between the observed salinity distribution and the simulated ones. AGIOr and ARC112r show an erosion of the salt gradient around 1000 m, and all three model configurations show a distinct shallowing of the halocline. This shallowing with increasing resolution suggests that vertical mixing, possibly driven by increased mesoscale activity, may play a role in the salt distribution here. In addition

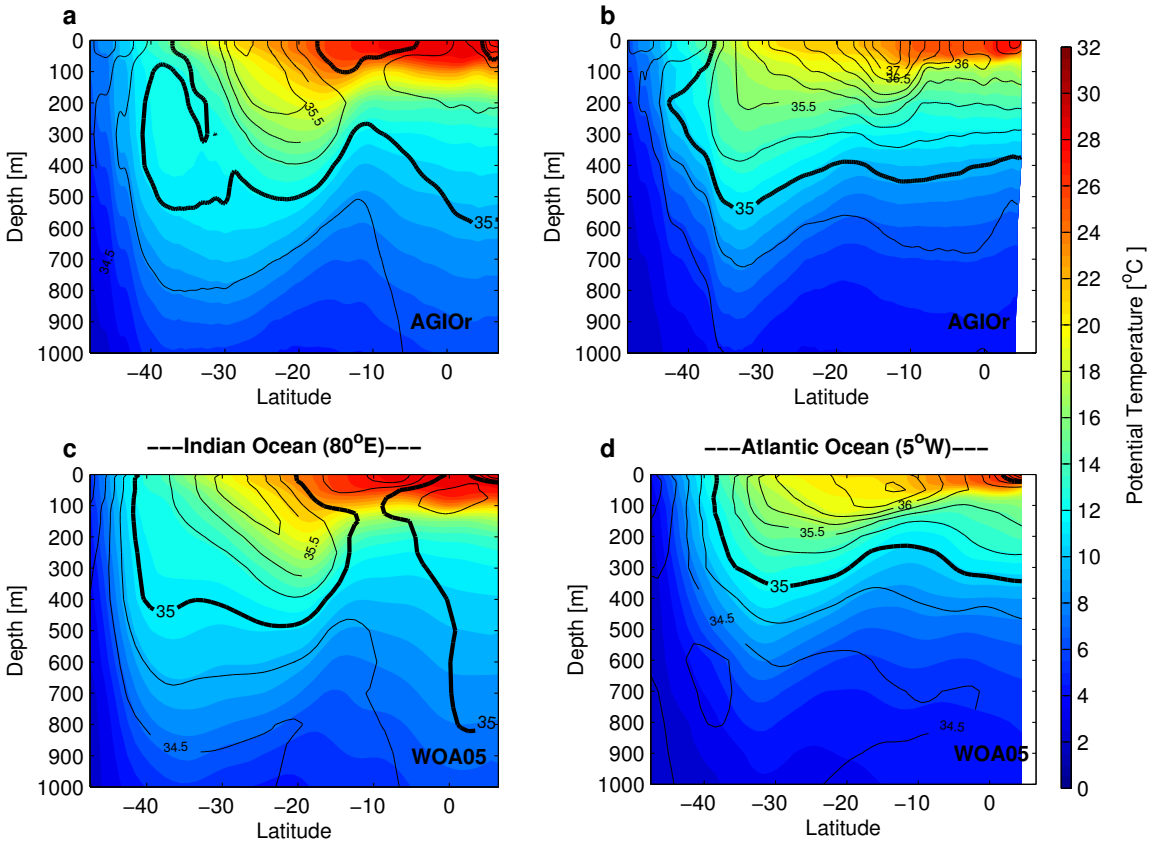

Figure 3.5: Meridional transects through the top 1000 m of the Indian Ocean at 80° (panels a and c) and the Atlantic Ocean (panels b and d). The top panels show the AGIOr fields, the bottom panel show the WOA05 climatological fields. Potential temperature is shown in shading, salinity is shown in the contours at 0.25 intervals from the heavy black 35 contour.

AGIOr and ARC112r show a notable surface bias in the Agulhas sector, though they show minimal deviation from each other in their SSS and SST signals, suggesting that there is no resolution dependance in the incorporation of bulk-forced surface data.

3.3.3 Hydrography: Water masses

Cross sections through the Atlantic and Indian Oceans (Fig. 3.5) show that the meridional distribution of upper ocean water masses is well captured. In the Indian Ocean it is clear that although the temperature distribution is reasonably well simulated, the salinity at 200 m is too high in the tropics (Fig. 3.5a), indicating an overly saline South Indian Central Water (SICW). The shoaling of the 35 contour at the equator also indicates suggests that the Indian Equatorial Water (IEW) is more confined to the surface layers than observed (Fig. 3.5a and c).

In the Atlantic, the 35 isohaline is $\backsim$100 m deeper in AGIOr north of 30°S. As a result, the simulated surface layers are substantially more saline than in the observations, while the ocean below 700 m is fresher. Further, the tropical Atlantic is warmer than observed down to around 700 m. In both transects, the distinct cooling and freshening of the upper-ocean south of 40°S, indicative of the transition to the southern ocean frontal zones, mirrors the observed signal.

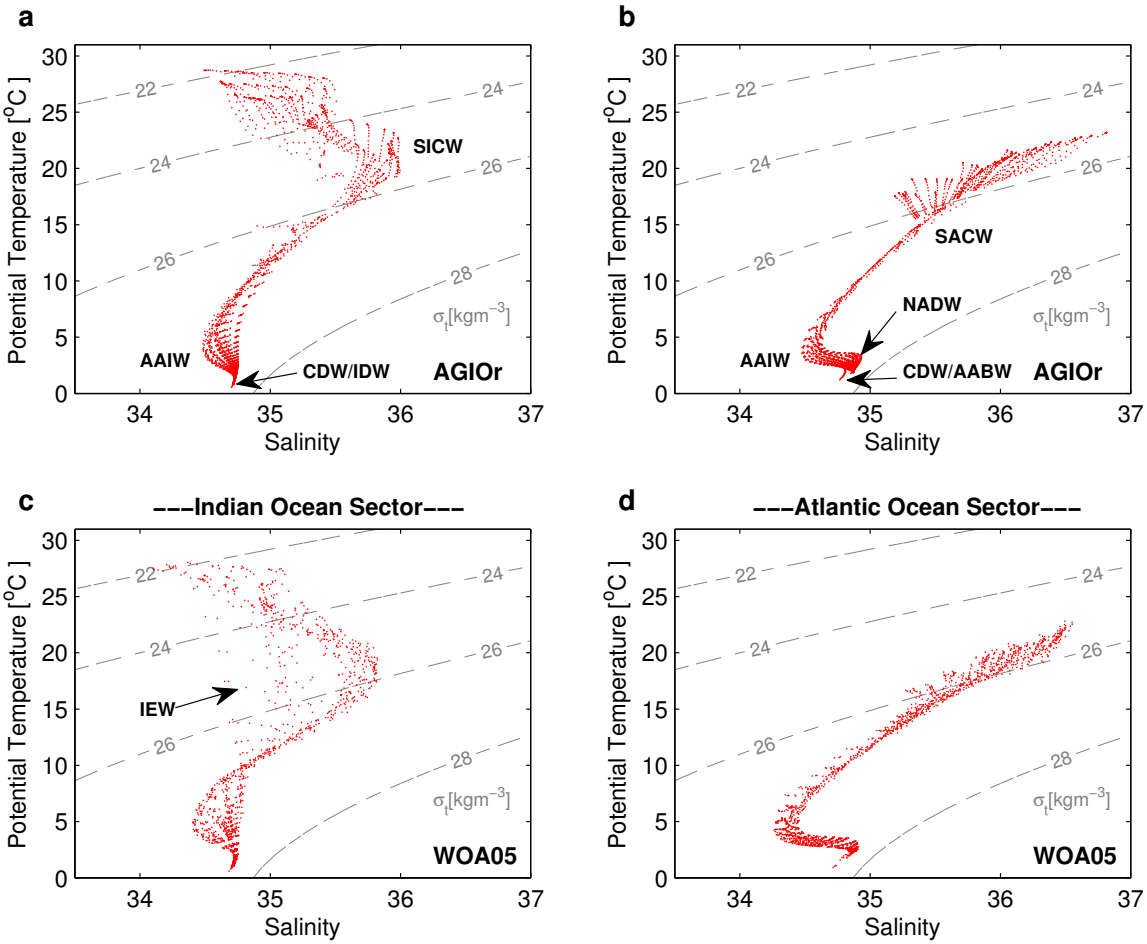

Figure 3.6: Water mass properties of the Indian Ocean sector (panels a and b) and Atlantic Ocean sector (panels b and d). The top panels show the AGIOr fields, the bottom panels the WOA05 climatological fields. The sectors are as shown in Fig. 2.8. The following water masses are labelled; Antarctic Intermediate Water (AAIW: S ∽34.7), Antarctic Bottom Water / Circumpolar Deep Water (AABW/CDW: S = 33.8 - 34.6), North Atlantic Deep Water (NADW: S ∽34.8), South Atlantic Central Water (SACW: ∽35.5), Indian Equatorial Water (IEW: S = 34.9 - 35.3), South Indian Central Water (SICW: S = 34.6 - 35.8) and Indian Deep Water (IDW: S ∽34.7) (see table 1.1).

Taking a census of the distribution of tracer properties in the Atlantic and Indian Ocean sectors shown in Fig. 2.8, it is clear that the major water masses of the two ocean basins are reproduced (Fig. 3.6). Antarctic Intermediate Water (AAIW) and Circumpolar Deep Water (CDW) pervade the deep layers of both basins, with Indian Deep Water (IDW) and Antarctic Bottom Water (AABW) present in the Indian and Atlantic Oceans, respectively. North Atlantic Deep Water (NADW) forms a substantial component on the deep and middle layers of the Atlantic. The middle layers are dominated by South Indian and South Atlantic Central Waters (SICW and SACW). However, the fresh Indian Equatorial Waters (IEW), present in observations (Fig. 3.6c) do not feature in the AGIOr signal ((Fig. 3.6a). Typically IEW is generated in the mid-Indian Ocean, north of 8°S (Emery, 2001). Failure to capture the IEW may indicate that the northern boundary of AGIOr prevents the correct formation of this water mass by failing to fully capture equatorial signals in the basin.

3.3.4 Interannual signals

Interannual variations in SSTs in the Indian Ocean basin can be expressed through the tropical (DMI) and sub-tropical (STIOD) dipole indices (Saji et al., 1999; Behera and Yamagata, 2001). Comparison of the these indices with observed values suggests that the atmosphere is appropriately communicated to into the surface ocean on an interannual timescale (Fig. 3.7). Time series for the DMI correlates well with observations, with a coefficient of 0.73 at the 99% confidence interval. Similarly, for the STIOD, there is a coefficient of 0.77 also at the 99% confidence interval. Further, all major events, appear to be captured in AGIOi, though the variability in the simulated index is lower than observed before 1975.

Although the dipole indices provide a way of assessing the ability of the bulk formulation to communicate the atmosphere to the sea-surface state, it provides minimal information about sub-surface signals in the tropical Indian Ocean. To assess this, the upper ocean heat content above the Seychelles-Chagos Thermocline Ridge, an area sensitive to both direct wind forcing and remote Rossby wave forcing (Hermes and Reason, 2009) has been used to create a time series for tropical cyclone heat potential (TCHP). Fig. 3.8 compares Indian Ocean TCHP time series extracted from ARC112i, SODA and XBT/Argo float based observations. ARC112i and SODA show a consistent TCHP signal, reflected in the high correlation coefficient between the two time series (r=0.77 at p=99%). ARC112i values also fall within 1 standard deviation of the observed values. Notably, years where observations suggest a spike in THCP (i.e. 1973, 1997 and 2007) also register in the interannual simulation.

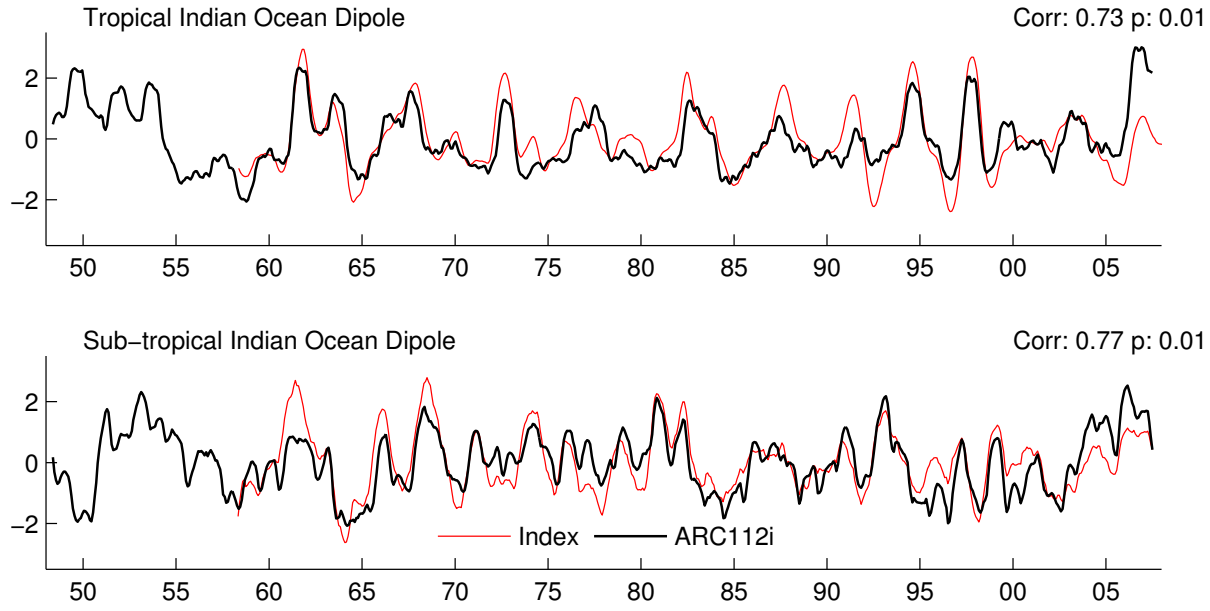

Figure 3.7: Comparison of Tropical and Sub-tropical Indian Ocean dipole indices, derived from the ARC112i, compared with the HadISST1-derived published values in Saji et al. (1999) and Behera and Yamagata (2001), respectively. A similar pattern is seen in AGIOi.

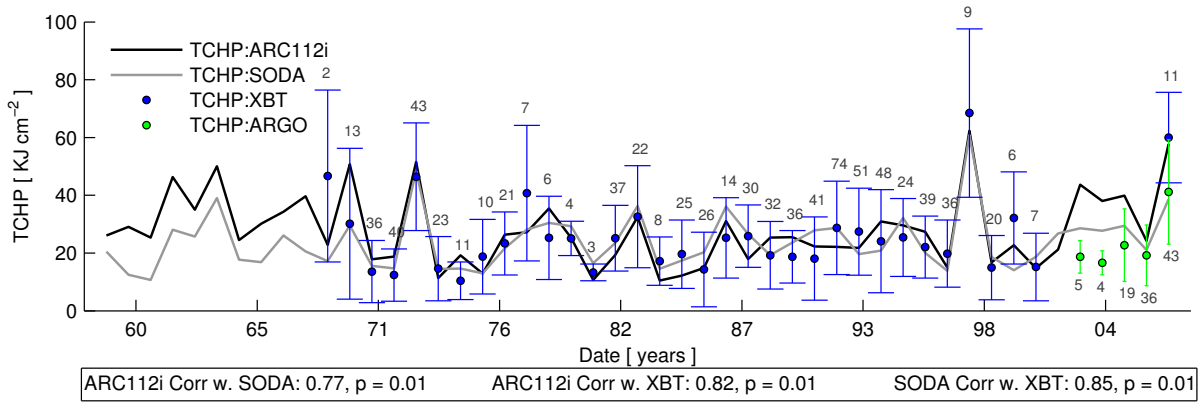

Figure 3.8: Tropical cyclone heat potential (TCHP) as extracted from ARC112i (black), SODA (grey), XBT(blue) and ARGO data (green). TCHP is extracted across a box spanning 50°E to 70°E, 12°S to 8°S and averaged across the November to April cyclone season for each year. Error bars cover ±1 standard deviation in the observed values. The number of observations for each cyclone season is shown. Red triangles indicate the number of tropical cyclone days for each season (Malan et al., 2013).

3.3.5 Basin-scale circulation and western boundary transports

The mean sea surface height (SSH) for the 1992-2007 period suggests that all interannual simulations exhibit a large-scale circulation that is consistent with observations (Fig. 3.9). There are suggestions that flow from the Pacific, via the ITF, is stronger than expected.

Barotropic streamlines entering the domain north of Australia echo this (Fig. 3.10), showing an influx of 20 Sv via the ITF. This flow, prescribed by the open boundary conditions, is slightly higher than the 16 Sv observed (Godfrey, 1989). South of Australia, a further 10-15 Sv flux enters the model domain at 155°E, via the Tasman leakage, a value that is consistent with observations (Sokolov and Rintoul, 2009) and inverse modelling studies (Ganachaud and Wunsch, 2000) at this longitude.

The barotropic transport functions (Fig. 3.10) show that the Indian Ocean tropical and subtropical gyre systems are well established, transporting 20 Sv and 80 Sv at their most intense. High speeds at 100 m speeds reflect the dominant upstream contributors to Agulhas Current variability; the MZC and EMC.

Transport contributions from the MZC and EMC reach a conflux in the northern Agulhas Current, forming a coherent western boundary flow south of 26°S. These upstream transport contributions are augmented by a further 30 Sv, derived from the SWIO sub-gyre, which recirculates retroflected Agulhas waters south of Madagascar (shown in the dark blue shading of Fig. 3.10). Barotropic transport contours indicate that most of this flow reaches the Agulhas retroflection. The incoherent transport path between the south Atlantic and Indian Ocean basins reflects the expression of Agulhas leakage via Agulhas Rings (Lutjeharms and Gordon, 1987). The southern branch of the supergyre is more clearly shown by the (arbitrary) zero transport line spanning the domain. South of this line, eastward transport indicates the Antarctic Circumpolar Current (ACC).

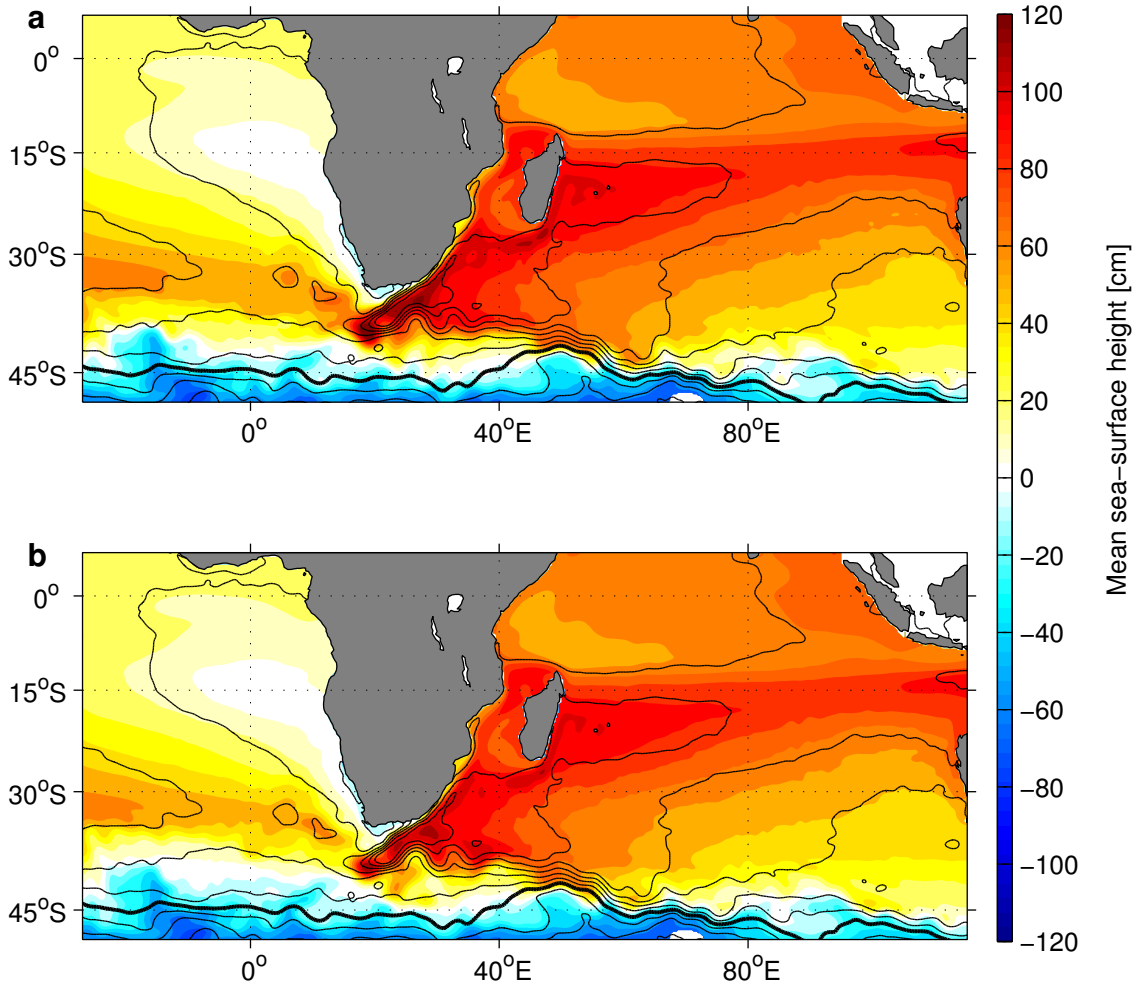

Figure 3.9: Mean sea-surface height fields for (a) AGIOi and (b) ARC112i for the 1992-2007 period, in shading. Black contours show the analogous fields, derived from the AVISO absolute dynamic topography, in 20 cm degradations. The heavy black lines show the arbitrary zero line for AVISO field.

Table 3.1 compares regional transports for each model with those observed. To facilitate this comparison, transports are calculated across the same transects used for the observations, and, where possible, using the same time-basis. For the Agulhas Current, Eulerian fluxes are calculated using the Physical Analysis of Gridded Ocean Data (PAGO[5]) toolkit. PAGO produces a best-fit step-function between specified points, using minimum interpolation to retain accuracy, and taking into account the native model grid. Eulerian and Lagrangian estimates for the Agulhas leakage are calculated across the Cape Basin, and northern sections of the Goodhope Line (as in Richardson (2007)), respectively. A full description of this methodologies used to calculated these estimates can be found in Chapter 3.

The Agulhas Current draws waters from the East Madagascar Current (EMC) and Mozambique Channel (MZC), which have measured transports of 20 Sv (Donohue and Toole, 2003) and 16.7 Sv (Ridderinkhof and de Ruijter, 2003), respectively. Modelled transports for the MZC

[5]http://www.whoi.edu/science/PO/pago

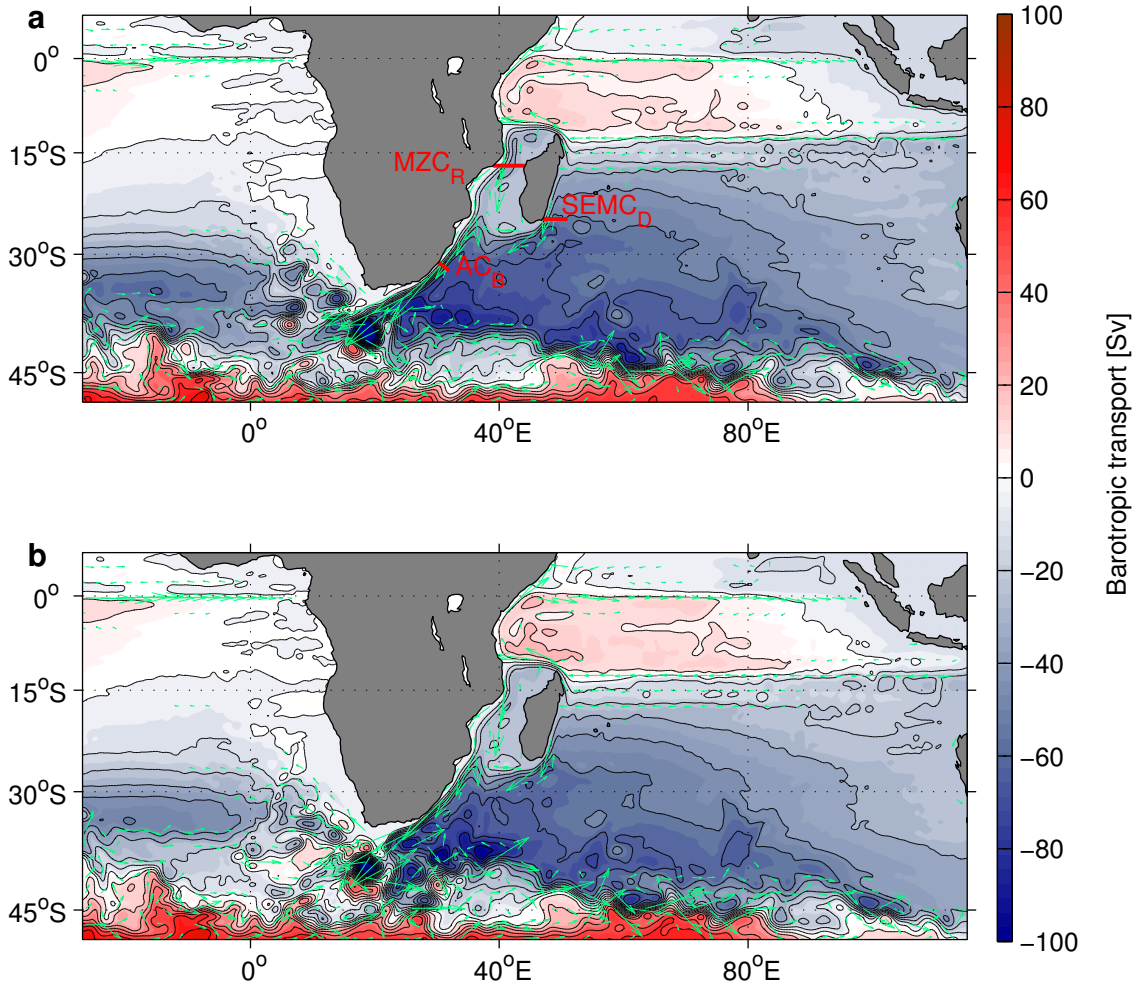

Figure 3.10: Barotropic transport function for (a) AGIOi and (b) ARC112i for the 1992-2007 period (shading) contoured at 10 Sv intervals. Green vectors show the velocity at 100 m. The AC_B, $SEMC_D$ and MZC_R sections are derived from Bryden et al. (2005), Donohue and Toole (2003) and Ridderinkhof and de Ruijter (2003), respectively, and are used to make comparisons with observations (Table 3.1)

are ∽9 Sv higher, at about 26.9 Sv for AGIOi and 25.3 Sv for AGIOi and ARC112i, respectively. Similarly for the EMC, regional values of ∽29 Sv are higher than the observed value. The eddying nature of the MZC, and dipole formation in the extension of the EMC are both captured in the AGIO and ARC112 parent configurations (Fig. 3.11). Further downstream, AGIOi and ARC112i record transports of 76.9 Sv and 76.1 Sv for the Agulhas Current at 32°S, almost exactly matching the 78.6 Sv observed (Bryden et al., 2005; Biastoch et al., 2009a). Mean regional transports for the climatological simulations are similar to their interannual counterparts, though the variability is lower, due to the shorter sampling period and lack of imposed interannual variability.

While the northern Agulhas is reasonably coherent, large solitary meanders sporadically occur. These features, known as Natal Pulses (Lutjeharms and Roberts, 1988) may form a link between the variability of the MZC and the timing of Agulhas Ring occlusion events (Schouten et al., 2002a). Fig. 3.12 shows an example of one such feature generated in ARC112i. The large

Table 3.1: Annual mean and transports (in Sv) for the interannual (suffix i; 1948-2007), and climatological (suffix r; year 41-60) reference simulations. Annual standard deviations are given for the models. To match observations, the mean Agulhas Current (AC_B) transport is calculated for the 1995-2004 period, with a 5-daily standard deviations. Transports are measured in the East Madagascar Current ($SEMC_D$), the Mozambique Channel (MZC_R) and Agulhas Return Current (RTN_L). AC_B, $SEMC_D$ and MZC_R transports are calculated across transects extracted from the references provided (Fig. 3.10). For AGIOi, ARC112r and ARC112r southwestward transport for AC_B is calculated through a stair-case section from original model velocities extracted using PAGO (http://www.whoi.edu/science/PO/pago). Agulhas leakage is quantified using Lagrangian (AL_L) and Eulerian (AL_E) approaches.

Configuration	MZC_R	$SEMC_D$	AC_B	AL_L	AL_E	RTN_L
AGIOi	26.9±3.3	29.2±5.2	76.9±19.9	32.7±3.5	27.6±2.8	30.5±4.8
ARC112i	25.3±3.3	28.5±4.1	76.1±20.4	18.9±3.2	18.8±2.7	31.1±4.6
OBSERVED	16.7[1]	20.0[2]	69.7±21.5[4]	15.0[6]	–	44.0[7]
		30.0[3]	78.6±19.7[5]			

[1]Ridderinkhof and de Ruijter (2003) & van der Werf et al. (2010), [2]Donohue and Toole (2003), [3]Nauw et al. (2008),[4]Bryden et al. (2005), [5]Biastoch et al. (2009a), [6]Richardson (2007), [7]Boebel et al. (2003b)

meander, which clearly visible at 35°S, is accompanied by a anti-cyclonic offshore eddy, and an inshore cooling at the surface.

3.3.6 Agulhas leakage; magnitude and mechanisms

Increasing spatial resolution has a clear effect on Agulhas leakage magnitude. At lower resolution, AL_L = 32.7 Sv for AGIOi. In comparison, AL_L for ARC112i is 18.9 Sv; closer to the 15 Sv derived from observed drifter paths (Richardson, 2007). AGIOi deviates from observations

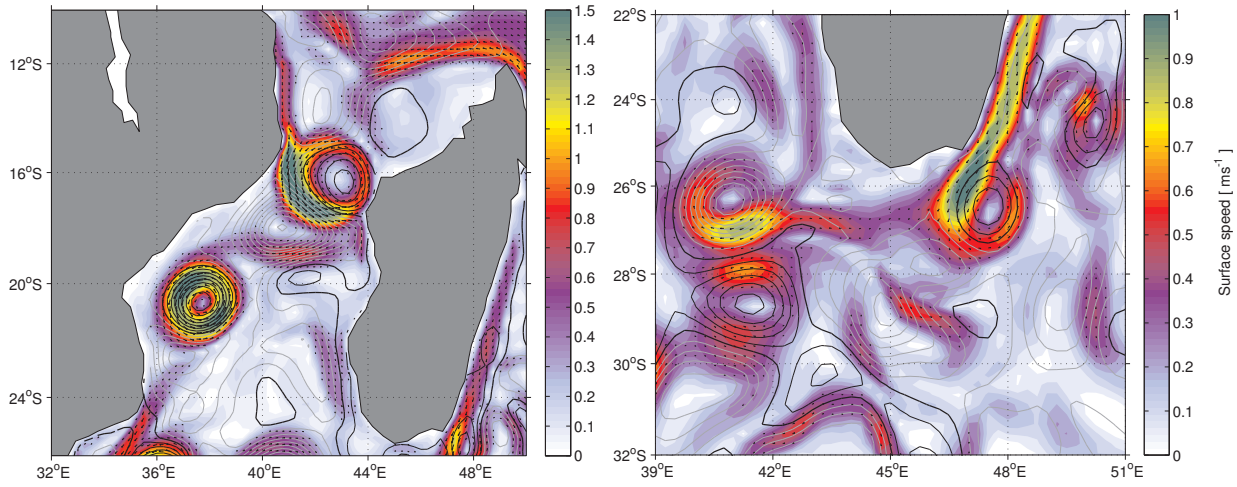

Figure 3.11: 5-daily snapshots of surface speed and SSH anomaly for January 2001, extracted from ARC112i. SSH anomaly, taken against the 1997-2006, is contoured at 5 cm intervals, with negative values in grey and the zero line delineated with the thick black line. Large anticyclonic eddies are clearly visible in the Mozambique Channel (left panel), and no western boundary current is in evidence. Large cyclonic and anti-cyclonic features at 40°E are indicative of a dipole formation in the extension of the EMC (right panel).

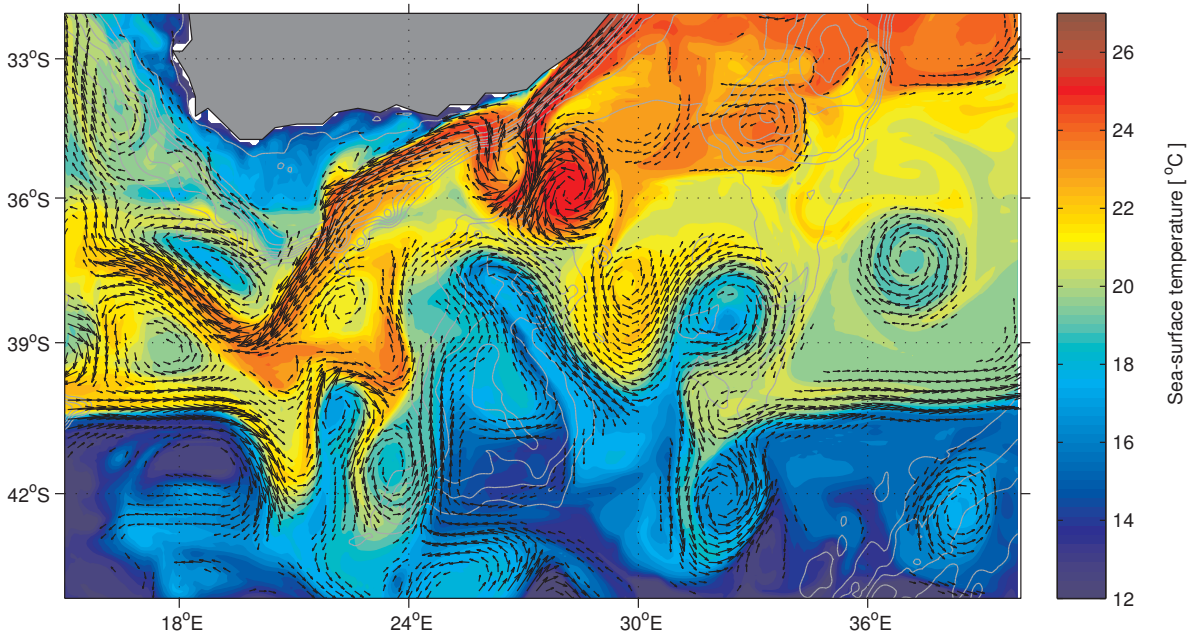

Figure 3.12: A snapshot of SST (shading) and surface speeds greater than 30 cms^{-1} (vectors) showing a Natal Pulse at ∽36°S in ARC112i on April 21st, 2001.

in the Agulhas Return Current, which is weaker and less coherent than observed (Boebel et al., 2003b), a consequence of its high leakage.

Leakage occurs through Agulhas Rings, which may take multiple paths through the Cape Basin (Dencausse et al., 2010a). Fig. 3.13 shows examples of these rings being produced in ARC112. Although ring occlusion is the dominant leakage mechanisms, inter-basin flux may occur through cyclonic eddies, filaments (Lutjeharms and Cooper, 1996) and, possibly, via the Goodhope Jet. Examples of the latter two features are shown in Fig. 3.14 and Fig. 3.15, respectively. The filament is clearly visible as a tendril of warm SST signal extending northwest from the retroflection into the substantially cooler south Atlantic, while the Goodhope Jet occurs as a coastal warming signal adjacent to the Agulhas Bank. The relative contributions of these mechanisms to the magnitude of the AL will be discussed in chapter 3.

3.3.7 Improvements in ARC112: Mesoscale variability

The Agulhas source and retroflection regions are characterised by high levels of mesoscale variability. The EKE patterns in (Fig. 3.16) suggest that both AGIOi and ARC112i capture this variability. High EKE values in the MZC reflect the appropriate formation of anti-cyclonic eddies, a consequence of the presence of Madagascar (Penven et al., 2006c; Ridderinkhof and de Ruijter, 2003). EKE values south of Madagascar are slightly lower than observed for AGIOi and ARC112i, suggesting that dipole formation in the EMC (de Ruijter et al., 2004; Siedler et al., 2009) is perhaps under-represented.

At increased resolution ARC112i shows a spatial EKE distribution closer to that observed.

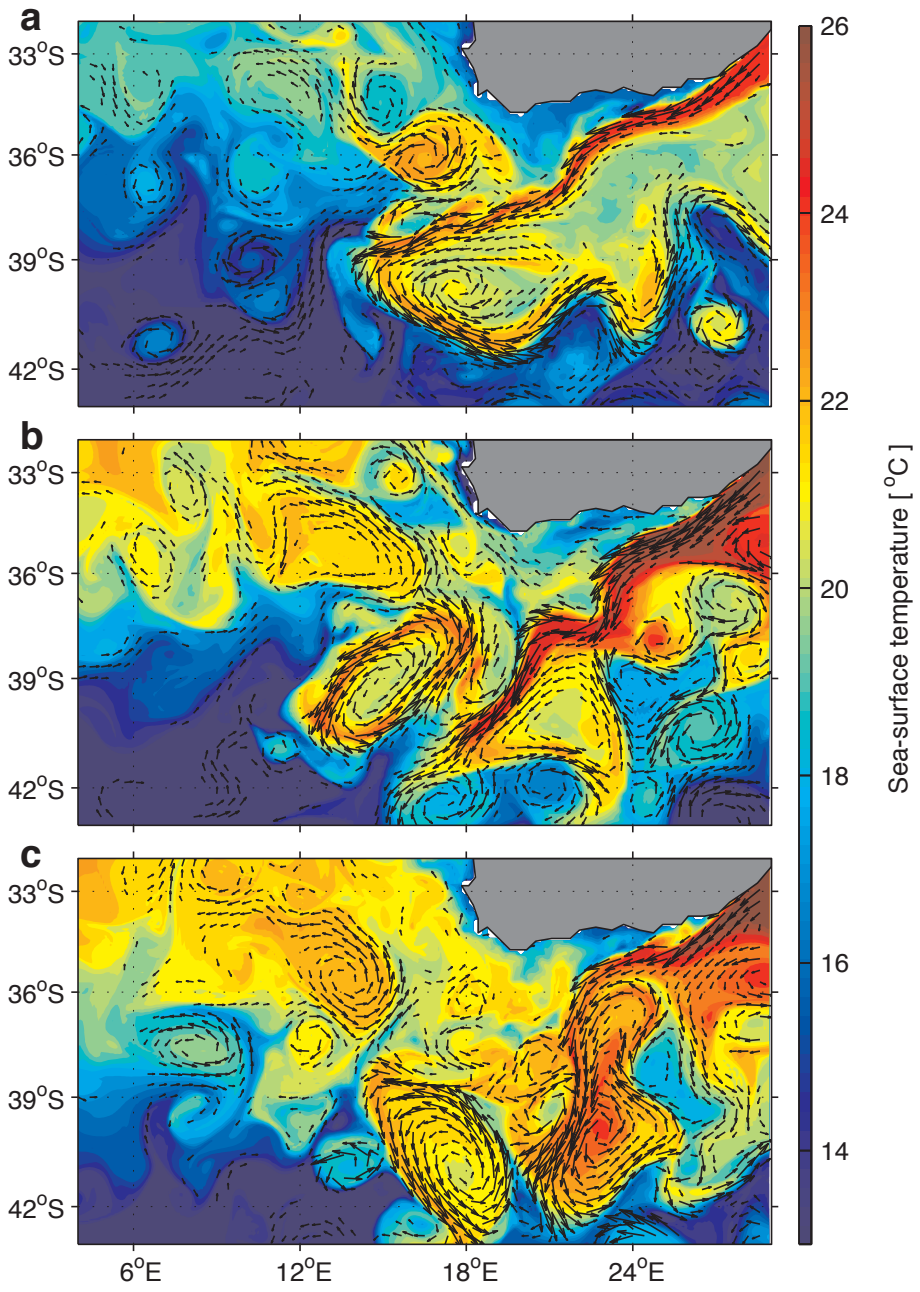

Figure 3.13: Snapshots of ARC112i SST (shading) and surface speeds greater than 30 cms^{-1} (vectors) show rings taking a) northern, b) central and c) southern ring paths, as described by (Dencausse et al., 2010a).

The return current EKE in ARC112i (Fig. 3.16 b)also shows an improvement over that of AGIOi. Inappropriate numerical choices may produce a modelled Agulhas Current that forms an unrealistic eddy-train or spurious upstream recirculation, expressed as high EKE along the South African coast and upstream of the retroflection, respectively. The EKE patterns of the eddying models used here are consistent with observations, suggesting a coherent WBC. Further, there is no indication of a consistently early retroflection. In the Atlantic, the EKE patterns are well spread, suggesting that there is no overtly preferential ring path. In general, due to

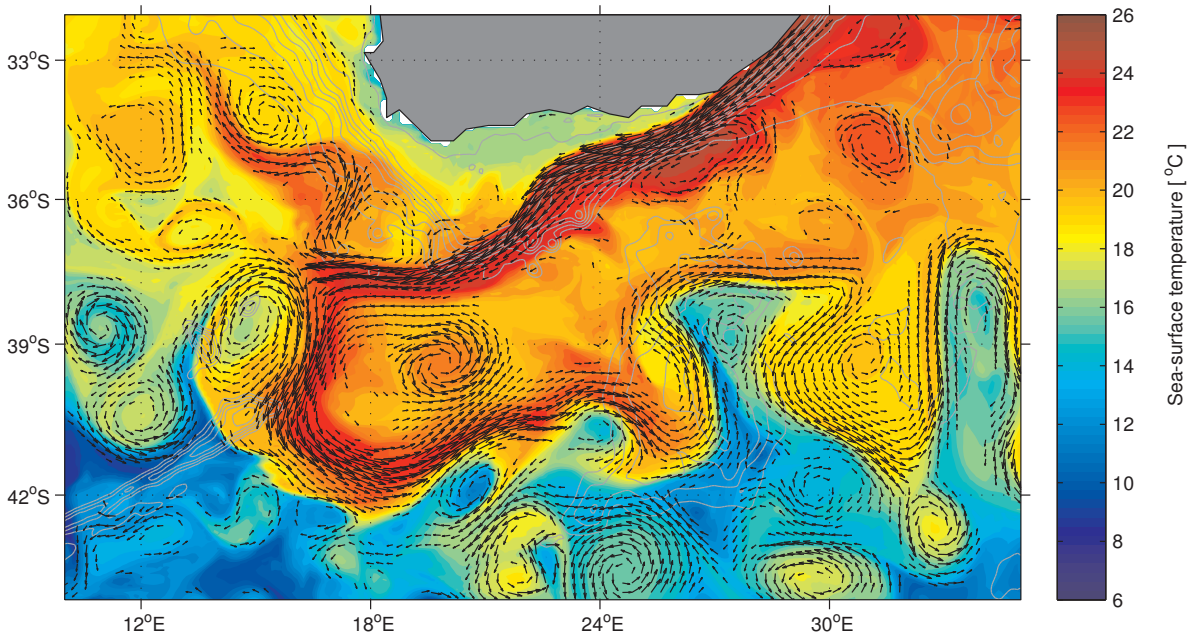

Figure 3.14: A snapshot of SST (shading) and surface speeds greater than 30 cms^{-1} (vectors) showing a filament in ARC112i on May 11^{th}, 2004.

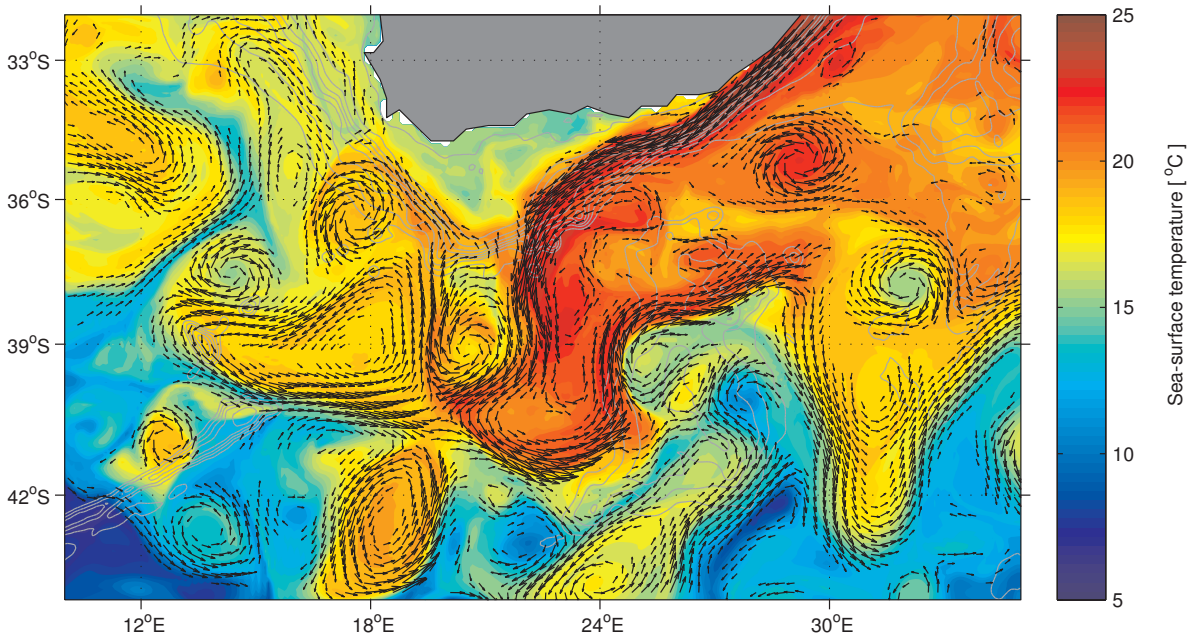

Figure 3.15: A snapshot of SST (shading) and surface speeds greater than 30 cms^{-1} (vectors) showing signs of a strong Goodhope Jet along the southwest coast in ARC112i on June 26^{th}, 2001. This feature is also evident in figures Fig. 3.12 to 3.14, but at reduced intensity.

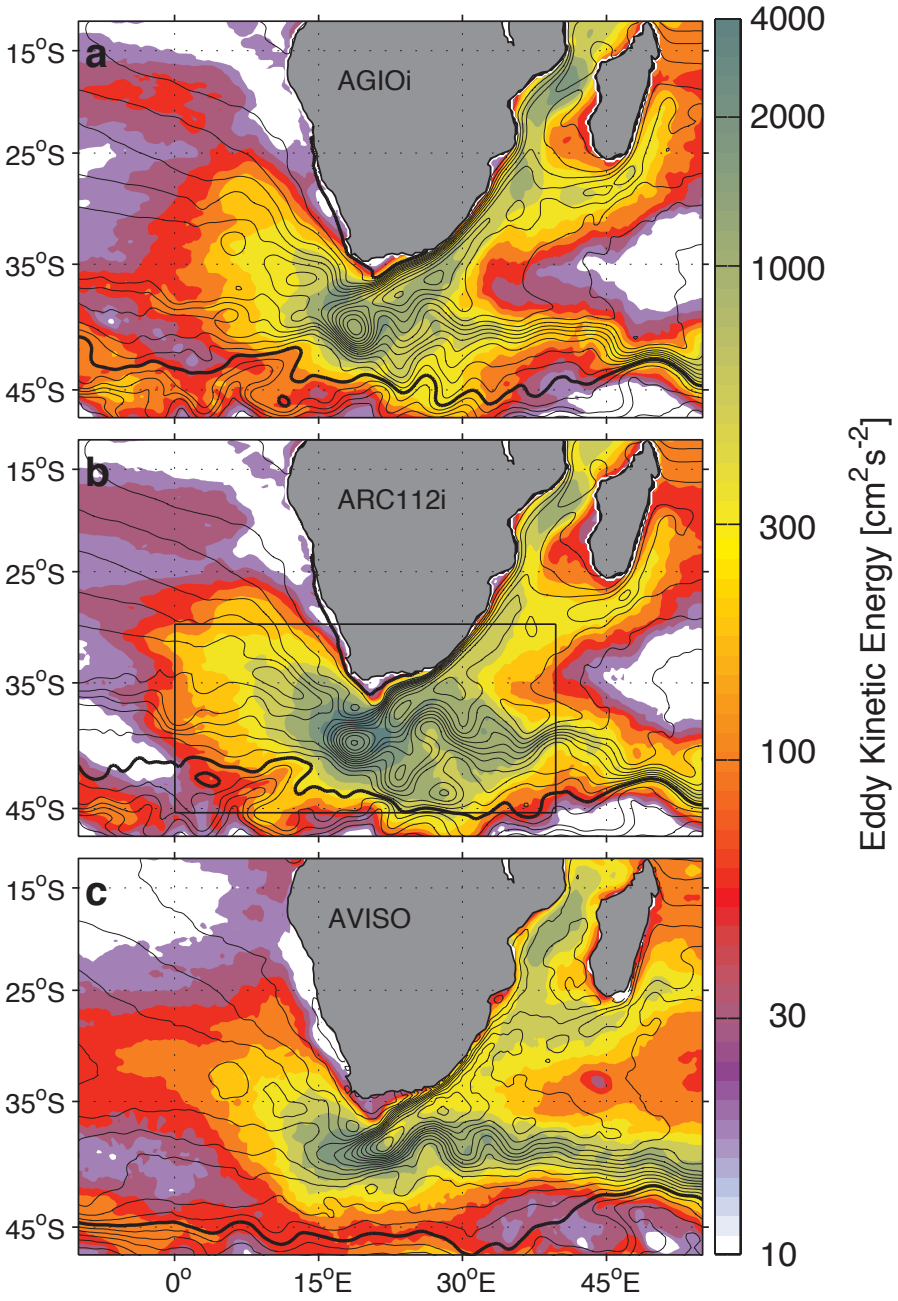

Figure 3.16: Eddy kinetic energy (EKE) for the 1992-2007 period derived from; a) AGIOi, b) ARC112i and c) AVISO. EKE is calculated from geostrophic velocities derived from the sea-surface height (SSH). Contours show 25 cm delineations of mean SSH for this period.

the objective mapping of the along-track data, the observed background signal is stronger and appears more smoothed than in the simulations.

In a recent paper, Backeberg et al. (2012) suggest that intensified winds have driven an increase in the mesoscale variability of the Indian Ocean. Fig. 3.17 compares the simulated EKE and MKE trends from 1992 to 2007 with those derived from altimetry. Both simulations and observations show an increase in MKE and EKE in the MZC and EMC. ARC112i shows a distinct increases in the MKE to the north of Madagascar and off of the south east coast,

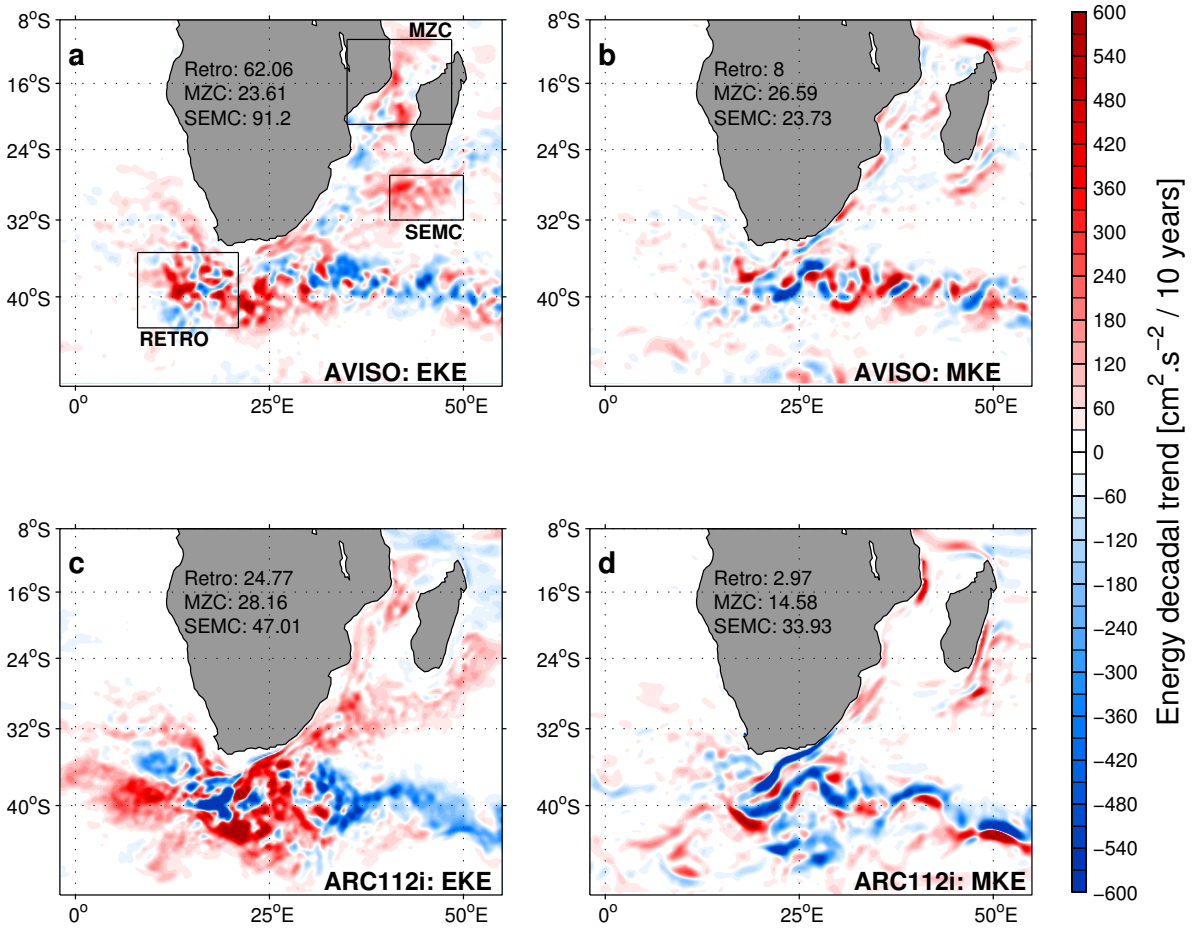

Figure 3.17: Mean kinetic (MKE) and eddy kinetic (EKE) energy tendency for the 1992-2007 period for (a), (b) AVISO and (c), (d) ARC112i. The annotated numbers show the spatially averaged change in EKE/MKE for the boxes shown in (a) in cm^{2}s^{-2}.decade^{-1}. The AVISO trends are identical to those shown by Backeberg et al. (2012).

consistent with observations. Increases in EKE in these areas are also seen in the altimetry record.

The retroflection signals in AGIOi (not shown) are not consistent with observations. However, both ARC112i and altimetry show a distinct negative tendency in the MKE in the Agulhas Current core, and an increasing MKE in the retroflection region. In addition, ARC112i expressed an increase in retroflection EKE, and a spatial pattern that has some notable similarities with that observed. Features seen in the observations such as; 1) the increases of EKE on the west coast of South Africa, 2) the decreases of EKE downstream of the retroflection, 3) increases in EKE to the south of the retroflection loop, are all echoed in the ARC112i pattern.

3.3.8 Improvements in ARC112: Retroflection position

The Ekman numbers for AGIOi and ARC112i, 1.6 x 10^{-8} and 7.7 x 10^{-9} respectively, suggest that both have inertially governed retroflections (Dijkstra and de Ruijter, 2001). However, bathymetric smoothing in AGIO reduces the protrusion of the Agulhas Bank, allowing the current to

overshoot the shelf in a near zonal direction (Fig. 3.18). Similar behavior is seen in experiments where the Agulhas Bank is excised (Speich et al., 2006). In contrast, the improved topography in ARC112i allows the 'jut' of the Agulhas Bank to be retained, causing the southwestward deviation in the jet prior to the retroflection. As a result, while both models display a more westward retroflection than that observed, the retroflection in AGIOi is more prograded, and occasionally crosses the GH line, where the leakage is computed. The consequences of this are fully discussed in chapter 4.

Downstream of the retroflection, improvements in the rendering of the Agulhas Plateau in ARC112 give rise to an Agulhas Return Current that is more phase-locked to bathymetry. This current path, in which the first meander rounds the Agulhas Plateau to the north, more closely mirrors observations (Boebel et al., 2003b) and may have consequences for Agulhas Ring generation. Pichevin et al. (2009) show that rings are generated through the westward propogation of meanders in the downstream current. As such, the topographic insulation in

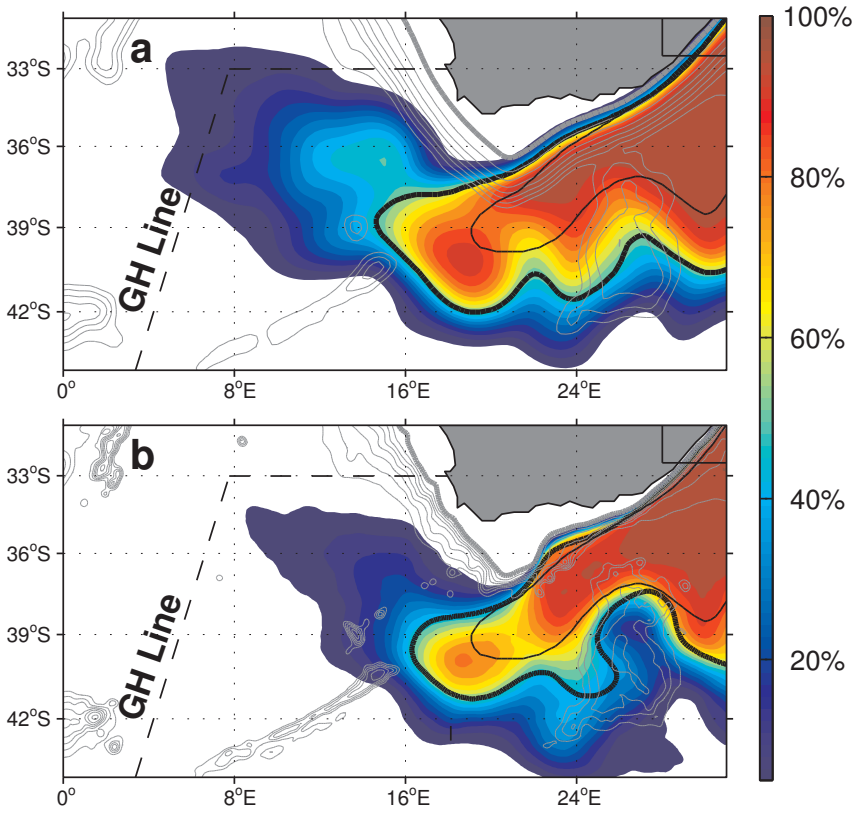

Figure 3.18: Spatial extent of the retroflection position derived from the 5-daily SSH for the 1992-2007 period (shown in shading). Grey contours represent bathymetry at 500 m depth intervals, with the thick grey line following the 500 m isobath. The thick black contour shows the model retroflection path for (a) AGIOi and (b) ARC112i as derived from the mean SSH for the period. The thin line shows the mean retroflection path similarly derived for AVISO. The dashed transect shows the GoodHope line (GH line).

ARC112 may result in a reduced ring production rate, and therefore contribute to the reduction in leakage seen at higher resolution.

3.3.9 Improvements in ARC112: The Agulhas Undercurrent

Comparison of velocity sections across the Agulhas Current at 32°S shows that a strong Agulhas Undercurrent is present in the ARC112r simulation (Fig. 3.19). This undercurrent, not seen in AGIOr, mirrors the observations of Beal and Bryden (1997) and echoes the findings of previous high resolution models (Biastoch et al., 2009a). The LADCP observations suggest that the undercurrent extends from 3200 m to 1200 m depth and extends 30 km offshore, with a speed of $\backsim$0.2 ms^{-1} (Beal and Bryden, 1997). These spatial and velocity scales of the simulated undercurrent in ARC112r are similar to those observed.

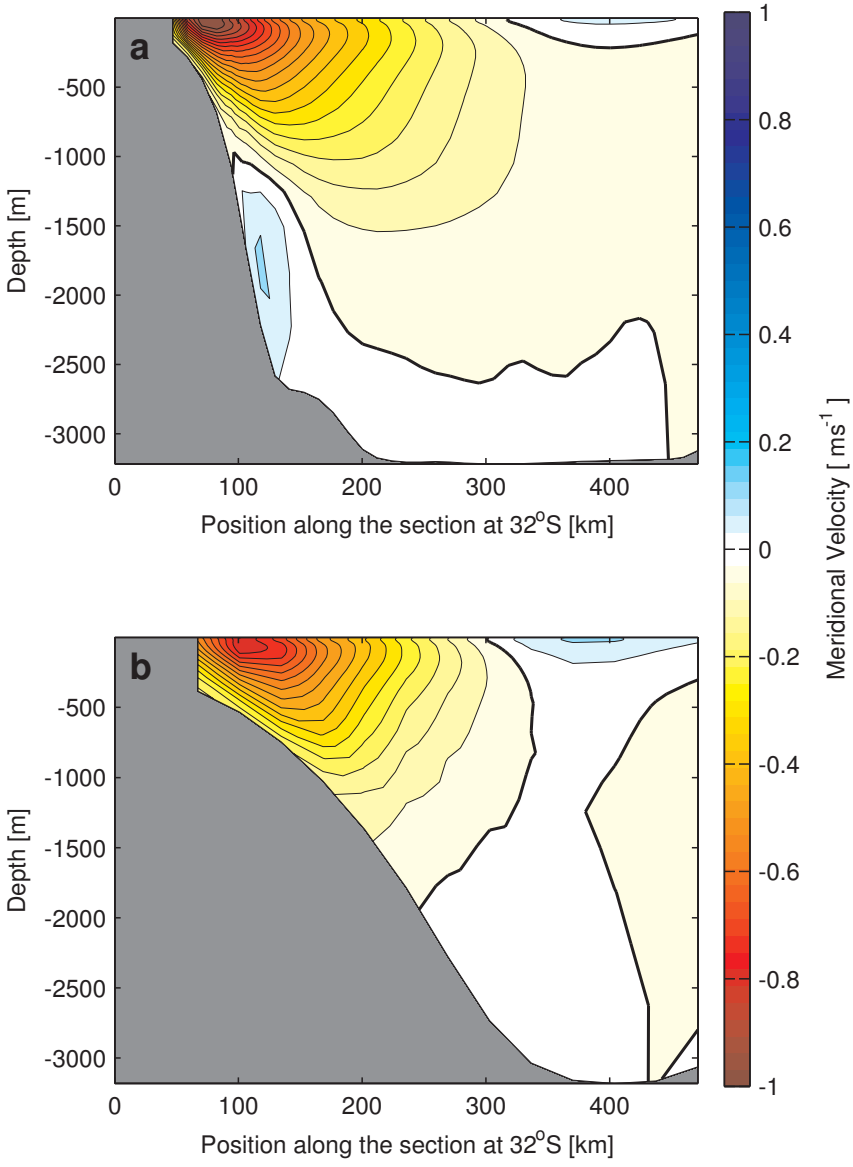

Figure 3.19: Meridional velocities across a zonal section through the Agulhas Current at 32°S for a) ARC112r and b) AGIOr. Positive flow is defined as northward.

3.4 Model suitability

3.4.1 Deviations in tracer properties

As mentioned previously, the sea-surface state in AGIOr and ARC112r is not explicitly prescribed. Rather it is determined through the bulk formulation of the atmospheric variables (Fairall et al., 1996). As a result, although damped to the air temperature value, SST has a limited degree of freedom. Typically, as uncoupled GCMs are unable to transmit precipitation in the atmosphere, they have in fresh water imbalance between the tropics and high-latitudes. Often a salinity restoring term is applied to correct for this, and ORCA05 is no exception (Durgadoo et al., 2013). However, the regional configurations presented here do not use any salinity restoring within the domain, and therefore salinity is the less well constrained.

Despite this comparative freedom, AGIOr and ARC112r show some success in re-producing a temperature field that is consistent with observations, both at the surface, and in the thermocline. Where larger anomalies do occur these tend to reflect the biases present in the large scale solution, such as in the tropical Atlantic (certainly a known area of substantial bias in coupled climate models e.g. Grodsky et al. (2012), Wahl et al. (2011)). However, in general, the thermocline in AGIOr and ARC112r is deeper than observed, especially in the sub-tropical Atlantic. Given that ARC112r records a leakage value close to that observed, it seems very unlikely that this deepening signal is a result of an over-expression of inter-basin flux, especially as the Agulhas thermocline in ARC112r is substantially shallower. Rather, it seems that this upper-ocean warming arises due to domain size or as a consequence of the model numerics.

The Indian Ocean remains the best preserved basin, with a realistic thermocline and strong halocline in both ARC112r and AGIOr, although the surface salinity value deviates from observations, potentially due to the loss of IEW. Interannual variability of the temperature signal in the upper ocean, validated through comparison with dipole indices and TCHP (figures 3.8 and 3.7 shows that the surface signal is appropriately conveyed into the upper ocean. As TCHP is determined by heat content above 26°C, this in turn suggests that, on an interannual basis, the depth of the 26°S is again appropriately simulated.

The salinity field is reproduced with less fidelity. Surface anomalies, especially in the tropical Atlantic, are substantial and the halocline is weaker and deeper than observed in both Atlantic and Indian Ocean sections. High values in the surface tropical Atlantic are to an extent attributable to the lack of river run-off, and may be partially determined by the external solution. However, there is a clear deterioration beyond what would be expected from these factors alone.

Substantial efforts have been made to improve the retention of water mass properties in ROMS through the reduction of spurious diapycnal mixing (Marchesiello et al., 2009), leading to the improvements shown in figure 2.9. However, rotation of the diffusion operator still leaves residual errors, which, although small, may contribute to the loss of water mass properties in large domains such as this. ROMS v.3 introduces an isoneutral scheme to further minimise these errors, but this new approach has not been implemented here.

Despite a weakening of the halocline, the major water masses of the Indian and Atlantic Ocean are clearly represented. The similarities between the observed and simulated water masses in figure 3.6 provide strong evidence that the constituent ingredients of each basin are well preserved. However, discrepancies in the depth distributions of these water masses in the top 500 m may effect basin-scale stratification, with consequences for the large-scale thermohaline properties of the basin.

Of the sections tested, the largest thermocline and halocline discrepancies appear in the Agulhas region. However, it is likely that WOA05 is least accurate here due to an under-sampling of the western boundary signal at low spatial resolution. This raises questions as to the behaviour of the retroflection in the face of changes to the regional baroclinity. However, this appears to be a question that appears to remain largely unaddressed. This aside, as the buoyancy flux between the Indian and Atlantic oceans has been put forward as a major non-linear driver of AMOC strength (Weijer et al., 2002), deviations in the vertical structure of the Agulhas Current may have an impact on convection in the North Atlantic.

3.4.2 Agulhas circulation and dynamics

The greater Agulhas system is highly complex; featuring a strong western boundary current and areas of pronounced mesoscale activity in the upstream source regions and south of Africa. Under the influence of the large-scale wind field, the non-linear combination of these factors results in the division of Agulhas at the retroflection. The magnitude of the AL, the thermohaline link between the Indian and Atlantic Oceans and the climatically relevant component of the system, is sensitive to events that occur on a multitude of spatial and temporal scales. Therefore, any model that hopes to simulate the variability in this system, must capture not only the large-scale transports, but mesoscale processes as well.

The Agulhas Current receives its volume flux from three sources; the MZC, SEMC and via recirculation in the SWIO sub-gyre. Simulated Agulhas transport at 32^{o}S agrees well with observations, however transport through the MZC and SEMC are higher than expected. This suggests that the sub-gyre contribution is low, which may in part be due to a weakened return current, a consequence of a high leakage value. Additionally, the SST field suggests that there may be excessively high mixing across the STF. Dencausse et al. (2011) point out that the STF is not continuous south of Africa, and should not be though of as an impenetrable barrier to eddy flux. Further, Le Bars et al. (2012) describe a third retroflection regime, under which turbulent flux across the STF places an asymptotic limit on leakage. Although it is unlikely that this limit has been reached (see chapters 5 & 6), it does point to circumstances where western boundary flux may be lost to the south. The propensity of ROMS to produce an eddy-rich field may potentially weaken the STF and allow this flux to be higher at lower wind-stress curl values.

The presence of Madagascar induces substantial mesoscale variability in the upstream source regions (Penven et al., 2006c), which may, in the case of MZC eddies, contribute to the timing of Agulhas Ring occlusion (Schouten et al., 2002a; Biastoch et al., 2008c). Although Biastoch

et al. (2008c) show that upstream eddies do not influence the leakage in the mean, the close match between the simulated EKE patterns for the source regions and those observed (figure 3.16), suggests that AGIO and ARC112 may preserve some of this mesoscale connection. Natal Pulses, one mechanism by which this upstream connection may form, are represented in both AGIO and ARC112.

Reanalysis data suggest a consistent increase in trade winds during this period, which has resulted in an increasing trend in mesoscale variability in the source regions and retroflection (Backeberg et al., 2012). The regional simulations mimic these trends in the source regions, but only ARC112i approximates the observed signal in the retroflection. This suggests a distinct difference between the behaviour of the two simulations, and underlines the improvements made by introducing higher resolution and improving topography.

In both regional configurations, the retroflection loop extents further westward than observed. These overly prograded (more extended) loops are coincident with leakages that are larger than the 15 Sv measured by Richardson (2007). Previous work relating the retroflection loop position to leakage magnitude (van Sebille et al., 2009a) suggests that the two are significantly, though weakly, correlated. However, van Sebille et al. (2009a) focus more on the event scale of ring occlusion, and not on the mean position of the retroflection. Further, Dencausse et al. (2010b) and Backeberg et al. (2012) used altimetry to show that the observed retroflection position has remained remarkably stable in the satellite era, while model hindcasts (e.g. Biastoch et al. (2009b); Rouault et al. (2009)) agree with near unanimity that leakage has increased substantially over this period. This suggests that there may not be such a clear link between the mean position of the retroflection and the mean leakage value.

Leakage occurs primarily through westward drifting Agulhas Rings. The smoothed topography in AGIO reduces the shelf angle, minimises the protrusion of the Agulhas Bank, and substantially reduces bathymetric steering around the Agulhas Plateau. All of these factors have been previously related to AL magnitude. Increased topographic smoothing and excising the Agulhas Bank was shown to increase leakage substantially by Speich et al. (2006), while removing the plateau allows the return current meanders to propagate westward freely, inducing ring occlusion (Speich et al., 2006; Pichevin et al., 2009). It therefore seems likely that in AGIO, the overly westward retroflection position, and increased leakage are both functions of the smoothed topography. However, while this topographical sensitivity may set the mean state, it does not undermine the ability of the retroflection to behave as an inertial jet; a critical feature for any realistic Agulhas Current (Dijkstra and de Ruijter, 2001). The concerns surrounding topographical interaction are largely addressed in ARC112. Here the shelf is steeper, the bank protrudes accurately an the return current is strongly steered to the north of the plateau in the first meander. Consequently, the AL is much nearer the observed value. Leakage by mechanisms other than rings are also in evidence (figure 3.15 and 3.14).

Early retroflections are a common problem in Agulhas modelling. In configurations that exhibit this behaviour, ring occlusion is often impossible as the angle of the coast prevents them

from escaping the main current (Zharkov and Nof, 2008a; Zharkov et al., 2010). Whilst upstream retroflection events do occur in both AGIO and ARC112, they do not result in a permanent phase-locking behind the Agulhas plateau, and are sporadic (a situation which has a precedent in observations (van Aken et al., 2013; Dencausse et al., 2010b)). This situation is reflected in the EKE patterns for AGIOi and ARC112i, which exhibit low EKE patterns upstream and approximate observations well (figures 3.16 and 3.17).

Numerous configurations report cases in which, post occlusion, rings follow an overtly preferential path across the south Atlantic. This pattern is symptomatic of an overly regular ring generation mechanism (possibly related to an over-dependence on Natal Pulse generation (van Leeuwen et al., 2000)) and is typically expressed as a narrow 'channel' of high EKE across the Cape Basin and wider region. In contrast, the EKE pattern in AGIOi and ARC112i matches altimetry closely, suggesting that the generated rings are well spread and able to follow multiple paths (figure 3.13), as observed by Dencausse et al. (2010a).

3.5 Conclusions

The behaviour of AGIO and ARC112 has been assessed through comparison with observations derived from altimetry, *in situ* measurements and transports derived from literature. Although the major water masses are in evidence, there are discrepancies in their distributions. Typically these deviations occur in highly variable regions (such as along the STF) and may also be partially attributable to the choice of boundary conditions. The interannual evolution of the thermal properties is well captured, both at the surface, and in the Indian Ocean thermocline. However, the deviations from WOA05 tracer fields suggest limitations in the ability of the regional configurations to conserve the basin-scale properties and water mass distributions on longer time-scales.

Dynamically, both AGIO and ARC112 show appropriate basin-scale circulation patterns, and although source region transports are high, western boundary fluxes are realistic. Although both AGIO and ARC112 feature inertially driven retroflections, the inclusion of the high-resolution nest in the latter greatly improves the interaction with topography. The resulting improvement in retroflection position, when compared to observations, is coincident with a leakage closer to that observed. However, neither configuration features an early retroflection position, and ring formation occurs in all simulations. Both configurations show a level of mesoscale variability consistent with altimetry products for the 1992-2007 period, and, in the case of ARC112i, trends in EKE match observations well.

In summary, despite some deviations in the distribution of tracer properties, AGIO and ARC112 appropriately capture the variability of the Indian Ocean and greater Agulhas, with dynamical responses that are accurate enough to allow the investigation the regional response to changes in the basin scale wind field with a degree of confidence.

Chapter 4

Quantifying Agulhas leakage magnitude and structure

4.1 Introduction

The Agulhas retroflection is one of the most turbulent areas in the global ocean (Schmitz and Luyten, 1991). The combined effects of a Agulhas Current transport, the inherently unstable nature of inertially governed retroflections (Dijkstra and de Ruijter, 2001) and the ejection of Agulhas Rings (Pichevin et al., 2009) contribute to a region with an eddy kinetic energy among the strongest observed. The formation of cyclones in the lee of the Agulhas Bank (Penven et al., 2001), splitting and modification of Agulhas Rings (Baker-Yeboah et al., 2010; Dencausse et al., 2010a), and effect of topography (Dencausse et al., 2010b,a; Speich et al., 2006) exacerbate the already complex flow pattern in the Cape Basin.

Consequently, accurate quantification of the inter-ocean exchange of Indian Ocean waters through the Agulhas leakage is a substantial challenge and observations of total Agulhas leakage are sparse, and highly variable. Estimates from geostrophy place the leakage between 4 Sv (Garzoli et al., 1996) and 15 Sv (Gordon et al., 1992). More recently, Richardson (2007) tracked subsurface drifters to reach an estimate of 15 Sv. The effect of this flux on the hydrography of the Cape Basin is substantial, with up to 50% of the water there of Indian Ocean origin (Garzoli and Goni, 2000). These waters have been observed to spread through four contributory leakage mechanisms; specifically through:

- Advection inside Agulhas rings and smaller cyclonic and anticyclonic vortices that may arise through ring splitting (Schouten and de Ruijter, 2000; Boebel et al., 2003a)
- Via filaments (Lutjeharms and Cooper, 1996)
- Through the direct leakage of predominantly intermediate waters (de Ruijter et al., 1999a)
- As a coastal jet at the shelf edge (Bang and Andrews, 1974)

In general the majority of inter-ocean flux is thought to occur via Agulhas rings, occluded from the retroflection at a rate of 5 ± 1 year^{-1} (Schouten et al., 2002a). Contributions from cyclonic eddies (Hall and Lutjeharms, 2011), filaments (Lutjeharms and Cooper, 1996; Whittle et al., 2008) and through direct flow are suggested as being of secondary importance. However, this picture often requires a substantial degree of inference with regard to the shape, profile, constituent waters and evolution of a 'typical' Agulhas Ring (Richardson, 2007; Boebel et al., 2003a). Estimates of total flux per ring vary substantially, from 0.65 Sv.ring^{-1} (Duncombe Rae et al., 1996) to 3 Sv.ring^{-1} (Gordon and Haxby, 1990), producing total ring flux estimates of between 3 Sv and 9 Sv, depending on ring formation rate (Richardson, 2007). van Ballegooyen et al. (1994) and measure total Agulhas Ring flux as 7 Sv for temperatures, T, greater than 8°C. Goni et al. (1997) report a similar value for T>10°C. However, a recent census of ring paths, derived from altimetry, shows that they may take one of three paths across the Cape Basin (Dencausse et al., 2010a); a northern path between the coast and Erica Seamount, a central path between the seamount and Agulhas Ridge, and a southern path south of, and subsequently across, the ridge. In the southern path, the ring may drift near, or even past, the STF, leading to substantial modification of the water mass properties of the eddy. Garzoli (1999) noted such a modification in a hydrographic study of three rings during the Benguela Current Experiment cruise.

Quantifying leakage can also present a challenge to numerical modellers. Many recent attempts focus on a Lagrangian approach, seeding floats in the Agulhas Current and collecting across a nominal Cape Basin section (Speich et al., 2001; Doglioli et al., 2006; Biastoch et al., 2008c, 2009b; van Sebille et al., 2009b). By design, this defines leakage as the proportion of Agulhas Current waters exported into the Atlantic. This approach, while flexible, typically excludes diffusive processes, and offline calculations possibly sacrifice precision in turbulent regions. Eulerian approaches also face limitations. Typically, appropriate fluxes can only be sampled by imposing water mass criteria or by adjusting the extent of the sampling transect. This is a substantial problem in eddy rich regions. Comparing the two methods, van Sebille et al. (2010c) found that Eulerian estimates of flux across the GoodHope line (GH-line) (Swart et al., 2008) may underestimate leakage by a factor of two.

Doglioli et al. (2006) determined the vorticity of leakage in a regional model by classifying Lagrangian float trajectories as 'loopers', particles that appear to circulate within eddies, and 'non-loopers', those that drift westward on a less perturbed path. They determined that only 30% of the total Agulhas leakage was trapped within eddies, with a 1.3:1 anticyclone to cyclone ratio, and the remainder as 'non-looping' flux. Substantial flux between Agulhas Rings was previously noted by Gordon et al. (1987), who measured a transient 10 Sv jet between two warm core eddies. While various subsequent studies have suggested that this 10 Sv inter-ring flux estimate is exceptionally high (Lutjeharms, 2006b).

While the simulations presented in Doglioli et al. (2006) were forced with climatological fields, recent hindcasts show a consensus increase in the magnitude of the Agulhas leakage (Rouault

et al., 2009; Biastoch et al., 2009b). However, these studies do not attempt to deconstruct this signal into fluxes attributable to individual mechanisms or changes in ring trajectories. The subsequent response of the Atlantic Meridional Overturning Circulation to South Atlantic buoyancy sources may in part depend on the nature of the leakage (Weijer et al., 2002), and the time evolution of water mass properties within coherent ring structures (de Ruijter et al., 1999a). As such determination of the relative contributions of the mechanisms described above may be of larger interest.

Here, long term trends in the Agulhas leakage will be compared using Lagrangian and Eulerian methods. In the latter case, a passive tracer is introduced allowing Indian Ocean waters to be explicitly labelled, reducing ambiguity. Using these approaches, the leakage is subsequently decomposed into eddying, non-eddy and coastal fluxes. Latterly, an eddy-tracking scheme is implemented, allowing simulated mesoscale variability and ring tracks to be compared with observations from altimetry.

4.2 Leakage quantification

4.2.1 The Lagrangian approach

Lagrangian fluxes are obtained using the ARIANE[1] package (Blanke and Raynaud, 1997). Lagrangian experiments are performed via the release floats across an initial Agulhas Current section at 32°S (Fig. 4.1, AC_L) and subsequently computing their positions by integrating the velocity fields forward in time. The incoming velocity field determines the initial position of each float, with no limitation placed on the depth of release. The AC_L transect stretches from the coast to the longitude of first recirculation of the western boundary current. The floats are collected across the remaining sections shown in Fig. 4.1a, with leakage (AL_L) measured across the approximate northern sections of the GH-line. The L and E subscripts will be used to denote respective Lagrangian and Eulerian passive tracer fluxes, throughout.

The position of the STF in the South East Atlantic and South West Indian Ocean is controversial. Using differing methodologies based on hydrography and/or SSH gradients Orsi et al. (1995), Belkin and Gordon (1996), Sokolov and Rintoul (2009) and, more recently, Graham and de Boer (2013) determined substantially different latitudes for the frontal systems south of Africa. The STF_L line, used here to nominally indicate the subtropical front, forms the southern boundary of the Lagrangian control volume at 44°S. This latitude is consistent with the most poleward extent of the STF derived from the model using the Orsi et al. (1995) method, where the STF is defined through the 12°C isotherm at 100 m depth. Setting the STF_L line at the most poleward extent of the STF minimises the likelihood of ARC floats being incorrectly sampled as the STF flux. At 44°S the STF_L remains outside of the ARC112 sponge layer.

[1](ARIANE v.2-2-6; http://www.univ-brest.fr/lpo/ariane/)

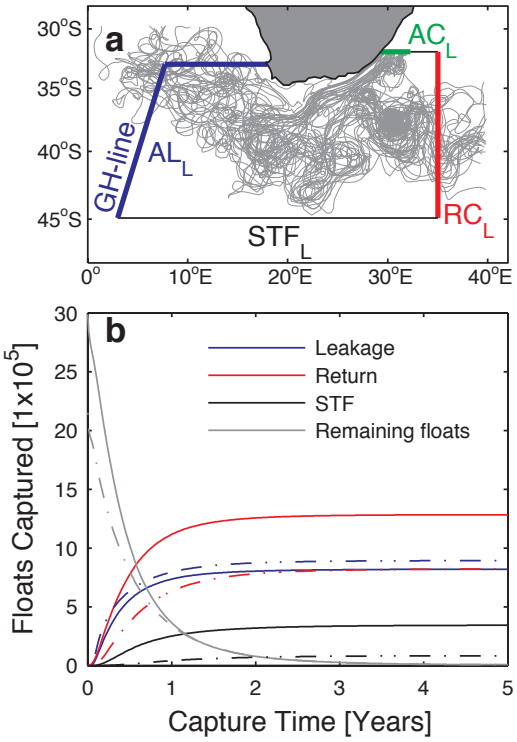

Figure 4.1: Panel (a) shows a schematic representation of the trajectories of particles released across the Agulhas Current. Lagrangian flux estimates for the Agulhas Current, leakage, return current and Subtropical Front are measured across the AC_L, AL_L, RC_L and STF_L transects. The AC_L transect follows the path of the GoodHope line (GH-line, Swart et al. (2008)). Panel (b) shows the float capture times for 5-year Lagrangian virtual float integrations in dashed lines for AGIOr and solid lines for ARC112r.

ARIANE can be run in two modes: quantitative, where volumes fluxes can be determined, and qualitative where float trajectories can be monitored. Both modes are used here. In quantitative mode ARIANE automatically determines the number of floats released according to the incoming current transport. Floats, each representing 0.1 Sv of the Agulhas Current, are dropped at 5-daily intervals across a single model year and integrated for a further four years, producing annual transport estimates for each section. A value of 0.1 Sv is appropriate for quantifying a large-scale western boundary current, such as the Agulhas, where transports exceed 65 Sv in the mean. While this limits precision to 0.1 Sv when determining volume transport, it equates to an error of less that 1% in with regard to the Agulhas leakage, which has a mean transport of 19 Sv. At each time step of the Lagrangian integration period, ~350,000 floats are considered in ARC112, and ~200,000 floats are considered in AGIO. The ARC112 and AGIO grids contains ~62,000 and ~7750 horizontal grid points in the integration region, respectively. Consequently, the float density is substantially greater than one per grid point and so provides a good representation of the flow at first order.

Float positions evolve in the linearly interpolated velocity fields until they are 'captured' at a receiving transect, at which point they are removed. The release and receiving transects form a closed box surrounding the control volume defined as the area bounded by the transects in

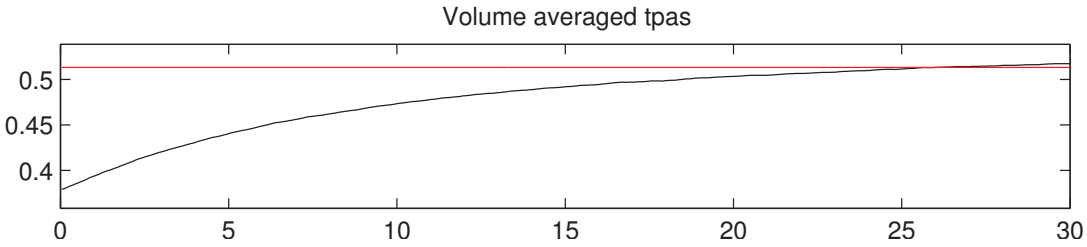

Figure 4.2: Evolution of the passive tracer during the initial spin-up period

Fig. 4.1a. Fig. 4.1b shows the cumulative capture times of floats at the receiving transects, and shows that, after a five-year integration period, only 0.3% of floats remain within the control volume. Due to changes in the elementary transport field, floats do not represent 0.1 Sv at their collection point. As such, float number is not proportional to transport, and despite similar float numbers received at the GH-line in ARC112r and AGIOr, the leakage differs substantially.

4.2.2 The Eulerian approach: passive tracer flux

Previous Eulerian estimates of Agulhas leakage relied on the imposition of either water mass criteria, or on determining the optimum geographical extent of the sampling transect. Comparing Eulerian and Lagrangian methods in a hindcast simulation van Sebille et al. (2010c) determined that the former would underestimate the leakage by up to a factor of two using these criteria due to a lack of specificity in selecting water masses. To overcome these limitations, Eulerian transports are derived from a passive tracer, introduced to explicitly label Indian Ocean waters, based on on the approach adopted by Le Bars et al. (2012) and Penven et al. (2011). The tracer, implemented at the start of the model spin-up period, is nudged to one to the east of 70°E, indicating 100% Indian Ocean waters, and to zero west of 20°W, representing Atlantic waters. Between these boundaries it is free to evolve through advection and diffusion. The tracer reaches statistical equilibrium during the spin-up period (Fig. 4.2) and fluxes are subsequently calculated from the 5-daily tracer and velocity fields. Agulhas Current and Agulhas leakage transport are calculated across the AC_E and Cape Basin (AL_E) sections, shown in Fig. 4.3. The AL_L section was chosen to match the northern branches of the GH-line. However, to avoid complications associated with rotating velocity components to calculate flux the western AL_E section is orientated meridionally.

Ring structures, expressed as regions of high tracer concentration, are clearly visible in Fig. 4.3. However, there is substantial spreading of the tracer outside of the confines of the rings. The Cape Basin and Southeast Atlantic is comprised of approximately 50% Indian Ocean water at 100 m, consistent with the observation based estimates of Garzoli and Goni (2000). The exchange of ring waters with the surrounding environment has been extensively modelled by de Steur (2004). They show that deformation of the ring shape gives rise to the formation of filaments at the ring edge, mixing up to 40% of the rings waters into the Cape Basin in the first few months of life. While de Steur (2004) considered this problem in an idealised setting

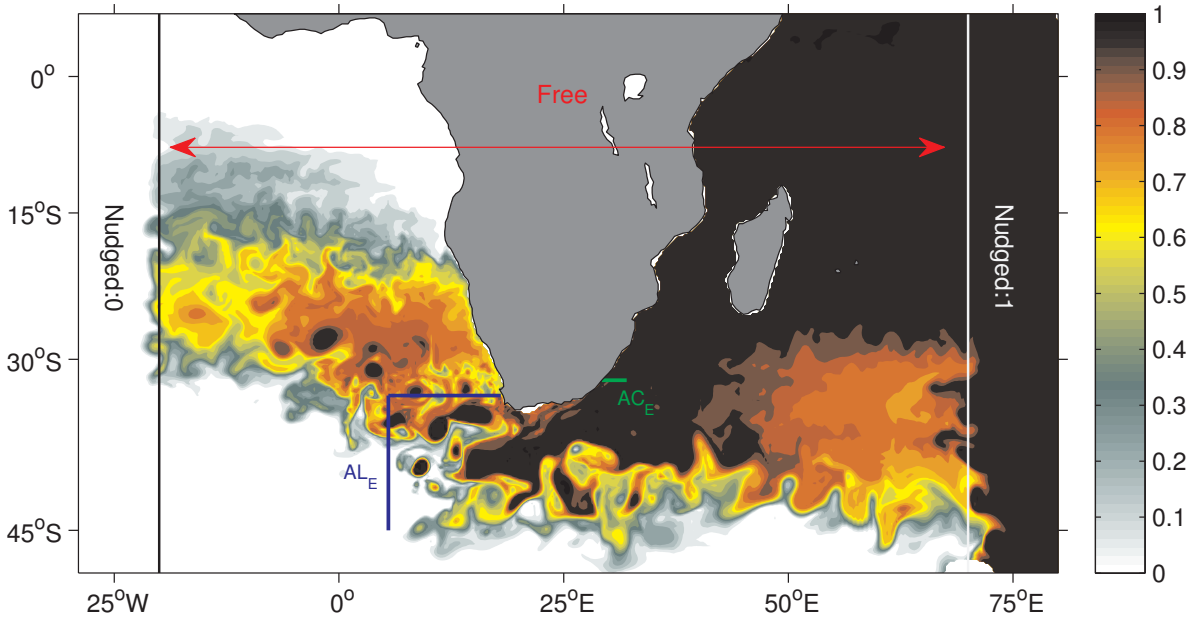

Figure 4.3: 5-daily snapshot of the passive tracer concentration (T_p) in ARC112r at 100 m. The tracer field is free to evolve between the 20°W and 70 °E, where it is nudged to 0 and 1 respectively. Eulerian estimates for the Agulhas Current and leakage are calculated across the respective AC_E and AL_E sections.

containing only one ring, the passive tracer imposed here implies that the same mechanism may be responsible for the extensive spread of Indian Ocean water masses observed by Garzoli and Goni (2000), but raises questions with regard to the attribution of flux at the GH-line as being predominantly encapsulated by rings.

4.2.3 Comparing approaches: inter-basin flux estimates

Lagrangian transport functions can be derived from the individual float profiles. These are shown for the ARC112i and AGIOi reference experiments in Fig. 4.4. Both simulations feature strong retroflections, with a pronounced first meander around the Agulhas Plateau at 25°E. However, downstream these meanders are more suppressed in AGIOi than in its high resolution counterpart. Consistent with the barotropic transport functions derived previously (Fig. 3.10), at ∽19 Sv, ARC112 shows a marked decrease in Agulhas leakage magnitude across the GH-line sections (Fig. 4.1) when compared to the AGIOi estimate of ∽33 Sv. In both cases, leakage predominantly crosses the northern GH-line section, indicative a strong flow through the northern ring path, identified by Dencausse et al. (2010a).

Strong inter-basin flux through the northern transect is reflected in the ARC112i vertical transport distribution across the GH-line section (Fig. 4.5a). The vertical transport profile, determined from the transport weighted crossing positions of the virtual floats, suggests that the leakage is predominantly confined to the top 1000 m in this model. Here, floats are removed once they cross the GH-line, so only a single crossing is permitted for each. However, van Sebille

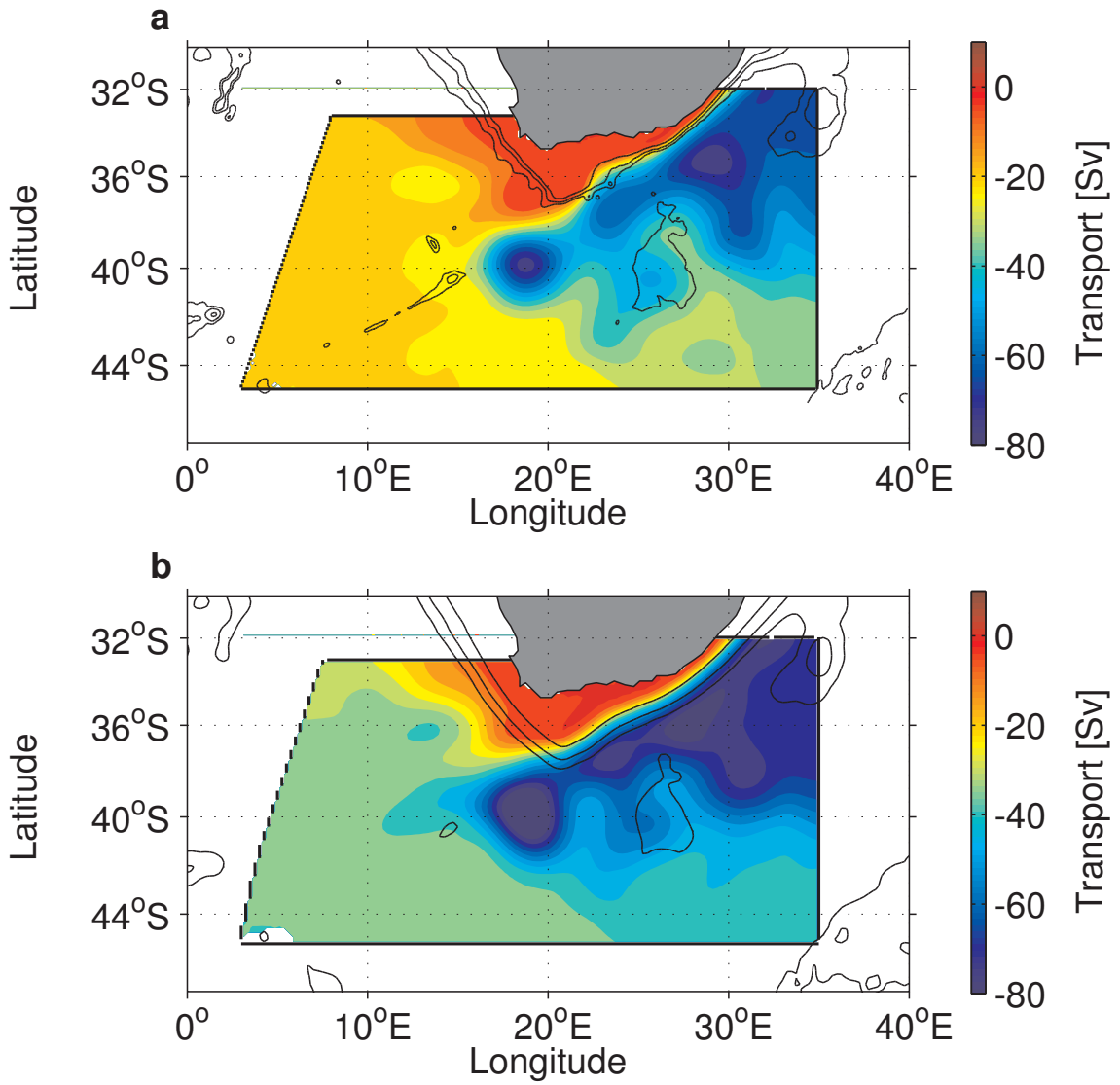

Figure 4.4: Average transport functions derived from virtual floats collected between 1948 and 2007 for (a) ARC112i and (b) AGIOi.

et al. (2010c) noted a similar surface distribution in the AG01 model, where multiple crossings were accounted for. In addition, an earlier Lagrangian based model study by Donners and Drijfhout (2004) also found a leakage confined to the top 1200 m. This implies that, despite floats being released over the full depth of the Agulhas Current, only the surface upstream waters are carried into the Atlantic.

Agulhas Rings have a strong barotropic component, but idealised modelling of them shows that they weaken in tangential 'swirl' velocity with depth (de Steur, 2004). In consequence, their circumferences contract and their ability to advert water westward is reduced. van Aken et al. (2003) also observed a substantial decrease in the relative vorticity of rings at depth. This inability to advect deeper waters may explain why the Lagrangian leakage seen here is confined to the surface layers.

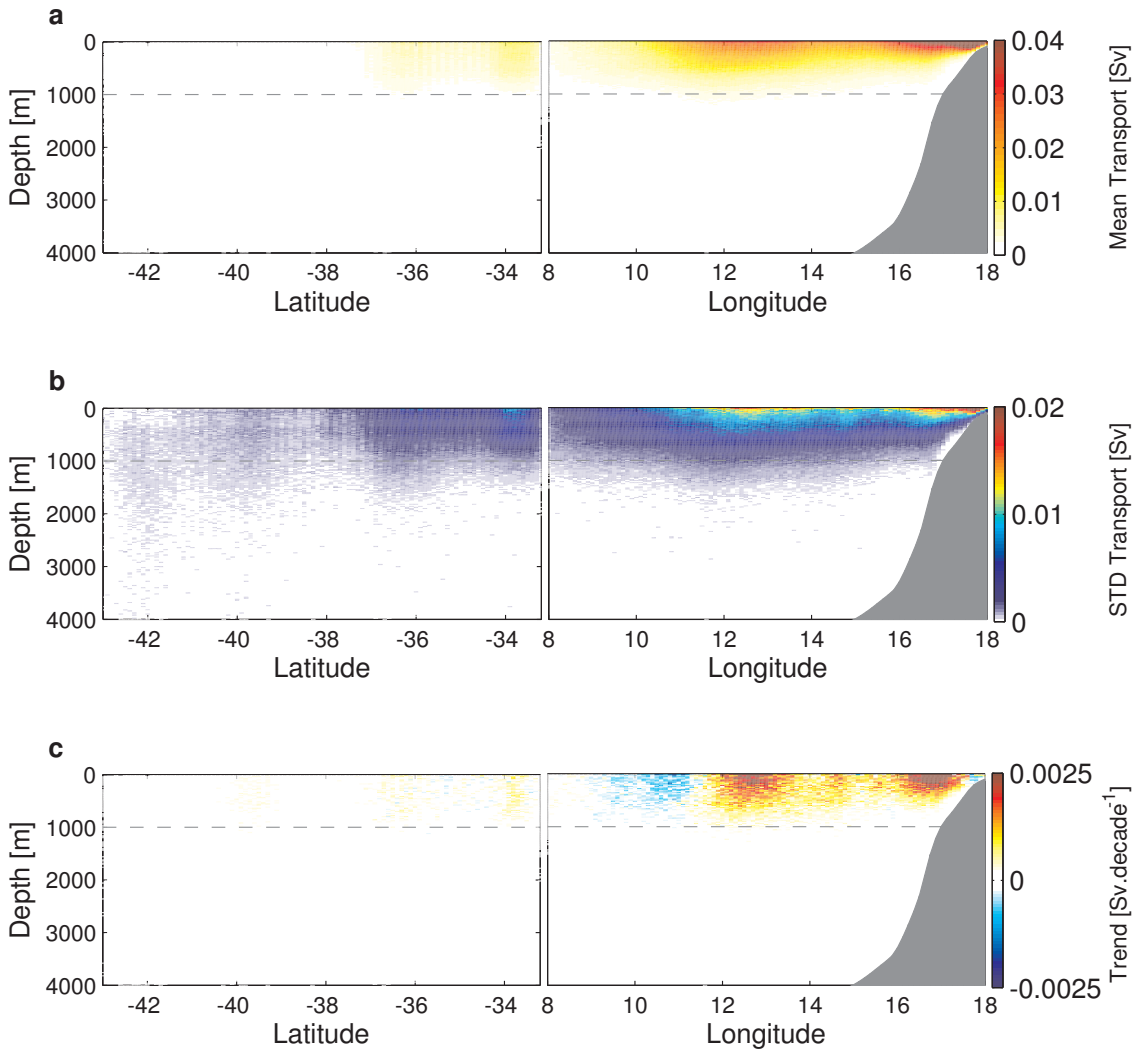

Figure 4.5: Vertical profile of the (a) mean, (b) annual standard deviation and (c) trend in Agulhas leakage for the ARC112i 1948-2007 period. Fluxes are derived from the transport weighted float crossings, binned into 0.25° horizontal by 20 m depth sections. The left and right panels correspond to the meridional and zonal sections of the GH-line transect (Fig. 4.1).

Two strong, distinct cores of transport flux are visible at 12.5°E and 17°E (Fig. 4.5a, right panel). Two weaker cores can be seen 34°S and 36.25°S. In all four cases, these cores correspond to the regions of maximum annual standard deviation, which are typically half of the mean value (Fig. 4.5b). Agulhas Rings have a strong barotropic signal (Olson et al., 1992) and, as such, the high interannual variability and increased depth penetration of these four regions may earmark them as the possible preferential ring paths. There is no Lagrangian flux into the Atlantic Ocean south of 37.5°S. This may be attributable to topographical shielding of the Agulhas Ridge, seen sloping southwest to 42°S, 10°E in Fig. 4.4. The paths that Agulhas rings take across the Cape Basin is discussed later in this chapter.

Multi-decadal trends in the vertical transport show a distinct strengthening of the flow inshore of 12°E, and a reduction in northward flux west of this (Fig. 4.5c, right panel). All

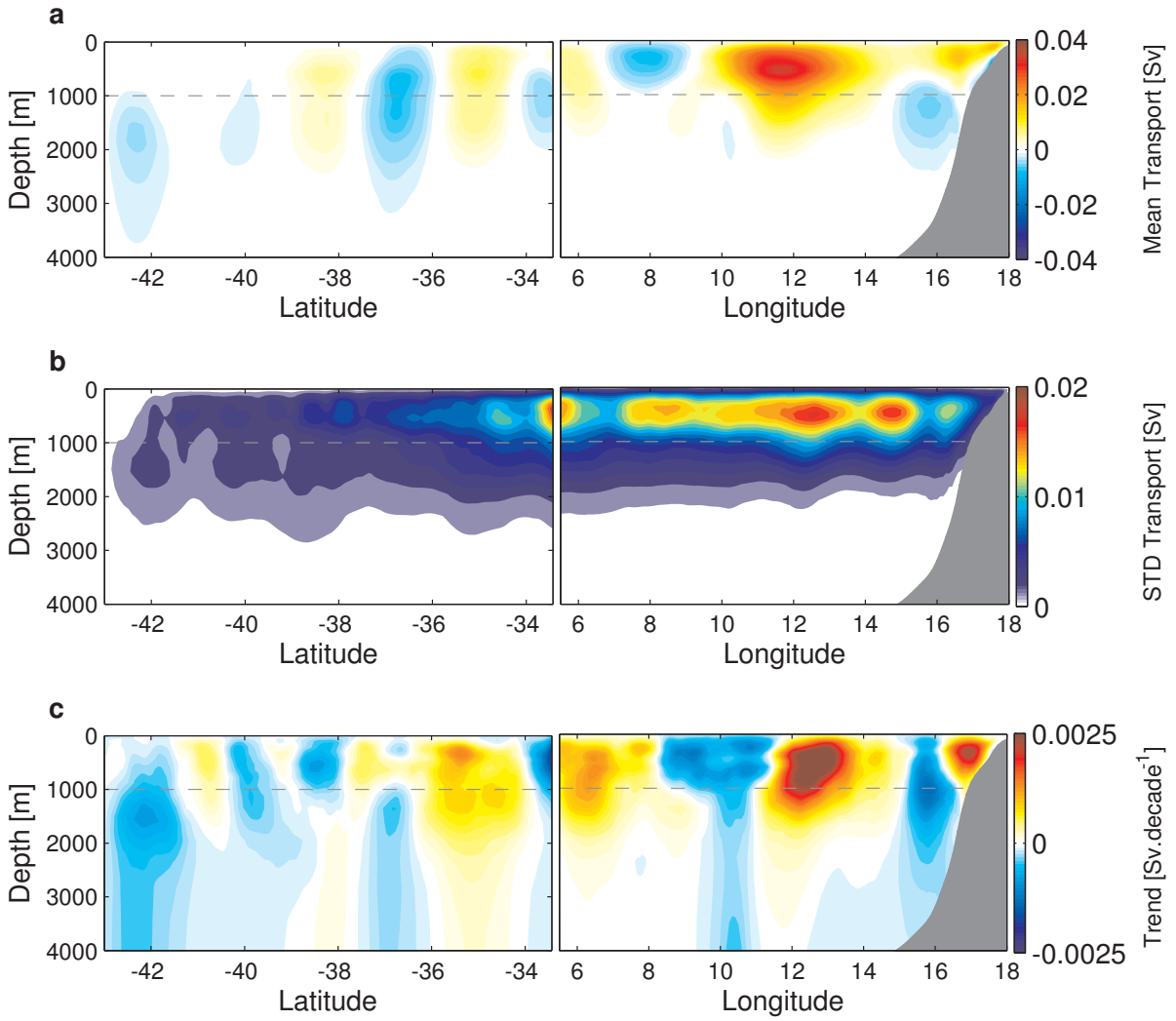

Figure 4.6: As in Fig. 4.5 but for fluxes derived from Eulerian passive tracer flux. The left and right panels correspond to the meridional and zonal AL_E Cape Basin sections shown on Fig. 4.3.

four previously identified ring cores, including those in the meridional section (Fig. 4.5c, left panel), are associated with increasing transport These changes reflect the 1992-2007 ARC112i and AVISO EKE signals (Fig. 3.17), where coastal and inshore flow clearly becomes more variable, while the northward channel at 10°E becomes less so. The increase in leakage transport across the zonal section (Fig. 4.5c, right panel) may be attributable to the recently observed intensification (Swart and Fyfe, 2012) and poleward migration (Thompson and Solomon, 2002) of the westerly winds. This is discussed more fully in chapter 6.

Comparing the Lagrangian flux depth distributions with the analogous passive tracer fields, shown in Fig. 4.6, yields some substantial differences. While the zonal track in Fig. 4.6 exactly overlies the Lagrangian one, the meridional track does not (for the reasons explained above), so care must be taken when comparing the left hand panels. Similar cores of high transport, and high variability can be seen in the surface layers east of 12°E (Fig. 4.6a and b, right panel), but the Eulerian signal extends to ∽2000 m, twice as far as the Lagrangian flux.

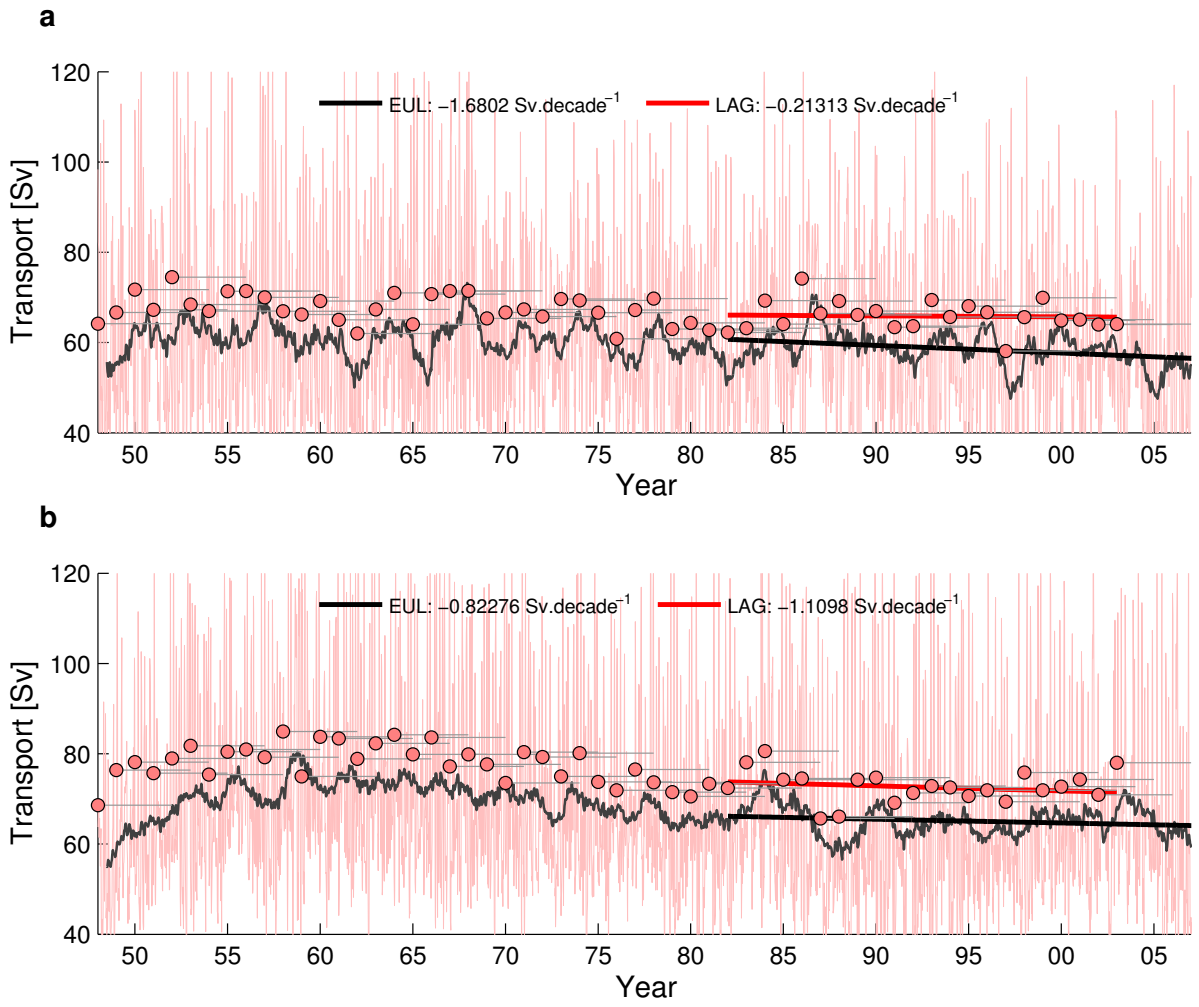

Figure 4.7: Time series of Agulhas Current transport at 32°S as calculated from the Eulerian (red line) and Lagrangian (red markers) approaches, for (a) ARC112i and (b) AGIOi. The thick grey line shows the annually smoothed Eulerian transport. The grey trails on the Lagrangian markers show the period over which each individual float release is integrated. The tendency in the signal (red and black lines) is shown over the 1982-2007 period, consistent with the period of observations shown by Rouault et al. (2009).

The Eulerian approach considers flux in both directions. Consequently, negative flux values are permitted, and annual variability is higher throughout. The negative flux underlying the ring path at 16°E, and the strong positive signal in the intermediate waters at 12°E are of particular interest. The former is possible evidence of passive tracer incorporation into the Intermediate Waters and NADW path into the Agulhas Undercurrent. The latter is consistent with an increased transport of Antarctic Intermediate water of Indian Ocean origin (I-AAIW) into the South Atlantic around 1200 m depth. This water mass, previously seen in the Argo float record is inferred to contribute 8.7 Sv to inter-basin flux (Rusciano et al., 2012). Rimaud et al. (2012) have studied the transport path of the I-AAIW using a Lagrangian scheme and high-resolution model configuration similar to the one presented here, identifying a transport path similar consistent with the one shown here. However, Rusciano et al. (2012) show that the

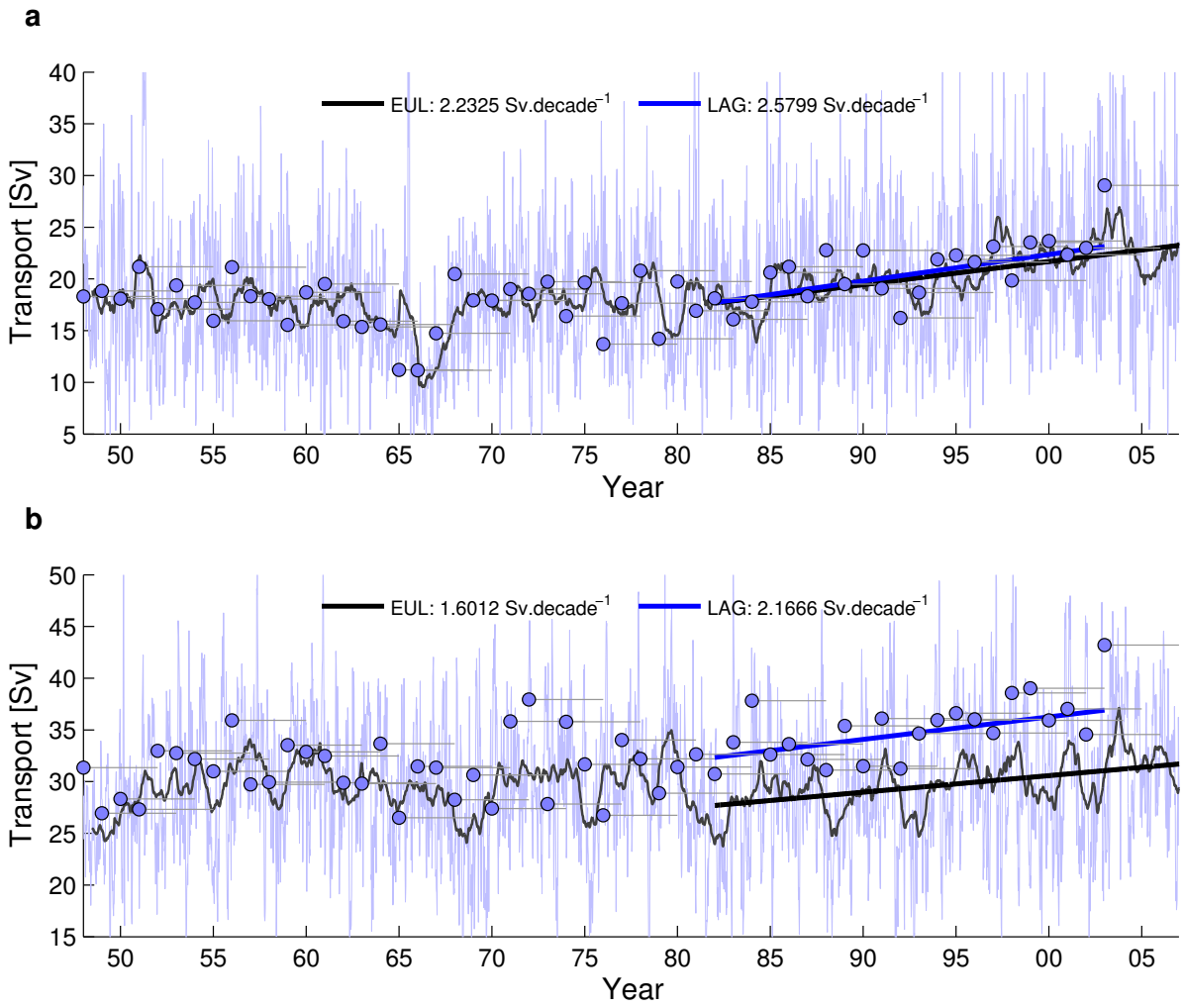

Figure 4.8: As in Fig. 4.7, but for analogous Agulhas leakage fluxes, shown in blue.

I-AAIW, at 1200 m should be the deepest water mass that is ejected from the Indian Ocean in the Agulhas leakage. In the Eulerian case it is clear that the leakage extends below this depth, suggesting that excess diffusion may be causing the passive tracer to be present at a greater depth than expected.

Time series of Agulhas Current and Agulhas leakage transport are constructed from the fluxes across the AC_L/AC_E and AL_L/AL_E transects, shown in Fig. 4.7 and Fig. 4.8, respectively. Both ARC112i and AGIOi are presented. ARC112i shows a weaker current than its low resolution counterpart, a result of increased non-linearity in the western boundary at finer grid scales. Further, independent of the model used, there is an $\backsim$5 Sv difference in the Eulerian and Lagrangian recorded Agulhas Current transport.

The Agulhas Current is highly variable on short timescales. Consecutive 5-daily transports vary as much as 65 Sv in ARC112i, with a standard deviation of 20.9 Sv. Interannual standard deviations for Lagrangian and Eulerian methods are 5.6 Sv and 3.3 Sv, respectively. AGIOi shows similar values. The interannual variability in both models is common to both AC_L and

AC_E. Irrespective of measurement technique, both models show a multi-decadal weakening in the Agulhas Current since the mid-1960s, consistent with the hindcast of Biastoch et al. (2009b), which also applied the CORE v.2b forcing fields.

AGIOi and ARC112i show a reasonably consistent Agulhas Current transport, but this is not the case for the Agulhas leakage. Two discrepancies predominate. Firstly, the mean values for AL_E for ARC112i (18.8±2.7) and AGIOi (27.6±2.8) differ substantially, though the interannual variability is similar. Secondly, while Lagrangian and Eulerian estimates for Agulhas leakage converge in ARC112i (AL_E=18.8±2.7, AL_L=18.9±3.2), they do not in AGIOi (AL_E=27.6±2.8, AL_L=32.7±3.5). Differences in Eulerian leakage can be attributed to changes in the behaviour of the Agulhas retroflection relating to model resolution. As noted in sections 2.5.1 and 2.5.2, the retroflections in AGIOi or ARC112i are not governed by viscosity. However, in the former configuration, the position of the retroflection is too far westward, a consequence of overly smoothed topography (Speich et al., 2006). This results in an overly expressed leakage in AGIOi as compared to ARC112i, which has more accurate topography.

In section 3.3.8 it was noted that the overly westward retroflection position in AGIOi causes it to occasionally cross the GH-line. While it is possible to configure the Lagrangian experiments to allow capturing transects to appear ÒtransparentÓ (i.e. they permit a degree of local recirculation), this capability has not been implemented here. Consequently, due to the way these experiments are configured, floats that would otherwise recirculated are unable to, causing an over-expression of the leakage from a Lagrangian perspective. This is not a concern in the Eulerian measurements, where flux can pass in both directions. This causes a divergence between the two measurement techniques at lower resolution. With increasing resolution, the retroflection position becomes more realistic and the two methods converge on a leakage estimate.

Multi-decadal variability in the AGIOi and ARC112i simulated Agulhas leakage show that, since the mid-1960s, the Agulhas leakage has increased, consistent with Biastoch et al. (2009b) and, to some extent, Rouault et al. (2009). Despite inconsistencies in mean leakage value, AGIOi and ARC112i show a similar tendency in Lagrangian and Eulerian leakage values, though the former is slightly larger. Despite being similarly forced, comparing the interannual variability in the two models yields little similarity. Changes in resolution clearly induces a substantial effect in the degree of non-linearity at the western boundary and in the behaviour of the retroflection itself. In addition, the lower leakage (and stronger return current) in ARC112i produces changes in the flow of the South West Indian Ocean gyre, altering the local flow pattern south of Madagascar (Fig. 3.10).

Previous comparisons of Eulerian and Lagrangian leakage estimates find that the former approach can substantially underestimate volume flux (van Sebille et al., 2010c). By introducing a passive tracer, constraints on the Eulerian method associated with transects extent and water mass properties are removed and the methodologies converge on a common flux value where the retroflection is more realistic (*i.e.* in ARC112, Fig. 4.8a). van Sebille et al. (2010c) assumed the

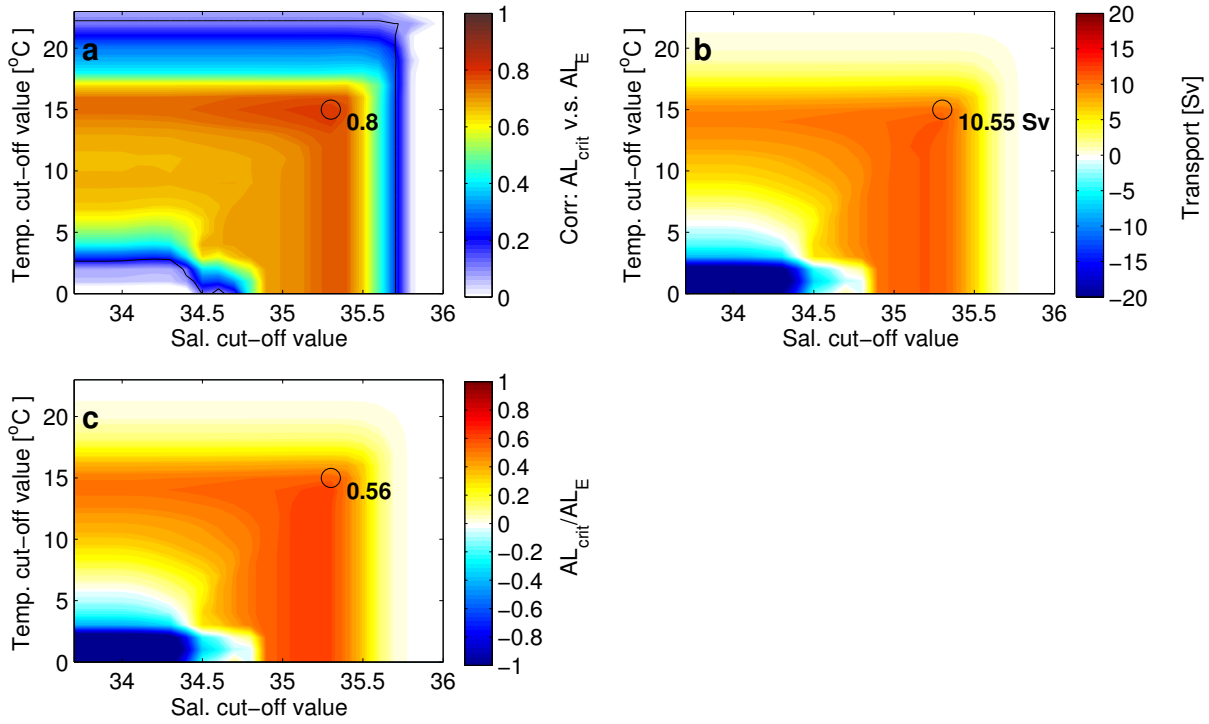

Figure 4.9: Agulhas leakage transports (AL_{crit}) at incremental salinity and temperature cut off values, compared with passive tracer estimates (AL_E). Panel (a) shows the correlation coefficient between AL_{crit} and AL_E for the 1948 to 2007 ARC112i experiment. The black contour bounds the $p < 0.01$ region, and the maximum correlation is shown. Panel (b) shows the mean transport determined from the AL_{crit} time series, with the value at the maximum correlation noted. Panel ((c) the ratio of the mean AL_{crit} value to the mean AL_E value, with the maximum ratio noted.

measured Lagrangian flux as the 'true' leakage estimate and correlated the interannual transport with an Eulerian flux constrained by temperature and salinity cut-off values. Here, a similar analysis is performed (Fig. 4.9), but the correlation is measured between the leakage at specific cut-off values (AL_{crit}) and the passive tracer value (AL_E). Maximum correlation ($r = 0.8$, $p = 0.01$) occurs at S>35.4, T>15. However, these criteria yield an AL_{crit} value of 10.55 Sv, which only represents 56% of the total leakage as measured by the passive tracer and virtual floats. Despite using the passive tracer value as the 'true' leakage measure, this result echoes that of van Sebille et al. (2010c), further underlining the difficulty of determining leakage using water mass criteria.

The mean water mass properties of the Eulerian flux across the Agulhas Current and leakage transects are shown in Fig. 4.10a & b, respectively. The Agulhas Current is clearly dominated by waters that arrive from the north and east, and therefore contain a significant percentage of Indian Ocean waters and a higher passive tracer concentration. The exception to this occurs in the dense CDW and NADW, visible in Fig. 4.10a as red points where T<2, S>34.75 (c.f. Fig. 3.6). Conversely, much of the sampled Agulhas leakage contains minimal Indian Ocean waters (passive tracer, Tpas<2%). It is also apparent that the T/S cut-off values that give the best correlation with the passive tracer flux (S>35.4, T>15) do not conform well to the distribution of water masses shown in Fig. 4.10b and fail to sample a large part of the leakage signal.

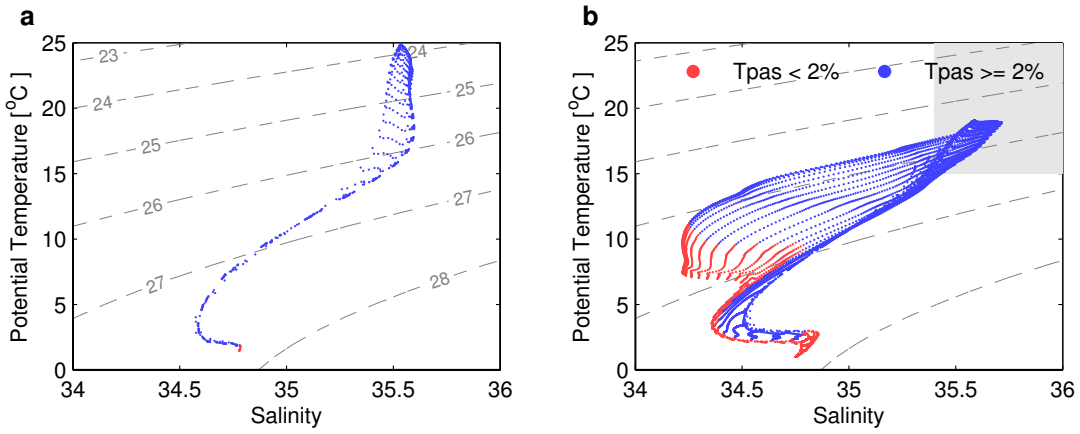

Figure 4.10: Mean water mass properties along the a) AC_E and b) AL_E sections for the 1948-2007 period. Blue and red dots show points where the passive tracer concentration is more and less than 2%, respectively. The grey region shows the water masses retained at the T/S 'cut-off' values (S>35.4, T>15) that give the maximum correlation between AL_E and AL_{crit}.

4.3 Separating Eulerian flux components

The Okubo-Weiss parameter (O_W) (Okubo, 1970; Weiss, 1991) compares the relative contributions of vorticity and strain to the deformation of the local flow field. It is calculated through equation 4.1, where S_n and S_s are the normal and shear terms of the strain tensor and ξ is the vertical component of relative vorticity (the curl of the horizontal flow).

$$O_W = S_n^2 + S_s^2 - \xi^2 \tag{4.1}$$

The individual strain (non-eddy) and relative vorticity (eddy) terms can be calculated from the u and v velocity components as follows.

$$S_n = \frac{\partial u}{\partial x} - \frac{\partial v}{\partial y}; \quad S_s = \frac{\partial v}{\partial x} + \frac{\partial u}{\partial y}; \quad \xi = \frac{\partial v}{\partial x} - \frac{\partial u}{\partial y} \tag{4.2}$$

In the strictest sense, the flow is dominated by vorticity everywhere $O_W < 0$. However, while model the SSH signal is consistent with its geostrophic velocities, expanding this approach to altimetry (as is done in the subsequent section) necessitates taking the second derivative of the SSH field to determine the geostrophic velocity components. As a consequence of measurement and interpolation in the SSH taken from altimetry, errors and discontinuities are emphasised and it is necessary to introduce a degree of filtering (Chelton et al., 2011; Souza et al., 2011). This filtering may introduce a bias, so it is typical to impose a more restrictive criteria, and flow is determined to be vorticity dominated when $O_W < -2\times10^{-12}$ s^{-2} (Chelton et al., 2007; Isern-Fontanet et al., 2006). Although the model fields are not filtered, for consistency with altimetry the same threshold is used to determine vorticity dominated flow here. Okubo-Weiss can be calculated on all σ-levels. Consequently, it allows the separation of the flow field into

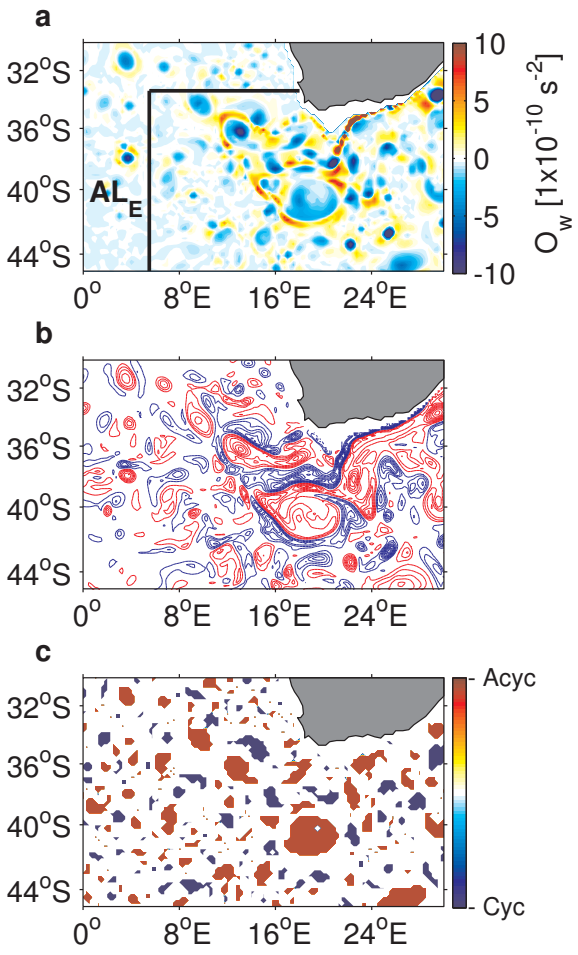

Figure 4.11: A 5-daily snapshot of a) the Okubo-Weiss parameter b) the vertical component of relative vorticity and c) the cyclonic/anticyclonic vorticity mask at 100 m in the ARC112i model during January 1999.

eddy and non-eddy dominated components. In the case of the Agulhas leakage, this allows the flux associated with rings to be separated from the total.

To determine the eddy contributions to the passive tracer flux, the value of the Okubo-Weiss parameter is calculated on all 32 depth levels from the 5-daily model velocity fields. The O_W values are then extracted along the AL_E transect shown in (Fig. 4.11a) and the flow is separated into eddy and non-eddy components. Cyclonicity is determined from the vertical component of the relative vorticity, which is extracted in the same fashion (Fig. 4.11b). When combined, these two criteria produce an eddy/cyclonicity mask (Fig. 4.11c) that can be used to determine cyclone, anticyclone and non-eddying leakage contributions. To isolate any inter-basin flux that may occur through coastal jets (Bang and Andrews, 1974), an additional mask is applied in regions where topography is shallower than 1000 m. Consequently, the total passive tracer flux across AL_E can be separated into the following components:

$$AL_E^{total} = AL_E^{coast} + AL_E^{non-eddy} + AL_E^{cyc} + AL_E^{acyc} \tag{4.3}$$

where, AL_E^{coast} is the coastal flux inshore of the 1000 m isobath, $AL_E^{non-eddy}$ is the non-eddy flux determined where $O_W \geq$ -2×10^{-12} s^{-2}, and AL_E^{cyc}/AL_E^{acyc} are the respective cyclonic/anticyclonic fluxes, determined through the relative vorticity mask where $O_W <$ -2×10^{-12} s^{-2}. Extracting these components across the AL_E transect in the ARC112i simulation yields the relative contributions shown in Fig. 4.12.

Of the total mean flux of 18.9 Sv, only 5.4 Sv ($\backsim$30%) is contained within eddy structures, with a division between anticyclones and cyclones of 2:1. Coastal flux accounts for 2.2 Sv. The largest contribution, 11.3 Sv, occurs through non-eddy processes; filaments, temporary jets and intra-eddy flux. While it may also occur through some direct inter-basin flux of intermediate waters, the vertical passive tracer profile (shown in Fig. 4.6), shows that leakage is confined to the top 2000 m.

In an earlier Lagrangian analysis, Doglioli et al. (2006) found a similar division of eddy/non-eddy flux, though they noted a 1.3:1 ratio of anticyclones to cyclones. However, the authors only performed the analysis in a climatological simulation. Here, each of the components shows significant multi-decadal variability. The flux attributable to anti-cyclones, including Agulhas Rings, shows a period of marked reduction between 1965 and 1985, which is partially compensated for eddy total eddy flux by an increase in cyclonic transport during this time. The coastal compon-

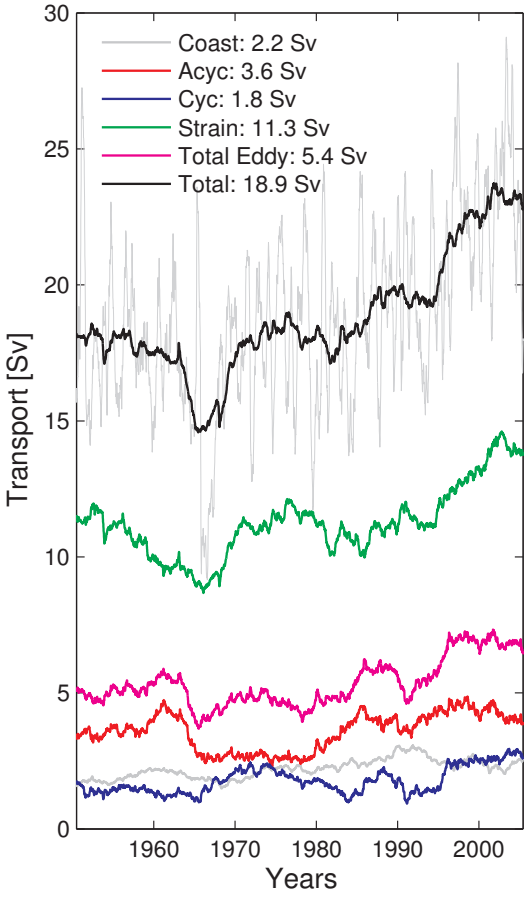

Figure 4.12: Annually smoothed time series of Agulhas leakage components derived from ARC112i

ent increases almost monotonically. Post-1980, all components show a multi-decadal increase, with the greatest change expressed by the non-eddy flux. In the mid-1960s, both the non-eddy and anti-cyclonic contributions show reductions in flux that account for a 3 Sv drop in total transport. This reduction is associated with an extremely eastward retroflection position, lasting for two years. However, while the intra-ring flux component recovers quickly, anticyclonic flux remains suppressed until 1980. Altimetric observations of the modern retroflection position have shown that extreme upstream events can have a prolonged effect on the phasing of the retroflection position, with potential consequences for ring generation (Dencausse et al., 2010b). However, the case shown here is much more extreme. While these results are consistent with previous studies (e.g. Doglioli et al. (2006)), it is necessary to test the fidelity of the simulated eddy field against observations to see if they may be applicable to reality.

4.4 The Eddy-tracking algorithm

Flow west of the Agulhas retroflection occurs almost entirely in the mesoscale. Derived quantities such as eddy kinetic energy allow the total expression of this simulated variability to be compared to altimetry (e.g. Fig. 3.16). However, it does do not provide information on the parameters and trajectories of individual eddies. Recent observations suggest that Agulhas Rings follow one of three paths across the Cape Basin (Dencausse et al., 2010a). To determine if the scales and paths of simulated Agulhas rings are consistent with those observed, an eddy tracking algorithm is implemented.

There are a number of ways to automatically detect and track eddies (Sadarjoen and Post, 2000; Penven et al., 2005; Isern-Fontanet et al., 2006; Chelton et al., 2007, 2011; Souza et al., 2011). Approaches using deformation and geometry are the most common. In the former approach, deformation in the surface field is quantified using the Okubo-Weiss parameter. However, as described above, interpolation and measurement errors in altimetry require that the Okubo-Weiss field is filtered to remove noise from the second derivative of SSH. The bias introduced by this filtering is accounted for by imposing a threshold value for vorticity dominated flow (-2×10^{-12} s^{-2}) (Chelton et al., 2007; Isern-Fontanet et al., 2006). The Okubo-Weiss parameter is much less noisy for the model, and is not filtered. However, the same threshold is used for consistency with observations.

In the geometric approach surface eddies are identified and tracked using criteria based on closed SSH loops (Chelton et al., 2011). As this approach does not require the second derivative of the SSH field, the geometric approach appears less problematic (Chelton et al., 2011; Souza et al., 2011). However, it does require a threshold for an SSH anomaly and/or a criteria for eddy shape. This is problematic for two reasons. Firstly, as the SSH anomaly criteria is resolution dependant it makes direct comparison of altimetry data with model fields problematic. Secondly, as Agulhas Rings experience a high-degree of modification in the Cape Basin it is not simple to define a 'typical' geometry.

To minimise the requirements for filtering and generalise the criteria for SSH anomalies, the approach presented here identifies eddies using a 'hybrid criteria' scheme that combines the Okubo-Weiss parameter with the geometric method. This scheme has been successfully applied to altimetry in the greater Agulhas system (Backeberg et al., 2012), and to altimetry and simulations in the Mozambique Channel (Halo et al., 2013).

4.4.1 Identifying eddies

Eddies are identified as follows, using the same parameters for models and altimetry:

1. Deformation eddy identification: The Okubo-Weiss parameter is calculated from geostrophic velocities. This is subsequently Hanning filtered twice to remove spurious noise. Regions where vorticity dominates (O_W < -2×10^{-12} s^{-2}) are selected.

2. Geometric eddy identification: Due to improvements in the mean ocean dynamic topography (Rio et al., 2011), loop criteria is based on absolute SSH fields. Advantageously this prevents the detection of current meanders, present in the sea level anomaly fields, as eddies. The SSH field itself is extracted from the weekly AVISO Mean Absolute Dynamic Topography (MADT) products of 5-daily model field and contoured at $\triangle$SSH=0.02 m intervals, the approximate accuracy of the altimetry products. In the case of the 1/12^{o} model configurations (e.g. ARC112i), the grid is degraded by a factor of three to facilitate a better comparison with the altimetry. The maximum radius of a detected loop is set at 400 km to prevent large scale ocean features, such as gyres, being mistakenly detected as eddies. Subsequent sensitivity tests have shown that the geometric eddy identification method is minimally sensitive to the $\triangle$SSH and maximum loop size values used.

3. Determining the hybrid criteria: Chelton et al. (2011) noted that, despite filtering O_W is likely to incorrectly select some areas as ocean eddies. Further, closed SSH loops may contain multiple SSH maxima (*ibid*). To minimise these inaccuracies, the two approaches are combined. Eddies are determined to be present only where O_W is negative **and** where a closed SSH loop exists. Any selected eddy must contain a local SSH extreme and O_W minima (Fig. 4.13).

4.4.2 Tracking eddies

The eddies are tracked using the method presented in Penven et al. (2005). An initial eddy, $e1$, at time t is compared to the eddy field in in the subsequent frame. The eddy is matched to an eddy, $e2$, at time $t = t + 1$ when the non-dimensional property-space distance ($X_{e1,e2}$) between the two is minimised (Eq. 4.4).

$$\Phi_{e1,e2} = \sqrt{\left(\frac{\triangle X}{X_o}\right)^2 + \left(\frac{\triangle R}{R_o}\right)^2 + \left(\frac{\triangle \xi}{\xi_o}\right)^2} \tag{4.4}$$

Where:

- $\triangle X$ is the spatial distance between $e1$ and $e2$
- $\triangle R$ is the change in diameter between $e1$ and $e2$
- $\triangle \xi$ is the change in relative vorticity between $e1$ and $e2$
- X_o is a characteristic length scale: 50 km
- R_o is a characteristic radius: 100 km (allowing for eddy-splitting)
- ξ_o is a characteristic relative vorticity: 1x10^{-5} s^{-1}

As an additional criteria, an eddy must retain the sign of its vorticity to be tracked between frames. Where this is violated, $\Phi_{e1,e2} = \infty$. All eddies are assigned a unique identifier, which the eddy retains throughout its lifetime. Where eddy splitting occurs new identifiers are issued to each of the daughter vortices. Where no subsequent matching eddy is found the track is terminated.

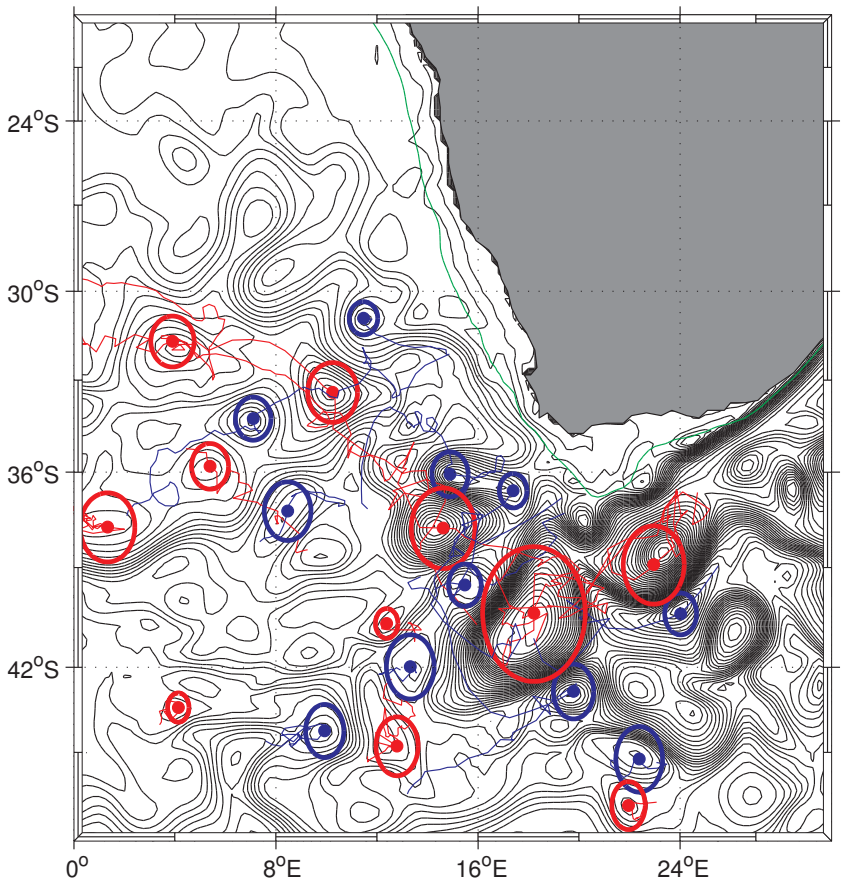

Figure 4.13: Eddies identified in the model SSH field in May 1992, contoured at 5 cm intervals for visualisation, only. 2 cm intervals are used in processing. Red and blue circles indicate anticyclones and cyclones, respectively. The red and blue lines show the trajectories of the eddies during their lifetime. Only eddies with lifetimes greater than 2 months are tracked. The green line traces the 500 m isobath.

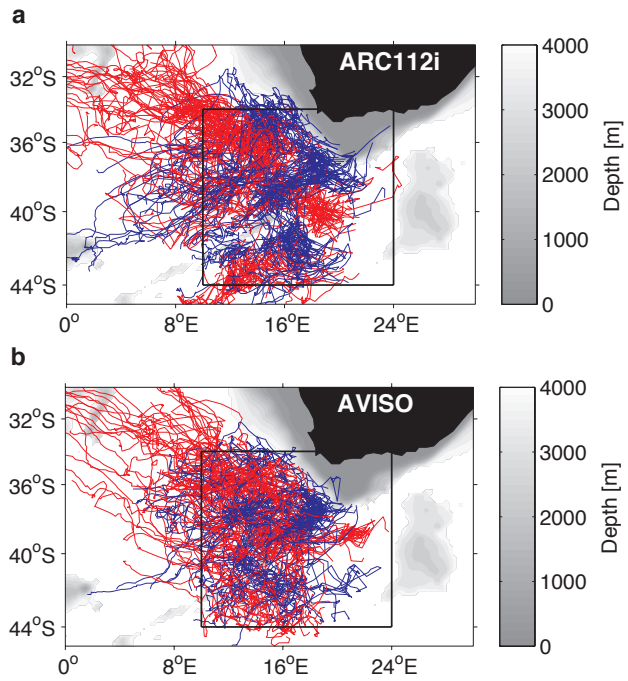

Figure 4.14: Trajectories of cyclones (blue) and anticyclones (red) in the Cape Basin from 1992 to 2007 derived from (a) ARC112i and (b) Aviso. Eddies are tracked from their generation site inside the black box and must persist west of 20°E to be counted.

4.4.3 The Cape Basin eddy field

In Fig. 4.14, the trajectories of all the eddies matching the criteria imposed above are mapped for the 1992-2007 period for ARC112i and eddies extracted from AVISO altimetry. Only eddies generated in or near the retroflection and persisting west of 20°E are considered. Both hindcast and altimetry signals show a predominance of anticyclonic eddies at the retroflection, surrounded by a band of cyclonic trajectories. These latter features predominate in the north, formed as lee eddies behind the Agulhas Bank (Penven et al., 2001). In both panels, the majority of the anticyclonic trajectories proceed northwestward, with secondary branches to the west and southwest, divided by the topography of the Agulhas Ridge. In the altimetry signal, two southern eddies cross the ridge to the north. No simulated eddies make this crossing, suggesting that the interaction between the barotropic signal of the eddies and the topography is not completely reproduced. Cyclonic eddies also persist on an eastward path, and appear to cover more distance in the model.

By spatially binning the trajectories, the prevalence of anticyclonic and cyclonic eddies can be determined over a grid, highlighting regions where eddies exhibit an increased frequency, shown in Fig. 4.15. Regions of increased anticyclonic eddy activity are clearly visible to the northeast and southeast of the retroflection in both the observations and simulation, although the northern branch appears over-expressed in the model. The formation of cyclones in the lee of the Agulhas Bank is again visible in Fig. 4.15c & d. A second source of variability at 33°S in the model is completely absent in the observations.

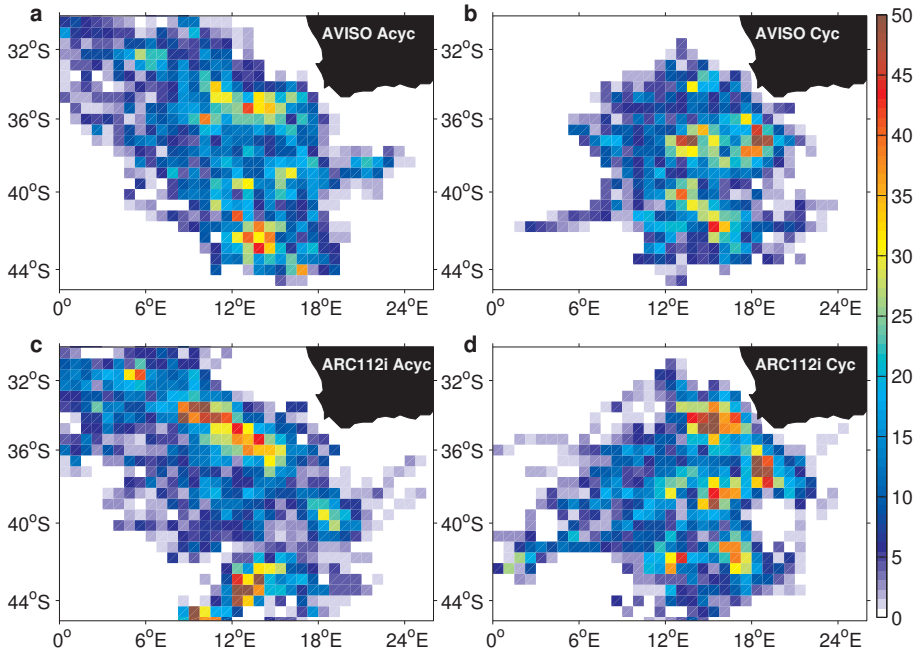

Figure 4.15: Gridded distribution of total eddy tracks for the 1992 to 2007 period spatially binned onto a 0.75° by 0.75° grid for (a) altimetry derived anticyclones, (b) altimetry derived cyclones, (c) model derived anticyclones and (d) model derived cyclones.

	North	*Central*	*South*	*None*	*Total*
Anticyclones					
Aviso	88(5.5±2.1)	60(3.8±2.6)	35(2.2±1.1)	17(1.1±1.1)	200(12.5±3.8)
ARC112i	79(4.9±1.4)	37(2.3±1.1)	39(2.4±1/3)	19(1.2±1.0)	174(10.9±2.2)
Cyclones					
Aviso	95(5.9±2.6)	39(2.4±1.3)	35(2.2±1.32)	27(1.7±1.1)	196(12.3±3.6)
ARC112i	91(5.7±2.3)	30(1.9±1.4)	32(2.0±1.0)	29(1.8±1.0)	182(11.4±2.3)

Table 4.1: Summary of the paths taken by Agulhas rings and cyclones between 1992 and 2007. Numbers given are for total (annual mean ± annual standard deviation).

Recently, Dencausse et al. (2010a) identified three paths that eddies can take across the Cape Basin, separated by the major bathymetric features. In the northern path, eddies travel northwestward between the Erica seamount at 15°E-38°S and the nearest coastal point to the northeast. Eddies passing between the seamount and the Agulhas Ridge are ascribed to a central path. Eddies travelling south of the Agulhas ridge follow the southern path. To assess the ability of the model to replicate the predominance of eddies in these three regions, the eddy tracks are separated into those that persist in the regions shown in Fig. 4.16. Eddies are assigned to the first zone that they enter.

The number of eddies found in each section is summarised in Table 4.1. The number and variability cyclones and anticyclones found in the northern and southern sections of the hindcast match well with the observations. However, anticyclones in the central path are underrepresented and in general, more eddies are detected in the altimetry than in the hindcast. The

total number of observed anticyclones detected per year (200) equates to 12.5 features per year, approximately twice the 5±1 year^{-1} estimate of Schouten et al. (2002a). The high numbers occurs due to the tracking of anticyclonic features that arise through ring splitting in the Cape Basin, as previously observed by Arhan et al. (1999). Dencausse et al. (2010a) tracked all anticyclonic features, rings and sub-rings, across the Cape Basin between 1992 and 2007 using SSH only, counting 199 events total. No distinction is made between rings and sub-rings here, but the aforementioned study suggests an approximately 50:50 distribution between them.

While the transport of Indian Ocean waters associated with Agulhas Rings is, in part, determined by their number, it is also determined by their size and speed. Eddy radius is calculated by the eddy-tracking algorithm. Model and altimetry frames are extracted on a respective 5-daily and 7-daily basis. To prevent the over-sampling of the Brownian agitation

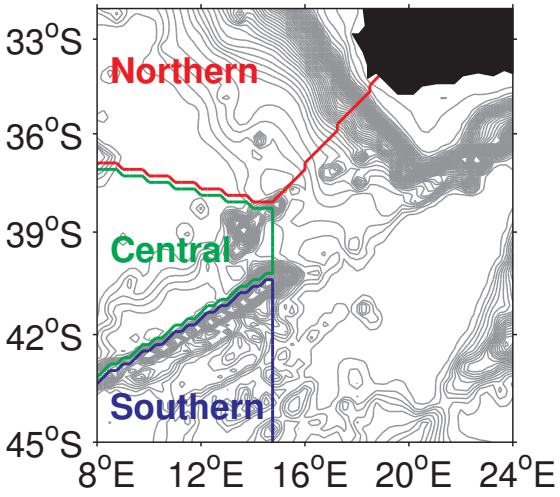

Figure 4.16: Map of the eddy classification zones used (consistent with Dencausse et al. (2010a)).

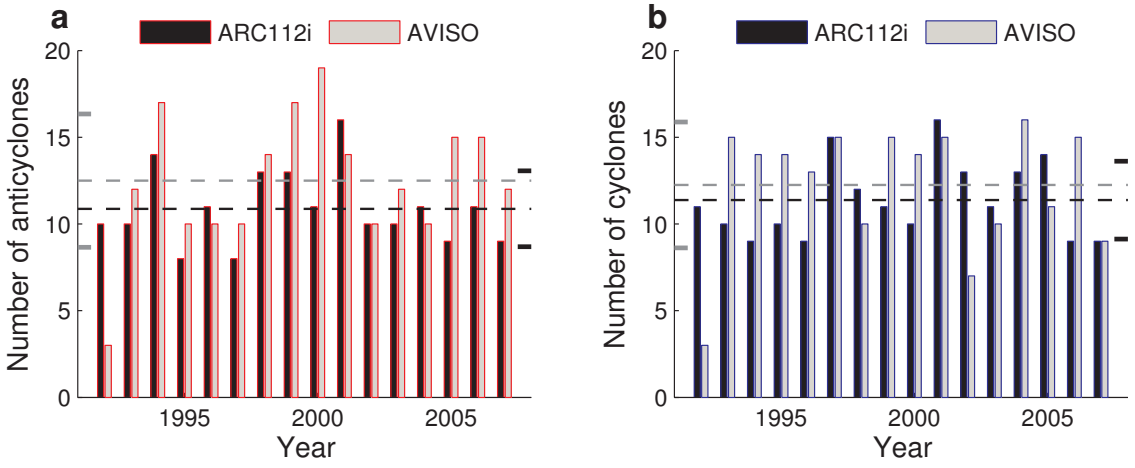

Figure 4.17: Annual averages of eddy numbers for the eddies tracked in Fig. 4.14. The black and grey dotted lines show the mean eddy number for the model and altimetry, respectively. Black and grey hash-marks show the ± 1 standard deviation in the model and observations, respectively.

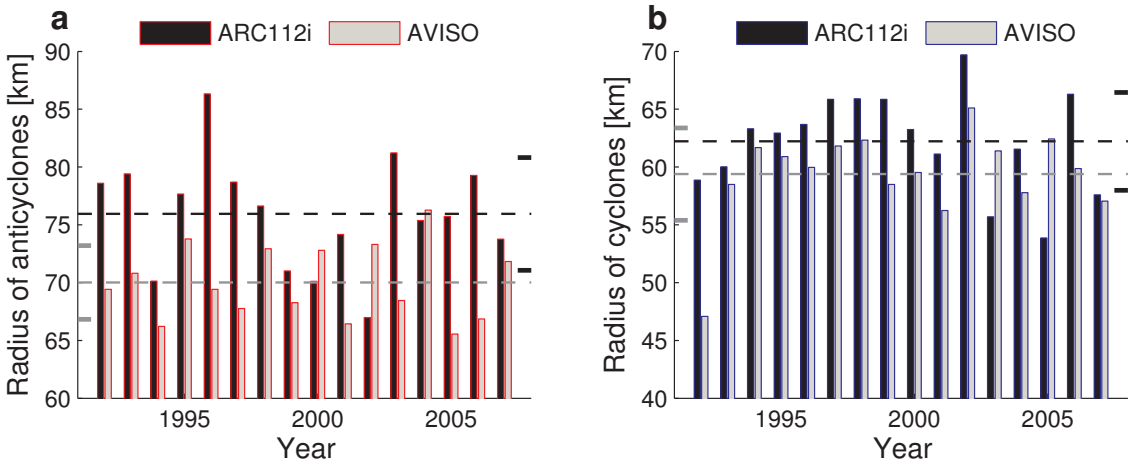

Figure 4.18: As in Fig. 4.17 but for eddy radius

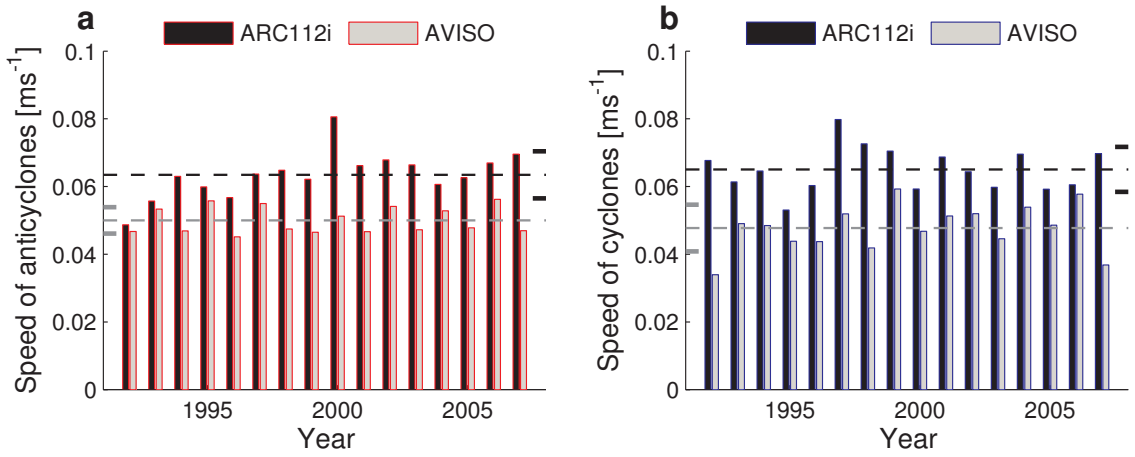

Figure 4.19: As in Fig. 4.17 but for eddy speed

component of eddy movement in the shorter timescale model product, speed is calculated based on the distance travelled in a monthly basis.

The mean and interannual variability in the number, radius and speed of cyclones and anticyclones detected in Fig. 4.14 are summarised in Figs. 4.17 to 4.19. The time series of eddy numbers, both for rings and cyclones, reflects the numbers in Table 4.1. Observations show more eddies of both polarities, with increased interannual variability. In the mean, similar numbers of cyclones and anti-cyclones are expressed, with suggestions that the interannual variability of the two are linked. The lowest observed occurrence of rings occurs simultaneously with the lowest occurrence of cyclones. The upstream retroflection observed in 2001 is reflected in low number of rings tracked in the following year.

Eddy radii, which appears to be accurately captured, shows little interannual variability. The largest feature observed and simulated anticyclonic features detected are 161 km and 209 km in radius, respectively, broadly matching the values reported by Arhan et al. (1999) but

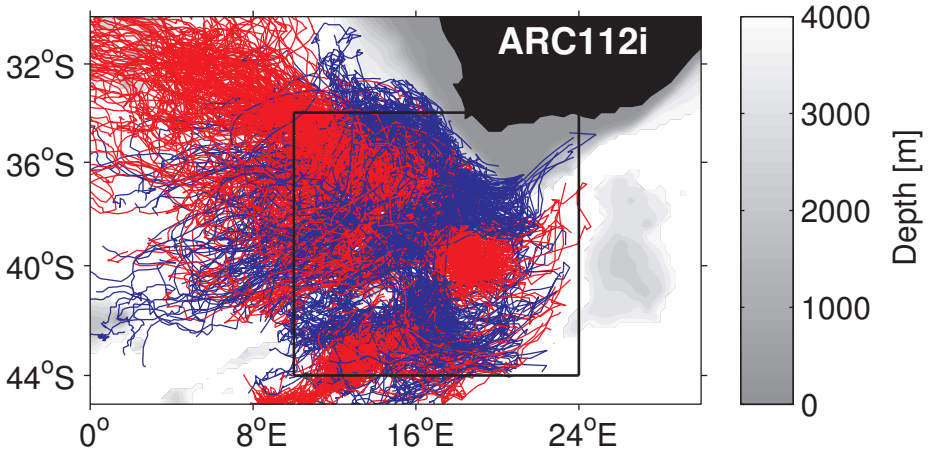

Figure 4.20: Trajectories of cyclones (blue) and anticyclones (red) in the Cape Basin from 1948 to 2007 derived from ARC112i. Eddies are tracked from their generation site inside the black box.

perhaps missing the largest features. Mean radius is substantially smaller at 76 km for simulated anticyclones, differing from the observed value by only 4 km. The smaller cyclones, ∽60 km in both the simulation and altimetry, are consistent with the observations of Boebel et al. (2003a).

Mean anticyclone speeds derived from altimetry fall within the standard deviation of *in site* measurements reported by Boebel et al. (2003a), while the mean cyclone speed derived here is faster than those previous observed (ibid). While eddy number and size appear well simulated, there are biases of +0.0135 ms^{-1} (+23%) and +0.0173 ms^{-1} (+32%) in anticyclone and cyclone speed, respectively. While attempts have been made to reduce the effects of Brownian motion in the temporal sampling of eddy speed, it is possible that the shorter time base of the model (5-daily) continues to contribute to a faster eddy speed derived from the simulations. There appears to be no interannual relationship between eddy size, number and speed.

With the exception of anticyclone speed, which is increasing in both the model and observations, none of the eddy parameters show a significant decadal tendency in the 1992-2007 period. This mirrors the findings of Backeberg et al. (2012), who used the same tools as presented here to conduct a full census of the retroflection region from altimetry, finding a significant positive trend only in meridional velocity of anticyclones. However, to facilitate a comparison with observations, thus far only eddies that arise between 1992 and 2007 have been considered. As the trajectories, number and size of the simulated eddies appear to be well approximated during this period, the analysis is expanded to the full 1948-2007 period, allowing multi-decadal variability to be implied.

The full census of eddy trajectories for this period is shown in Fig. 4.20, which shows a similar trajectory pattern to that shown for the observational period (Fig. 4.14a) but with increased trajectory density throughout. All three ring paths (northern, central and southern) are still in evidence, however, as before, no eddies are seen crossing the Agulhas Ridge. Previously, using the Okubo-Weiss parameter described in section 4.3, separation of the passive tracer flux across the AL_E transect into eddy and non-eddy components indicated that, since 1948, both

cyclone and anticyclone flux has increased. Fig. 4.21 summarises the decadal variability in eddy specifics from 1948 to 2007. Long term trends suggest that changes in eddy driven leakage can be attributed to increases in eddy number, speed and size. However, the only statistically significant changes are in respect of increases in cyclone size (with 95% confidence) and, most strongly, anticyclone speed (with 99% confidence). The marked reduction in Agulhas leakage in the mid-1960s occurs simultaneously with substantial reductions in eddy speed and size, and appear to have been preceded by a sharp reduction in cyclone number.

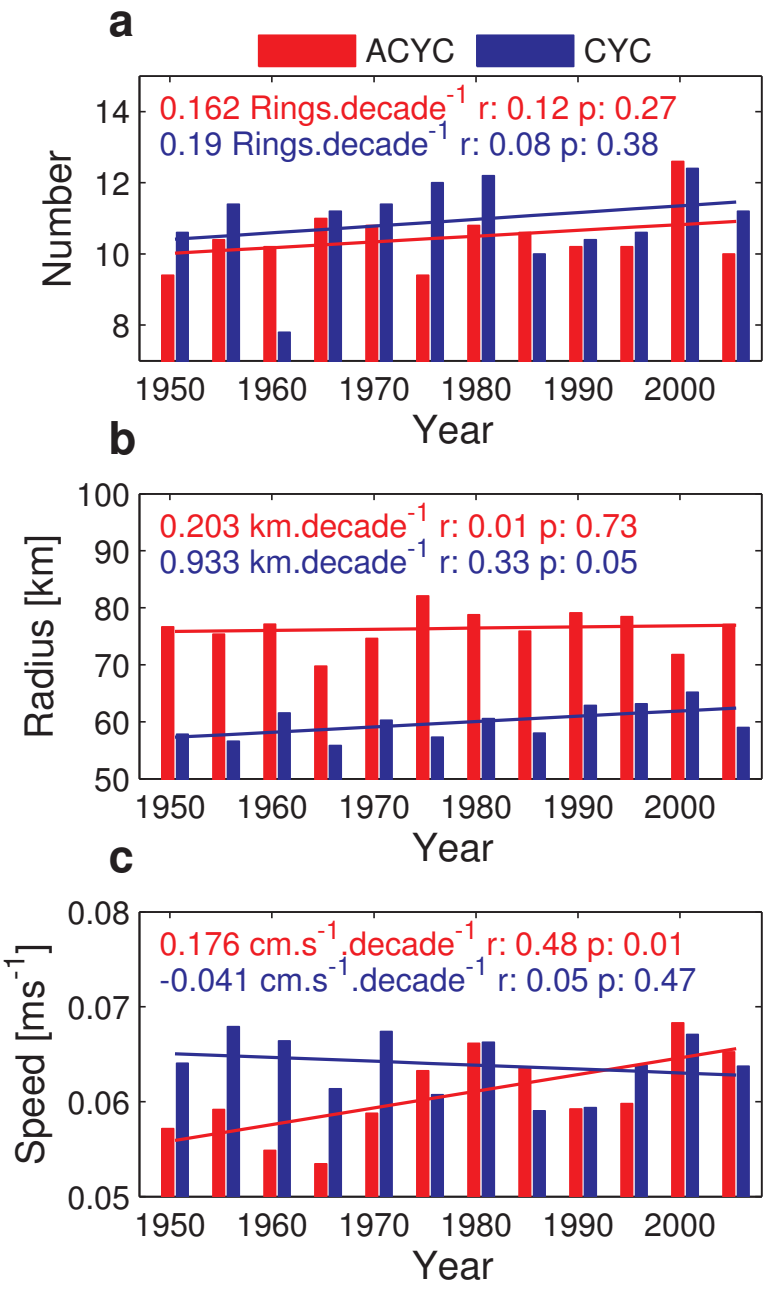

Figure 4.21: Summary of 5-yearly averages of eddy properties tracked in ARC112i between 1948 and 2007.

4.5 Discussion

4.5.1 Comparing quantification methods

Most estimates of Agulhas leakage magnitude derived from observations place it between 2 Sv and 15 Sv (de Ruijter et al., 1999a; Richardson, 2007). Modelling values are much more variable, reaching 40 Sv at the upper limit of estimates (Speich et al., 2006). Typically, lower resolution models feature higher Agulhas leakage values, possibly resulting from the increased numerical viscosity of the retroflection at the coarse grid scales (Dijkstra and de Ruijter, 2001). However, increased resolution is no guarantee of a realistic leakage, and many of the models featuring a very strong leakage are in the eddy-permitting regime or higher (Speich et al., 2006).

AGIOi and ARC112i conform to the general paradigm of decreasing mean inter-basin flux with increasing resolution, with only the latter expressing a value that is consistent with observations. It has been previously suggested that, at $1/4^{o}$, ROMS (and by extension AGIOi) may be overly viscous (van Sebille et al., 2010a), but the effective resolution and low Ekman number of AGIO (shown in section 2.5.1) and minimal horizontal viscosity (HMIX panel in Fig. 2.17b) suggests otherwise. Further, both simulations produce Agulhas Rings. Rather than as a result of increased viscosity, the difference in mean leakage value between AGIOi and ARC112i may be attributable to the differing effects of bathymetry on the current path, and the overly westward extent of the retroflection loop in the former case, where the Agulhas Bank is highly smoothed (Fig. 3.18). This results not only in an overall increase in the expressed leakage when the retroflection loop is erroneously westward, but in a marked discrepancy between the Agulhas leakage values reported through Lagrangian and Eulerian techniques. This discrepancy disappears when the retroflection is more realistically positioned, as it is in ARC112i. It is important to note that the divergence in Lagrangian and Eulerian fluxes noted in AGIOi may be construed as a compromised experimental setup with regard to the collection of virtual floats. However, if the models presented are to be compared with existing observations, the choice of collection transect (i.e. at the GoodHope Line) is somewhat prescribed. The passive tracer approach was introduced to somewhat ameliorate this problem.

Consequently, while many models apparently produce a 'realistic' leakage with regard to magnitude, much of this accuracy may depend on how this leakage is quantified. The dependance of the leakage magnitude on quantification method is underlined by van Sebille et al. (2010c), who compared Eulerian and Lagrangian fluxes in the same model. While the former approach is more amenable to comparison with hydrographic observations, for example with hydrography at the GoodHope Line, it proves problematic in terms of specificity. To accurately separate the Agulhas leakage from other regional transports (such as through the ACC, or via NADW flux in the deep branch of the AMOC), the Eulerian flux must be preferentially limited by the geographical extent of the measuring transect, by characteristic water mass criteria, or by both. Although it is less amenable to comparisons with observations, here, in an attempt to subvert these limitations, an explicit passive tracer has been introduced into the simulations, removing

constraints based on either water masses or transect extent.

Within the context of the OGCM simulation tested by van Sebille et al. (2010c), imposing specific T/S criteria and optimising the integration region produced an Eulerian Agulhas leakage flux value only half that derived from the Lagrangian approach. Here, a similar result is derived from comparisons between the passive tracer determined leakage and that derived at various T/S cut-off values in ARC112i. Where the best correlation between the two measures arises, at S>35.4, T>15, the leakage is underestimated by 44%. The likely occurs due to the exclusion of Indian Ocean water masses, predominantly South Indian Central Water, that are diluted through mixing with Antarctic Intermediate Waters and South Atlantic Central Water in the intermediate layers (Fig. 3.6) (Gordon et al., 1992; Boebel et al., 2003a).

Irrespective of how volume flux is measured, both models show a multi-decadal increase in Agulhas leakage and decrease in Agulhas Current since the 1960s. ARC112i, the model with the greatest degree of fidelity when compared to observations, shows a positive tendency of +2.2 Sv.decade^{-1} / +2.6 Sv.decade^{-1} (AL_E / AL_L). The sign of this signal is consistent with the previously reported model values of Biastoch et al. (2009b) (AG01: +1.2 Sv.decade^{-1} from 1968-2007) and Rouault et al. (2009) (SAfE: +3.9 Sv.decade^{-1} from 1982-2007), with a magnitude that falls between the two. Notably, the steadily decreasing Agulhas Current transport in ARC112i, while consistent with that reported by Biastoch et al. (2009b), differs from other hindcasts, most notably Rouault et al. (2009), in sign. The models used here employ the same forcing as used in the Biastoch et al. (2009b) configuration, and draw their boundary conditions from the similarly forced ORCA05 OGCM. It is interesting to note that, under consistent forcing the previously divergent ROMS (SAfE) and NEMO (AG01) models agree in behaviour. As differences in model numerics does not appear to be immediately responsible for the existing discrepancy in behaviour, perhaps it is possible to explain the differences in the long term variability in the context of the prevailing wind signals present in various forcing products. Dynamical explanations of this multi-decadal variability and the interplay between Agulhas Current and leakage are the focus of the remaining two chapters of this thesis.

Philosophically, comparing Lagrangian and Eulerian leakage estimates introduces a certain ambiguity. While the former ascribes leakage to be only those Agulhas Current waters that persist into the Atlantic, the latter widens this definition to include all Indian Ocean waters that persist westward. The difference is perhaps a subtle one, as the Agulhas Current is the overwhelmingly dominant transport path via which the Indian to Atlantic flux can occur. Yet, while the term 'Agulhas leakage' implies a firm association with flux in the upstream western boundary current, which in recent practice has been quantified by the Lagrangian approach at 32^{o}S (Biastoch et al., 2009b; van Sebille et al., 2009b; Durgadoo et al., 2013), if the critical downstream response is in the behaviour of the AMOC, perhaps this definition is too narrow as it may preclude more localised recirculation in the subgyre.

4.5.2 Agulhas leakage structure

In the introduction to this chapter, four Agulhas leakage mechanisms were presented as contributing to total inter-basin flux. Of these, anticyclonic Agulhas Rings form the dominant link between the Indian and Atlantic Oceans in terms of volume flux and water mass advection. However, due to substantial modification during their transits across the Cape Basin, the idea of localised 'pockets' of Indian Ocean waters being advected into the South Atlantic is somewhat misleading. Combining *in situ* Lagrangian float tracks with altimetry, Boebel et al. (2003a) were the first to suggest the idea of a Cape Cauldron, characterised by vigorous mixing and stirring in the South East of the Cape Basin. Modification of Agulhas Rings by deformation of the ring boundary (de Steur, 2004), eddy-splitting (Arhan et al., 1999), cyclone generation (Baker-Yeboah et al., 2010), interaction with topography (Baker-Yeboah et al., 2010; Herbette et al., 2002), eddy-eddy interactions and convection driven by surface interactions all serve to disperse the Indian Ocean waters across the Cape Basin. Consequently, a hydrographic survey of the South East Indian Ocean by Garzoli and Goni (2000) determined that up to 50% of the surface waters were of Indian Ocean origin.

The proportions of Agulhas leakage retained within eddies has been investigated before. In a previous Lagrangian study, Doglioli et al. (2006) used a climatologically forced regional model to determine that only 30% of the transport across the Cape Basin is trapped within the eddies themselves. Here, in an analogous approach, the Okubo-Weiss parameter to is used separate the eddy and non-eddy components of the Eulerian flow. This yields a similar result, with 28.5% of the flow contained within eddies during the 1948-2007 period. Within this eddy flux component, Doglioli et al. (2006) found a cyclone to anticyclone transport ratio of 1.3:1, whereas a 2:1 ratio is derived here. As such, while passive tracer concentration, and therefore Indian Ocean water percentage, remain highest within Agulhas Rings even as they leave the Cape Basin (Fig. 4.3), they contribute only 20% to the total flux. Consequently, while coastal flow plays a small part through a shelf edge jet described by Bang and Andrews (1974), the majority of the flux occurs due to the mixing of leakage sourced waters into the background flow of the South Atlantic subtropical gyre.

The $1/12^{o}$ nested configuration used in ARC112i is similar to that used in the Doglioli et al. (2006) study, making it somewhat less easy to determine whether of not these results can be generalised across other models, or are configuration dependant. However, the anticyclonic and cyclonic eddy scales in ARC112i compare favourably with those derived from altimetry (Table 4.1) and from hydrography and *in situ* floats by Arhan et al. (1999) and Boebel et al. (2003a), respectively. Consequently, there is a suggestion that attempts to reconstitute Aguhas leakage from Indian Ocean waters retained within Agulhas Rings, and their generation frequency may potentially underestimate total flux by a substantial margin.

Through modelling studies of inter-basin exchange, Matano and Beier (2003) determined that while Agulhas Rings are surface intensified, expressing mixed barotropic/baroclinic modes, cyclones show a dominant barotropic mode, tending to be intensified at the bottom. The surface

intensification associated with Agulhas Rings is evident in the vertical distribution of both the Lagrangian and Eulerian transports (Fig. 4.5 and 4.6), which dissipate with depth. However, suggestions of a barotropic signal in the Eulerian transport trends may be indicative of the role played by cyclones in determining total flux.

Donners et al. (2004) modelled Agulhas Ring dynamics in a high resolution OGCM, determining that Agulhas Rings were only able to maintain their water mass properties with any degree of longevity where the azimuthal velocity was greater than twice the translational velocity. This condition was rarely true below 800 m, and in consequence, Indian Ocean water masses were quickly mixed into the turbulent Cape Basin. van Aken et al. (2003) reached a similar conclusion through the hydrographic profiling of a young Agulhas Ring 'Astrid' in March, 2000 noting that much of the original water mass properties were lost below 800 m. The dissipation of Eulerian transport with depth shown here may then be related to the mixing of the passive tracer out of the ring below around 1000 m, which may be especially acute given the bias towards increased translational velocity within the model.

4.5.3 Eddy field fidelity and variability

A common issue with many models of the Agulhas leakage is a preference for Agulhas Rings to bias towards taking a single path across the Cape Basin and South Atlantic (Maltrud and McClean, 2005). In contrast, Dencausse et al. (2010a) recently identified three paths that observed Agulhas Rings can take across the Cape Basin. Comparison of the the eddy trajectories extracted from the model with those derived from altimetry suggests that, in the 1992 to 2007 period, ARC112i reproduces the spread and specifics of the Cape Basin eddy field with a high degree of fidelity. In their analysis, Dencausse et al. (2010a) found the central path to be the most commonly taken, but here the northward path shows the greatest number of eddies. This discrepancy is ascribed to differences in the methodology used to identify eddies and the two-month limitation imposed on eddy lifetime in this study.

Substantial numbers of simulated eddies are tracked in all three observed paths, but, compared to observations, anticyclones are underestimated in the central path by almost 40%. Of all three paths, the central one presents the greatest topographical barrier to westward flux. It is possible that the under-representation of eddies in the central path is therefore the results of the dissipation and splitting of Agulhas Rings by seamounts, an effect previously described by Herbette et al. (2002). Similarly, while observed anticyclones in the southern path are eventually able to cross the Agulhas Ridge to the north, their simulated counterparts are not. This may again indicate that the interaction between Agulhas Rings and topography in the model is not correctly simulated as a result of topographic smoothing, insufficient vertical resolution or increased velocities at depth, increasing the potential for splitting and erosion (Herbette et al., 2002).

An alternative explanation is that the simulated eddies in the southern path may be subducted such that they can no longer be tracked as they transit north across the ridge. Garzoli

(1999) noted that rings that cross the STF are significantly modified in terms of their water mass structure. ARC112 shows a bias to increased salinity and temperature at the surface in the Southern Ocean, as shown in section 3.3, Fig. 3.2 and 3.3, possibly destabilising the local density structure resulting in the subduction of simulated anticyclones. A final possibility is that the eddies are subducted through the interaction with outcroppings of a simulated STF that may be slightly further north than observed (Herbette et al., 2004), though the 12°S isotherm at 100 m appears to agree well with that observed by Orsi et al. (1995).

Cyclones are by far the most numerous in the northern path, centering on two cores of activity directly to the west of the Agulhas Bank and further north up the west coast of Africa at 34°S. At the former site, cyclones are generated as lee eddies arising from the detachment of the Agulhas Current from the Agulhas Bank (Penven et al., 2001). At the latter site, cyclones may form as a result of the interaction between Agulhas Rings and topography. This process, described by Baker-Yeboah et al. (2010) facilitates the mixing of slope waters onto the Benguela shelf and links the increased prevalance of these cyclones in the model with the over-abundance of anti-cyclones taking the northern path near the coast.

Within the context of this study, simulated eddies, both cyclonic and anticyclonic, approximate observations well with regard to their size. However, the largest eddy detected in the observations is 322 km in diameter, notably smaller than the largest ring surveyed by (Arhan et al., 1999). In part, this may be the result of sampling the mean properties of the eddies across their lifetime, assuming, consistent with observations, that they decrease in size with time. Cyclone dimensions are much more consistent with the observations of Boebel et al. (2003a), though the authors record a 3:2 distribution of cyclones to anticyclones, while a 1:1 ratio is detected here. This deviation can be explained by the larger tracking region covered in this analysis, and the increased likelihood of further ring splitting in the Cape Basin outside of the KAPEX region surveyed by Boebel et al. (2003a).

With the exception of anticyclonic eddy speed, no statistically significant tendency are seen in either the simulated or observed eddy parameters during the 1992 to 2007 period, mirroring the previous results of Backeberg et al. (2012). Expanding the analysis to include the entire 1948-2007 hindcast (Fig. 4.21) indicates that the trend in ring speed, along with a positive trend in cyclone size, is robust on a multi-decadal time scale. The coherence between the time series of total leakage and anticyclone speed heavily suggests that the is a dominant contributor to the measured increase in inter-basin flux since the mid-1960s. As Agulhas Rings are likely to see greater mixing with their surroundings as translational velocity increases (Donners et al., 2004), it seems likely faster travelling rings may also drive a strengthening of the non-eddy governed leakage component. However, it should be noted that Agulhas ring speed within the context of the model shows a bias towards faster eddies that are faster than observed, perhaps artificially accentuating this signal.

4.6 Conclusions

In order to investigate the magnitude and structure of the Agulhas leakage, a number of complimentary techniques have been applied to two hindcast simulations of varying resolution. Quantification of the total leakage has been performed using Lagrangian and Eulerian fluxes, where the latter is inferred from a passive tracer used to explicitly label Indian Ocean waters. The Eulerian Agulhas leakage measurement is subsequently separated into cyclonic, anticyclonic and non-eddy governed components by applying the Okubo-Weiss parameter throughout the model levels. Lastly, to place these leakage estimates in the context of the surface eddy variability, an eddy tracking scheme has been used to assess the trajectories of vortex features, comparing them to altimetric observations. The following conclusions have been reached;

- Using a Eulerian passive tracer provides an effective and specific way of measuring Agulhas leakage magnitude and structure.
- Quantifying Agulhas leakage using Eulerian methods based on specific T/S properties underestimates inter-basin flux by up to 50% when compared to more explicit passive tracer based transports. This is consistent with previous Lagrangian studies (e.g. van Sebille et al. (2010c))
- Increased resolution produces a lower mean Agulhas leakage, with a value that is closer to observations, irrespective of the measurement technique used. However, while Eulerian and Lagrangian methods converge in the case of a more realistic retroflection position (in ARC112i), the Lagrangian approach may overestimate inter-basin flux in cases where the retroflection is overly westward (in AGIOi).
- The Agulhas leakage is predominantly confined to the surface layers (top 1500 m). At the GoodHope Line only 30% is contained within eddies with a 2:1 anticyclonic to cyclonic ratio. The majority occurs through intra-ring flux due to mixing of ring water masses with the surrounds.
- Consistent with the observations of (Garzoli and Goni, 2000), passive tracer spread in the Cape Basin indicates that up to 50% of the surface water there is of Indian Ocean origin.
- The ARC112i model represents all three observed eddy paths (Dencausse et al., 2010a) with a high degree of fidelity in regard to ring and cyclone trajectory, number and radius, but eddy speeds are higher than observed.
- Multi-decadal increases in the eddy and non-eddy flow components contribute to an Agulhas leakage that increases from the mid 1960s, showing a significant degree of interannual and decadal variability. The Agulhas Current, which also exhibits strong interannual variability, weakens during the same period. Strengthening transport in the eddying portion of the flow can be attributed to increases in the speed of Agulhas Rings and progressively larger cyclonic features, but are dominated by variability in the non-eddy flow component.

Chapter 5

Greater Agulhas sensitivity to changes in the Indian Ocean trade winds

5.1 Introduction

South of Africa, the Agulhas Current retroflects, turning sharply eastward and flowing back into the Indian Ocean. The Agulhas leakage, a collective term for waters that persist into the South Atlantic after ejection from this retroflection, forms a key link in the "warm-water" route of the global thermohaline circulation (Beal et al., 2011; Gordon, 1986). Long-term variability in the exchange of these waters may have consequences for the inter-decadal strength of the Atlantic Meridional Overturning Circulation (Weijer et al., 2002; Biastoch et al., 2008b) and possibly plays a role in the termination of glacial phases (Peeters et al., 2004). Leakage magnitude is mediated by the dynamics of the greater Agulhas system, under the influence of the large-scale winds (de Ruijter et al., 1999a; Biastoch et al., 2008c; Rouault et al., 2009; van Sebille et al., 2009b; Zharkov and Nof, 2008a). Reanalysis products show that Indian Ocean trade winds have recently intensified (Backeberg et al., 2012). However, an unclear western boundary response during this period (Biastoch et al., 2009b; Rouault et al., 2009), suggests a need to clarify the response of the Agulhas Current and leakage to trade-wind variability.

As a result of the turbulence of the Cape Basin, leakage observations are highly variable at between 2 Sv and 15 Sv (de Ruijter et al., 1999a; Richardson, 2007) (as discussed in Chapter 4). In contrast, the southern Agulhas Current is better constrained at $\backsim$70 Sv (Bryden et al., 2005). However, theoretical arguments suggest the existence of an exploitable dynamical relationship between Agulhas Current transport and downstream leakage, which may allow the latter to be inferred from western boundary transport (Beal et al., 2009; van Sebille et al., 2010a).

The mechanistic interplay between the current and leakage has been extensively studied using idealised numerical simulations that focus on Agulhas retroflection dynamics. Using a weakly non-linear, one-layer model, de Ruijter (1982) argue that inertia, which allows the Agulhas

Current to overshoot the continental shelf as a free-jet, is critical in establishing the retroflection. Positive vorticity accumulation in the poleward flowing jet turns it eastward, forming an Agulhas Return Current with a transport determined by the decrease in wind stress curl across the inertial boundary layer. Here, a larger decrease produces a stronger return current, and in consequence, a weaker leakage. Boudra and de Ruijter (1986) and de Ruijter and Boudra (1985) confirm this inertial relationship in baroclinic and barotropic cases. Subsequently, Ou and de Ruijter (1986) show that stronger upstream transport causes an earlier coastal separation and a more eastward retroflection position. Although retroflections are possible in high-friction cases (Boudra and Chassignet, 1988; Chassignet and Boudra, 1988), only those governed by inertia are physically valid (Dijkstra and de Ruijter, 2001), as high-friction produces a non-physical barrier to inter-ocean transport in the former case. Recently, Le Bars et al. (2012) describe a third regime where leakage reaches an asymptotic limit at high wind stress due to increased cross frontal mixing in the return current and the southward export of Indian Ocean waters.

Indian Ocean winds have recently undergone substantial change. Reanalysis products show a positive trend in wind-stress curl between 18°S and 25°S from 1993 to 2009 (Backeberg et al., 2012), predominantly driven by trade wind intensification (Han et al., 2010). Concurrently, a strengthening (Swart and Fyfe, 2012) and poleward migration (Thompson and Solomon, 2002; Gillett and Thompson, 2003) of the southern hemisphere westerlies, has intensified the supergyre linking the South Indian, South Atlantic and South Pacific oceans (Cai, 2006).

Reanalysis forced hindcasts, performed with high-resolution ocean models suggest that, post-1970, these wind changes have driven a substantial leakage increase (Biastoch et al., 2009b; Rouault et al., 2009), warming the South Atlantic (Lee et al., 2011). Although both hindcasts show a warming of the Agulhas Current in the this period, Biastoch et al. (2009b) show a weakening Agulhas Current, while Rouault et al. (2009) record a strengthening. Analysing the Biastoch et al. (2009b) simulation, van Sebille et al. (2009b) argue that the anti-correlation between reduced current strength and increased leakage has a dynamical basis, following the inertial outcropping mechanism of Ou and de Ruijter (1986). However, Ou and de Ruijter (1986) do not discuss leakage in their idealized study, and altimetry suggests that the position of the retroflection has remained constant since 1992 (Dencausse et al., 2010b; Backeberg et al., 2012).

Notably, the Biastoch et al. (2009b) and Rouault et al. (2009) hindcasts apply different reanalysis forcing. Superimposed trade and westerly wind signals may produce non-linear effects that are difficult to disentangle. In this context, investigating a dynamical link between the Agulhas Current and leakage is problematic as responses to upstream transport changes cannot be readily isolated from westerly induced effects further south. Using similar models to this study, Durgadoo et al. (2013) show a strong leakage response to changes in westerly wind strength. However, inertial arguments suggest that Agulhas Current transport may also influence leakage. As recent observations show that trade winds, which partially drive current strength, are intensifying, two questions become apparent. Firstly, how does the Agulhas Current respond to trade-wind driven variability? Secondly, what are the consequences for Agulhas leakage?

Here, using four ocean models of increasing horizontal resolution, the sensitivity of the greater Agulhas Current system to changes in the trade wind stress is tested, under conditions that mirror and exceed the recent trends seen in the reanalysis products (Backeberg et al., 2012). It is demonstrated that the inertia of the Agulhas Current, driven by these changes, has a minimal influence on the magnitude of the Agulhas leakage; a 'decoupling' that becomes more pronounced as resolution increases. It is concluded that, in the eddy-resolving simulation tested here, the upstream transport of the Agulhas Current may not be a reliable proxy for the Agulhas leakage.

5.2 Applying anomalies: Modifying trade wind stress

Between 1993 and 2009 reanalysis products show a positive trend in wind stress curl between 10°S and 26°S (Backeberg et al., 2012, supplementary), driven by trade wind intensification (Han et al., 2010). Although this variability influences Agulhas Current transport (Rouault et al., 2009), the effect on the leakage is unknown. To investigate this response a series of anomalies are developed to modify the winds between the equator and 32.5°S, which are assumed here to constitute the trade winds. The anomalies are based on the zonally averaged zonal wind stress from 20° to 115°E, as extracted from a climatological reference run forced with the CORE v.2b normal year surface fluxes (Large and Yeager, 2009). The anomalies are designed to geometrically modulate zonal trade wind stress strength by ±20% and ±40% (Fig. 5.1). The meridional wind stress is unchanged. The ±20% anomalies cause a change in wind stress curl approximate to the standard deviation of the annual mean value seen in the CORE v.2b 1948-2007 winds (Fig. 5.1c). The anomalies are applied across the Indian Ocean basin at every model time-step (Fig. 5.1d). The drag coefficient and heat exchanges remain unaffected. Thus, only the dynamical effects of the modulated winds are considered.

5.3 Experimental summary

5.3.1 AGIO experiments

A summary of the model experiments performed in given in Table 5.1. Four sensitivity experiments are performed with the AGIO model, described in chapters 2 and 3, using all four anomaly patterns shown in Fig. 5.1. Boundary conditions for these sensitivity experiments are drawn from the monthly mean of year 1 to 60 of the ORCA05r climatological run.

5.3.2 ARC112 experiments

As shown in chapter 3, horizontal resolution (Dijkstra and de Ruijter, 2001) and the representation of regional bathymetry (Speich et al., 2006; Matano, 1996) play a key role in the behaviour of the Agulhas retroflection and, subsequently, the magnitude of the leakage. To assess the effect on resolution on the dynamical link between Agulhas Current transport and leakage, the

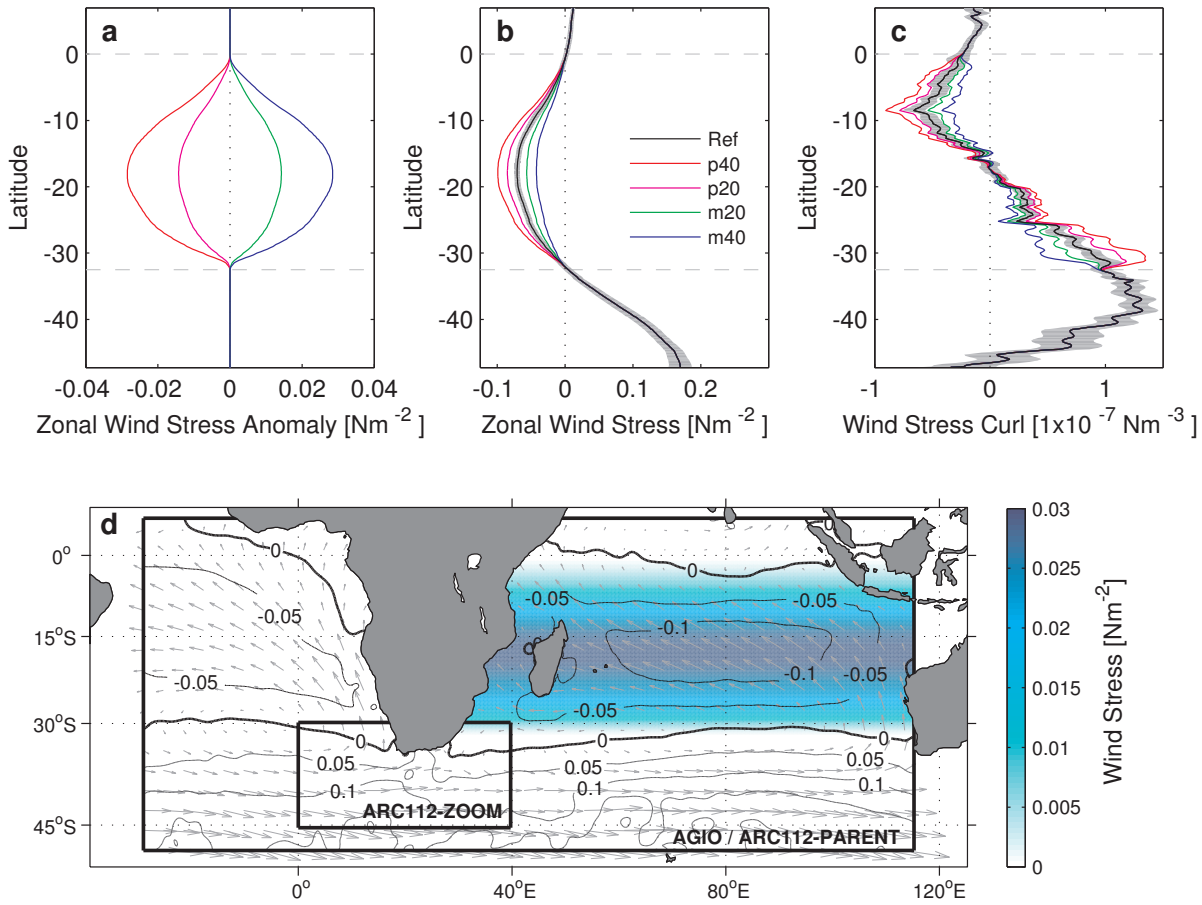

Figure 5.1: Zonal averages of, (a) zonal wind stress anomalies, (b) zonal wind stress and (c) zonal wind stress curl for the trade wind sensitivity experiments. No anomaly is applied outside of the grey dashed lines. The black line describes the 20-year mean climatological reference value. The grey shaded area in (b) and (c) covers the annual standard deviation in the 1948-2007 wind stress curl extracted from the ARC112i hindcast. The full extent of the AGIO and ARC112 parent domain is shown by the large black box. Anomalies are applied over the area shown in colour; AGIOm40 is shown in this case. The contours and vectors show the magnitude and direction of the AGIOr wind stress. The extent of the ARC112 high-resolution nest is shown by the small black box.

±40% anomaly experiments are repeated using the ARC112 eddy-resolving configuration, the ARC112xx experiments shown in Table 5.1.

5.3.3 Global model experiments

To test the robustness of the relationship between Agulhas Current and leakage, a similar set of experiments was performed in two OGCM configurations; ORCA05 and INALT01. Both sets of experiments were performed at the Helmhotlz Centre for Ocean Science, GEOMAR, Kiel.

ORCA05 is an established coarse resolution global ocean-only model configuration that successfully reproduces ocean circulation at the large scale (Biastoch et al., 2008a). It is based on version 3.1.1 of the NEMO code (Madec, 2008) and includes the LIM2 sea-ice module (Fichefet and Maqueda, 1997). The tri-polar grid, Mercator gridded south of 20°N, has a nominal hori-

zontal resolution of 1/2°. Vertically, 46 z-levels are used, with partial cells in the bottom level to better represent topography. A free-slip condition is used at the lateral boundaries.

INALT01 (Durgadoo et al., 2013) is an update of the AG01 configuration (Biastoch et al., 2009a). It consists of a parent model identical to ORCA05, but includes a regional nest, extending from 70°W to 70°E and 50°S to 8°N at 1/10° horizontal resolution. Nest embedding is accomplished using the AGRIF approach previously described. INALT01 is eddy-resolving, promoting a realistic rendering of the greater Agulhas system. As in the basin-scale models, surface fluxes for ORCA05 and INALT01 come from the CORE v.2b data set.

All four configurations undergo a primary, 30-year spin-up. In sensitivity experiments, anomalies, applied at every time-step, are linearly ramped in over year 31. After an anomaly spin-period (year 32-40), during which the experiments reach a steady state, the 5-daily output from years 41 to 60 are analysed.

5.3.4 Variable boundary condition experiments

To test the sensitivity to the large-scale dynamics at the open boundaries a secondary set of experiments is performed with variable boundary conditions. In this case the ORCA05 OGCM is re-run from years 1-60, but with the ±40% anomaly applied. Three sets of boundary conditions are drawn from climatologies of 41-60 of these experiments (ORCA05p40 and ORCA05m40),

Experiment	*Forcing/Anomaly*	*Boundary Conditions*	*Analysis Period*
ORCA05r	CNY	Not applicable	41-60
ORCAp40	CNY+40% ztws	Not applicable	41-60
ORCAp20	CNY+20% ztws	Not applicable	41-60
ORCAm20	CNY-20% ztws	Not applicable	41-60
ORCAm40	CNY-40% ztws	Not applicable	41-60
AGIOr	CNY	ORCA05 mon. clim.	41-60
AGIOp40	CNY+40% ztws	ORCA05 mon. clim.	41-60
AGIOp20	CNY+20% ztws	ORCA05 mon. clim.	41-60
AGIOm20	CNY-20% ztws	ORCA05 mon. clim.	41-60
AGIOm40	CNY-40% ztws	ORCA05 mon. clim.	41-60
AGBCr	CNY	ORCA05r mon. clim. (41-60)	21-40
AGBCp40	CNY+40% ztws	ORCAp40 mon. clim. (41-60)	21-40
AGBCm40	CNY-40% ztws	ORCAm40 mon. clim. (41-60)	21-40
INALT01r	CNY	Not applicable	41-60
INALT01p40	CNY+40% ztws	Not applicable	41-60
INALT01m40	CNY-40% ztws	Not applicable	41-60
ARC112r	CNY	ORCA05 mon. clim.	41-60
ARC112p40	CNY+40% ztws	ORCA05 mon. clim.	41-60
ARC112m40	CNY-40% ztws	ORCA05 mon. clim.	41-60

Table 5.1: Summary of sensitivity experiments performed and the changes applied to the zonal trade wind stress (ztws). CNY refers to the Core v.2b normal year forcing fields, CI to the analogous 1948-2007 annually varying fields (Large and Yeager, 2009). Unless otherwise specified, the ORCA05 monthly climatology (mon. clim.) is based on years 1-60 of the reference run.

and are referred to by the AGBC prefix in Table 5.1. Here, the appropriate trade wind anomaly is applied at initialisation and analysis is performed after a 20 year spin period.

5.4 Agulhas leakage quantification

As discussed in Chapter 4, quantifying Agulhas leakage in the turbulent Cape Basin is challenging. Here, to allow comparison with the OGCM configurations, a Lagrangian approach is also used. However, in the case of the regional models, this is compared with Eulerian passive tracer fluxes. An in-depth description of these two approaches is presented in chapter 4.

5.5 Basin-scale circulation changes

The large-scale circulation shows well established tropical and subtropical gyres in both models, with barotropic transports of -20 Sv and 80 Sv in ARC112r (Fig. 5.2a). Away from the western boundary, gyre transports compare well with theoretical values from Sverdrup theory. Discrepancies between barotropic and Sverdrup transports are attributed to the influx of $\backsim$20 Sv via the ITF, evident in the streamlines entering the domain north of Australia. The simulated ITF is slightly stronger than the 16 Sv observed (Godfrey, 1989).

In both AGIO and ARC112, transport contributions from the source regions reach a confluence in the northern Agulhas Current, forming a coherent western boundary flow at 26°S. Barotropic transport contours show most of this flow reaching the retroflection. ARC112r has slightly increased in upstream recirculation compared to its interannual counterpart (Fig. 3.16b). The incoherent transport path between the South Atlantic and Indian Ocean basins reflects the expression of Agulhas leakage via rings. The southern branch of the supergyre is clear in the (arbitrary) zero-transport line spanning the domain. South of this line, eastward transport indicates the Antarctic Circumpolar Current (ACC).

Between the equator and 15°S, strengthening trade winds produce a more negative wind stress curl value (Fig. 5.1c). The associated increase in cyclonic vorticity input produces a stronger tropical gyre in all models, evident in the barotropic transports of ARC112 (Fig. 5.2b & c). Augmented circulation is expressed in faster flow at 100 m in the South Equatorial Current (SEC), North East Madagascar Current (NEMC), East African Coastal Current (EACC) and South Equatorial Counter Current (SECC) (Fig. 5.2c). A symmetrical response is seen when the trade winds weaken (Fig. 5.2b).

South of 15°S, increased positive wind stress curl drives an intensification in the anticyclonic transport of the subtropical gyre in all four configurations (Fig. 5.2b). The converse is seen in Fig. 5.2c. Strong circulation anomalies, associated with changes in the SEMC, arise to the east and south of Madagascar, between 26°S and 30°S, where changes in the wind-stress curl are most pronounced and changes in the input of anticyclonic vorticity are greatest (Fig. 5.1c). Anomalies in gyre transport become less intense south of 32.5°S as imposed changes in wind stress curl are confined to latitudes north of this.

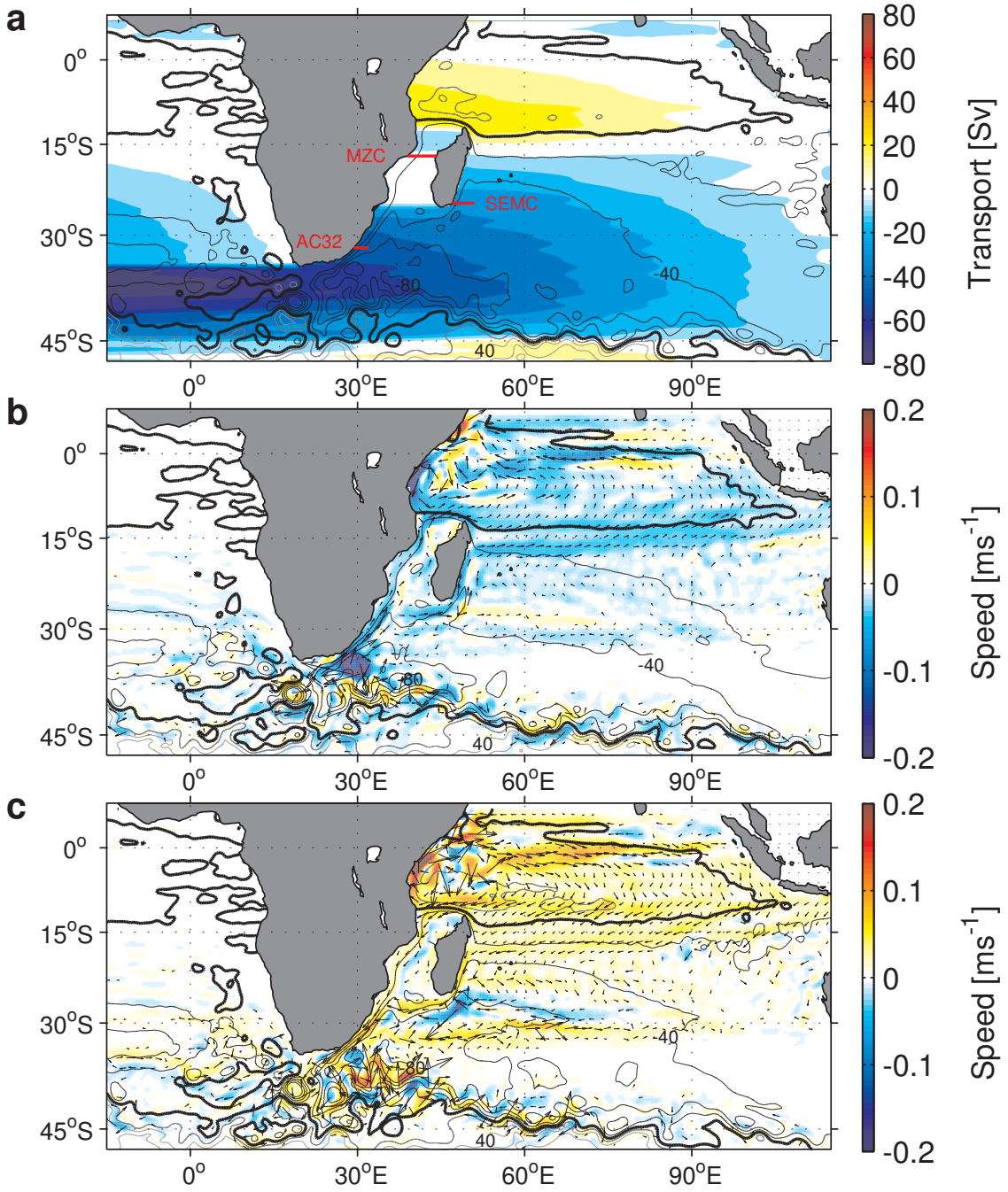

Figure 5.2: Panel (a) shows the annual mean barotropic transport for the ARC112r simulation in black contours. Shading shows the Sverdrup transport, derived from the wind field for the same simulation, with ψ=0 at the eastern boundary. Barotropic transports across the black transects are shown in Table 5.2. Contours showing the mean barotropic transport function overlaid on anomalies in speed at 100 m, shown in colour and vector, for (b) ARC112m40 and (c) ARC112p40 respectively.

At the southern tip of Madagascar, the SEMC extends in two modes (Siedler et al., 2009). The southern mode retroflects, connecting the SEMC to the transient, eastward-flowing, South Indian Counter Current (SICC) through eddies and ejecting the remainder westwards (Siedler et al., 2006, 2009). Under intensified trade winds, increased transport and speed between Mada-

Configuration	MZC	ΔMZC	SEMC	$\Delta SEMC$	$AC32$	$\Delta AC32$
ARC112m40	22.7	-2.5	18.2	-6.5	61.7	-8
ARC112r	25.2	—	24.7	—	69.7	—
ARC112p40	27.4	+2.2	30.1	+5.4	79.0	9.3

Table 5.2: Mean barotropic transports (in Sv) for the source regions for ARC112 sensitivity experiments. Extraction transects are shown in Fig. 5.2.

gascar and the African coast at 27°S (Fig. 5.2c) suggest an increase in the proportion of ejected waters in all configurations. Consequently, contributions to the SICC decrease, producing negative speed and transport anomalies offshore of Madagascar at 27°S.

In all cases, source region transports increase with subtropical gyre strength (Table 5.2). The SEMC shows a near linear response to changes in wind stress curl, consistent with estimates derived from Sverdrup theory (Fig. 5.2). Linear circulation changes in the MZC are less pronounced due to the bifurcation of the NEMC at the African coast, the edding nature of the flow and the smaller change in wind stress curl at 13°S (compared to 27°S).

Throughout, stronger source region transports are reflected at the western boundary, where transport and speed increase as increased wind stress curl (Fig. 5.2b & c, Table 5.2). This response is discussed in section 5.7. In all simulations, a strengthening Agulhas Return Current accompanied stronger WBC flow (Fig. 5.2c). However, the anomaly signal becomes convoluted downstream as the return current sheds transport (Boebel et al., 2003b). None of the sensitivity experiments show any changes in return current speed or transport east of 85°E, suggesting that adjustment to the wind changes predominantly occurs within the Indian Ocean basin.

The barotropic transport of the south east Atlantic Ocean remains largely unchanged in ARC112r and AGIO. Further, changes in current speed are minimal outside of the Cape Basin. There is no significant change in either the barotropic transport or speed of the ACC in any simulation (Fig. 5.2).

5.6 Mesoscale variability

The SEMC, MZC and retroflection regions are characterised by pronounced mesoscale variability (Fig. 3.16). Anomalies in mean (MKE) and eddy kinetic energy (EKE) for the ARC112 sensitivity experiments are shown in Fig. 5.3 and Table 5.3.

The Agulhas source regions show a near-linear transport response to increased wind stress curl (Table 5.2). North of Madagascar, this translates to a symmetrical response in MKE, with increased transport associated with large positive anomalies in the NEMC (Fig. 5.3a). As a consequence of the predominantly eddy-driven flow, MKE in the MZC remains small in ARC112. Increased (decreased) variability in the northern channel and Comoros gyre occurs concurrent with stronger (weaker) winds in both eddy-resolving configurations, due to the increased (decreased) barotropic instability associated with modified SEC transport (Biastoch and Krauss,

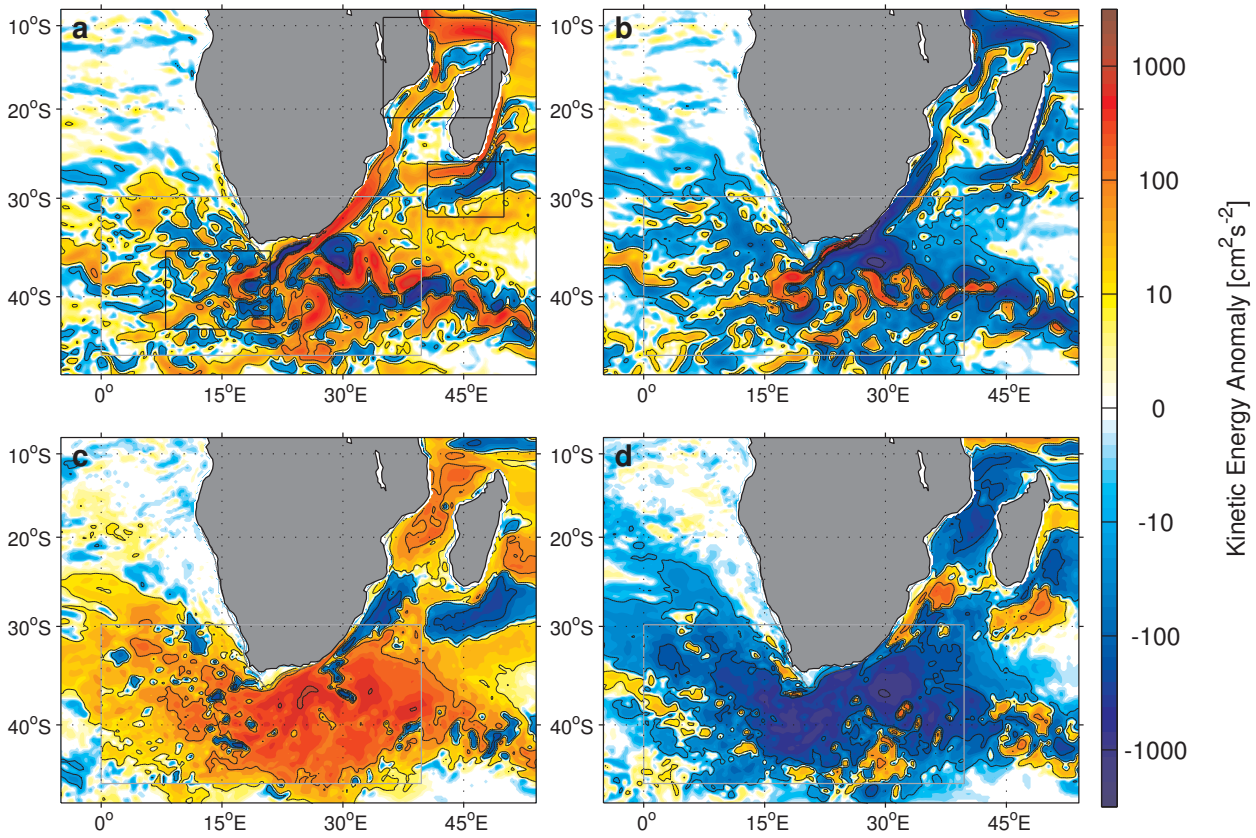

Figure 5.3: Mean kinetic energy anomalies for (a) ARC112p40 and (b) ARC112m40. Eddy kinetic energy anomalies for (c) ARC112p40 and (d) ARC112m40. Black contours follow the ±10, 100 and 1000 cm^2s^{-2} isolines. The light grey black box delineates the ARC112 nest boundary. Area means for the black boxes spanning the Mozambique Channel, South East Madagascar Current and retroflection regions in panel (a) are given in Table 5.3.

1999; Backeberg and Reason, 2010). In contrast, the southern channel and northern Agulhas show negative EKE anomalies when winds intensify, possibly attributable to the eddies ejected from the SEMC (Quartly and Srokosz, 2004), or increased incorporation of variability into the mean Agulhas. The patterns expressed under intensified winds are consistent with those observed by Backeberg et al. (2012).

East of Madagascar, the SEMC shows strongly positive (negative) MKE anomalies at stronger (weaker) winds. Offshore, anomalies of opposite polarity at 28°S are consistent with reduced (increased) transport changes in the SICC, a consequence of the SEMC circulation changes noted previously. However, the net effect in SEMC MKE is minimal (Table 5.3). Weaker SEMC retroflections are associated with increased eddy production, evident in positive EKE anomalies between Madagascar and the African Coast, and reduced eddy variability in the SICC (Table 5.3).

Flow in the stable northern Agulhas, North of 32°S, is more confined to the mean under intensified winds, evident in the positive MKE and negative EKE anomalies seen here. Further south, where flow becomes more turbulent, large positive anomalies suggest a more variable

Configuration	$MZC_{EKE/MKE}$	$SEMC_{EKE/MKE}$	$RETRO_{EKE/MKE}$
ARC112m40	561/398	249/100	1177/330
ARC112r	616/493	234/114	1391/333
ARC112p40	699/503	191/100	1541/344
OBSERVED	521/207	421/64	928/175

Table 5.3: Kinetic energy values (in $cm^2\ s^{-2}$) calculated from 5-daily ARC112 sea-surface height fields from across the retroflection (RETRO), Mozambique Channel (MZC) and South East Madagascar Current (SEMC) boxes shown in Fig. 5.6. Observed values for eddy (EKE) and mean (MKE) kinetic energies are calculated from 7-day AVISO altimetry products for the 1992-2007 period.

Agulhas enters the retroflection region at increased transport (Fig. 5.3a & c). In the case of weaker winds, the offshore Agulhas shows a pronounced decrease in MKE and EKE, consistent with the upstream recirculation shown in Fig. 5.2b.

Mean kinetic energy (MKE) is representative of the mean current path. In the mean kinetic anomalies shown in Fig. 5.3a and Fig. 5.3b for the ARC112p40 and ARC112m40 experiments, respectively, there are notable anomalies inshore of the Agulhas Current south of 35°S. In the case of the ARC112p40 experiment (Fig. 5.3a), the negative inshore anomaly, and positive offshore anomaly is indicative of a stronger current that occurs further offshore, consistent with a more meridional coastal separation. The opposite case is evident for the ARC112m40 case (Fig. 5.3b). Here the mean flow of the Agulhas Current appears stronger inshore, even though offshore and upstream flow decreases, This may be indicative of a weakened separation.

The retroflection and Cape Basin show large changes in EKE and MKE. Positive anomalies associated with stronger trade winds, which suggests increases in retroflection turbulence and potential changes in Agulhas ring formation. Positive anomalies in Agulhas Current MKE and retroflection EKE are reflected in the return current, consistent with the changes in speed and transport that were noted previously (Fig. 5.2c). Despite this, South Atlantic anomalies are low across all models ($O10\ cm^2 s^{-2}$) outside of the Cape Basin.

5.7 Western boundary responses

Linear Sverdup theory implies that changes in wind stress curl modulate vorticity input, and should be reflected in WBC transport. Fig. 5.4 compares WBC transports derived from the Sverdrup relationship, with barotropic transports from AGIO and ARC112. As expected, Sverdrup transport increases with latitude between 20°S and 35°S (Fig. 5.4a), a consequence of increasing wind stress curl. Applying the ±40% anomalies produces a corresponding change in implied poleward transport north of 32.5°S. South of this, where no anomaly is applied, transport returns to the reference value. East of Madagascar, barotropic transports in AGIO and ARC112 (Fig. 5.4b & c, respectively) follow a similar pattern, showing an accumulation of poleward volume flux. Bar plots (Fig. 5.4, right) show the relative contributions of vorticity terms (as described in section 2.5.2), vertically integrated over the top 1000 m, and zonally

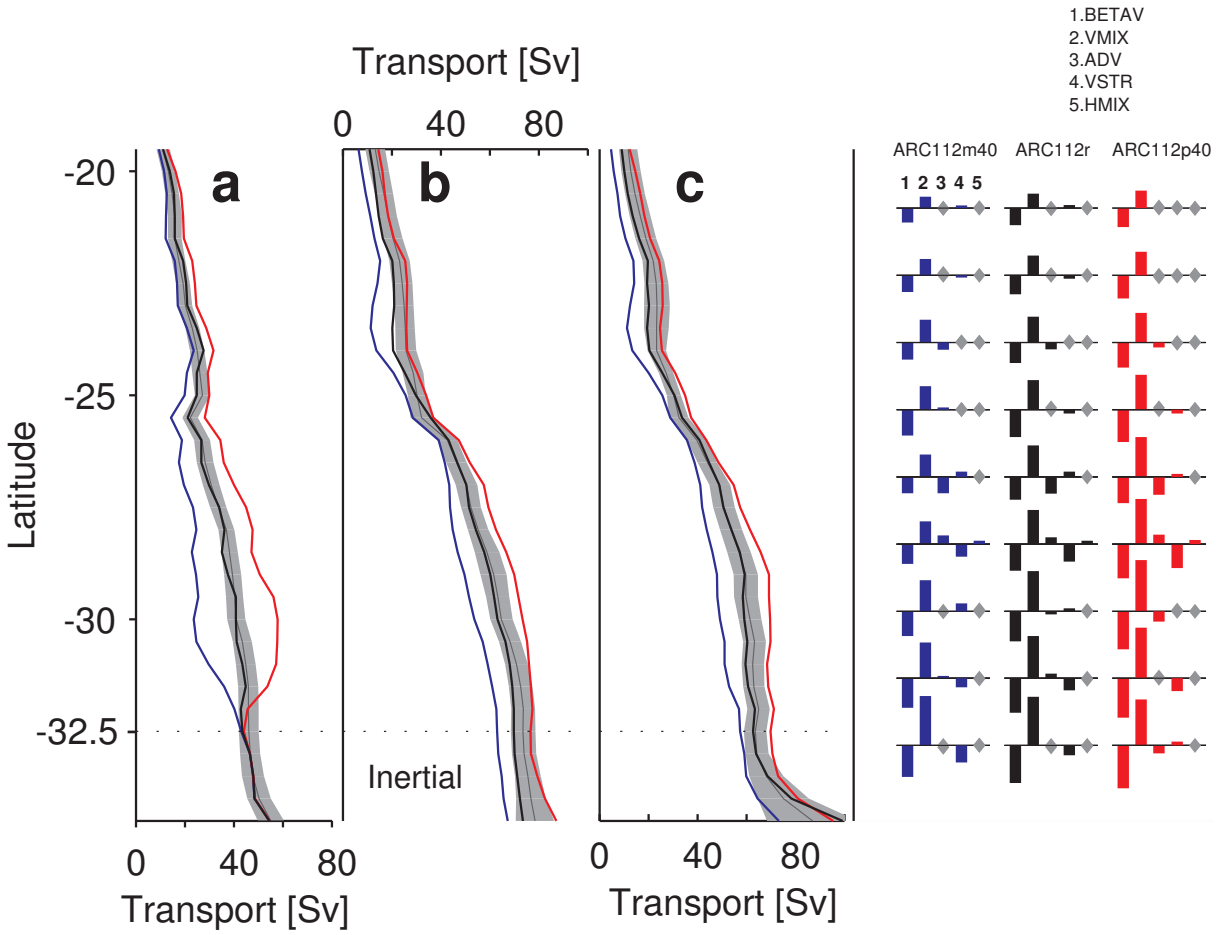

Figure 5.4: Changes in western boundary transport with latitude derived from a) the Sverdrup relation, and barotropic transport functions for b) AGIO and c) ARC112. Blue, black and red lines represent the -40%, reference and +40% experiments. Barotropic transport values are calculated as the difference between the maximum stream function value within 250 km of the 500 m isobath and the coastal value. The grey lines show the analogous quantities from the 1948-2007 interannual experiments, with the grey envelope showing the annual standard deviation. Relative importance of the zonally and vertically integrated vorticity balance terms are shown in the bars on the right for selected latitudes. From left to right: BETAV, VMIX, ADV, VSTR, HMIX. Bar colours correspond to the associated sensitivity experiment (blue ARC112m40, black ARC112r, red ARC112p40). Grey diamonds indicate near zero terms.

integrated across the Indian Ocean. East of Madagascar (equatorward of 26°S), the BETAV and VMIX bars almost balance in all experiments, indicating a Sverdrup balance between wind stress curl and planetary vorticity. Low horizontal viscosity is reflected in the small HMIX values throughout.

South of Madagascar (26°S), advection of ITF waters through the MZC disrupts the Sverdrup balance. Advection is compensated by vortex stretching between 28°S and 30°S. However, barotropic anomalies of ±10 Sv in AGIO and ARC112 are low compared with ±17 Sv dictated by theory, attributable to eddy-mean interaction at the boundary (Biastoch et al., 2009a). Consequently, although barotropic transport shows a near-linear relationship with wind stress curl, transport diverges from the theoretical estimates further south.

Due to inertia, barotropic transports anomalies persist poleward south of 32°S (Fig. 5.4b & c). This is reflected in the increased BETAV term, which is balanced by vortex stretching (and advection in ARC112p40), rather than through VMIX, which remains at a near fixed value. At 34°S, ARC112p40 and ARC112r transports converge, suggesting a degree of readjustment. In contrast, transport at weaker winds is greatly reduced. In AGIO, where upstream recirculation occurs less frequently, the values do not converge.

5.8 Agulhas leakage sensitivity to Agulhas Current transport

Annual mean Lagrangian transport estimates for the Agulhas Current and leakage are summarised in Fig. 5.5a. The results from the two OGCM configurations tested are included to allow for direct comparison. Agulhas Current transport increases near-linearly with wind stress. ORCA05/INALT01 show a ±3 Sv change. ARC112/AGIO show a larger ±8 Sv change, that is reflected in the Eulerian transports (Fig. 5.5b). As Eulerian estimates capture equator- and poleward velocity components, the Agulhas Undercurrent is sampled, producing lower transport values.

While current response is consistent across the models, leakage response is not (Fig. 5.5a & b). At lower resolution, ORCA05 shows an anti-correlation between the two transports . Conversely, leakage in AGIO increases with wind stress (Fig. 5.5a & b, blue triangles). In both cases, differences between mean leakage values exceed the reference annual mean standard deviation (Table 5.4), suggesting that internal variability cannot account for the inter-experiment changes. The correlation between current and leakage seen in AGIO is reflected in the passive tracer fluxes. The offset in values is ascribed to the westward retroflection position, discussed previously in chapters 3 and 4.

As resolution increases, leakage changes decrease and model behaviour converges (Table 5.4). In ARC112 and INALT01, the models that most closely approximate observations (see Fig. 3.16, Table 3.1 for ARC112), changes in upstream transport are associated with minimal changes in leakage (squares and stars in Fig. 5.5a & b). Inter-experiment differences in leakage magnitude fall within one standard deviation of the annual mean reference value, suggesting that differences are well within the internal variability of the system. This 'decoupling' is echoed in the passive tracer values for ARC112 (Fig. 5.5b). Convergence of the two leakage quantification methods suggests that Eulerian methods are valid when Indian Ocean waters are appropriately labelled and that any loss of Lagrangian precision is small.

Stronger Agulhas Current transports are reflected in higher volume flux in return current and across the STF (Fig. 5.5c). Transports across the STF_L and RC_L sections increase with wind stress in all cases, a result that is most pronounced in ARC112 where the largest changes in western boundary transport occur. Although ARC112 shows a higher transport across the STF than expected ($\backsim$7.5 Sv), only 6.7% of these floats cross west of 10°E, and no substantial under-sampling of the leakage occurs. This assertion is supported by the agreement between the

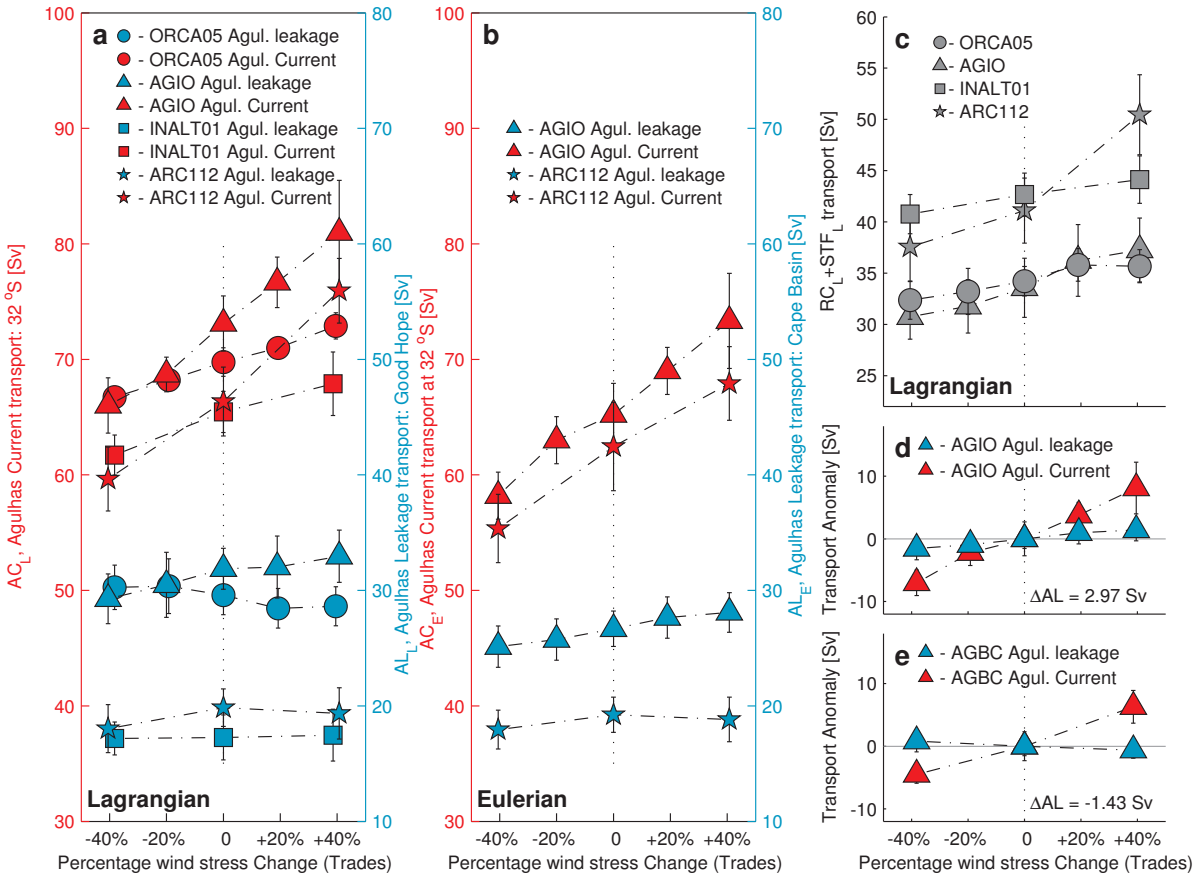

Figure 5.5: Changes in Agulhas Current transport and leakage magnitude with trade wind stress. Annual mean estimates derived from (a) Lagrangian flux (all models) and (b) Eulerian passive tracer flux (for basin-scale configurations). Blue and red values correspond to the Agulhas leakage and Agulhas Current, respectively. Panel (c) show the sum of the Lagrangian transport estimates for the Agulhas Return Current and across the Subtropical Front. Panels (d) and (e) compare the Eulerian transport anomalies for the Agulhas Current and leakage for the AGIO sensitivity experiments with the transport anomalies from the variable boundary AGBC experiments (described in Table 5.1). The delta values show the change on Agulhas leakage for each series (see Table 5.4).

Configuration	*Resolution*	ΔAC	$STD(AC_{ref})$	ΔAL	$STD(AL_{ref})$	$\lvert\Delta AL/\Delta AC\rvert$
ORCA05_L	$1/2^o$	6.2 Sv	1.2 Sv	-1.9 Sv	1.7 Sv	0.31
AGIO_L	$1/4^o$	15.0 Sv	2.4 Sv	3.7 Sv	1.8 Sv	0.25
AGIO_E	$1/4^o$	15.1 Sv	2.7 Sv	2.9 Sv	1.5 Sv	0.20
AGBC_E	$1/4^o$	10.8 Sv	2.3 Sv	-1.4 Sv	**1.5 Sv**	0.13
INALT01_L	$1/10^o$	6.2 Sv	1.8 Sv	0.3 Sv	**1.9 Sv**	0.05
ARC112_L	$1/12^o$	16.3 Sv	2.9 Sv	1.3 Sv	**1.8 Sv**	0.08
ARC112_E	$1/12^o$	12.6 Sv	3.8 Sv	0.9 Sv	**1.8 Sv**	0.07

Table 5.4: Summary of the changes in Agulhas Current (ΔAC) and Agulhas leakage (ΔAL) across the sensitivity experiments. Subscripts L and E refer to the Lagrangian and Eulerian flux estimates shown in Fig. 5.4. Standard deviations are given for the reference experiment, bold values indicate where this exceeds ΔAL (no significant change). The right hand column shows the sensitivity of the leakage to changes in the Agulhas Current transport.

Eulerian and Lagrangian leakage estimates. Rather, it is likely that the STF section captures some of the return current transport when meanders occur far to the south (Fig. 3.18b).

Here, the focus is on the Agulhas response to local and basin-scale processes within the Indian Ocean. However, (Durgadoo et al., 2013) show that the large-scale can also play a role in determining retroflection behaviour, via adjustment of the ACC. To test for any large scale control over the relationship described above, a second set of AGIO experiments are performed using boundary conditions derived from ORCA05m40 and ORCA05p40 experiments (see Table 5.1: AGBC).

Fig. 5.5 d & e compare the transport anomalies seen in the AGIO and AGBC sensitivity experiments. In the latter case, the leakage response to changes in upstream inertia is further reduced (Table 5.4). This suggests that climatological boundary conditions used may cause AGIO to overestimate the link between WBC transport and leakage. This result is consistent with a suggested decoupling. Further, as ARC112 shows only minimal leakage sensitivity, it seems unlikely that boundary condition changes would modify this result.

5.9 Retroflection position

Using the methodology described in section 3.2.9, retroflection positions were derived from the SSH fields for the AGIO and ARC112 sensitivity experiments. These are shown in Fig. 5.6. Note that this methodology returns an observed pattern consistent with Dencausse et al. (2010b); an approximately Gaussian distribution centred around 18.5°E (Fig. 5.6 grey bars).

Applying this method to AGIOr and ARC112r (Fig. 5.6 black traces), it is clear that the former has a more prograded retroflection than that observed, with the westward skewed distribution eroding the upstream maximum. In contrast, ARC112r has a defined symmetrical peak at 15°E, about which the distribution is well constrained, more closely resembling observations.

Although ARC112r and AGIOr reference states clearly differ, Agulhas transport modulation does not drive substantial changes in retroflection distribution in either case. Standard deviations, similar in both models, remain broadly consistent throughout, and, in AGIO, no shift in mean is apparent. In ARC112, increased (decreased) WBC transport makes upstream recirculation events +4% (-2%) more (less) likely, expressed in the higher (lower) peak at 22°S (Fig. 5.6b). A 1° eastward shift in ARC112p40 mean position is attributable to this effect. However, retroflections predominantly still occur around 15°E throughout, with no longitudinal shift in the dominant peak (Fig. 5.6b). Sporadically, large perturbations in the observed Agulhas Current produce extreme retroflection events (van Aken et al., 2013). While upstream recirculations occur in all ARC112 experiments, extreme events (east of 24°E) are rare, and absent from ARC112m40, causing the large negative anomaly in 100 m speed near ∽35°S seen in Fig. 5.2b.

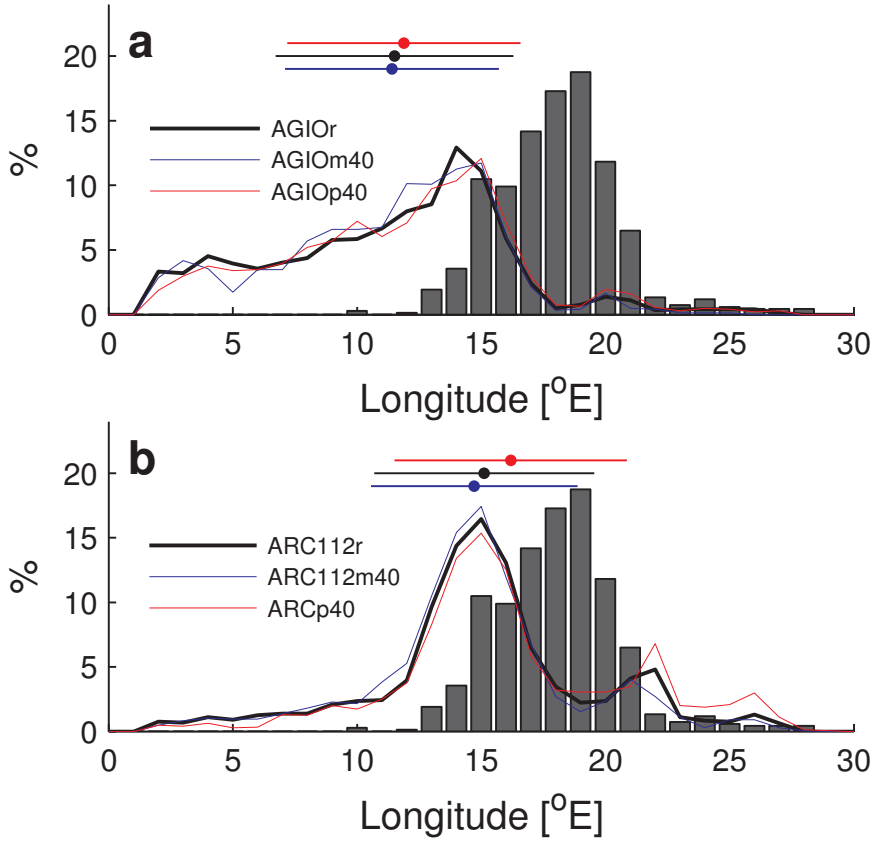

Figure 5.6: Probability distribution of retroflection longitudes for (a) AGIO and (b) ARC112 sensitivity experiments. The 1992-2007 retroflection position distribution for observed values derived from AVISO altimetry are shown in the grey bars. Coloured horizontal bars show the mean and standard deviation of the distribution for each sensitivity experiment.

5.10 Retroflection vorticity

Following the same approach as used to produce Fig. 2.17 in section 2.5.2, it is possible to compare the balance of vorticity terms in the ARC112 sensitivity experiments, as shown in Fig. 5.7. It is clear that the increased meridional transport of the current is reflected in the stronger β term in the ARC112p40 case (Fig. 5.7b). However, at increased transport there is a notable break in the β term contours east of the Agulhas Bank at 23°E. Further, BETAV appears stronger in the Agulhas Return Current meanders, echoing the increased meridional transport in the first meanders.

The HMIX term represents horizontal viscosity, and arises as a result of the Smagorinsky parameterisation (Smagorinsky, 1963) used at the western boundary. While the term remains small throughout, a reduction in the HMIX to the east of the Agulhas Bank in the ARC112p40 case reflects the movement of the current away from the shore at increased inertia. This increased inertial overshoot is also expressed through the stronger positive HMIX pattern inshore of the current at the shelf break. In the ARC112m40 experiment, the current does not overshoot the shelf break at 35°S, and takes a more coastal path. This change of current path echoes the

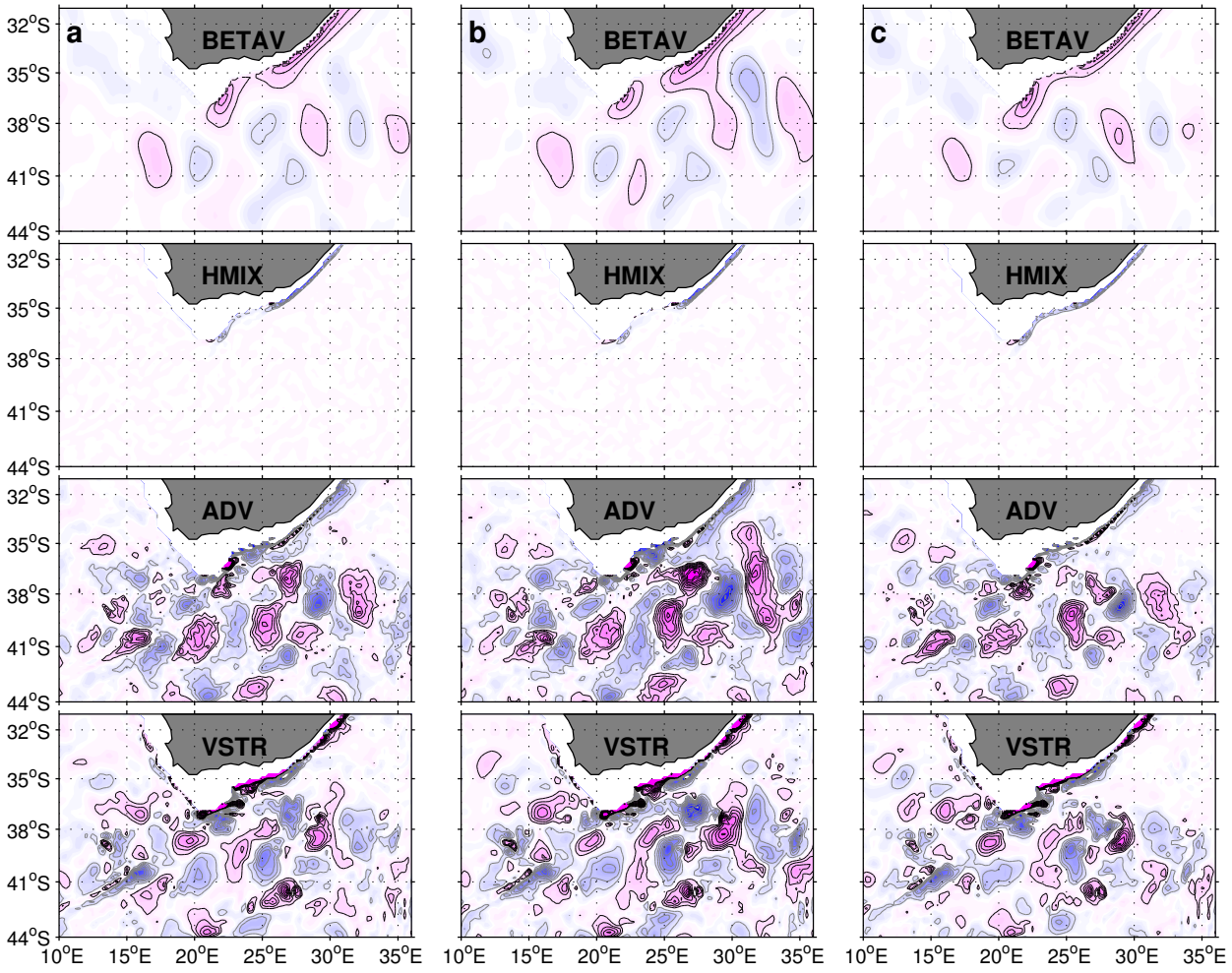

Figure 5.7: Depth integrated vorticity balance terms for the top 300 m of ARC112r, derived via Eq. 2.32 to Eq. 2.34. Columns **a** through **c** show the fields for the ARC112r, ARC112p40 and ARC112m40 experiments. BETA, HMIX and ADV and VSTR are contoured at $4x10^{-12}$ s^{-2} intervals. Negative (positive) vorticity regions are contoured in grey (black) and shaded blue (purple).

previously noted patterns in the MKE, discussed in section 5.6. However, despite an increased overshoot in ARC112p40, there is an interaction with topography at the tip of the Agulhas Bank in all experiments, evident in the HMIX and BETAV patterns throughout Fig. 2.17. This implies that the increased Agulhas Current inertia acquired from stronger trade winds, is not sufficient to modify the retroflection path to such an extent that it is unable to avoid the Agulhas Bank.

From the vorticity balance, it is clear that the retroflection is predominantly governed by advection (ADV) and vortex stretching (VSTR), with the β-effect playing a small role in the return current meanders. Notably, the vortex stretching and advection terms along 40°S strengthen at increased inertia, representative of increased return current flow when the Agulhas Current transport is high. Well defined VSTR and ADV patterns around the Agulhas Plateau at 26°E strengthen with current transport, indicating a potentially strong topographical control downstream of the retroflection (Matano, 1996; Speich et al., 2006).

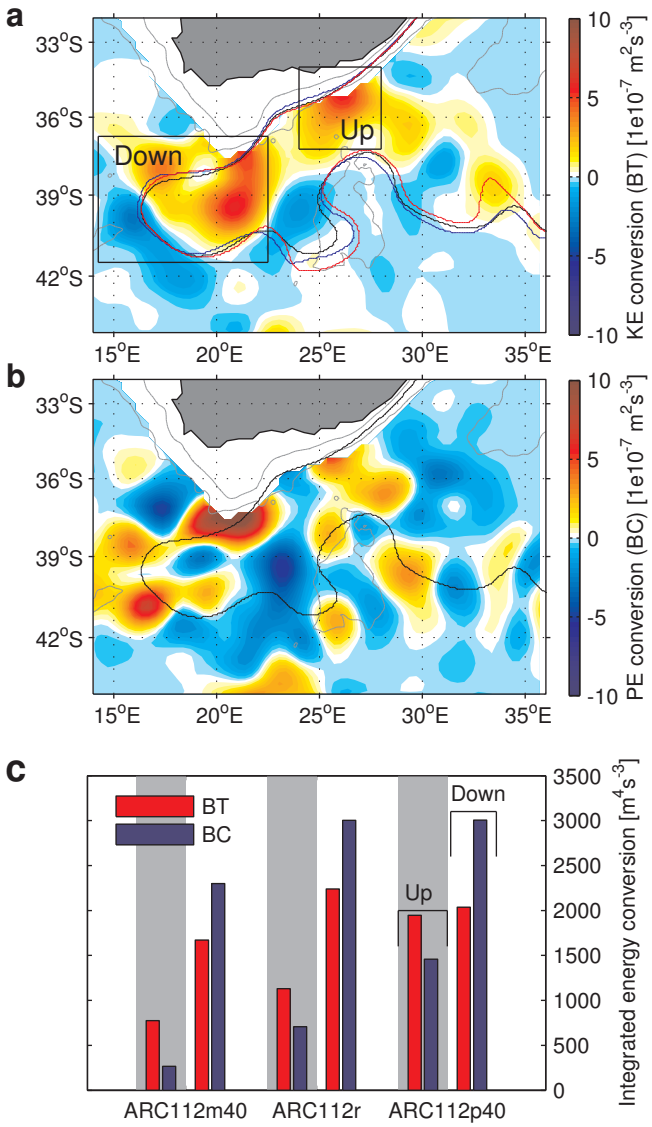

Figure 5.8: Spatial distribution of depth integrated (a) barotropic (BT) and (b) baroclinic (BC) instability in the top 1000 m of the ARC112r experiment, inferred from the kinetic and potential energy conversion terms. The black, red and blue contours track the 20-year mean retroflection positions for ARC112r, ARC112m40 and ARC112p40 experiments. Grey contours show the 400 m and 3000 m isobaths. The values of the BC and BT terms, integrated across the upstream (Up) and downstream (Down) boxes, are summarised in panel (c).

5.11 Ring formation processes

Agulhas rings, the mechanism via which most leakage occurs, form at the retroflection due to mixed barotropic (BT) and baroclinic (BC) instability (Chassignet and Boudra, 1988). Indicators for BT and BC can be derived from the potential (5.1) and kinetic energy (5.2) conversion terms, which are integrated over the top 1000 m (Biastoch and Krauss, 1999; Tsugawa and Hasumi, 2010). Primed values represent anomalies from the 5-daily mean horizontal velocities $\bar{u}/\bar{v}$ and potential density $\bar{\rho}$. The horizontal average of the potential density across the domain, represents the reference state, $\widetilde{\rho}$.

$$g \iiint_H^0 \frac{\overline{u'\rho'}\partial\overline{\rho}/\partial x + \overline{v'\rho'}\partial\overline{\rho}/\partial y}{d\widetilde{\rho}/dz} dV \tag{5.1}$$

$$- \iiint_H^0 \left(\overline{u'u'}\frac{\partial\bar{u}}{\partial x} + \overline{u'v'}(\frac{\partial\bar{u}}{\partial y} + \frac{\partial\bar{v}}{\partial x}) + \overline{v'v'}\frac{\partial\bar{v}}{\partial y} \right) dV \tag{5.2}$$

The spatial changes in barotropic and baroclinic instability in the retroflcetion region are summarised in Fig. 5.8. Barotropic instability characterises much of the region bounded by the ARC112r retroflection (Fig. 5.8a). The shelf break, Agulhas Bank and retroflection extremity, the likely site of ring formation, show an increased propensity for eddy generation, reflected in high BT and BC values (Fig. 5.8b). Spatially integrated values (Fig. 5.8c) show that increased inertia drives increased instability in the upstream current around the shelf break, consistent with with the large EKE changes here (Fig. 5.3). Downstream, baroclinic instability increases, but barotropic changes are smaller, suggesting that ring formation may not be as heavily impacted. Notably, downstream values are lower at reduced wind stress, despite inertial theory suggesting a stronger leakage in this case. Increases in upstream BT are echoed by large negative anomalies in the return current, suggesting that eddies are increasingly incorporated into the mean flow here when flow strengthens.

5.12 Discussion

Sverdrup dynamics dictate that, to the first order, western boundary transport is determined by the zonally integrated wind-stress curl across an ocean basin. However, the results presented here show that, although the Agulhas Current responds linearly to wind stress north of 32.5°S, the magnitude of the response differs from Sverdrup estimates. Biastoch et al. (2009b) previously noted this discrepancy, ascribing it to topographical shielding (Matano et al., 2002) and eddy-mean interactions (Biastoch et al., 2009a). Here, expanding on this, demonstrating that on decadal timescales, transport anomalies generated by upstream trade wind variability can propagate southward under the influence of western boundary inertia, reaching the retroflection despite no direct wind forcing here. Consequently, although intensified trade winds may result in a stronger Agulhas Current, the exact response cannot be directly inferred Biastoch et al. (2009b), emphasising the need for direct monitoring (Beal et al., 2009).

Model behaviour in turbulent regions, is highly sensitive to numerical choices and horizontal resolution (Backeberg et al., 2009; Barnier et al., 2006; Dijkstra and de Ruijter, 2001). For robustness, the dynamical link between the Agulhas Current and leakage is investigated using two model platforms; ROMS and NEMO. While model behavior differs at lower resolution (eddy-permitting and below), the sensitivity of the Agulhas leakage to incoming transport invariably decreases as resolution becomes finer. In the eddy-resolving regime the models converge, and the two configurations (ARC112 and INALT01) present a common response; one where trade wind driven Agulhas Current variability, has no significant effect on the leakage.

The Agulhas retroflection mediates the division of the Agulhas Current into the eastward return current and westward leakage components; the latter being of primary climatic interest (de Ruijter et al., 1999a; Beal et al., 2011). Key to retroflection dynamics is the balance between viscosity and inertia (Dijkstra and de Ruijter, 2001). Low Ekman numbers and HMIX terms imply inertially governed retroflections in both AGIO and ARC112 and the derived vorticity balance for the latter shows a pattern consistent with Boudra and Chassignet (1988); specifically, an inertial overshoot associated with inshore isopycnal doming, and a retroflection governed by relative vorticity advection and vortex stretching. However, in the simulations performed here, a stronger inertial overshoot does not result in the earlier retroflection suggested by Ou and de Ruijter (1986), due to continued topographical interaction with the Agulhas Bank and Agulhas Plateau. Subsequently, upstream changes in inertia are reflected in the stronger vortex stretching and advection terms in the first meander of the return current; symptomatic of the increased transport here.

Control of the retroflection position by bathymetry has been noted both in previous numerical model studies (Matano, 1996; Speich et al., 2006) and observations (Dencausse et al., 2010b). In AGIO, substantial smoothing of this bathymetry is shown to reduce the angle of the shelf break and the prominence of the Agulhas Bank. This minimises the propensity for inertial overshoot and permits an overly westward retroflection and an enhanced leakage. However, a comparative immobile retroflection position, as seen in ARC112, is consistent with modern observations, which show that, excepting the 2001 extreme event, it has remained remarkably stable since 1992 (Dencausse et al., 2010b; Backeberg et al., 2012). Further support comes from palaeoceanographic studies that suggest Last Glacial Maximum retroflection longitudes near to the present position (Franzese et al., 2009).

Chassignet and Boudra (1988) show that ring formation occurs through mixed barotropic-baroclinic instability. Tsugawa and Hasumi (2010) suggest that barotropic instability may drive increased Agulhas variability, through Natal Pulses. A similar upstream response is noted here, when inertia is higher. While Biastoch and Krauss (1999) find that the retroflection is governed by baroclinic instability, it is the transfer of mean to kinetic energy (BT) that appears key to ring formation Chassignet and Boudra (1988). Here, BT is found this to be near constant in the retroflection loop, and increased upstream eddy production, reflected in regional EKE anomalies, is incorporated back into the mean in the return current.

The semi-continuous subtropical front is not a barrier to southward flux (Dencausse et al., 2011). Le Bars et al. (2012) identify a turbulent retroflection regime, where leakage is asymptotically limited by increased cross frontal mixing in the return current. Under intensified trade winds a stronger southward flux at the retroflection is seen, along with greatly increased EKE along the subtropical front. While these experiments differ from Le Bars et al. (2012), as the westerly winds are not modified, these results suggest the possibility of inertially driven increases in southward export of Indian Ocean waters.

Two recent hindcast studies have explored the long-term behavior of the Agulhas system

(Biastoch et al., 2009b; Rouault et al., 2009). While they agree on a leakage increase since the 1980s, they record respective negative and positive trends in Agulhas Current transport. It has been argued that the anti-correlation seen by Biastoch et al. (2009b) is causal (van Sebille et al., 2009b). However, the results presented here suggest that this may not be the case. The AGIO model used here is similar to the Rouault et al. (2009) SAfE configuration. However, the interannual forcing applied (Table 5.1, subscript i) is consistent with that used to force the AG01 model presented in Biastoch et al. (2009b). Under this forcing, both the models discussed here show long term trends consistent with AG01. However, physically, AGIOi differs little from SAfE, suggesting that the differing trends seen between Rouault et al. (2009) and Biastoch et al. (2009b) may be attributable to the choice of forcing and/or boundary conditions.

Recent intensification of the westerly winds has been documented in observations and coupled models Swart and Fyfe (2012). Durgadoo et al. (2013) find that the leakage responds strongly to intensified westerlies, increasing in magnitude despite no immediate change in Agulhas transport at 32°S (a consistent result, included in the Durgadoo et al. (2013) study, is presented in chapter 6). Here, a complementary result is shown; Agulhas Current transport responds strongly to trade wind intensity, with minimal change in leakage. Having established a mechanism by which the two systems can vary independently, it is suggested that, while correlations between them may exist in the short term, they may not be indicative of a reliable dynamical connection. Rather they arise with changes in both trades and westerlies part of the larger atmospheric circulation.

Observations and reanalysis products suggest that Indian Ocean winds are intensifying (Han et al., 2010; Gillett and Thompson, 2003; Swart and Fyfe, 2012), producing an attendant response in Agulhas mesoscale variability (Backeberg et al., 2012). Comparing the kinetic energy anomalies for ARC112p40 with observed trends (Backeberg et al., 2012) yields clear similarities. A common increase in EKE and MKE in the NEMC, the increased (decreased) EKE in the north (south) of the MZC, and a mean intensification in the northern Agulhas Current, suggests that the observed responses are dynamically attributable to trade wind intensification. South of 25°S, the applied anomalies do not match the observed trend and it is therefore unsurprising that the variability observed here is not well represented.

Although coherent in its southern reaches, the Agulhas Current carries the imprint of mesoscale variability generated around Madagascar. Multiple studies have linked eddy generation in the MZC and SEMC to Agulhas Ring formation (Penven et al., 2006c; Schouten et al., 2002a). Here, pronounced changes are induced in source region EKE, and it is surprising to find that the leakage is minimally effected. However, in idealised studies, Pichevin et al. (1999) show that upstream current meanders have no influence on ring generation, a result consistent with the observed discrepancy between of ring formation, 5 ± 1 year^{-1} (Schouten et al., 2002a), and Natal Pulse rates, 1.6 year^{-1} (Rouault and Penven, 2011). Similarly, upstream transport pulses may accelerate ring generation, but do not impact ring formation rates (Pichevin et al., 1999). Further, OGCM experiments confirm that excluding source region variability from eddy-resolving models effects ring path and timing, but does not produce a change in leakage (Biastoch et al.,

2008c).

As observations show an increase in retroflection turbulence since 1993, and hindcast experiments showing a recent increase in Agulhas leakage, it has been suggested that altimetry derived EKE may be used as a proxy for inter-basin flux (Backeberg et al., 2012). However, Durgadoo et al. (2013) show cases where increased turbulence is associated with decreased inter-basin flux, and here it is shown that changes in EKE do not mandate any leakage change, suggesting that the two quantities do not have an obvious relationship.

The ACT array (Beal et al., 2009) is designed to produce a hydrographic record of the Agulhas Current that can be used to calibrate a co-incident altimetry track for long term monitoring. Due to the inferred anti-correlation between current transport and leakage (van Sebille et al., 2009b), it has been suggested that ACT may provide a proxy for the latter (van Sebille et al., 2010a). This is an attractive proposition, as annual estimates for the leakage are hard to derive from *in situ* observations. In reality, it is unlikely that the trade and westerly winds will vary independently, as both are part of the large-scale climate system. However, the apparent freedom with which the Agulhas Current can change, with little downstream consequence necessitates treating any correlation with a degree of skepticism. In this regard, the ACT array becomes necessary in establishing a long-term Agulhas Current times series, but efforts towards direct monitoring of the Agulhas leakage remain essential.

5.13 Conclusions

Four model configurations, of varying resolution, have been used to quantify the response of the Agulhas leakage to changes in the Agulhas Current, driven by changes in the wind stress north of 32.5°S. This response has been investigated using complementary methodologies based on Lagrangian virtual floats and Eulerian passive tracer flux. It is show that an intensification of the trade winds drives a stronger flow in both the tropical and sub-tropical gyres. This is reflected in the transport and in the Agulhas source regions, and modification of the eddy variability in MZC and SEMC. The combined contributions from the source regions produce Agulhas Current transport anomalies at 32°S, which persisting into the retroflection under inertia.

Changes in Agulhas Current transport are shown to have a diminishing influence on the Agulhas leakage as resolution increases. In the eddy-resolving case, model behavior converges and, on a multi-decadal timescale, annual mean changes in the Agulhas Current exceeding ±8 Sv elicit no significant change in leakage magnitude. This behaviour is confirmed through complementary Eulerian and Lagrangian leakage quantification methods, which converge as retroflection position improves.

Trade wind stress anomalies imposed in the sensitivity experiments induce a variability greater than twice the annual standard deviation seen in the 1948-2007 CORE v.2b reanalysis winds. From this, it is concluded that, during this period, modification of the mean transport of the Agulhas Current by the trade winds has minimal effect on the annual mean inter-basin

flux. Rather, it is more likely that changes in the magnitude of the leakage are predominantly the result of modulation of the wind stress curl in the latitude of the westerly winds. This is discussed in chapter 6 and in Durgadoo et al. (2013).

Previous hindcast experiments present a conflicting picture of the dynamical link between the Agulhas Current and leakage (Biastoch et al., 2009b; Rouault et al., 2009; van Sebille et al., 2009b). Under the interpretation presented here, these results can be reconciled. The interannual experiments performed here show a common weakening in the Agulhas Current with time. However, it is shown that variability in the trade winds can give rise to a strengthening or weakening of the Agulhas Current, with no consequence for the Agulhas leakage. As the Agulhas leakage is driven by the westerly winds (Durgadoo et al., 2013), it is suggested that these trends arise as a consequence of the forcing products used and that correlations between upstream transport and Agulhas leakage may not be indicative of a dynamical link. While observational arrays may be able to exploit these correlations, their potential transience should be reconsidered.

Chapter 6

Southern hemisphere westerly wind driven Agulhas leakage variability

6.1 Introduction

The Agulhas leakage represents a key climatic link between the Indian and Atlantic Oceans (de Ruijter et al., 1999a), forming the northern branch of the 'super-gyre' connecting the subtropical gyres of the two basins (Ridgway and Dunn, 2007) and influencing the strength of the AMOC (Weijer et al., 2002). Motivated by changes in reanalysis winds between the equator and 32°S since 1993 (Backeberg et al., 2012, supplementary), chapter 5 focussed on how this link responds to changes in trade wind strength. The magnitude of the Agulhas leakage was shown to be minimally sensitive to changes in Agulhas Current inertia under these conditions, but the sensitivity of the greater Agulhas system to the changes in the westerly wind pattern was not addressed. However, this side of the problem was considered by Durgadoo et al. (2013), and this chapter expands on the work conducted collaboratively and published therein, using the ROMS regional model configurations discussed in chapters 2 and 3.

Observations and CMIP simulations show a recent strengthening (Swart and Fyfe, 2012) and poleward migration (Thompson and Solomon, 2002) of the southern hemisphere westerlies (SHW). Coupled climate simulations suggest that these responses are consistent with the loss of stratospheric ozone (Gillett and Thompson, 2003), and are projected to continue under further anthropogenic forcing. In the ocean, the primary response is an intensification of the super-gyre connecting the subtropical Atlantic and Indian Ocean (Cai, 2006), where the Agulhas system is embedded (Beal et al., 2011). Consequently, the westerly winds have been suggested to play a key role in determining Agulhas leakage magnitude (de Ruijter et al., 1999a; Pichevin et al., 1999; Le Bars et al., 2012; Durgadoo et al., 2013).

Dynamical arguments suggest that the equatorial migration of the westerly winds should result in a decreased leakage, due to the enhanced inertial choking when the gateway between the subtropical front and the coast of Africa is reduced (de Ruijter et al., 1999a). By the inverse argument, the observed poleward shift in the SHW is expected to produce a larger leakage (*ibid*).

However, numerical studies are less clear on the response to changes in westerly wind strength. In a series of high-resolution baroclinic simulations, Le Bars et al. (2012) show an increase in Agulhas leakage with the large-scale westerly wind stress, which reaches an asymptotic limit where cross frontal mixing between the return current and STF becomes substantial. Conversely, Nof et al. (2011) simulate cases where the momentum flux of the Agulhas Retroflection, a key process by which rings form (Pichevin et al., 1999) is opposed by an increased wind stress, nullifying ring formation and reducing leakage. As such, the combined effects of a poleward migration and strengthening of the winds is hard to predict (Beal et al., 2011).

Hindcast simulations link a progressive poleward shift of the SHW in the last three decades with a substantial increase in Agulhas leakage (Biastoch et al., 2009b; Rouault et al., 2009). Biastoch and Böning (2013) extrapolated this link into the future, forcing a high-resolution OGCM with a wind stress consistent with the projections of a coupled climate model. Here, a further strengthening and poleward migration of the westerly winds produced an even stronger leakage, suggesting a continued increase in inter-basin flux under anthropogenic forcing. However, it remains unclear as to whether the changes in leakage are attributable to the poleward shift, or the continued strengthening, of the SHW.

Arguments for the control of the Agulhas leakage by shifts in the westerly winds come from the palaeorecord. Converse to the modern case, substantial reductions in the Agulhas leakage during glacial maxima (Peeters et al., 2004) may be related to a equatorward migration of the subtropical front and the zero line of wind stress curl (Bard and Rickaby, 2009). Analysis of sediment flux shows a reduced flux at the last glacial maximum (LGM) (Franzese et al., 2006), but the retroflection position most likely mirrors the modern location (Franzese et al., 2009). Using a coarse resolution coupled model, Sijp and England (2008) performed sensitivity experiments shifting the SHW equatorward 6^{o}S. They record a substantial decrease in the Agulhas leakage in this case, accompanying a near severing of the super-gyre linking the subtropical Indian and Atlantic. During glacial terminations, sudden pulses of Indian Ocean water are detected in the South Atlantic (Peeters et al., 2004) and have been linked to the resumption of the AMOC (Knorr and Lohmann, 2003). Intensifications and/or northward migrations of the SHW may also enhance cross frontal mixing in the Agulhas Return Current, modifying the hydrography of the South West Indian Ocean sub-gyre on a millennial scale (Simon et al., 2013).

Here, the response of the Agulhas system to changes in the SHW are investigated using the AGIO regional model (presented in chapters 2 and 3). To separate the effects of SHW position and strength, a suite of wind stress anomalies, analogous to those presented for the trade winds in chapter 5, are independently applied across the model domain. The role of the ACC and the effects of cross frontal mixing on the magnitude of the Agulhas leakage flux are also considered. The results are compared with those derived from a similar set of experiments that have been been performed with global coarse and eddy-resolving simulations, presented by Durgadoo et al. (2013).

6.2 Applying anomalies: Modifying westerly wind stress

The westerly winds are modified using the similar approach to that detailed in section 5.2. The CORE v.2b reanalysis products suggest that since 1960, the zonal mean wind stress curl across the Indian Ocean has increased by ∼25% between 35°S and 48°S. CMIP5 ensembles suggest that this intensification will continue by a further 10% by the end of the 21st century (Swart and Fyfe, 2012). To mirror these changes, anomalies have been devised to geometrically modify westerly wind intensity by ±20% and ±40% south of 32°S (Fig. 6.1a - c). The anomalies are applied across the model domain from 29°E to 115°W (Fig. 6.1d), and are linearly ramped in using the approach described in the previous chapter. The zero line of wind stress curl remains at the reference latitude throughout this set of experiments.

Models and observations offer no consensus on the strength and latitude of the SHW at the LGM (Sime et al., 2013), however palaeo-data synthesis suggests that a strengthening and equatorward displacement are the most likely signals (Kohfeld et al., 2013). Conversely, since

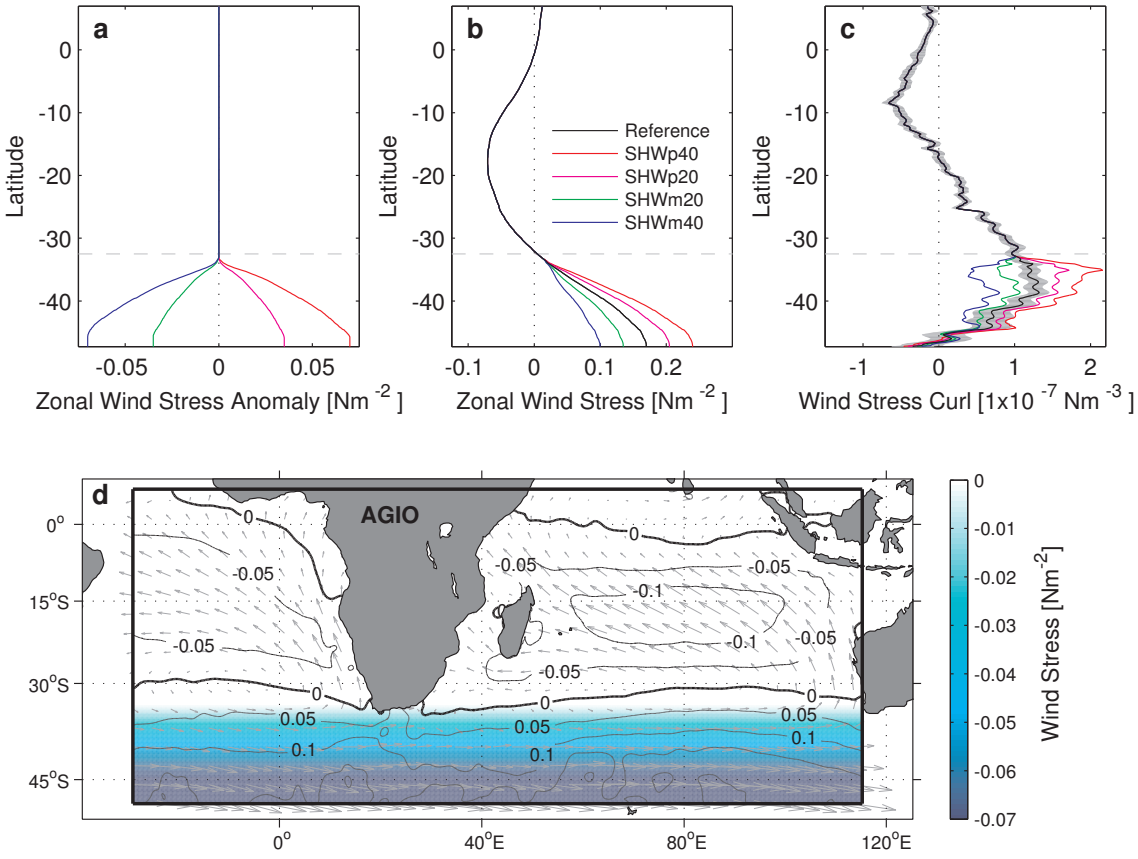

Figure 6.1: Zonal averages of, (a) zonal wind stress anomalies, (b) zonal wind stress and (c) zonal wind stress curl for the westerly wind strength sensitivity experiments. No anomaly is applied north of the grey dashed lines. The black line describes the 20-year mean climatological reference value. The grey shaded area in (b) and (c) covers the annual standard deviation in the 1948-2007 wind stress curl extracted from the AGIOi hindcast. The full extent of the AGIO domain is shown by the black box. Anomalies are applied over the area shown in colour; AGIO-SHWm40 is shown in this case. The contours and vectors show the magnitude and direction of the AGIOr wind stress.

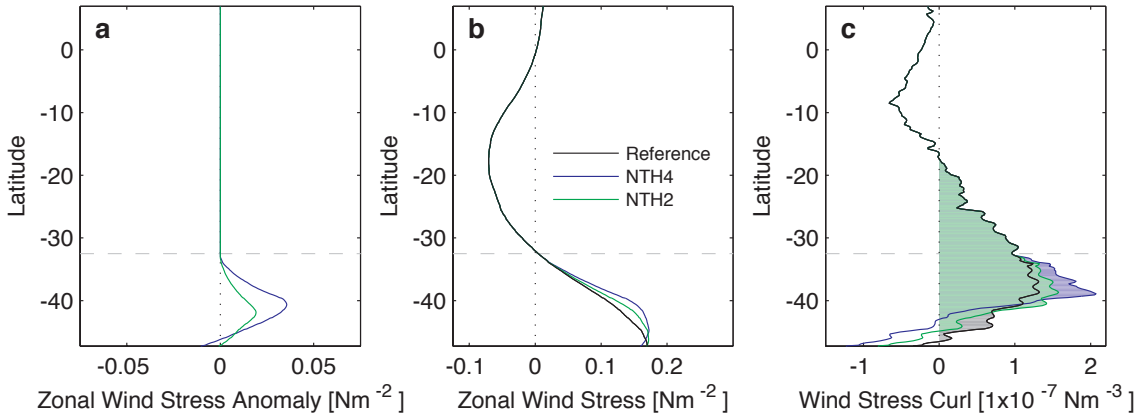

Figure 6.2: As in Fig. 6.1 but for the westerly wind shift experiments. The zero line of wind stress curl is shifted equatorwards by 2° (NTH2) and 4° (NTH4). The integrated wind energy, shown in grey and blue shading under the positive wind stress curl envelope in the sensitivity experiments, is within 2.5% of the reference value, shown in grey shading.

1948, the CORE v.2b reanalysis product shows a poleward migration of the zero line of wind stress curl of ∼2°S (Biastoch et al., 2009b), which may double under further anthropogenic forcing (Biastoch and Böning, 2013). The southern boundary of the AGIO domain prevents the imposition of anomalies that shift the westerly winds further southward as the zero line of wind stress curl would fall outside of the domain. However, to investigate the response of the Agulhas system under pseudo-glacial conditions, a second set of experiments is performed where the zero line of wind stress curl across the AGIO domain is shifted equatorwards by 2° (NTH2) and 4° (NTH4) (Fig. 6.2). During these experiments, the integrated wind energy in the positive wind stress curl envelope remains within 2.5% of the reference value.

6.3 Experimental Summary

6.3.1 AGIO experiments

The AGIO westerly wind sensitivity experiments are presented in table 6.1. In addition to the reference simulation, six sensitivity experiments are performed, independently modifying the intensity of the westerly winds (AGIO-SHWxxx; Fig. 6.1), and the latitude of the zero line of wind stress curl (AGIO-NTHx; Fig. 6.2). Boundary conditions for these sensitivity experiments are drawn from a climatology of year 1 to 60 of the ORCA05 reference run.

6.3.2 Global model experiments

A similar set of westerly wind sensitivity experiments are performed using two global models, the coarse resolution ORCA05 (Biastoch et al., 2008a) and eddy-resolving INALT01 (Durgadoo et al., 2013) configurations. Both global models are forced with the same CORE v.2b surface fields as AGIO and are described in section 5.3.3. In the case of the global models sensitivity experiments (shown in table 6.1) circumpolar westerly wind anomalies are applied. As neither

global model is constrained by a southern boundary, wind shift experiments where the zero line of wind stress curl is shifted poleward are also performed.

6.3.3 Variable boundary condition experiments

Applying the circumpolar westerly wind anomalies in the global models is likely to result in a concomitant response in the Antarctic Circumpolar Current (ACC) (Durgadoo et al., 2013). In the AGIO-SHWxxx and AGIO-NTHx experiments, the ORCA05 climatological boundary conditions are used, explicitly preventing any anomaly driven ACC variability at the domain boundary. To assess the regional response of the Agulhas leakage to changes in the ACC, three additional experiments are performed. In the AGIO-ACC series of experiments (Table 6.1), boundary conditions are drawn from a climatology of year 41-60 of the ORCA05 reference run (AGIO-ACCr), ORCA-SHWp40 (AGIO-ACCp40) and ORCA-NTH4 (AGIO-ACCNTH4) experiments. In each of these AGIO-ACC experiments, the appropriate, dynamically consistent anomaly is applied. In this way the influence of any global ACC adjustment can be assessed.

Experiment	*Forcing/Anomaly*	*Boundary Conditions*	*Analysis Period*
ORCA05r	CNY	Not applicable	41-60
ORCA-SHWp40	CNY+40% zwws	Not applicable	41-60
ORCA-SHWp20	CNY+20% zwws	Not applicable	41-60
ORCA-SHWm20	CNY-20% zwws	Not applicable	41-60
ORCA-SHWm40	CNY-40% zwws	Not applicable	41-60
ORCA-STH4	CNY-4°S zwws	Not applicable	41-60
ORCA-STH2	CNY-2°S zwws	Not applicable	41-60
ORCA-NTH2	CNY+2°N zwws	Not applicable	41-60
ORCA-NTH4	CNY+4°N zwws	Not applicable	41-60
AGIOr	CNY	ORCA05 mon. clim.	41-60
AGIO-SHWp40	CNY+40% zwws	ORCA05 mon. clim.	41-60
AGIO-SHWp20	CNY+20% zwws	ORCA05 mon. clim.	41-60
AGIO-SHWm20	CNY-20% zwws	ORCA05 mon. clim.	41-60
AGIO-SHWm40	CNY-40% zwws	ORCA05 mon. clim.	41-60
AGIO-NTH2	CNY+2°N zwws	ORCA05 mon. clim.	41-60
AGIO-NTH4	CNY+4°N zwws	ORCA05 mon. clim.	41-60
AGIO-ACCp40	CNY+40% zwws	ORCA-SHWp40 (41-60)	21-40
AGIO-ACCNTH4	CNY+4°N zwws	ORCA-NTH4 (41-60)	21-40
INALT01r	CNY	Not applicable	41-60
INALT01-SHWp40	CNY+40% zwws	Not applicable	41-60
INALT01-SHWm40	CNY-40% zwws	Not applicable	41-60
INALT01-STH2	CNY-2°S zwws	Not applicable	41-60
INALT01-NTH4	CNY+4°N zwws	Not applicable	41-60

Table 6.1: Summary of sensitivity experiments performed and the changes applied to the zonal westerly wind stress (zwws). CNY refers to the Core v.2b normal year forcing fields, CI to the analogous 1948-2007 annually varying fields (Large and Yeager, 2009). Unless otherwise specified, the ORCA05 monthly climatology (mon. clim.) is based on years 1-60 of the reference run.

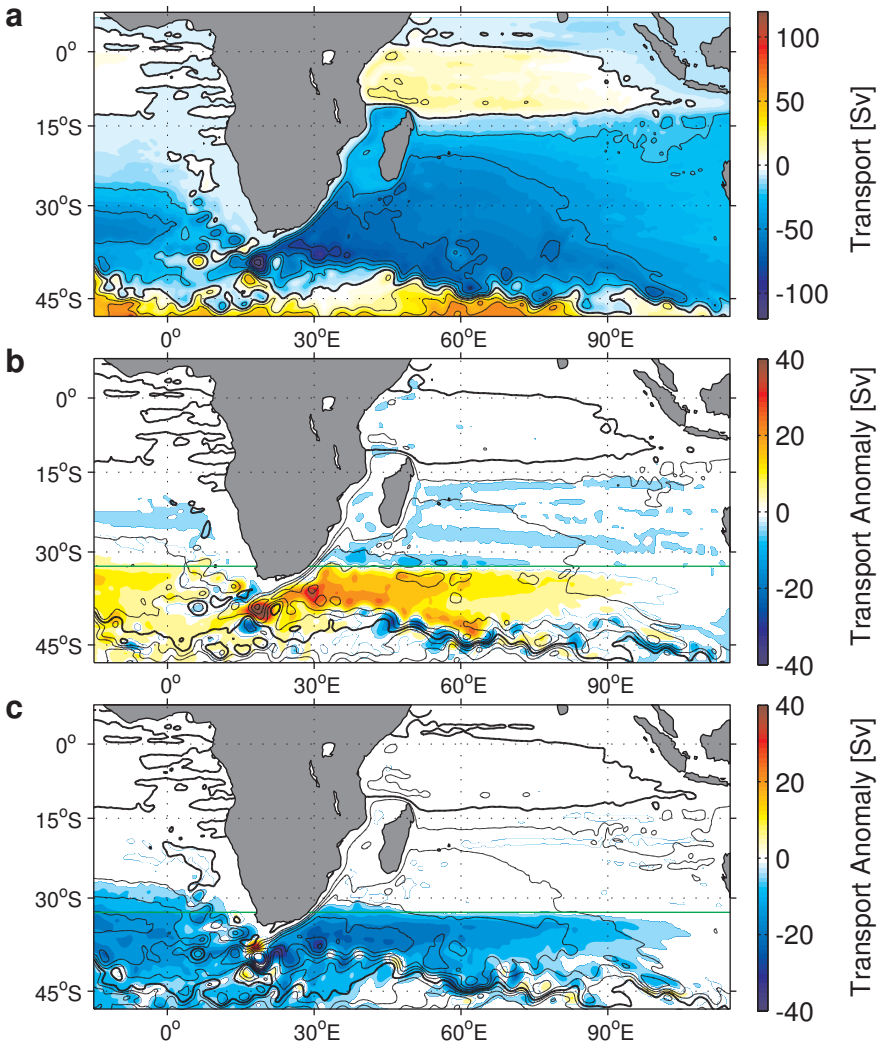

Figure 6.3: Barotropic transport function for (a) AGIOr in colour and shading, and barotropic transport function and transport anomaly for (b) AGIO-SHWm40 and (c) AGIO-SHWp40 in black contours and shading respectively. Barotropic transport functions are contoured at 20 Sv intervals. The green line shows the northern extent of the applied SHW anomaly.

6.4 Results

6.4.1 Equilibrium responses 1: westerly wind intensity

Imposing the westerly wind intensity anomalies induces a substantial change in the circulation of the subtropical gyres of the South Indian and South Atlantic Ocean (Fig. 6.3). Decreased positive wind stress curl associated with the SHWm40 anomaly results in a decrease in anticyclonic circulation south of 32°S (Fig. 6.3b). This is most notably in the South West Indian Ocean subgyre, where transport is reduced by up to 30 Sv in the south west extremity. As a result of the large drop in zonal mean wind stress curl around 32°S in the SHWm40 case (Fig. 6.1c), there is a small increase in the intensity of the anticyclonic circulation south of Madagascar as the subgyre is displaced. Conversely, in the SHWp40 case, increased positive wind stress

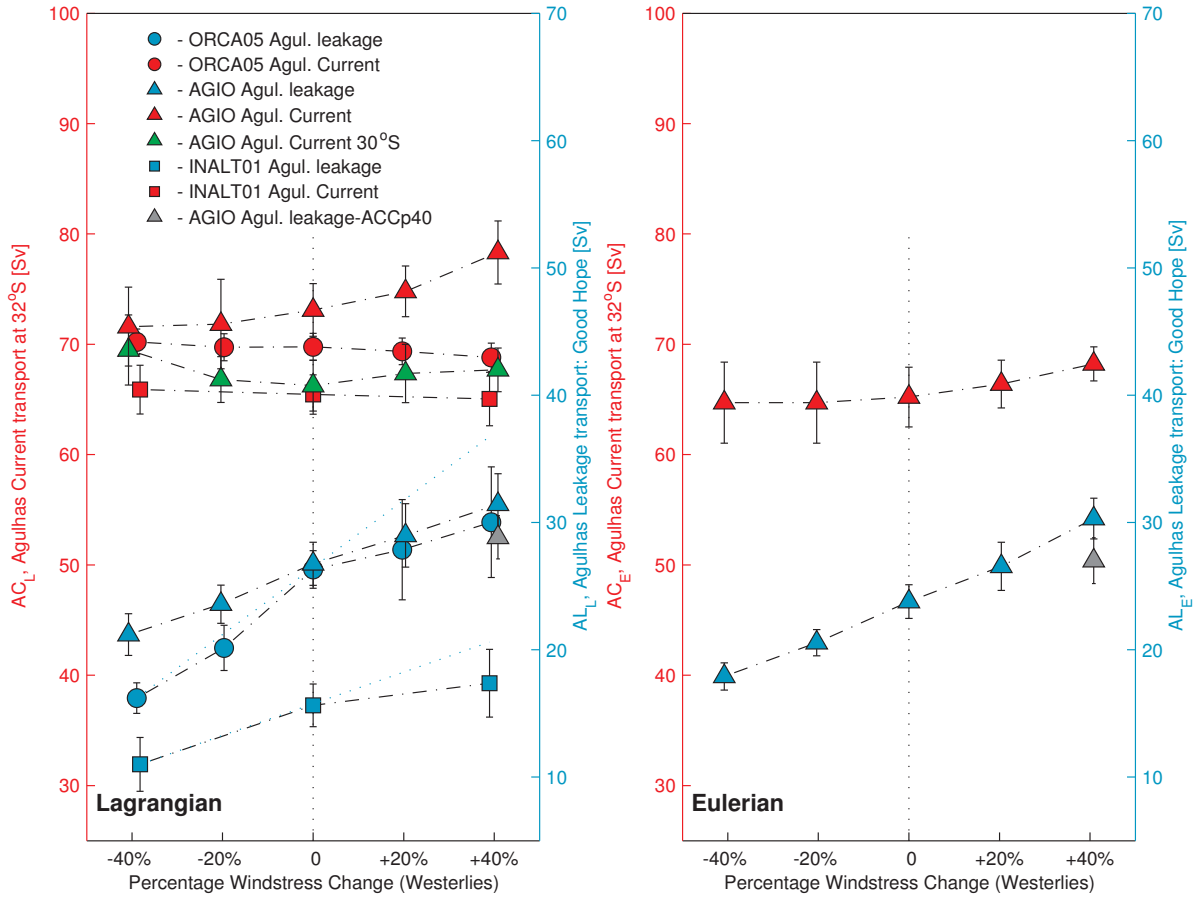

Figure 6.4: Changes in Agulhas Current transport and leakage magnitude with westerly wind stress, assessed in AGIO and two global models; ORCA05 and INALT01. Annual mean estimates derived from (a) Lagrangian flux (all models) and (b) Eulerian passive tracer flux for AGIO. Blue and red values correspond to the Agulhas leakage and Agulhas Current, respectively. The green triangles show the Lagrangian Agulhas Current flux as measured at 30°S across the sensitivity experiments. The grey triangles show the leakage value in the AGIO-ACCp40 experiment, the Agulhas Current matches the AGIO-SHWp40 value in this case. Thin blue-dotted lines highlight the nonlinearity in the global model leakage response.

curl drives a intensification and small northward expansion of the subtropical gyre (Fig. 6.3c). Circulation in the Indian Ocean remains largely unaffected north of 30°S, and flux through the Mozambique Channel and via the SEMC remain at a near constant value throughout. Changes in the intensity of the Indian Ocean subtropical gyre are echoed in the South Atlantic Ocean, suggesting a associated modulation of the Agulhas leakage and the supergyre as a whole.

Circulation changes can be explained within the context of linear Sverdrup theory. As positive wind stress increases, so do negative Ekman velocities across the region, resulting in an increase in equatorward Sverdrup transport across the southern branch of the Indian Ocean supergyre. Through continuity, this must be balanced by an increase in poleward flow in the western boundary south of the zero anomaly zone. Increases in the intensity of the southern branch of the supergyre implies that westward leakage transport may also increase. The SHWp40 case (Fig. 6.3c), where the Indo-Atlantic branch of the supergyre appears to be in-

tensified, is consistent with previous investigations of the global ocean circulation response to stronger westerly winds implied by recent NCEP reanalysis trends (Cai, 2006) and global model experiments (Biastoch and Böning, 2013; Durgadoo et al., 2013).

The response of the greater Agulhas system to modified westerly wind intensity is summarised in Fig. 6.4. Invariably, all models show an Agulhas leakage which increases with positive westerly wind stress curl (Fig. 6.4a, blue shapes). Within the context of the experiments here, this suggests that the leakage plays a passive role in the circulation of the supergyre, and is determined by the basin-scale circulation patterns in the South Indian Ocean and South Atlantic Ocean (Durgadoo et al., 2013). The similarity in the magnitude of the responses in AGIO (1/4°), ORCA05 (1/2°) and INALT01(1/4°) with regard to the change in leakage with westerly wind stress, indicates that, while model resolution may determine the mean leakage

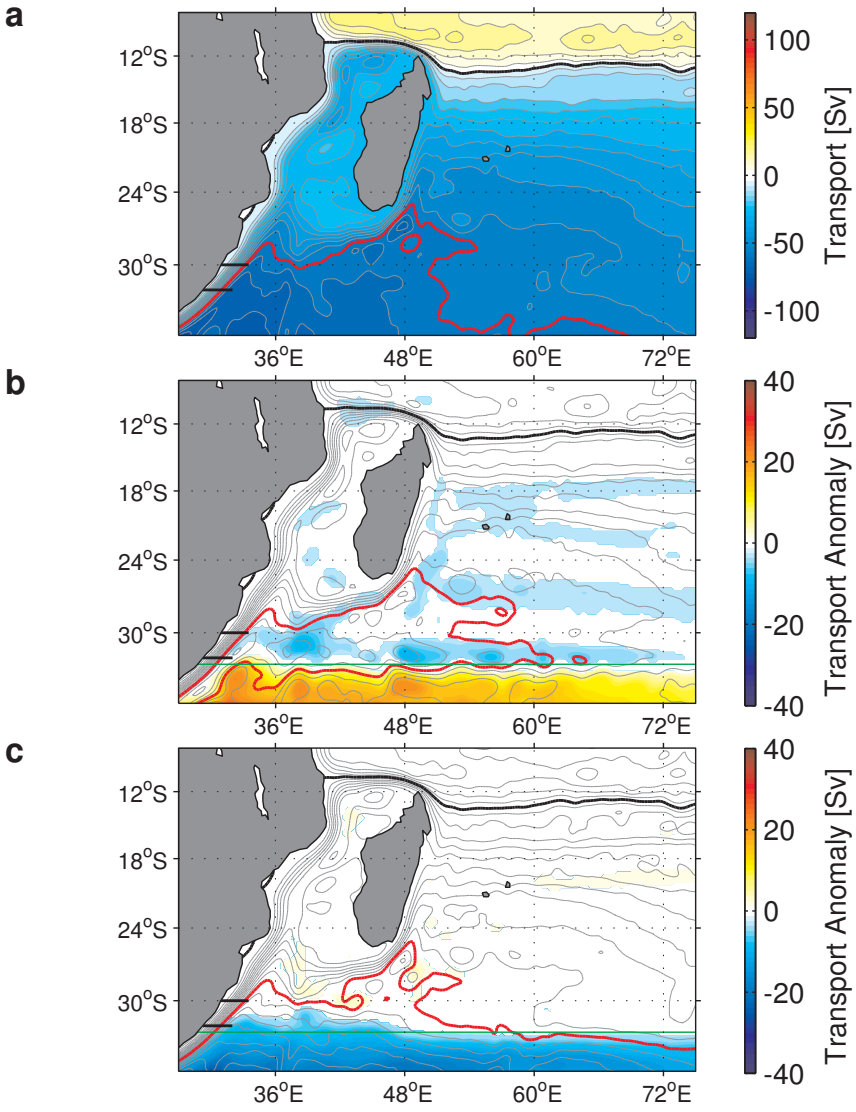

Figure 6.5: As in Fig. 6.3 but for the Agulhas source regions, countered at 5 Sv intervals. The black and red contours follow the 0 and 55 Sv contour line. The black transects indicates the AC32 and AC30 float release section for the ARIANE experiments described in Fig. 6.4.

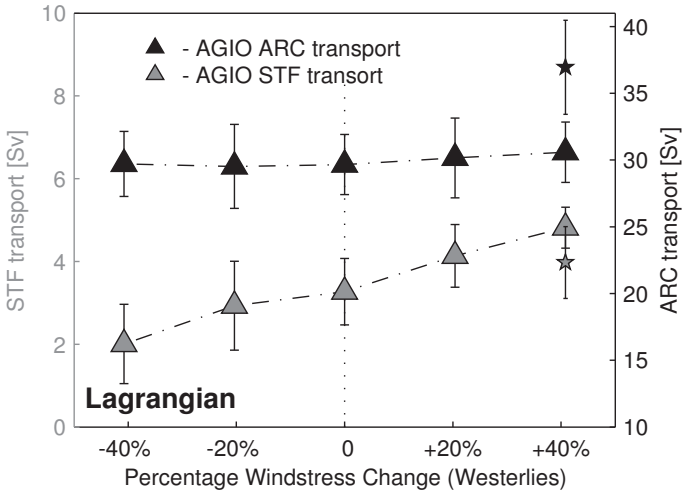

Figure 6.6: Transport across the STF_L and RC_L transects in the westerly wind intensity experiments. Stars shows the analogous values for the AGIO-ACCp40 experiment.

value, the sensitivity to changes in the basin scale winds is largely independent of grid-spacing. This is used as justification for the decision to not repeat the AGIO suite of experiments with the ARC112 configuration. Notably, while AGIO shows a linear response in leakage, as measured by both Lagrangian and Eulerian approaches, INALT01 and ORCA05 show a non-linear response, which is weaker when wind stress is increased. This non-linearity, and the implied existence of a potential threshold in Agulhas leakage at high wind stress values is consistent with the results of Le Bars et al. (2012), and will be discussed further in section 6.4.3.

Discrepancies in the behaviour of the Agulhas Current between the three models seem more pronounced. When measured at 32°S, INALT01 and ORCA05 show small decreases in western boundary current transport. Conversely, AGIO shows a non-linear increase. However, this increase is attributable to the northward expansion of the gyre in the SHWp20/SHWp40 experiments, as shown in Fig. 6.5. When measured at 30°S (Fig. 6.4a, green triangles), the Agulhas Current flux shows a slight (though non-linear) decrease in response to strengthening westerly winds, consistent with the global model values measured further south. This suggests an inconsistency in the response of the gyre in the regional and global models, which does not appear to expand northwards of 32°S in the latter.

Consistent with Le Bars et al. (2012), the flux across the STF increases with strengthening wind stress (Fig. 6.6, grey), rising from 2 Sv in the SHWm40 experiment to 5 Sv in the SHWp40 simulation. The response in the Agulhas Return Current appears minimal, with a total change of only 1 Sv throughout the experiments. However, in part this is due to the to the sampling of the displaced subgyre in the SHWm40 case (see the closed circulation loop along 30°S in Fig. 6.3b). Floats crossing the RC_L transect at 35°E are predominantly determined to be in the return current itself. However, plotting the final float positions for this transect by latitude (Fig. 6.7) shows that the displaced subgyre recirculation is also included in the RC_L transport estimate.

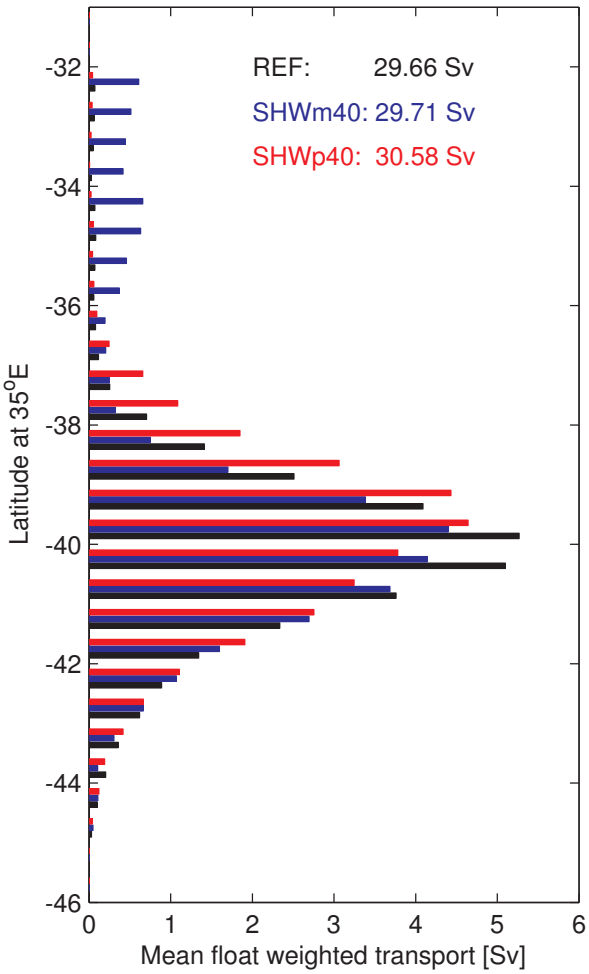

Figure 6.7: Transport across the RC_L section by latitude in the westerly intensity experiments.

6.4.2 Equilibrium responses 2: westerly wind shifts

North of the sub-tropical front, the basin scale circulation response to the NTH4 anomaly (Fig. 6.8) is similar to that previously shown for the SHWp40 case. The equatorward shift in the zero line of wind stress curl results in an increase in the positive curl value north of 40°S due to the stronger meridional gradient in the zonal wind ($\partial\tau_x/\partial y$ increases as ∂y decreases). South of the STF, the response differs and the cyclonic flow in the ACC strengthens due to the increasingly negative wind stress curl here. As before, the Indian Ocean shows no circulation changes north of 32°S, and the South Atlantic subtropical gyre response is similar to that seen in the Indian Ocean.

As in the previous section, increases in wind stress curl, here driven by northward shifting of the zero line, produce an increase in Agulhas leakage in all three models (Fig. 6.9). The effect is less pronounced than in the SHWp20/SHWp40 intensity experiments, as the modulation of wind stress curl is not as large. The Agulhas Current response is also similar to what was seen in the previous section, with AGIO showing a increase in western boundary current flux at 32°S as recirculation in the intensified subgyre expands slightly to the north.

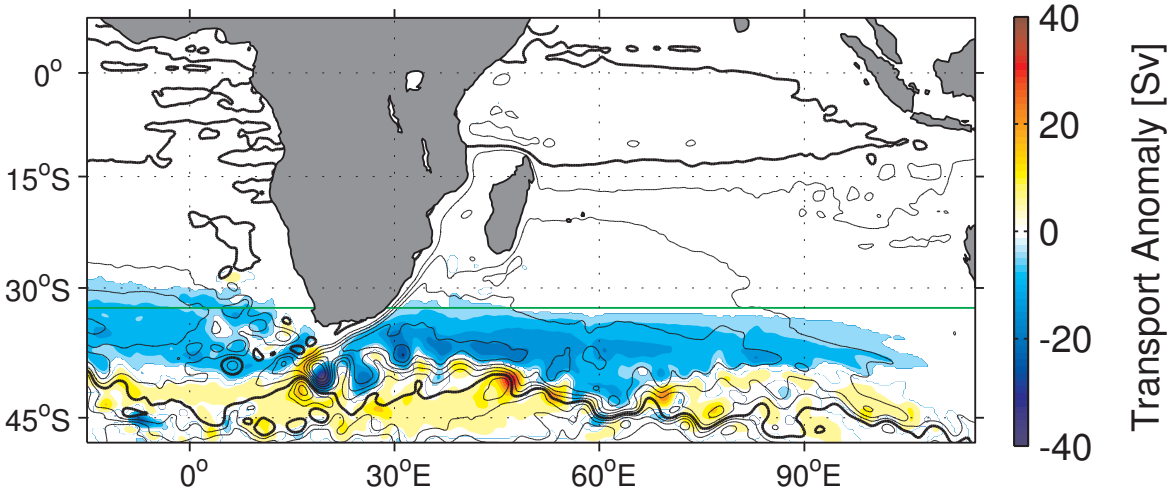

Figure 6.8: As in Fig. 6.3 but for the AGIO-NTH4 experiment.

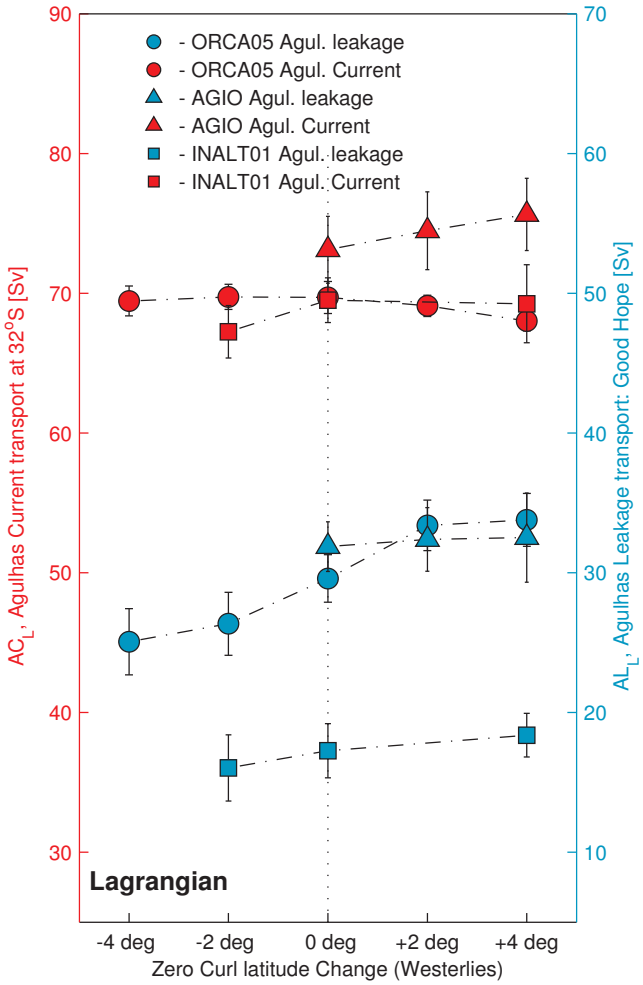

Figure 6.9: As in Fig. 6.4 panel *a*, but for the westerly wind shift experiments.

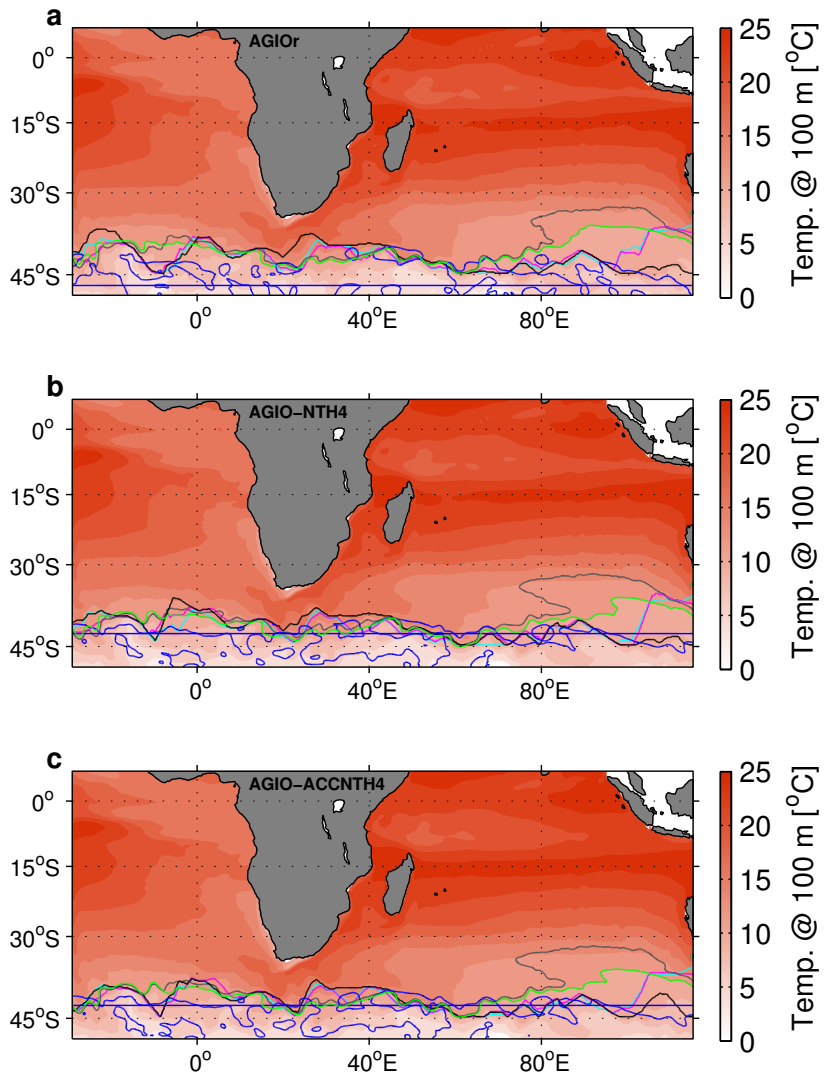

Figure 6.10: Temperature at 100 m and position of specified fronts in (a) AGIOr, (b) AGIO-NTH4 and (c) AGIO-ACCNTH4. The green contour represents the 12°C at 100 m (Orsi et al., 1995). The black, magenta and cyan contours represents the respective maximum meridional gradients in surface SSH and salt and temperature gradients at 100 m. The dark grey contours show the positions of the SSTF measured by the 35.0 isohaline (Belkin and Gordon, 1996). The blue contour and line show the respective positions of the zero line of wind stress curl and mean zero line of wind stress curl across the domain.

From Fig. 6.10, it is clear that despite a substantial equatorward shift in the zero line of wind stress curl of 3.9° in the AGIO-NTH4 experiment (panel *b* and Table 6.2), there is no concomitant displacement of the STF. The positions of the maximum SSH gradient, maximum temperature and salt gradients at 100 m, the 12°C isotherm at 100 m (Orsi et al., 1995) and the 35.0 isohaline (Belkin and Gordon, 1996) deviate from the reference value by a maximum poleward value of 0.6°. To remove the possibly that regional boundary conditions are constraining the front position, the same analysis is performed in the AGIO-ACCNTH4 experiments, where ORCA05-NTH4 derived boundary conditions are applied. In this case, the deviations from the reference run do not exceed 0.2°.

	AGIOr	NTH4	ACCNTH4
Lat. zero wind stress curl (blue)	**-46.7**	**-42.8**	**-42.8**
Lat. 12°C isotherm (green)	-41.2	-41.0	-41.0
Lat. max. merid. temp gradient (magenta)	-41.9	-41.9	-42.1
Lat. max. merid. salt gradient (cyan)	-42.1	-41.5	-41.9
Lat. max. merid. SSH gradient (black)	-42.1	-41.5	-42.1
Lat. SSTF (grey)	-39.2	-39.0	-39.1

Table 6.2: Mean latitude of the contours shown in Fig 6.10.

6.4.3 The role of the Antarctic Circumpolar Current

As mentioned above, the global models show a non-linear leakage response to changes in westerly wind intensity, while AGIO does not. While the ACC is free to globally adjust in ORCA05 and INALT01, its large-scale structure and transport in AGIO is fixed by the application of the ORCA05r boundary conditions. Le Bars et al. (2012) suggest that cross-frontal mixing between the ARC and ACC may play a role in determining leakage. At extreme values of wind stress curl, the Agulhas leakage is asymptotically limited to a maximum value under a turbulent regime where cross frontal mixing between the ARC and ACC becomes substantial. Durgadoo et al. (2013) record such an effect in the global models presented here (INALT01 and ORCA05), noting that, due to Rossby wave adjustment of the ACC, the Agulhas leakage value falls back to near the reference value 20 years after the anomaly is applied. The AGIO-SHW experiments are immune to this adjustment as the ORCA05r boundary condition values are imposed. Consequently, AGIO shows a linear response to westerly winds intensity, while as a result of the adjustment of the ACC, ORCA05 and INALT01 do not. To ascertain if the regional model shows a consistent response, the AGIO-ACCp40 experiment is performed using boundary conditions extracted form year 41-60 of the ORCA05-SHWp40 run (Table 6.1).

The twenty year mean values for the Agulhas Current is consistent with the AGIO-SHWp40 value, but the leakage for this experiment is shown in the grey triangle on Fig. 6.4. Similarly, the values for STF and return current flux are show in the stars on Fig. 6.6. Consistent with the global models, the leakage in AGIO-ACCp40 shows a lower value than previously seen in the non-adjusting case, confirming the the role that ACC adjustment plays in determining, and reducing, the leakage value. Surprisingly, transport across the STF, while still higher than the reference value in AGIO-ACCp40, is lower than in the ACC-SHWp40 case. However, Agulhas Return Current transport is much higher, suggesting that further cross frontal mixing may occur east of 35°E in this simulation.

6.4.4 Revisiting modern-day multi-decadal variability

In the CORE v.2b interannual reanalysis fields used to force the AGIOi and ARC112i hindcasts (as well as the AG01 hindcast of Biastoch et al. (2009b)), the zero line of wind stress curl shows a poleward shift of 2° and ∼25% increase in wind stress curl between 35°S and 48°S since 1960 (Fig. 6.11). Through the arguments presented here, changes in the magnitude of the westerly winds should be associated with changes in the Agulhas leakage if the ACC has not yet had time to adjust. Fig. 6.12 shows the correlation between the anomaly in the zonal mean westerly wind stress curl between 45°S and 41°S and the transport anomaly in the Agulhas leakage. In the first instance (panels *a* and *b*) the time series is not detrended, and the low frequency linear trend in both leakage magnitude and westerly wind stress curl remains present. Positive correlations, significant at >99% are seen in both models, irrespective of the leakage quantification method used. Further, the results from the AGIO-SHWm40/p40 experiments (shown in blue stars) lie along the linear regression line in all cases.

However, it is clear from the distribution of transport values that higher leakage values

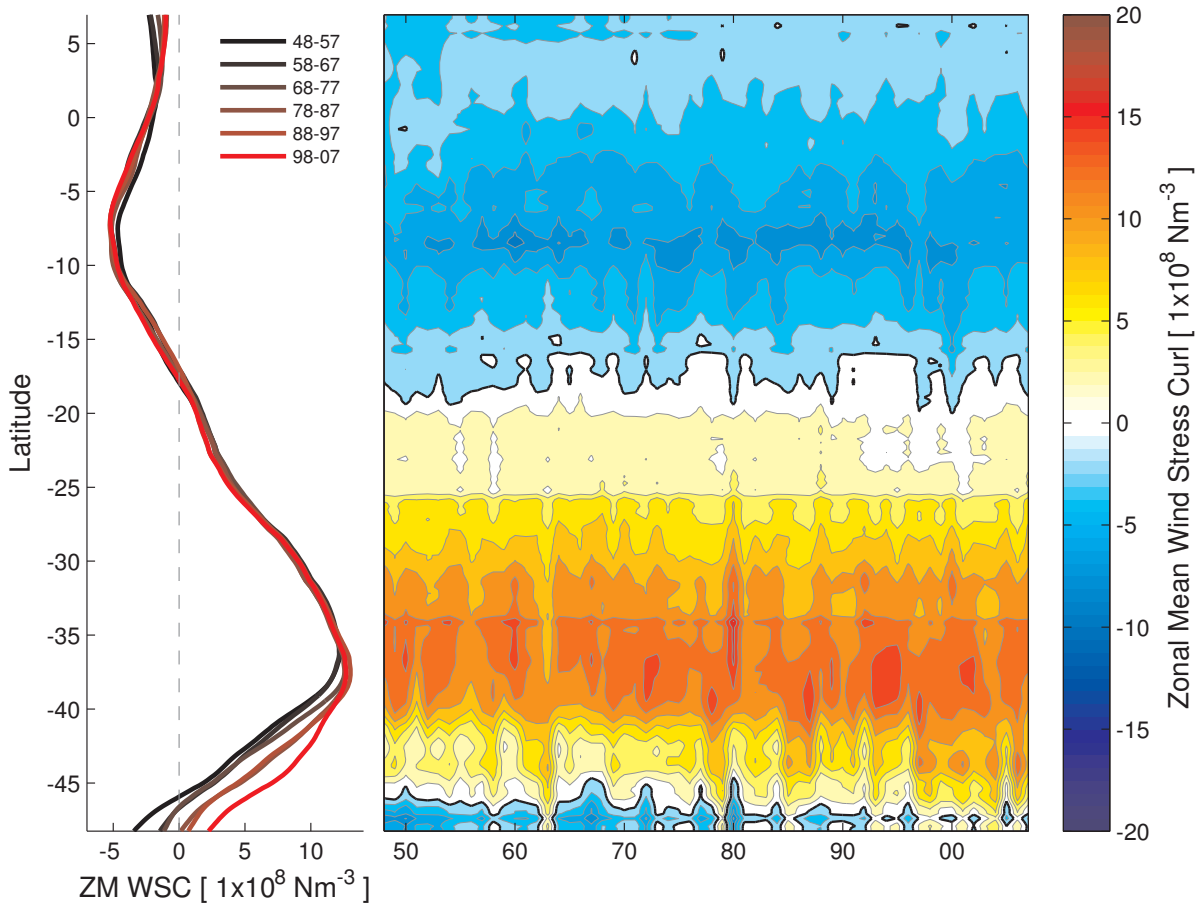

Figure 6.11: Left panel; Decadal change in zonally mean wind stress curl between 20°E and 115°E. Right panel; Hovmoller plot of the annual zonal mean wind stress curl. The southern zero line is shown in the heavy black contour between 48°S and 45°S. The Hovmoller plot is limited in the south by the extent of the AGIO model domain.

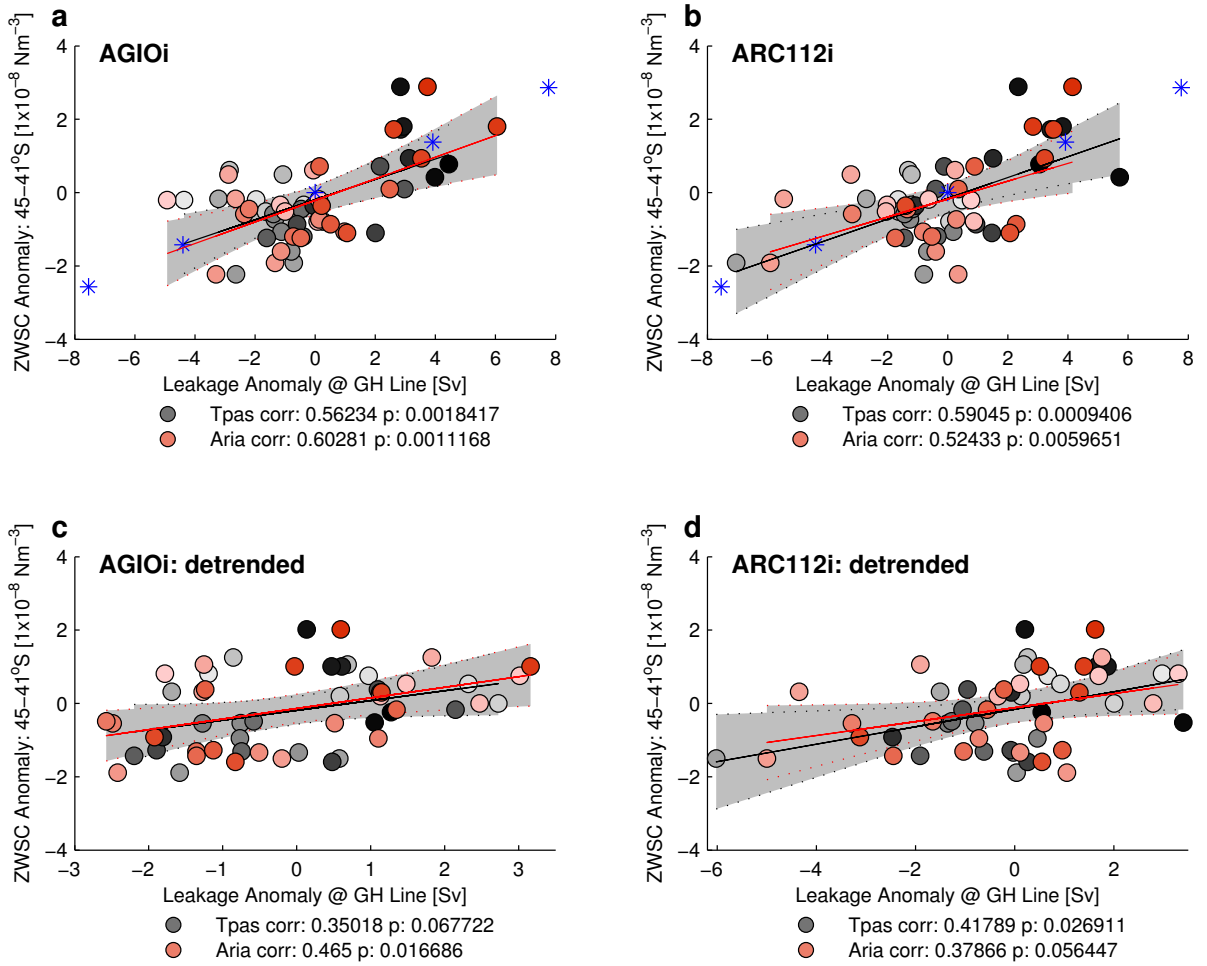

Figure 6.12: Correlations between time series of the Agulhas leakage anomaly (from the 1948-2007 mean) and the zonal mean wind stress curl between 41°S and 45°S for (a) AGIOi, (b) ARC112i, (c) detrended AGIOi time series and (d) detrended ARC112i time series. Grey-scale dots represent biannual Agulhas leakage values measured by Lagrangian floats. Red-scale dots represent biannual Agulhas leakage values measured by Eulerian passive tracer flux. Dot colour is scaled by time, with darker dots indicating values which occur later in the record. r and p values for the correlations are given below each plot (Tpas= Eulerian, Aria=Lagrangian). The linear regression line for each time series is given in the respective colour, surrounded by the shaded 95% confidence interval. The blue stars in panels *a* and *b* represent the Lagrangian Agulhas leakage and wind stress curl anomalies derived from the AGIO-SHWm40/p40 experiments (Table 6.1).

overwhelmingly occur later in the time series (darker grey and red colours indicate later time series value). To remove the low frequency bias, the same correlation is conducted on the detrended time series (panels *c* and *d*). While the correlations weaken, both AGIOi and ARC112i show a positive correlation between the westerly wind stress and Agulhas leakage magnitude that is significant at >93% in all cases, and at >98% in the Lagrangian determined leakage estimates in AGIOi (panel *c*). This suggests that the dynamical link between the westerly winds and Agulhas leakage does not solely arise due to the long term trend in the two signals, but is indicative of an dynamical interannual link between the two.

Conversely, when the same analysis is performed, but comparing the transport of the Agulhas

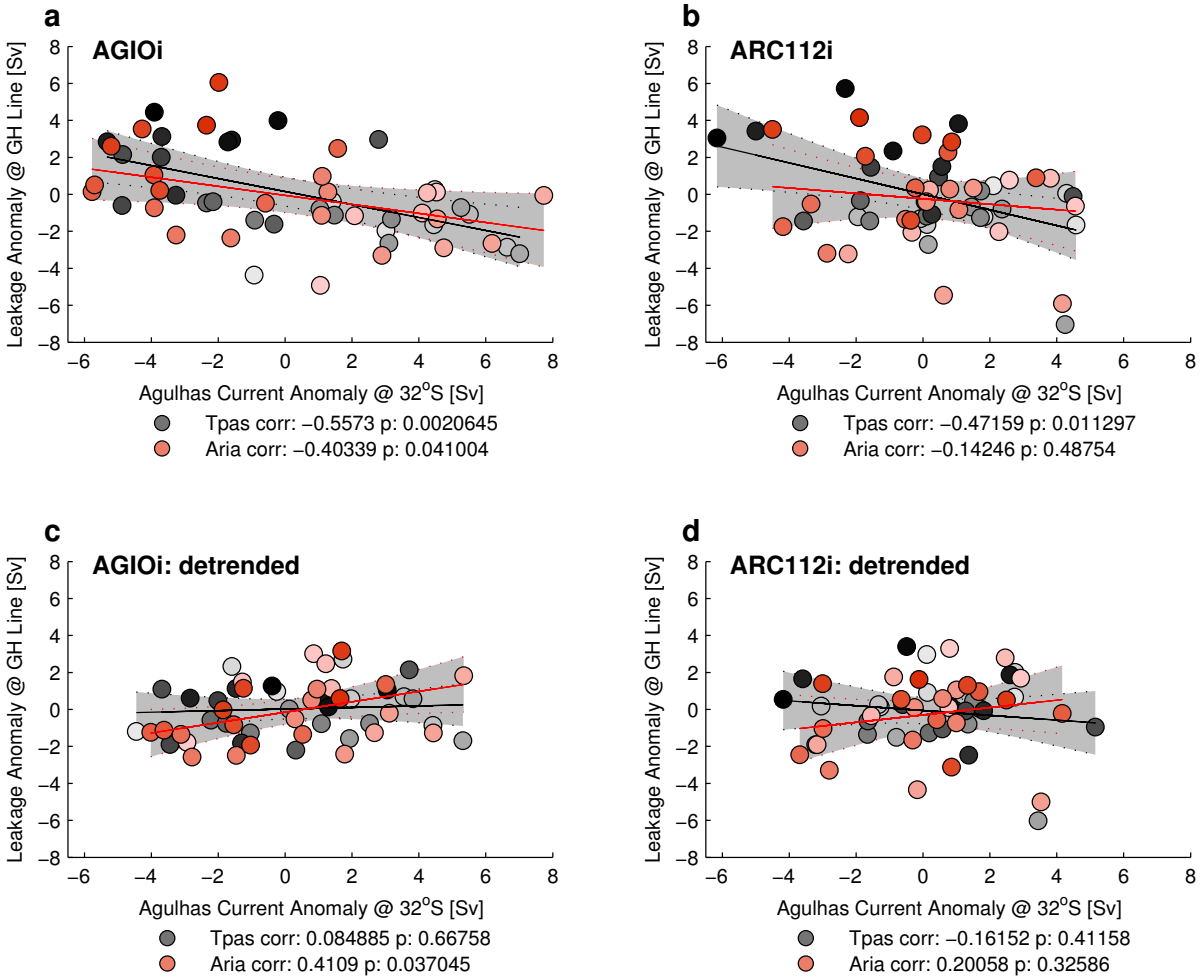

Figure 6.13: As in Fig .6.12 but for Agulhas Current transport anomaly versus Agulhas leakage anomaly.

Current with the Agulhas leakage (Fig. 6.13), it appears that the anti-correlation between the two (previously documented by van Sebille et al. (2009b)), is only present here as a result of the long term trends in the two signals. While both AGIOi (panel *a*) and ARC112i (panel b) show a statistically significant anti-correlation where the long term variability is included (excepting the ARC112i Lagrangian estimate), the former shows a small positive correlation between the two once the time-series is detrended (panel *c*) and ARC112i suggests that no correlation is present (panel *d*). These latter results are consistent with the findings of chapter 5 where Agulhas Current strength in AGIO was shown to positively influence the leakage, while in ARC112 the two appear to be largely decoupled.

6.5 Discussion

Palaeoceanographic studies suggest that changes in the latitude of the STF, driven by a shifting of the zero line of wind stress, may play a key role in determining the transition between glacial and interglacial states (Bard and Rickaby, 2009; Zahn et al., 2010; Caley et al., 2012). Under

this hypothesis, an equatorward shift in the zero line would 'choke' the Agulhas gateway due to the decreased distance between the STF and the African continent, reducing leakage during glacial periods (de Ruijter et al., 1999a). Here, the opposite response is seen. However, the state of the westerly winds during the Last Glacial Maximum (LGM: $\sim$ 17 kyr ago) is an issue of much debate. Modelling studies variously suggest an intensification and poleward shift in the southern hemisphere westerlies (Anderson et al., 2002; Wyroll et al., 2000), weakening winds with no shift (Rojas et al., 2009), and an equatorward shift (Toggweiler et al., 2006). Consequently, interpreting the results presented here under the conditions present at the Last Glacial Maximum is subject to a substantial degree of uncertainty.

Peeters et al. (2004) and Franzese et al. (2006) infer significant decreases in leakage during the LGM. This reduction may have been accompanied by an ACC that was stronger that than at present (Franzese et al., 2006; Otto-Bliesner et al., 2006), while the retroflection position most likely mirrors the modern day (Franzese et al., 2009). The results shown here suggest that reductions in the magnitude of the Agulhas leakage may be associated with one of three cases; (1) a poleward shift in the westerly winds, (2) a weakening of the westerly winds, or (3) a substantial increase in the transport of the ACC, driving a reduction in leakage through turbulent mixing between the return current and water masses south of the STF (Le Bars et al., 2012), possibly increasing the ventilation of the subtropical Indian Ocean gyre by water masses from the Southern Ocean (Simon et al., 2013).

It is crucial to note that, despite quantifying its position with multiple methods, none of the experiments express a substantial change in the latitude of the STF. Only the surface winds are changed during these experiments. All other surface fields, such as air temperature and precipitation remain at their reference values. While Graham et al. (2012) determined that the southern fronts of the ACC are strongly constrained by topography, they argue that the STF is predominantly wind controlled. In the experiments performed here it is clear that here the dynamical effect of the winds alone is not sufficient to modify its position, perhaps due to the constraints placed on the forcing. In addition, the timescales of the simulations presented here is too short to capture the indirect effects of the winds on processes such as deep and bottom water formations, which may in turn modify the positions of the frontal systems of the ACC (Downes et al., 2011; Spence et al., 2010; Graham et al., 2012). In contrast, Sijp and England (2008) performed sensitivity experiments in which a northward westerly shift was applied in a coupled model of intermediate complexity where air-sea heat and salt fluxes were free to evolve. The authors recorded an associated northward displacement in the STF in their simulation. However, substantial differences between the very coarse resolution model used by Sijp and England (2008) (a 3.6^{o} longitude by 1.8^{o} latitude grid) and those presented here make it difficult to compare the results directly given the likely very different representations of the western boundary system and Agulhas retroflection.

In the modern climate paradigm, two hindcasts by Rouault et al. (2009) and Biastoch et al. (2009b) assert that the Agulhas leakage has increased in recent decades, ascribing the signal to

changes in the southern hemisphere westerlies. In the latter case, the strengthening of the leakage is specifically ascribed to a poleward shift. Swart and Fyfe (2012) questioned the robustness of this shift in reanalysis and climate models, suggesting instead that the intensification of the winds is the dominant signal. The sensitivity analysis presented here suggests that a poleward migration of the zero line of wind stress curl would serve to reduce the leakage, while a strengthening of the winds would result in an increase. The multi-decadal increase in Agulhas leakage seen in the AGIOi and ARC112i (shown in Fig. 4.8 in chapter 4) shows an ∼25% increase in the leakage value post 1960, consistent with the increase in wind stress curl between 35°S and 48°S seen in the CORE v.2b reanalysis fields in the same period. The statistically significant linear relationship between the Agulhas leakage transport anomaly and zonal mean wind stress curl in the mid-latitude Indian Ocean in both AGIOi and ARC112i is consistent with the results of the SHWxxx sensitivity experiments (Fig. 6.12). Consequently, it seems that the recent trends in Agulhas leakage may be attributable to the ocean response to an ongoing strengthening of the westerly winds, where the ACC has not yet adjusted. Biastoch and Böning (2013) suggest that this trend is set to continue into the future. However, recovering stratospheric ozone (Son et al., 2010) may serve to reduce the intensification of the westerlies (Watson et al., 2012), possibly resulting in a reduced leakage toward the end of the 21st Century. This process may be additionally exacerbated by the adjustment of the ACC.

Recent hindcast analysis by van Sebille et al. (2009b) and Rouault et al. (2009) have linked the transport of the Agulhas Current to the leakage, noting a respective anti-correlation and correlation between the two transports. In chapter 5 it was shown that changes in the inertia of the Agulhas Current driven by trade wind variability has almost no effect on the Agulhas leakage providing that the grid-spacing is eddy-resolving. This left an open question as to how the leakage could be modified. The parallel set of experiments conducted in this chapter show that the leakage can respond strongly to changes in westerly wind intensification without a change in the western boundary transport at 32°S. Intensification of the subtropical gyre predominantly occurs south of 32° in this case, a consequence of the anomaly pattern imposed (Fig. 6.3). Consequently, western boundary transport increases south of 32°S through an intensification of the subgyre recirculation, and not through modification of the upstream source regions. In reality, it is unlikely that the trade and westerly winds will vary separately, leading to an array on non-linear responses in the greater Agulhas system. Together the findings of chapters 5 and 6 present ways in which the Agulhas Current transport and leakage can be modified with a high degree of independence, and present an explanation for the modern trends seen in the latter. These results do not exclude the findings of van Sebille et al. (2009b) or Rouault et al. (2009) but do minimise the importance of the statistical link between Agulhas Current transport and Agulhas leakage, reflected in the lack of a statistical link seen between the detrended biennial transports (Fig. 6.13).

6.6 Conclusions

The AGIO model is used to systematically test the response of the greater Agulhas system to independent idealised changes in the intensity and position of the southern hemisphere westerly winds. Changes in the intensity of the westerlies are found to have greatest impact on Agulhas leakage. Initially the leakage shows a linear response, increasing with intensified wind stress in a manner consistent with the change in Sverdrup transport across the southern branch of the supergyre. However, in the case of intensified winds, the large-scale adjustment of the ACC serves to reduce the leakage anomaly through increases in cross frontal mixing.

Counter to previous studies, poleward shifts in the zero line of wind stress curl are shown to induce an increase (decrease) in Agulhas leakage. This is due to the redistribution of momentum flux across the southern branch of the supergyre and an increase (decrease) in the wind stress curl equatorward (poleward) of the zero line. However, throughout the experiments, the dynamical effect of the imposed wind anomalies is insufficient to move the position of the STF. This raises concerns that the decadal timescale of the simulations and/or fixed air-sea fluxes may inhibit its poleward migration, potentially under-representing the role that it may play in determining the response of the system on glacial to interglacial timescales.

The results are compared to similar experiments performed with two global models, and are found to be consistent in response. Consequently, while resolution may play a primary role in determining the mean leakage value, it does not appear to determine the sensitivity to the leakage to changes in the basin-scale wind pattern. Further, the large-scale determination of the Agulhas leakage in this case suggests that the energetics of the retroflection may not play a significant role in determining the leakage, echoing the results of the previous chapter, where eddy-kinetic energy and leakage showed no relationship.

Multi-decadal changes in the Agulhas leakage expressed in the regional model hindcasts are analysed within the context of changes in the southern hemisphere westerly winds. It is determined that the recent $\sim$25% increase in leakage since 1960 is likely attributable to a $\sim$25% increase in positive wind stress curl over the Indian Ocean between 35^oS and 45^o, and not to the poleward migration of the zero line of wind stress curl (which, by this analysis would be associated with a leakage reduction). It is shown that modification of Agulhas leakage may occur through an intensification of the subgyre, and may not be reflected in transport changes in the Agulhas Current at 32^oS. As such, while the AGIOi and ARC112i hindcasts show statistically significant anti-correlations between transport of the Agulhas Current and leakage on long timescale, these relationships largely vanish once the time-series are detrended, This suggests that the leakage responds more strongly to the large-scale wind field than it does to local inertial processes.

Chapter 7

Final conclusions: Key findings and further research

This study was designed to address the following key questions, as presented in chapter 2:

- What is the structure and magnitude of the Agulhas leakage, and how has this changed in recent times? **(Chapter 4)**
- How do the source regions of the Agulhas Current respond to changes in the trade wind pattern across the Indian Ocean? **(Chapter 5)**
- How do these changes propagate downstream in the western boundary, and what is the effect on the Agulhas leakage? **(Chapter 5)**
- What effect do the westerly wind changes have on the Agulhas leakage? **(Chapter 6)**
- Can separation of the wind fields into the trade and westerly wind systems provide an insight into the interannual trends in the Agulhas Current and leakage? **(Chapter 6)**

Here, the work conducted in this thesis is summarised, culminating in a point-by-point address of these key questions and a discussion of the future application and expansion of this research.

7.1 Concluding summary

Two Regional Ocean Modelling System configurations, AGIO and ARC112, have been developed to determine the response of the greater Agulhas system to changes in the trade and westerly wind patterns of the South Indian Ocean and South Atlantic Ocean **(Chapter 2)**. The basin-scale responses have been investigated on interannual time scales and through a series of idealised climatological sensitivity experiments. The AGIO configuration captures the mesoscale variability of the greater Agulhas system, including the source regions, at eddy-permitting resolution. ARC112 builds on this capability through the deployment of an eddy-resolving nest that spans the Southern Agulhas Current, retroflection and Cape Basin.

The performance of the two configurations has been extensively assessed through comparisons with observed tracer field distributions, altimetry, *in situ* measurements, comparison with oceanographic reanalysis products and time series of Indian Ocean climatic modes **(Chapter 3)**. The simulated Indian Ocean and Atlantic Ocean water mass properties are shown to be consistent with those present in the WOA05 climatology. However, AGIO and ARC112 are limited in their ability to accurately simulate the distribution of these water mass properties, especially in regions of high turbulence. These deviations are variously attributable to the lack of a river run-off scheme, inherited bias from the ORCA05 boundary conditions, the cumulative effects of residual errors in diffusion, which are more severe in larger domains, and possible inaccuracy in the WOA05 fields at the western boundary. Interannually, AGIO and ARC112 express sea-surface temperature anomalies consistent with the Tropical and Subtropical Indian Ocean dipole modes, reflecting favourably on the performance of the bulk formulation in translating the forcing fields into the surface ocean. Comparison of tropical cyclone heat potential in ARC112 with SODA and estimates derived from ARGO floats and the XBT record confirms that the basin-scale configurations appropriately simulate interannual thermal signals in the thermocline.

Simulated mean SSH for the 1992-2007 period compares well with AVISO absolute dynamic topography, implying that the basin-scale circulation in AGIO and ARC112 is well approximated. However, while the Agulhas Current transport compares well with published flux estimates at 32^oS, transport from the upstream source regions is shown to be higher than that observed, while contributions derived from subgyre recirculation are smaller. The magnitude and pattern of simulated mean and EKE across the upstream Agulhas are consistent with that derived from altimetry, reflecting an eddy dominated Mozambique Channel, dipole formation in the SEMC and coherent mean flow at the western boundary. Despite being inertially governed, the mean retroflection position in both AGIO and ARC112 is further west than expected, though less so in the latter, where higher resolution improves the representation of topography. Both configurations express circulation and EKE pattern that are similar to that derived from altimetry at the retroflection, producing Agulhas rings and avoiding spurious systemic upstream recirculations. However, the imposition of the high-resolution nest in ARC112 results in a substantial improvement in the representation of the Agulhas leakage. Passive tracer based Eulerian leakage estimates fall from a mean value of 27.6 Sv in the AGIOi hindcast to 18.9 Sv in ARC112i. The latter value is more comparable with results implied from observed Lagrangian drifters. In addition, ARC112 mirrors the observed EKE and MKE trends seen between 1992 and 2007.

Multi-decadal changes in the structure and magnitude of the Agulhas leakage are investigated using complementary Eulerian and Lagrangian approaches. Eulerian techniques are based on the imposition of a passive tracer that explicitly labels Indian Ocean waters. Lagrangian fluxes are determined using the ARIANE package. Comparison with passive tracer based leakage estimates shows that the Eulerian fluxes based on water mass criteria are likely to underestimate leakage by up to 50%. While annual Lagrangian and passive tracer-based Eulerian leakage fluxes are consistent at high-resolution (e.g. in ARC112), the overly westward retroflection position in

AGIO produces a discrepancy between the two. The leakage is predominantly confined to the top 1500 m. Separation of the vorticity and non-vorticity governed components through an Okubo-Weiss parameterisation shows that, at the GoodHope Line, only 30% of the exported Indian Ocean waters are contained within eddies. Of this, there is a 2:1 ratio of transport in anti-cyclones and cyclones. In total, this flux of Indian Ocean waters makes up $\backsim$50% of the thermocline waters on the Cape Basin, which are well mixed across the region, with the remaining waters of Atlantic origin. The Agulhas Current and leakage exhibit a substantial degree of interannual and decadal variability. In the last 50 years, the former shows a long-term decrease in transport, while the latter shows a strengthening. The dominant flux increase arises through the non-eddy flow components. Multi-decadal increases in the eddying component are much weaker, especially for anticyclones.

Using an eddy detection and tracking scheme, based on a hybrid-criteria that combines the use of the Okubo-Weiss parameter and closed SSH loops, the trajectories and specifics of simulated Agulhas Rings and cyclones are compared with altimetry. The ARC112i hindcast is able to reproduce eddies in all three of the recently observed paths across the Cape Basin. The trajectories, number, radii of anti-cyclones and cyclones in these three paths are reproduced with a high degree of fidelity, though the central path is under-represented and eddy speeds show a 25% positive bias in eddy speed, which is partially attributable to differences in the sampling timebase. The small multi-decadal increase in the magnitude of the eddy component of the Agulhas leakage is attributed to an increase in Agulhas Ring speed over time and a progressive increase in the size of cyclones in the Cape Basin.

The sensitivity of the greater Agulhas system to changes in the magnitude of the Indian Ocean trade winds is assessed through the imposition of a series of idealised wind stress anomalies. Transports in the MZC and SEMC increase linearly with wind stress. In the former case this is associated with increased mesoscale variability associated with MZC eddies. In the latter, increased westward flux in the SEMC reduces the contributions to the SICC, increasing EKE between the SEMC and Africa, and reducing it offshore and to the east. While the Agulhas Current at 32^o is shown to vary linearly with changes in wind-stress, the transport anomaly is less than that expected through the Sverdrup relationship. Here, it is demonstrated that these transport anomalies persist southward due to western boundary inertia, reaching the retroflection. However, despite substantial changes in Agulhas Current transport of up to 20 Sv, there is only a substantial change in the leakage at coarse and eddy-permitting resolution. In the eddy resolving case, the leakage shows almost no sensitivity to western boundary inertia, a result that is confirmed in a global model under similar conditions. The retroflection position is shown to vary little in this case, and the western boundary transport anomaly is reflected in increased transport in the Agulhas Return Current and across the subtropical front. The decoupling between the transport of the Agulhas Current and magnitude of the leakage suggests that there is not a strong dynamical link between the two. Further, large changes in EKE during these experiments suggest that it may not be a suitable proxy for leakage.

In a final set of sensitivity studies, the sensitivity of the greater Agulhas system to changes in the westerly winds is considered. Under these conditions, the leakage shows a linear response to changes in westerly wind intensity, which arises due to modification of the southern branch of the supergyre and increased equatorward Sverdrup transport that augments the local recirculation in the subgyre. It is demonstrated that these changes may occur without substantial modification of the Agulhas Current at 32^{o}S. Independent modification of the current and leakage through the trade and westerly winds, respectively, implies that the trends seen in the AGIOi and ARC112i hindcast, as well as in other recent modelling studies, can be ascribed to the long-term changes in the appropriate wind belt. Under this interpretation, correlations (or anti-correlations) between Agulhas Current transport and Agulhas leakage magnitude may be present, but do not represent an exploitable link between the two.

Further sensitivity experiments, where the influence of the ACC is considered, suggest that more vigorous flow south of the subtropical front may reduce the leakage via an increase in cross frontal mixing between the frontal system and the return current. Latterly, in chapter 6, an investigation of the response of the Agulhas system to a northward migration of the zero line of wind stress curl resulted in an increase in leakage, due to a redistribution of wind energy and momentum flux to north of the zero line of wind stress curl. No concomitant shift in the subtropical front was seen in these simulations, suggesting that longer term thermohaline forcing may play a role in determining its position. This suggests that a previously held palaeoclimatic hypothesis, that, at the Last Glacial Maximum, an equatorward migration of the westerly winds may concomitantly result in an associated equatorward shift in the subtropical front and a reduction in Agulhas leakage (Bard and Rickaby, 2009; Zahn et al., 2010), may need revisiting.

7.2 Key Findings

The key results of this work are laid-out below in a point-by-point address of the main questions;

Chapter 4: What is the structure and magnitude of the Agulhas leakage, and how has this changed in recent times?

Within the context of an eddy-resolving hindcast, the Agulhas leakage is shown to have a mean transport of 18.9 Sv at the GoodHope line, and in the Cape Basin is predominantly confined to the top 1500 m where Indian Ocean water masses comprise up to 50% of the thermocline water. Division of the leakage into non-eddy, eddy and coastal fluxes yields respective contributions of 60%, 30% and 10%, with the eddy component split between anticyclonic and cyclonic contributions at a ratio of 2:1. Agulhas Rings and cyclones, captured in all three observed trajectory paths through an eddy tracking scheme, are shown to contribute to a multidecadal increase in Agulhas leakage through respective increases in speed and size. However, the dominant contributor to the strengthening leakage is through non-eddy flux.

Chapter 5: How do the source regions of the Agulhas Current respond to changes in the trade wind pattern across the Indian Ocean?

Changes in wind stress curl, driven by an intensification or reduction of the trade winds produce a linear response in the transports in the Mozambique Channel and in the South East Madagascar Current. In the channel, these changes are associated with increases in eddy flux and higher mesoscale variability. East of Madagascar, the link between the South East Madagascar Current and South Indian Counter Current weakens as winds intensify and the former becomes stronger. Consequently, the mean flow and mesoscale variability between the island and the African coast increases under intensified winds, while the SICC becomes weaker and more stable. The opposite situation occurs under weakened winds.

Chapter 5: How do these changes propagate downstream in the western boundary, and what is the effect on the Agulhas leakage?

The Agulhas Current responds linearly to changes in trade wind stress, but the response is less than expected by Sverdrup dynamics due to eddy-mean interaction the western boundary and the inclusion of ITF water masses. Increased advection is compensated for by vortex stretching between 28^oS and 30^oS. Due to inertia, transport anomalies in the western boundary persist to the retroflection, despite no direct wind forcing anomaly being applied here. Modification of the upstream transport of the Agulhas Current at 32^oS has no effect on the magnitude of the Agulhas leakage at eddy-resolving resolution. Agulhas Current transport anomalies are reflected in the downstream transport in the return current and across the subtropical front.

Chapter 6: What effect do the westerly wind changes have on the Agulhas leakage?

Intensified westerly winds produce an intensification of the southern branch of the supergyre, and an increase in equatorward Sverdrup transport in the Indian Ocean. The resulting increase in subgyre recirculation and, through continuity, modification of the northern branch of the supergyre drives in a linear increase in the Agulhas leakage, determined at the basin scale. The Agulhas Current is not necessarily affected. Secondarily, adjustment off the ACC to increases in westerly wind intensity reduces the magnitude of the leakage anomaly, due to increased cross frontal mixing in the return current. Northward shifts in the zero line of wind stress curl redistribute the momentum flux of the wind, increasing the maximum curl value to the north, and driving an increase in leakage. This is in contrast to a previously proposed palaeoceanographic mechanism under which a reduction of leakage occurs during a northward shift of the winds at the Last Glacial Maximum (Bard and Rickaby, 2009; Zahn et al., 2010).

Chapter 6: Can separation of the wind fields into the trade and westerly wind systems provide an insight into the interannual trends in the Agulhas Current and leakage?

The Agulhas Current responds strongly to changes in trade wind stress, with no consequences for the leakage. The leakage responds strongly to changes in the westerly winds, without necessarily affecting the Agulhas Current. Provided the ACC does not fully adjust, recent changes in the leakage may be attributable to recently observed intensification of the westerly winds, irrespective of the changes in the volume transport of the Agulhas Current. Consequently, differing multidecadal trends in the Agulhas transport at 32^o, reported in recent hindcasts (Biastoch et al., 2009b; Rouault et al., 2009), may arise due to differing trends in the strength of trade winds, but are unrelated to the Agulhas leakage.

7.3 Further research

While ARC112 and AGIO satisfactorily simulate the greater Agulhas system, producing and expanding upon a set of results that are consistent with global models, there is substantial scope for improvement and a number of ways in which these results can be expanded.

There are two specific ways in which the current AGIO/ARC112 configurations can be improved. Firstly, to address the current issues with the distribution of tracer properties it would be advantageous to repeat the hindcast simulation using boundary conditions drawn from SODA, and to include the most recent developments in ROMS v.3, which include an improved implementation of the rotated diffusion operator along iso-neutral surfaces. Ideally, this would allow for better constraint of the tracer values at the boundary, and improve the conservation of these properties within the domain. The incorporation of a river run off scheme may also serve to improve the representation of the tropical East Atlantic and the Mozambique Channel through the addition of, for example, the Congo River and Zambezi River, amongst others. Secondly, the latter may also be improved by extending the western boundary of the domain to South America, allowing the tropical Atlantic to be fully realised as well as capturing the full Indo-Atlantic branch of the supergyre.

While the ring tracking programme used here has been proven effective at identifying and following the surface expression of anticyclones and cyclones in the Cape Basin it does not allow for a quantitative analysis of the flux of Indian Ocean waters out of Agulhas Rings. Expanding the ring tracking method to determine of coherent features in the vertical, possibly via the combined use of an Okubo-Weiss parameter and closed loops of steric height, may allow for a fuller representation of the eddy field. Subsequent comparison of this field with the distribution of the Indian Ocean passive tracer would facilitate a better understanding of the mixing processes that define that define the hydrography of the Cape Basin. The approach was previously considered by de Steur (2004), but only with single idealised eddies, and is worth

extrapolating further.

To encapsulate a wider range of potential palaeoclimatic scenarios, it may be useful to extend to sensitivity analysis to include more extreme states. Of greatest interest would be incremental northward shifts in the zero line of wind stress curl to isolate whether a severing of the supergyre through the dynamic effects of the winds is possible, and, if so, under what conditions. In addition, it would perhaps be interesting to compare the current climatological results with regionally simulations forced with boundary conditions derived from simulations of the Last Glacial Maximum, such as those produced by the Palaeoclimate Model Intercomparison Project (PMIP).

Cross-frontal mixing in the retroflection region is determined from the flux of Lagrangian virtual floats across the nominal STF_L section. However, this may prove limiting in two respects. Firstly, mixing may occur over the entire extent of the return current and here the eastern boundary of the Lagrangian control domain is placed at 35^oE. Secondly, the static STF_L transect does not accurately represent the meanders in the front, nor its spatial and temporal evolution. As the passive tracer is initialised at 70^oE, it also cannot be used to quantify the southward flux of Indian Ocean waters east of this point. Accurate quantification with passive tracers may be a viable option, but will require future a re-initialisation of tracers which label Indian Ocean and Southern Ocean waters and a more expansive representation of the ACC.

Extending this idea further, the role of the ACC in determining the magnitude of the leakage remains something of an open question. Although recent studies such as the ones made by Le Bars et al. (2012) and Durgadoo et al. (2013) have identified conditions under which cross frontal mixing may become substantial, the focus tends toward responses to changes in westerly wind stress. Specific focus on processes that govern the interface between the Agulhas Return Current and the ACC, via the subtropical front may be essential in determining the response of the leakage on palaeoclimatic timescales.

References

Alory, G., Wijffels, S., and Meyers, G. (2007). Observed temperature trends in the Indian Ocean over 1960–1999 and associated mechanisms. *Geophys. Res. Lett.*, 34(2):L02606.

Anderson, R., Chase, Z., Fleisher, M., and Sachs, J. (2002). The Southern Ocean's biological pump during the Last Glacial Maximum. *Deep Sea Res. Part II*, 49:1909–1938.

Antonov, J., Seidov, D., Boyer, T., Locarnini, R., Mishonov, A., Garcia, H., Baranova, O., Zweng, M., and Johnson, D. R. (2010). World Ocean Atlas 2009, Volume 2: Salinity. *Ed. NOAA Atlas NESDIS 69, U.S. Government Printing Office, Washington, D.C.*, page 184.

Arakawa, A. and Lamb, V. (1977). Computational design of the basic dynamical process of the UCLA general circulation model. *Methods in Computational Physics*, 17:173–265.

Arhan, M., Mercier, H., and Lutjeharms, J. R. E. (1999). The disparate evolution of three Agulhas rings in the South Atlantic Ocean. *J. Geophys. Res. Oceans*, 104(C9):20987–21005.

Ashok, K., Guan, Z., and Yamagata, T. (2001). Impact of the Indian Ocean dipole on the relationship between the Indian monsoon rainfall and ENSO. *Geophys. Res. Lett.*, 28(23):4499–4502.

Backeberg, B. (2010). Modelling the mesoscale variability in the greater Agulhas Current system using a Hybrid Coordinate Ocean Model. *Ph.D. thesis, University of Cape Town.*

Backeberg, B. C., Bertino, L., and Johannessen, J. (2009). Evaluating two numerical advection schemes in HYCOM for eddy-resolving modelling of the Agulhas Current. *Ocean Sci.*, 5:173–190.

Backeberg, B. C., Penven, P., and Rouault, M. (2012). Impact of intensified Indian Ocean winds on mesoscale variability in the Agulhas system. *Nature Clim. Change*, 2:1–5.

Backeberg, B. C. and Reason, C. J. C. (2010). A connection between the South Equatorial Current north of Madagascar and Mozambique Channel Eddies. *Geophys. Res. Lett.*, 37:L04604.

Bader, J. (2003). The impact of decadal-scale Indian Ocean sea surface temperature anomalies on Sahelian rainfall and the North Atlantic Oscillation. *Geophys. Res. Lett.*, 30(22):2169.

Baker-Yeboah, S., Flierl, G., Sutyrin, G., and Zhang, Y. (2010). Transformation of an Agulhas eddy near the continental slope. *Ocean Sci.*, 6:143–159.

Bang, N. (1970). Major eddies and frontal structures in the Agulhas Current retroflexion area in March, 1969. *Symposium "Oceanography South Africa 1970", South African National Committee for Oceanographic Research*, page 16.

Bang, N. and Andrews, W. (1974). Direct current measurements of a shelf-edge frontal jet in the southern Benguela system. *J. Mar. Res.*, 32:405–417.

Bard, E. and Rickaby, R. (2009). Migration of the subtropical front as a modulator of glacial climate. *Nature*, 460:380–383.

Barnett, T. P., D.W.Pierce, AchutaRao, K., Gleckler, P., Santer, B., J.M.Gregory, and Washington, W. (2005). Penetration of human-induced warming into the world's oceans. *Science*, 309:284–287.

Barnett, T. P., Pierce, D. W., and Schnur, R. (2001). Detection of anthropogenic climate change in the world's oceans. *Science*, 292:270.

Barnier, B., Madec, G., Penduff, T., Molines, J.-M., Treguier, A., Le Sommer, J., Beckmann, A., Biastoch, A., Boning, C. W., Denng, J., Derval, C., Durand, E., Gulev, S., Remy, E., Talandier, C., Theetten, S., Maltrud, M., McClean, J., and de Cuervas, B. (2006). Impact of partial steps and momentum advection schemes in a global ocean circulation model at eddy-permitting resolution. *Ocean Dynamics*, 56(5-6):543–567.

Beal, L. M. and Bryden, H. (1997). Observations of an Agulhas undercurrent. *Deep Sea Res. Part I*, 44(9-10):1715–1724.

Beal, L. M. and Bryden, H. L. (1999). The velocity and vorticity structure of the Agulhas Current at 32 °S. *J. Geophys. Res.*, 104(C3):5151–5176.

Beal, L. M., Chereskin, T. K., Lenn, Y. D., and Elipot, S. (2006). The Sources and Mixing Characteristics of the Agulhas Current. *J. Phys. Oceanogr.*, 36:2060–2074.

Beal, L. M., Cipollini, P., and Lutjeharms, J. (2009). ACT: Towards a multi-decadal index of Agulhas Current transport. *Proceedings of OceanObs'09*, pages 1–3.

Beal, L. M., de Ruijter, W., Biastoch, A., Zahn, R., and 136, S. W. G. (2011). On the role of the Agulhas system in ocean circulation and climate. *Nature*, 472(7344):429–36.

Beal, L. M., Field, A., and Gordon, A. L. (2000). Spreading of Red Sea overflow waters in the Indian Ocean. *J. Geophys. Res.*, 105:8549–8564.

Behera, S. and Yamagata, T. (2001). Subtropical SST dipole events in the southern Indian Ocean. *Geophys. Res. Lett.*, 28(2):327–330.

Belkin, I. and Gordon, A. (1996). Southern Ocean fronts from the Greenwich meridian to Tasmania. *J. Geophys. Res.*, 101:3675–3696.

Biastoch, A., Beal, L., Lutjeharms, J., and Casal, T. (2009a). Variability and coherence of the Agulhas Undercurrent in a high-resolution ocean general circulation model. *J. Phys. Oceanogr.*, 39(10):2417–2435.

Biastoch, A. and Böning, C. (2013). Anthropogenic impact on Agulhas leakage. *Geophys. Res. Lett.*, 40:1138–1143.

Biastoch, A., Böning, C., Getzlaff, J., Molines, J.-M., and Madec, G. (2008a). Causes of interannual-decadal variability in the meridional overturning circulation of the mid-latitude North Atlantic Ocean. *J. Climate*, 21:6599–6615.

Biastoch, A., Böning, C., and Lutjeharms, J. (2008b). Agulhas leakage dynamics affects decadal variability in Atlantic overturning circulation. *Nature*, 456(7221):489–492.

Biastoch, A., Böning, C., Schwarzkopf, F. U., and Lutjeharms, J. (2009b). Increase in Agulhas leakage due to poleward shift of Southern Hemisphere westerlies. *Nature*, 462(7272):495–498.

Biastoch, A. and Krauss, W. (1999). The role of mesoscale eddies in the source regions of the Agulhas Current. *J. Phys. Oceanogr.*, 29:2303–2317.

Biastoch, A., Lutjeharms, J., Böning, C., and Scheinert, M. (2008c). Mesoscale perturbations control inter-ocean exchange south of Africa. *Geophys. Res. Lett.*, 35(20):L20602.

Biastoch, A., Reason, C. J. C., Lutjeharms, J., and Boebel, O. (1999). The importance of flow in the Mozambique Channel to seasonality in the greater Agulhas Current system. *Geophys. Res. Lett.*, 26(21):3321–3324.

Blanke, B. and Raynaud, S. (1997). Kinematics of the Pacific Equatorial Undercurrent: An Eulerian and Lagrangian approach from GCM results. *J. Phys. Oceanogr.*, 27:1038–1053.

Blunier, T., Chappellaz, J., Schwander, J., Dällenbach, A., Stauffer, B., Stocker, T. F., Raynaud, D., Jouzel, J., Clausen, H. B., Hammer, C. U., and Johnsen, S. J. (1998). Asynchrony of Antarctic and Greenland climate change during the last glacial period. *Nature*, 394:739–743.

Boebel, O., Lutjeharms, J., Schmid, C., Zenk, W., Rossby, T., and Barron, C. (2003a). The Cape Cauldron: a regime of turbulent inter-ocean exchange. *Deep Sea Res. Part II*, 50:57–86.

Boebel, O., Rossby, T., Lutjeharms, J., Zenk, W., and Barron, C. (2003b). Path and variability of the Agulhas Return Current. *Deep Sea Res. Part II*, 50(1):35–56.

Boudra, D. and Chassignet, E. (1988). Dynamics of Agulhas retroflection and ring formation in a numerical model. Part I: The vorticity balance. *J. Phys. Oceanogr.*, 18:280–303.

Boudra, D. and de Ruijter, W. (1986). The wind-driven circulation of the South Atlantic-Indian Ocean—II. Experiments using a multi-layer numerical model. *Deep Sea Res. Part I*, 33(4):447–483.

Bryden, H. and Beal, L. (2001). Role of the Agulhas Current in Indian Ocean circulation and associated heat and freshwater fluxes. *Deep Sea Res. Part I*, 48(8):1821–1845.

Bryden, H., Beal, L., and Duncan, L. (2005). Structure and transport of the Agulhas Current and its temporal variability. *J. Oceanogr.*, 61:479–492.

Byrne, D., Gordon, A., and Haxby, W. (1995). Agulhas Eddies: a synoptic view using Geosat ERM data. *J. Phys. Oceanogr.*, 25:902–917.

Cai, W. (2006). Antarctic ozone depletion causes an intensification of the Southern Ocean super-gyre circulation. *Geophys. Res. Lett.*, 33(3):L03712.

Caley, T., Giraudeau, J., Malaize, B., Rossignol, L., and Pierre, C. (2012). Agulhas leakage as a key process in the modes of Quaternary climate changes. *P Natl Acad Sci Usa*, 109(18):6835–6839.

Carton, J. and Giese, B. (2008). A reanalysis of ocean climate using Simple Ocean Data Assimilation (SODA). *Mon. Weather Rev.*, 136(8):2999–3017.

Chapman, P., Marco, S., Davis, R., and Coward, A. (2003). Flow at intermediate depths around Madagascar based on ALACE float trajectories. *Deep Sea Res. Part II*, 50:1957–1986.

Chassignet, E. and Boudra, D. (1988). Dynamics of Agulhas retroflection and ring formation in a numerical model. Part II: Energetics and ring formation. *J. Phys. Oceanogr.*, 18:304–319.

Chassignet, E. and Garraffo, Z. (2001). Viscosity parameterization and the Gulf Stream separation. *Proceedings 'Aha Huliko'a Hawaiian Winter Workshop. U. of Hawaii. January*, pages 39–43.

Chelton, D., Schlax, M., and Samelson, R. (2011). Global observations of nonlinear mesoscale eddies. *Prog. Oceanogr.*, 91:167–216.

Chelton, D., Schlax, M., Samelson, R., and Szoeke, R. (2007). Global Observations of large oceanic eddies. *Geophys. Res. Lett.*, 34:L15606.

Chelton, D., Szoeke, A., Schlax, M., Naggar, K., and Siwertz, N. (1998). Geographical variability of the first-baroclinic Rossby radius of deformation. *J. Phys. Oceanogr.*, 28:433–460.

Davis, R. E. (2005). Intermediate-Depth Circulation of the Indian and South Pacific Oceans Measured by Autonomous Floats. *J. Phys. Oceanogr.*, 35:683–707.

de Ruijter, W. (1982). Asymptotic analysis of the Agulhas and Brazil Current systems. *J. Phys. Oceanogr.*, 12:361–373.

de Ruijter, W., Aken, H., Beier, E., Lutjeharms, J., Matano, R., and Schouten, M. (2004). Eddies and dipoles around South Madagascar: formation, pathways and large-scale impact. *Deep Sea Res. Part I*, 51:383–400.

de Ruijter, W., Biastoch, A., Drijfhout, S., Lutjeharms, J., Matano, R., Pichevin, T., van Leeuwen, P., and Weijer, W. (1999a). Indian-Atlantic interocean exchange: Dynamics, estimation and impact. *J. Geophys. Res.*, 104(C9):20885.

de Ruijter, W. and Boudra, D. (1985). The wind-driven circulation in the South Atlantic-Indian Ocean—I. Numerical experiments in a one-layer model. *Deep Sea Res. Part I*, 32(5):557–574.

de Ruijter, W., Ridderinkhof, H., Lutjeharms, J., Schouten, M., and Veth, C. (2002). Observations of the flow in the Mozambique Channel. *Geophys. Res. Lett.*, 29(10):1502.

de Ruijter, W., Ridderinkhof, H., and Schouten, M. (2005). Variability of the southwest Indian Ocean. *Philosophical Transactions of the Royal Society A: Mathematical, Physical and Engineering Sciences*, 363(1826):63–76.

de Ruijter, W., van Leeuwen, P., and Lutjeharms, J. (1999b). Generation and evolution of Natal Pulses: Solitary meanders in the Agulhas Current. *J. Phys. Oceanogr.*, 29(12):3043–3055.

de Steur, L. (2004). Tracer Leakage from Modeled Agulhas Rings. *J. Phys. Oceanogr.*, 34:1387–1399.

Debreu, L., Marchesiello, P., Penven, P., and Cambon, G. (2012). Two-way nesting in split-explicit ocean models: Algorithms, implementation and validation. *Ocean Modell.*, 49:1–21.

Debreu, L., Vouland, C., and Blayo, E. (2008). AGRIF: Adaptive grid refinement in Fortran. *Comput. Geosci.*, 34:8–13.

Dencausse, G., Arhan, M., and Speich, S. (2010a). Routes of Agulhas rings in the southeastern Cape Basin. *Deep Sea Res. Part II*, 57:1406–1421.

Dencausse, G., Arhan, M., and Speich, S. (2010b). Spatio-temporal characteristics of the Agulhas Current retroflection. *Deep Sea Res. Part I*, 57:1392–1405.

Dencausse, G., Arhan, M., and Speich, S. (2011). Is there a continuous Subtropical Front south of Africa? *J. Geophys. Res.*, C02027:1–14.

Dijkstra, H. and de Ruijter, W. (2001). On the physics of the Agulhas Current: Steady retroflection regimes. *J. Phys. Oceanogr.*, 31(10):2971–2985.

DiMarco, S., Chapman, P., Nowlin Jr, W., Donohue, K., Luther, M., Johnson, G., and Toole, J. (2002). Volume transport and property distribution of the Mozambique Channel. *Deep Sea Res. Part II*, 49:1481–1511.

Doglioli, A., Veneziani, M., Blanke, B., Speich, S., and Griffa, A. (2006). A Lagrangian analysis of the Indian-Atlantic interocean exchange in a regional model. *Geophys. Res. Lett.*, 33(14):L14611.

Donners, J. and Drijfhout, S. (2004). The lagrangian view of South Atlantic interocean exchange in a global ocean model compared with inverse model results. *J. Phys. Oceanogr.*, 34:1019–1035.

Donners, J., Drijfhout, S., and Coward, A. (2004). Impact of cooling on the water mass exchange of Agulhas rings in a high resolution ocean model. *Geophys. Res. Lett.*, 31(16):L16312.

Donohue, K., Firing, E., and Beal, L. (2000). Comparison of three velocity sections of the Agulhas Current and Agulhas Undercurrent. *J. Geophys. Res.*, 185:28585–28593.

Donohue, K. and Toole, J. (2003). A near-synoptic survey of the Southwest Indian Ocean. *Deep Sea Res. Part II*, 50:1893–1931.

Downes, S., Budnick, S., Sarmiento, J., and Farneti, R. (2011). Impacts of wind stress on the Antarctic Circumpolar Current fronts and associated subduction. *Geophys. Res. Lett.*, 38:L11605.

Duncombe Rae, C. (1991). Agulhas retroflection rings in the South Atlantic Ocean; an overview. *S. Afr. J. Mar. Sci.*, 11:327–344.

Duncombe Rae, C., Garzoli, S., and Gordon, A. (1996). The eddy field of the southeast Atlantic Ocean: a statistical census from the Benguela Sources and Transport project. *J. Geophys. Res.*, 101:11949–11964.

Durgadoo, J. V., Loveday, B. R., Reason, C. J. C., Penven, P., and Biastoch, A. (2013). Agulhas leakage predominantly responds to the Southern Hemisphere Westerlies. *J. Phys. Oceanogr.*, 43:2113–2131.

Emery, W. J. (2001). Water Types and Water Masses. *Encyclopedia of Ocean Sciences*, 4:3179–3187.

Epica Community Members (2006). One-to-one coupling of glacial climate variability in Greenland and Antarctica. *Nature*, 444:195.

Fairall, C., Bradley, E., Rogers, D., and Edson, J. (1996). Bulk parameterization of air-sea fluxes for tropical ocean-global atmosphere coupled-ocean atmosphere response experiment. *J. Geophys. Res.*, 101(C2):3747–3764.

Fetter, A., Lutjeharms, J., and Matano, R. (2007). Atomspheric driving forces for the Agulhas Current in the subtropics. *Geophys. Res. Lett.*, 34(L15605):1–6.

Ffield, A., Toole, J., and Wilson, D. (1997). Seasonal circulation in the south Indian Ocean. *Geophys. Res. Lett.*, 24(22):2773–2776.

Fichefet, T. and Maqueda, M. (1997). Sensitivity of a global sea ice model to the treatment of ice thermodynamics and dynamics. *J. Geophys. Res.*, 102(C6):12609–12646.

Field, A. and Gordon, A. L. (1992). Vertical mixing in the Indonesian thermocline. *J. Phys. Oceanogr.*, 22:184–195.

Fine, R., Jr, W. S., Bullister, J., Rhein, M., Min, D., Warner, M., Poisson, A., and Weiss, R. (2008). Decadal ventilation and mixing of Indian Ocean waters. *Deep Sea Res. Part I*, 55(1):20–37.

Fine, R. A. (1993). Circulation of Antarctic Intermediate Water in the South Indian Ocean. *Deep Sea Res. Part I*, 40:2021–2042.

Franzese, A., Hemming, S., and Goldstein, S. (2009). Use of strontium isotopes in detrital sediments to constrain the glacial position of the Agulhas Retroflection. *Paleoceanography*, 24(2):PA2217.

Franzese, A., Hemming, S., Goldstein, S., and Anderson, R. (2006). Reduced Agulhas leakage during the Last Glacial Maximum inferred from an integrated provenance and flux study. *Earth and Planetary Science Letters*, 250(1-2):72–88.

Ganachaud, A. and Wunsch, C. (2000). Improved estimates of global ocean circulation, heat transport and mixing from hydrographic data. *Nature*, 408:453–457.

Ganopolski, A. and Rahmstorf, S. (2001). Rapid changes of glacial climate simulated in a coupled climate model. *Nature*, 409(6817):153–8.

Garzoli, S. (1999). Three Agulhas rings observed during the Benguela Current Experiment. *J. Geophys. Res.*, 104(C9):20971–20985.

Garzoli, S. and Goni, J. (2000). Combining altimeter observations and oceanographic data for ocean circulation and climate studies, in: Satellites, Oceanography and Society. *Elsevier Oceanography Series*, 63:79–97.

Garzoli, S., Gordon, A., Kamenovich, V., Pillsbury, D., and Duncombe-Rae, C. (1996). Variability and sources of the southeastern Atlantic circulation. *J. Mar. Res.*, 54:1039–1071.

Gillett, N. P. and Thompson, D. (2003). Simulation of recent Southern Hemisphere climate change. *Science*, 302:273–275.

Godfrey, J. (1989). A Sverdrup model of the depth-integrated flow for the world ocean, allowing for island circulation. *Geophys. Astro. Fluid*, 45:89–112.

Godfrey, J. (1996). The effect of the Indonesian throughflow on ocean circulation and heat exchange with the atmosphere: A review. *J. Geophys. Res.*, 101(C5):12217–12237.

Goni, G., Garzoli, S., Roubicek, A., Olson, D., and Brown, O. (1997). Agulhas ring dynamics from TOPEX/POSEIDON satellite altimeter data. *J. Mar. Res.*, 55:861–883.

Gordon, A. (1985). Indian–Atlantic transfer of thermocline water at the Agulhas retroflection. *Science*, 227:1030–1033.

Gordon, A. (1986). Interocean exchange of thermocline water. *J. Geophys. Res*, 91(C4):5037–5046.

Gordon, A., Bosley, K., and Aikman, F. (1995). Tropical Atlantic water within the Benguela upwelling system at 27 S. *Deep Sea Res. Part I*, 42(1):1–12.

Gordon, A. and Haxby, W. (1990). Agulhas eddies invade the South Atlantic: evidence from Geosat altimeter and shipboard CTD survey. *J. Geophys. Res.*, 93:3117–3125.

Gordon, A., Lutjeharms, J., and Grundlingh, M. L. (1987). Stratification and circulation at the Agulhas Retroflection. *Deep Sea Res.*, 34:565–589.

Gordon, A. and McClean, J. (1999). Thermohaline Stratification of the Indonesian Seas: Model and Observations. *J. Phys. Oceanogr.*, 29(2):198–216.

Gordon, A., Weiss, R., Jr Smethie, W., and Warner, M. (1992). Thermocline and Intermediate Water Communication Between the South Atlantic and Indian Oceans. *J. Geophys. Res.*, 97(C5):7223–7240.

Graham, R. M. and de Boer, A. M. (2013). The Dynamical Subtropical Front. *J. Geophys. Res. Oceans*, pages n/a–n/a.

Graham, R. M., de Boer, A. M., Heywood, K. J., Chapman, M. R., and Stevens, D. P. (2012). Southern Ocean fronts: Controlled by wind or topography? *J. Geophys. Res.*, 117(C8):C08018.

Gregory, J. M., Dixon, K. W., Stouffer, R. J., Weaver, A. J., Driesschaert, E., Eby, M., Fichefet, T., Hasumi, H., Hu, A., Jungclaus, J. H., Kamenkovich, I. V., Levermann, A., Montoya, M., Murakami, S., Nawrath, S., Oka, A., Sokolov, A. P., and Thorpe, R. B. (2005). A model intercomparison of changes in the Atlantic thermohaline circulation in response to increasing atmospheric CO2 concentration. *Geophys. Res. Lett.*, 32:L12703.

Grodsky, S. A., Carton, J. A., Nigam, S., and Okumura, Y. M. (2012). Tropical Atlantic Biases in CCSM4. *J. Climate*, 25:3684.

Grundlingh, M. (1979). Observation of a large meander in the Agulhas Current. *J. Geophys. Res.*, 84(C7):3776–3778.

Grundlingh, M. (1980). On the volume transport of the Agulhas Current. *Deep Sea Res.*, 27:557–563.

Grundlingh, M. L. (1983). On the Course of the Agulhas Current. *South African Geographical Journal*, 65:49–57.

Haidvogel, D. and Beckmann, A. (1999). Numerical ocean circulation modeling. *Ser. Environ. Sci. Manage*, 2:318.

Hall, C. and Lutjeharms, J. R. E. (2011). Cyclonic eddies identified in the Cape Basin of the South Atlantic Ocean. *J. Mar. Syst.*, 85(1-2):1–10.

Halo, I., Backeberg, B. C., Penven, P., Ansorge, I., Reason, C., and Ullgren, J. (2013). Eddy properties in the Mozambique Channel: A comparison between observations and two numerical ocean circulation models. *Deep Sea Res. Part II*, in press.

Han, W., Meehl, G. A., Rajagopalan, B., Fasullo, J. T., Hu, A., Lin, J., Large, W. G., wang Wang, J., Quan, X.-W., Trenary, L. L., Wallcraft, A., Shinoda, T., and Yeager, S. (2010). Patterns of Indian Ocean sea-level change in a warming climate. *Nature Geoscience*, 3(8):546–550.

Hanawa, K. and L.D.Talley (2001). Mode waters. Ocean Circulation and Climate: Observing and Modeling the Global Ocean. *International Geophysical Series; G. Siedler, J. Church, and J. Gould, Eds.*, 77:373–386.

Harris, T. F., Legeckis, R., and van Foreest, D. (1978). Satellite infra-red images in the Agulhas Current system. *Deep Sea Res.*, 25:543–548.

Hastenrath, S. and Greischar, L. (1991). The monsoonal current regimes of the tropical Indian Ocean: observed surface flow fields and their geostrophic and wind-driven components. *J. Geophys. Res.*, 96(C7):12619.

Hedström, K. S. (1997). User's Manual for an S-Coordinate Primitive Equation Ocean Circulation Model (SCRUM) Version 3.0. *Tech. rep., Institute of Marine and Coastal Sciences, Rutgers University, USA.*

Herbette, S., Morel, Y., and Arhan, M. (2002). Erosion of a Surface Vortex by a Seamount. *J. Phys. Oceanogr.*, 33:1664–1679.

Herbette, S., Morel, Y., and Arhan, M. (2004). Subduction of a Surface Vortex under an Outcropping Front. *J. Phys. Oceanogr.*, 34:1610–1627.

Hermes, J. and Reason, C. (2009). The sensitivity of the Seychelles-Chagos thermocline ridge to large-scale wind anomalies. *ICES Journal of Marine Science*, 66:1–12.

Isern-Fontanet, J., Garcia-Ladona, E., and Font, J. (2006). Vortices of the Mediterranean Sea: An Altimetric Perspective. *J. Phys. Oceanogr.*, 36:87–103.

Jacket, D. and MacDougall, T. (1995). Stabilization of hydrographic data. *J. Atmos. Sci.*, 12:381–389.

Jackett, D. and MacDougall, T. (1997). A Neutral Density Variable for the World's Oceans. *Amer. Met. Soc.*, 27:237–263.

Jacobs, S. and Georgi, D. (1977). Observations on the Southwest Indian/Antarctic Ocean. *Deep Sea Res.*, 24:43–84.

Josey, S., Kent, E., and Taylor, P. (2002). Wind stress forcing of the ocean in the SOC climatology: Comparisons with the NCEP-NCAR, ECMWF, UWM/COADS, and Hellerman and Rosenstein Datasets. *J. Phys. Oceanogr.*, 32:1993–2019.

Jury, M. and Huang, B. (2004). The Rossby wave as a key mechanism of Indian Ocean climate variability. *Deep Sea Res. Part I*, 51(12):2123–2136.

Jury, M. R., Valentine, H. R., and Lutjeharms, J. R. E. (1993). Influence of the Agulhas Current on Summer Rainfall along the Southeast Coast of South Africa. *Journal of Applied Meteorology*, 32:1282–1287.

Kalnay, E., Kanamitsu, M., Kistler, R., Collins, W., Deaven, D., Gandin, L., Iredell, M., Saha, S., White, G., and Woollen, J. (1996). The NCEP/NCAR 40-year reanalysis project. *Bulletin of the American Meteorological Society*, 77(3):437–471.

Kindle, J. (1991). Topographic effects on the seasonal circulation of the Indian Ocean. *J. Geophys. Res.*, 96(C9):16827–16837.

Knorr, G. and Lohmann, G. (2003). Southern Ocean origin for the resumption of Atlantic thermohaline circulation during deglaciation. *Nature*, 424:532–536.

Kohfeld, K. E., Graham, R. M., de Boer, A. M., Sime, L. C., Wolff, E. W., Quéré, C. L., and Bopp, L. (2013). Southern Hemisphere westerly wind changes during the Last Glacial Maximum: paleo-data synthesis. *Quaternary Science Reviews*, 68(C):76–95.

Krug, M. and Tournadre, J. (2012). Satellite observations of an annual cycle in the Agulhas Current. *Geophys. Res. Lett.*, 39(15):L15607.

Kwon, Y.-O., Alexander, M. A., Bond, N. A., Frankignoul, C., Nakamura, H., Qiu, B., and Thompson, L. A. (2010). Role of the Gulf Stream and Kuroshio-Oyashio Systems in Large-Scale Atmosphere-Ocean Interaction: A Review. *J. Climate*, 23:3249.

Large, W., McWilliams, J., and Doney, S. (1994). Oceanic vertical mixing: A review and a model with a nonlocal boundary layer parameterization. *Rev. Geophys.*, 32(4):363–403.

Large, W. and Yeager, S. (2004). Diurnal to decadal global forcing for oceans and sea-ice models: the data ses and flux climatologies. *NCAR Technical Note*, pages 1–112.

Large, W. and Yeager, S. (2009). The global climatology of an interannually varying air–sea flux data set. *Climate Dynamics*, 33:341–364.

Latif, M. and Barnett, T. (1995). Interactions of the tropical oceans. *J. Climate*, 8(4):952–964.

Le Bars, D., de Ruijter, W., and Dijkstra, H. A. (2012). A new regime of the Agulhas Current retroflection: turbulent choking of Indian-Atlantic leakage. *J. Phys. Oceanogr.*, 42:1158–1172.

Lee, S.-K., Park, W., van Sebille, E., Baringer, M. O., Wang, C., Enfield, D. B., Yeager, S. G., and Kirtman, B. P. (2011). What caused the significant increase in Atlantic Ocean heat content since the mid-20th century? *Geophys. Res. Lett.*, 38:17607.

Lee, T., Fukumori, I., Menemenlis, D., Xing, Z., and Fu, L. (2002). Effects of the Indonesian throughflow on the Pacific and Indian Oceans. *J. Phys. Oceanogr.*, 32(5):1404–1429.

Leipper, D. F. and Volgenau, D. (1972). Hurricane heat potential of the Gulf of Mexico. *J. Phys. Oceanogr.*, 2:218–224.

Levitus, S. and Boyer, T. (1994a). World Ocean Atlas 1994, Vol 3: Salinity. *NOAA Atlas NESDIS 3, U. S. Government Printing Office, Washington D.C.*, pages 1–93.

Levitus, S. and Boyer, T. (1994b). World Ocean Atlas 1994. Vol 4: Temperature. *NOAA Atlas NESDIS 4, U. S. Government Printing Office, Washington D.C.*, pages 1–117.

Levitus, S., J.I.Antonov, Boyer, T., Locarnini, R., H.E.Garcia, and A.V.Mishonov (2009). Global ocean heat content 1955–2008 in light of recently revealed instrumentation problems. *Geophys. Res. Lett.*, 36(L07608):1–5.

Levitus, S., J.I.Antonov, Wang, J., Delworth, T., K.W.Dixon, and Broccoli, A. (2001). Anthropogenic warming of Earth's climate system. *Science*, 292:267–270.

Li, L., Nowlin, W., and Jilan, S. (1998). Anticyclonic rings from the Kuroshio in the South China Sea. *Deep Sea Res. Part I*, 45:1469.

Locarnini, R., MIshonov, A., Antonov, J., Boyer, T., Garcia, H., Baranova, O., Zweng, M., and Johnson, D. R. (2010). World Ocean Atlas 2009, Volume 1: Temperature. *NOAA Atlas NESDIS 68, U.S. Government Printing Office, Washington, D.C.*, page 184.

Lutjeharms, J. (1981). Features of the southern Agulhas Current circulation from satellite remote sensing. *S. Afr. J. Sci.*, 77:231–236.

Lutjeharms, J. (1988a). On the role of the East Madagascar Current as a source of the Agulhas Current. *S. Afr. J. Mar. Sci.*, 84:236–238.

Lutjeharms, J. (1988b). Remote sensing corroboration of retroflection of the East Madagascar Current. *Deep Sea Res. Part I*, 35:2045–2050.

Lutjeharms, J. (2006a). The Agulhas Current. *Springer, Berlin*.

Lutjeharms, J. (2006b). Three decades of research on the greater Agulhas Current. *Ocean Science Discussions*, 3(4):939–995.

Lutjeharms, J. and Ansorge, I. (2001). The Agulhas return current. *J. Mar. Syst.*, 30(1-2):115–138.

Lutjeharms, J., Bang, N., and Duncan, C. (1981). Characteristics of the currents east and south of Madagascar. *Deep Sea Res. Part I*, 28(A):879–899.

Lutjeharms, J., Catzel, R., and Valentine, H. (1989). Eddies and other border phenomena of the Agulhas Current. *Continental Shelf Research*, 9:597–616.

Lutjeharms, J. and Cooper, J. (1996). Interbasin leakage through Agulhas Current filaments. *Deep Sea Res. Part I*, 43(2):213–215.

Lutjeharms, J. and Gordon, A. (1987). Shedding of an Agulhas ring observed at sea. *Nature*, 325:138–140.

Lutjeharms, J., Penven, P., and Roy, C. (2003). Modelling the shear edge eddies of the southern Agulhas Current. *Continental Shelf Research*, 23(11-13):1099–1115.

Lutjeharms, J. and Valentine, H. (1988). On mesoscale ocean eddies at the Agulhas Plateau. *S. Afr. J. Sci.*, 84:194–200.

Lutjeharms, J., Valentine, H., and Ballegooyen, R. (2000). The hydrography and water masses of the Natal Bight. *South African Cont. Shelf. Res.*, 20:1907–1939.

Lutjeharms, J. R. (2006c). The coastal oceans of south-eastern Africa. *The Sea, Chicago*, 14:783–834.

Lutjeharms, J. R. E. and Boebel, O. (2003). Agulhas cyclones. *Deep Sea Res. Part II*, 50:13–34.

Lutjeharms, J. R. E. and Roberts, H. R. (1988). The Natal Pulse: An extreme transient on the Agulhas Current. *J. Geophys. Res.*, 93:631–645.

Lutjeharms, J. R. E. and van Ballegooyen, R. (1988). The retroflection of the Agulhas Current. *J. Phys. Oceanogr.*, 18:1570–1583.

Macdonald, A. (1998). The global ocean circulation: A hydrographic estimate and regional analysis. *Prog. Oceanogr.*, 41(3):281–382.

Madec, G. (2008). NEMO ocean engine. *Note du Pole de modelisation, Institut Pierre Simon Laplace (IPSL), France.*

Malan, N., Reason, C. J. C., and Loveday, B. R. (2013). Variability in tropical cyclone heat potential over the Southwest Indian Ocean. *J. Geophys. Res. Oceans*, 118:1–13.

Maltrud, M. E. and McClean, J. L. (2005). An eddy resolving global 1/10 degree ocean simulation. *Ocean Modelling*, 8:31.

Mantalya, A. W. and Reid, J. L. (1995). On the origins of deep and bottom waters of the Indian Ocean. *J. Geophys. Res.*, 100:2417–2439.

Marchesiello, P., Barnier, B., and de Miranda, A. (1998). A sigma-coordinate primitive equation model for studying circulation in the south Atlantic, part i: meridional transports and seasonal variability. *Deep Sea Res. Part I*, 45:573–608.

Marchesiello, P., Debreu, L., and Couvelard, X. (2009). Spurious diapycnal mixing in terrain-following coordinate models: The problem and a solution. *Ocean Modell.*, 26(3-4):156–169.

Marchesiello, P., McWilliams, J., and Shchepetkin, A. (2001). Open boundary conditions for long-term integration of regional oceanic models. *Ocean Modell.*, 3(1-2):1–20.

Marshall, J. and Plumb, R. (2007). Atmosphere, Ocean and Climate Dynamics: An Introductory Text. *Academic Press*, page 334.

Matano, R. and Beier, E. (2003). A kinematic analysis of the Indian/Atlantic interocean exchange. *Deep Sea Res. Part II*, 50(1):229–249.

Matano, R., Simionato, C., and Strub, P. (1999). Modeling the wind-driven variability of the South Indian Ocean. *J. Phys. Oceanogr.*, 29(2):217–230.

Matano, R. P. (1996). A Numerical Study of the Agulhas Retroflection: The Role of Bottom Topography. *J. Phys. Oceanogr.*, 26:2267–2279.

Matano, R. P., Beier, E., Strub, P., and Tokmakian, R. (2002). Large-scale forcing of the Agulhas variability: The seasonal cycle. *J. Phys. Oceanogr.*, 32(4):1228–1241.

McCartney, M. (1977). Subantarctic Mode Water. A voyage of discovery. *M. V. Angel, Ed., Pergamon*, pages 103–119.

Meehl, G. A., Covey, C., Mcavaney, B., Latif, M., and Stouffer, R. J. (2005). Overview of the coupled model intercomparison project. *Bull. Amer. Meteor. Soc.*, 86(1):89–93.

Morrison, J. M. (1997). Intermonsoonal changes in the T-S properties of the near-surface waters of the northern Arabian Sea. *Geophys. Res. Lett.*, 24:2553–2556.

Murray, S. P. and Johns, W. (1997). Direct observations of seasonal exchange through the Bab el Mandab Strait. *Geophys. Res. Lett.*, 24:2557–2560.

Nauw, J. J., van Aken, H. M., Webb, A., Lutjeharms, J. R. E., and de Ruijter, W. (2008). Observations of the southern East Madagascar Current and undercurrent and countercurrent system. *J. Geophys. Res.*, 113(C8):C08006.

Nof, D. and Pichevin, T. (1996). The Retroflection Paradox. *J. Phys. Oceanogr.*, 26:2344–2358.

Nof, D., Zharkov, V., Ortiz, J., Paldor, N., Arruda, W., and Chassignet, E. (2011). The arrested Agulhas retroflection. *J. Mar. Res.*, 69:1–33.

Okubo, W. (1970). Horizontal dispersion of floatable particles in the vicinity of velocity singularities such as convergencies. *Deep Sea Res.*, 17:445–454.

Olson, D., Fine, R., and Gordon, A. (1992). Convective modifications of water masses in the Agulhas. *Deep Sea Res.*, 39(S1):163–181.

Orsi, A., Whitworth, T., and Nowlin, W. (1995). On the meridional extent and fronts of the Antarctic Circumpolar Current. *Deep Sea Res. Part I*, 42(5):641–673.

Otto-Bliesner, B., Brady, E., Clauzet, G., Tomas, R., Levis, S., and Kothavala, Z. (2006). Last glacial maximum and Holocene climate in CCSM3. *J. Climate*, 19(11):2526–2544.

Ou, H. and de Ruijter, W. (1986). Separation of an inertial boundary current from a curved coastline. *J. Phys. Oceanogr.*, 16:280–289.

Özgökmen, T. M., Chassignet, E. P., and Paiva, A. M. (1997). Impact of Wind Forcing, Bottom Topography, and Inertia on Midlatitude Jet Separation in a Quasigeostrophic Model. *J. Phys. Oceanogr.*, 27:2460.

Palastanga, V., van Leeuwen, P., and de Ruijter, W. (2006). A link between low-frequency mesoscale eddy variability around Madagascar and the large-scale Indian Ocean variability. *J. Geophys. Res.*, 111(C9):C09029.

Park, Y., Gamberoni, L., and Charriaud, E. (1993). Frontal structure, water masses and circulation in the Crozet Basin. *J. Geophys. Res.*, 98:12361–12385.

Peeters, F., Acheson, R., Brummer, G., de Ruijter, W., Schneider, R., Ganssen, G., Ufkes, E., and Kroon, D. (2004). Vigorous exchange between the Indian and Atlantic oceans at the end of the past five glacial periods. *Nature*, 430:661–665.

Penven, P., Chang, N., and Shillington, F. (2006a). Modelling the Agulhas Current using SAfE (Southern Africa Experiment). *Geophys. Res. Abstr*, 8:04225.

Penven, P., Debreu, L., Marchesiello, P., and McWilliams, J. C. (2006b). Evaluation and application of the ROMS 1-way embedding procedure to the central california upwelling system. *Ocean Modell.*, 12:157.

Penven, P., Echevin, V., Pasepera, J., Colas, F., and Tam, J. (2005). Average circulation, seasonal cycle, and mesoscale dynamics of the Peru Current System: A modeling approach. *J. Geophys. Res.*, 110:C10021.

Penven, P., Herbette, S., and Rouault, M. (2011). Ocean modelling in the Agulhas Current system. *Proc. Nansen-Tutu Conf., Cape Town, South Africa, Nansen-Tutu Centre for Marine Environmental Research.*

Penven, P., Lutjeharms, J., and Florenchie, P. (2006c). Madagascar: A pacemaker for the Agulhas Current system. *Geophys. Res. Lett*, 33:L17609.

Penven, P., Lutjeharms, J., Marchesiello, P., Roy, C., and Weeks, S. (2001). Generation of cyclonic eddies by the Agulhas Current in the lee of the Agulhas Bank. *Geophys. Res. Lett.*, 28(6):1055–1058.

Penven, P., Marchesiello, P., Debreu, L., and Lefèvre, J. (2008). Software tools for pre-and post-processing of oceanic regional simulations. *Environ. Modell. Softw.*, 23(5):660–662.

Peterson, R. G. and Stramma, L. (1991). Upper level circulation in the South Atlantic Ocean. *Prog. Oceanogr.*, 26:1–73.

Pichevin, T., Herbette, S., and Floc'h, F. (2009). Eddy Formation and Shedding in a Separating Boundary Current. *J. Phys. Oceanogr.*, 39(8):1921–1934.

Pichevin, T., Nof, D., and Lutjeharms, J. (1999). Why are there Agulhas rings? *J. Phys. Oceanogr.*, 29(4):693–707.

Potemra, J. T., Lukas, R., and Mitchum, G. T. (1997). Large-scale estimation of transport from the Pacific to the Indian Ocean. *J. Geophys. Res. Oceans*, 102(C13):27795–27812.

Quartly, G., Buck, J., Srokosz, M., and Coward, A. (2006). Eddies around Madagascar - The retroflection re-considered. *J. Mar. Syst.*, 63:115–129.

Quartly, G. D. and Srokosz, M. A. (2004). Eddies in the southern Mozambique Channel. *Deep Sea Res. Part II*, 51(1-3):69–83.

Reason, C. (2001). Evidence for the influence of the Agulhas Current on regional atmospheric circulation patterns. *J. Climate*, 14(12):2769–2778.

Reason, C. (2002). Sensitivity of the southern African circulation to dipole sea-surface temperature patterns in the South Indian Ocean. *International Journal of Climatology*, 22(4):377–393.

Reason, C., Allan, R., Lindesay, J., and Ansell, T. (2000). ENSO and climatic signals across the Indian Ocean basin in the global context: Part I, Interannual composite patterns. *International Journal of Climatology*, 20(11):1285–1327.

Reid, J. (2003). On the total geostrophic circulation of the Indian Ocean: flow patterns, tracers, and transports. *Prog. Oceanogr.*, 56(1):137–186.

Rennell, J. (1832). An investigation of the currents of the Atlantic Ocean, and of those which prevail between the Indian Ocean and the Atlantic. *J. G. and F. Rivington, London*, page 359.

Richardson, P. (1983). Gulf Stream Rings. *Eddies in Marine Science*, A. R. Robinson, Ed., Springer-Verlag:19–64.

Richardson, P. (2007). Agulhas leakage into the Atlantic estimated with subsurface floats and surface drifters. *Deep Sea Res. Part I*, 54(8):1361–1389.

Richardson, P. and Garzoli, S. (2003). Characteristics of intermediate water flows in the Benguela Current as measured with RAFOS floats. *Deep Sea Res. Part II*, 50:87–118.

Ridderinkhof, H. and de Ruijter, W. (2003). Moored current observations in the Mozambique Channel. *Deep Sea Res. Part II*, 50(12-13):1933–1955.

Ridgway, K. R. and Dunn, J. R. (2007). Observational evidence for a Southern Hemisphere oceanic supergyre. *Geophys. Res. Lett.*, 34:13612.

Rimaud, J., Speich, S., Blanke, B., and Grima, N. (2012). The exchange of Intermediate Water in the southeast Atlantic: Water mass transformations diagnosed from the Lagrangian analysis of a regional ocean model. *J. Geophys. Res.*, 117(C08034):1–21.

Rio, M. H., Guinehut, S., and Larnicol, G. (2011). New CNES-CLS09 global mean dynamic topography computed from the combination of GRACE data, altimetry, and in situ measurements. *J. Geophys. Res.*, 116:C07018.

Rojas, M., Moreno, P., Kageyama, M., Crucifix, M., Hewitt, C., Abe-Ouchi, A., Ohgaito, R., Brady, E., and Hope, P. (2009). The Southern Westerlies during the last glacial maximum in PMIP2 simulations. *Clim. Dyn.*, 32(4):525–548.

Rouault, M., Penven, P., and Pohl, B. (2009). Warming in the Agulhas Current system since the 1980's. *Geophys. Res. Lett.*, 36(12):L12602.

Rouault, M., White, S., Reason, C., Lutjeharms, J., and Jobard, I. (2002). Ocean-atmosphere interaction in the Agulhas Current region and a South African extreme weather event. *Weather and Forecasting*, 17(4):655–669.

Rouault, M. J., Mouche, A., Collard, F., Johannessen, J. A., and Chapron, B. (2010). Mapping the Agulhas Current from space: An assessment of ASAR surface current velocities. *J. Geophys. Res. Oceans*, 115:C10026.

Rouault, M. J. and Penven, P. (2011). New perspectives on Natal Pulses from satellite observations. *J. Geophys. Res.*, 116:C07013.

Rusciano, E., Speich, S., and Ollitraut, M. (2012). Interocean exchanges and the spreading of Antarctic Intermediate Water south of Africa. *J. Geophys. Res.*, 117(C10010):1–21.

Sadarjoen, I. A. and Post, F. (2000). Techniques and Applications of Deformable Surfaces. *H. Hagen and H.C. Rodrian IEEE CS Press.*

Saji, N., Goswami, B., Vinayachandran, P., and Yamagata, T. (1999). A dipole mode in the tropical Indian Ocean. *Nature*, 401(6751):360–363.

Saji, N. and Yamagata, T. (2003). Possible impacts of Indian Ocean dipole mode events on global climate. *Climate Research*, 25(2):151–169.

Sasaki, H., Komori, N., Takahashi, K., Masumoto, Y., and Sakuma, H. (2005). Fifty years time-integration of global eddy-resolving simulation. *Tech Report: Earth Simulator Centre, Japan.*

Saunders, P., Coward, A., and de Cuevas, B. (1999). Circulation of the Pacific Ocean seen in a global ocean model- Ocean Circulation and Climate Advanced Modelling project(OCCAM). *J. Geophys. Res.*, 104(C8):18281–18299.

Schmid, C., Boebel, O., Zenk, W., Lutjeharms, J., Garzoli, S., Richardson, P., and Barron, C. (2003). Early evolution of an Agulhas ring. *Deep Sea Res. Part II*, 50:141–166.

Schmitz, J. and Luyten, J. (1991). Spectral time scales for mid-latitude eddies. *J. Mar. Res.*, 49(1):75–107.

Schmitz, W. (1996). On the eddy field in the Agulhas Retroflection, with some global considerations. *J. Geophys. Res.*, 101(16):16259–16271.

Schott, F., Fieux, M., Kindle, J., Swallow, J., and Zantopp, R. (1988). The boundary currents east and north of Madagascar 2. Direct measurements and model comparisons. *J. Geophys. Res.*, 93(C5):4963–4974.

Schott, F. and McCreary, J. (2001). The monsoon circulation of the Indian Ocean. *Prog. Oceanogr.*, 51(1):1–123.

Schott, F., Xie, S., and McCreary, J. (2009). Indian Ocean circulation and climate variability. *Rev. Geophys.*, 47(1):RG1002.

Schott, F. A. and Fischer, J. (2000). Winter monsoon circulation of the northern Arabian Sea and Somali Current. *J. Geophys. Res.*, 105:6359–6376.

Schouten, M. and de Ruijter, W. (2000). Translation, decay and splitting of Agulhas rings in the southeastern Atlantic Ocean. *J. Geophys. Res.*, 105(C9):21913–21925.

Schouten, M. and de Ruijter, W. (2003). Eddies and variability in the Mozambique Channel. *Deep Sea Res. Part II*, 50:1987–2003.

Schouten, M., de Ruijter, W., and van Leeuwin, P. (2002a). Upstream control of Agulhas ring shedding. *J. Geophys. Res.*, 107(C8):3109.

Schouten, M., de Ruijter, W., van Leeuwin, P., and Dijkstra, H. (2002b). An oceanic teleconnection between the equatorial and southern Indian Ocean. *Geophys. Res. Lett.*, 29(16):1812.

Schulman, E. E. (1975). A study of topographic effects. *Numerical models of ocean circulation*, pages 147–165.

Seidel, D. J., Fu, Q., Randel, W. J., and Reichler, T. J. (2008). Widening of the tropical belt in a changing climate. *Nat. Geosci.*, 1:21–24.

Shchepetkin, A. and McWilliams, J. (1998). Quasi-monotone advection schemes based on explicit locally adaptive dissipation. *Mon. Weather Rev.*, 126:1541–1580.

Shchepetkin, A. and McWilliams, J. (2003). A method for computing horizontal pressure-gradient force in an oceanic model with a nonaligned vertical coordinate. *J. Geophys. Res.*, 108(C3):3090.

Shchepetkin, A. and McWilliams, J. (2005). The regional oceanic modeling system (ROMS): a split-explicit, free-surface, topography-following-coordinate oceanic model. *Ocean Modell.*, 9(4):347–404.

Shchepetkin, A. and McWilliams, J. (2008). Handbook of numerical analysis: Computation methods for ocean and atmosphere. *Computational kernel algorithms for fine-scale, multi-process, lon-term oceanic simulations.*, pages 119–181.

Siedler, G., Rouault, M., Biastoch, A., Backeberg, B., Reason, C. J. C., and Lutjeharms, J. R. E. (2009). Modes of the southern extension of the East Madagascar Current. *J. Geophys. Res.*, 114:C01005.

Siedler, G., Rouault, M., and Lutjeharms, J. R. E. (2006). Structure and origin of the subtropical South Indian Ocean Countercurrent. *Geophys. Res. Lett.*, 33(24):L24609.

Sijp, W. and England, M. (2008). The effect of a northward shift in the southern hemisphere westerlies on the global ocean. *Prog. Oceanogr.*, 79(1):1–19.

Sime, L. C., Kohfeld, K. E., Quéré, C. L., Wolff, E. W., de Boer, A. M., Graham, R. M., and Bopp, L. (2013). Southern Hemisphere westerly wind changes during the Last Glacial Maximum: model-data comparison. *Quaternary Science Reviews*, 64(C):104–120.

Simon, M. H., Arthur, K. L., Hall, I. R., Peeters, F. J. C., Loveday, B. R., Barker, S., Ziegler, M., and Zahn, R. (2013). Millennial-scale Agulhas Current variability and its implications for salt-leakage through the Indian–Atlantic Ocean Gateway. *Earth and Planetary Science Letters*, 383(C):101–112.

Smagorinsky, J. (1963). General circulation experiments with primitive equations. *Mon. Weather Rev.*, 91:99–164.

Sokolov, S. and Rintoul, S. (2009). Circumpolar structure and distribution of the Antarctic Circumpolar Current fronts: 2. Variability and relationship to sea surface height. *J. Geophys. Res.*, 114:C11018.

Son, S., Gerber, E., Perlwitz, J., and et al (2010). Impact of stratospheric ozone on Southern Hemisphere circulation change: A multimodel assessment. *J. Geophys. Res.*, 115:D00M07.

Song, Y. and Haidvogel, D. (1994). A semi-implicit ocean circulation model using a generalized topography-following coordinate system. *J. Comput. Phys.*, 115:228–244.

Souza, J., de Montegut, C., and Le Traon, P. (2011). Comparison between three implementations of automatic identification algorithms for the qualification and characterization of mesoscale eddies in the South Atlantic Ocean. *Ocean Sci.*, 7:317–334.

Speich, S., Blanke, B., and Cai, W. (2007). Atlantic meridional overturning circulation and the Southern Hemisphere supergyre. *Geophys. Res. Lett.*, 34(L23614):1–5.

Speich, S., Blanke, B., De Vries, P., Drijfhout, S., Doos, K., Ganachaud, A., and Marsh, R. (2002). Tasman leakage: A new route in the global ocean conveyor belt. *Geophys. Res. Lett.*, 29(10).

Speich, S., Blanke, B., and Madec, G. (2001). Warm and cold water routes of an OGCM thermohaline conveyor belt. *Geophys. Res. Lett.*, 28:311–314.

Speich, S., Lutjeharms, J. R. E., Penven, P., and Blanke, B. (2006). Role of bathymetry in Agulhas Current configuration and behaviour. *Geophys. Res. Lett.*, 33:L23611.

Spence, P., Fyfe, J., Montenegro, A., and Weaver, A. (2010). Southern Ocean response to strengthening winds in an eddy-permitting global climate model. *J. Clim.*, 23:5332–5343.

Stammer, D. (2008). Response of the global ocean to Greenland and Antarctic ice melting. *Geophys. Res. Lett.*, 113:C06022.

Steele, M., Morfley, R., and Ermold, W. (2001). PHC: A global ocean hydrography with high-quality Artic Ocean. *J. Climate*, 14:2079–2087.

Stramma, L. (1991). The South Indian Ocean Current. *J. Phys. Oceanogr.*, 22:421–430.

Stramma, L. and England, M. (1999). On the water masses and mean circulation of the South Atlantic Ocean. *J. Geophys. Res.*, 104(C9):1–21.

Stramma, L. and Lutjeharms, J. (1997). The flow field of the subtropical gyre of the South Indian Ocean. *J. Geophys. Res.*, 102(C5):5513–5530.

Susanto, R. D., Gordon, A. L., and Sprintall, J. (2007). Observations and proxies of the surface layer throughflow in Lombok Strait. *J. Geophys. Res. Oceans*, 112:C03S92.

Swallow, J., Fieux, M., and Schott, F. (1988). The boundary currents east and north of Madagascar: 1. Geostrophic currents and transports. *J. Geophys. Res. Oceans*, 93:4951.

Swallow, J. C., Schott, F., and Fieux, M. (1991). Structure and transport of the East African Coastal Current. *J. Geophys. Res. Oceans*, 96:22245.

Swart, N. C. and Fyfe, J. C. (2012). Observed and simulated changes in the Southern Hemisphere surface westerly wind-stress. *Geophys. Res. Lett.*, 39:16711.

Swart, N. C., Lutjeharms, J., Ridderinkhof, H., and de Ruijter, W. (2010). Observed characteristics of Mozambique Channel eddies. *J. Geophys. Res. Oceans*, 115:C09006.

Swart, S., Speich, S., Ansorge, I. J., Goni, G. J., Gladyshev, S., and Lutjeharms, J. R. E. (2008). Transport and variability of the Antarctic Circumpolar Current south of Africa. *J. Geophys. Res. Oceans*, 113:9014.

Talley, L. D., Pickard, G. L., Emery, W. J., and Swift, J. H. (2011). Descriptive physical oceanography: an introduction. *Elsevier*.

Thompson, D. W. J. and Solomon, S. (2002). Interpretation of recent Southern Hemisphere climate change. *Science*, 296:895–899.

Thoppil, P. G., Richman, J. G., and Hogan, P. J. (2011). Energetics of a global ocean circulation model compared to observations. *Geophys. Res. Lett.*, 38:15607.

Tilburg, C. E., Hurlburt, H. E., O'Brien, J. J., and Shriver, J. F. (2001). The Dynamics of the East Australian Current System: The Tasman Front, the East Auckland Current, and the East Cape Current. *Journal of Physical Oceanography*, 31:2917.

Toggweiler, J. R., Russell, J., and Carson, S. (2006). Midlatitude westerlies, atmospheric CO2, and climate change during the ice ages. *Palaeogeography*, 21:1–15.

Toggweiler, J. R. and Samuels, B. (1995). Effect of Drake Passage on the global thermohaline circulation. *Deep Sea Res. Part I*, 42(4):477–500.

Tomczak, M. and Godfrey, J. (1994). Regional Oceanography: An Introduction. *Bull. Amer. Meteor. Soc.*, 2:390.

Toole, J. M. and Warren, B. (1993). A hydrographic section across the subtropical South Indian Ocean. *Deep Sea Res. Part I*, 40:1973–2019.

Treguier, A., Boebel, O., Barnier, C., and Madec, G. (2003). Agulhas eddy fluxes in a 1/6 ° Atlantic model. *Deep Sea Res. Part II*, 50:251–280.

Tsugawa, M. and Hasumi, H. (2010). Generation and Growth Mechanism of the Natal Pulse. *J. Phys. Oceanogr.*, 40:1597–1612.

van Aken, H., Lutjeharms, J. R. E., Rouault, M., Whittle, C., and de Ruijter, W. (2013). Observations of an early Agulhas current retroflection event in 2001: A temporary cessation of inter-ocean exchange south of Africa? *Deep Sea Res. Part I*, 72:1.

van Aken, H., van Veldhoven, A., Veth, C., de Ruijter, W., van Leeuwen, P., Drijfhout, S., Whittle, C., and Rouault, M. (2003). Observations of a young Agulhas ring, Astrid, during MARE, the Mixing of Agulhas Rings Experiment, in March 2000. *Deep Sea Res. Part II*, 50:167–195.

van Ballegooyen, R., Grundlingh, M. L., and Lutjeharms, J. (1994). Eddy fluxes of heat and salt from the southwest Indian Ocean into the southeast Atlantic Ocean: a case study. *J. Geophys. Res.*, 99:14,053–14,070.

van der Vaart, P. and de Ruijter, W. (2001). Stability of western boundary currents with an application to pulse-like behavior of the Agulhas Current. *J. Phys. Oceanogr.*, 31:2625–2644.

van der Werf, P., van Leeuwin, P., Ridderinkhof, H., and de Ruijter, W. (2010). Comparison between observations and models of the Mozambique Channel transport: Seasonal cycle and eddy frequencies. *J. Geophys. Res.*, 115(C02002):1–16.

van Gogh, J. (1857). Uitkomsten van Wetenskap en Ervaring aangaande winden en zeestromingen in sommige gedeelten van den oseaan. *Koninklijk Nederlandsch Meteorologisch Instituut, Bosch en Zoon*, page 74.

van Leeuwen, P., de Ruijter, W., and Lutjeharms, J. (2000). Natal Pulses and the formation of Agulhas rings. *J. Geophys. Res.*, 105:6425–6436.

van Sebille, E., Barron, C., Biastoch, A., van Leeuwen, P., Vossepoel, F., and de Ruijter, W. (2009a). Relating Agulhas leakage to the Agulhas Current retroflection location. *Ocean Sci.*, 5:511–521.

van Sebille, E., Beal, L., and Biastoch, A. (2010a). Sea surface slope as a proxy for Agulhas Current strength. *Geophys. Res. Lett.*, 37(9):L09610.

van Sebille, E., Biastoch, A., van Leeuwin, P., and de Ruijter, W. (2009b). A weaker Agulhas Current leads to more Agulhas leakage. *Geophys. Res. Lett.*, 36(3):L03601.

van Sebille, E., van Leeuwen, P., Biastoch, A., and de Ruijter, W. (2010b). On the fast decay of Agulhas rings. *J. Geophys. Res.*, 115(C3):C03010.

van Sebille, E., van Leeuwin, P., Biastoch, A., and de Ruijter, W. (2010c). Flux comparison of Eulerian and Lagrangian estimates of Agulhas leakage: A case study using a numerical model. *Deep Sea Res. Part I*, 57:319–327.

Veronis, G. (1973). Model of world ocean circulation, I: Wind-driven, two layer. *J. Mar. Res.*, 31:228–288.

Wahl, S., Latif, M., Park, W., and Keenlyside, N. (2011). On the Tropical Atlantic SST warm bias in the Kiel Climate Model. *Clim Dyn*, 36(5-6):891–906.

Walker, N. and Mey, R. (1988). Ocean/atmosphere heat fluxes within the Agulhas Retroflection region. *J. Geophys. Res.*, 93:15,473–15,483.

Wallcraft, A., Birol-Kara, A., Hurlburt, H., and Rochford, P. (2003). The NRL Layered Global Ocean Model (NLOM) with an Embedded Mixed Layer Submodel: Formulation and Tuning. *J. Atmos. Ocean Tech.*, 20:1601–1615.

Wang, L., Koblinsky, C., and Howden, S. (2001). Annual Rossby Wave in the Southern Indian Ocean: Why Does It "Appear" to Break Down in the Middle Ocean? *J. Phys. Oceanogr.*, 31(1):54–74.

Watson, P., Karoly, D., Allen, M., Faull, N., and Lee, D. (2012). Quantifying uncertainty in future Southern Hemisphere circulation trends. *Geophys. Res. Lett.*, 39:L23708.

Webster, P., Moore, A., Loschnigg, J., and Leben, R. (1999). Coupled ocean–atmosphere dynamics in the Indian Ocean during 1997–98. *Nature*, 401(6751):356–360.

Weijer, W., de Ruijter, W., and Dijkstra, H. (2001). Stability of the Atlantic overturning circulation: Competition between Bering Strait freshwater flux and Agulhas heat and salt sources. *J. Phys. Oceanogr.*, 31(8):2385–2402.

Weijer, W., de Ruijter, W., Dijkstra, H., and van Leeuwen, P. (1999). Impact of interbasin exchange on the Atlantic overturning circulation. *J. Phys. Oceanogr.*, 29(9):2266–2284.

Weijer, W., de Ruijter, W., Sterl, A., and Drijfhout, S. (2002). Response of the Atlantic overturning circulation to South Atlantic sources of buoyancy. *Global Planet. Change*, 34(3-4):293–311.

Weiss, J. (1991). The dynamics of enstrophy transfer in two-dimensional hydrodynamics. *Physica D*, 48:273–294.

Whittle, C., Lutjeharms, J. R. E., Duncombe-Rae, C., and Shillington, F. (2008). Interaction of Agulhas filaments with mesoscale turbulence: a case study. *S. Afr. J. Sci.*, 104:135–139.

Winther, N. G., Morel, Y. G., and Evensen, G. (2007). Efficiency of high order numerical schemes for momentum advection. *J. Mar. Syst.*, 67:31.

Wust, G. (1960). Proposed International Indian Ocean Expedition, 1962–1963. *Deep Sea Res.*, pages 245–249.

Wyroll, K., Dong, B., and Valdes, P. (2000). On the position of Southern Hemisphere westerlies at the Last Glacial Maximum: An outline of AGCM simulation results and evaluation of their implications. *Quat. Sci. Rev.*, 19:881–898.

Wyrtki, K. (1971). Oceanographic Atlas of the International Indian Ocean Expedition. *National Science Foundation, Washington, D.C.*, page 531.

Xie, S., Annamalai, H., Schott, F., and McCreary, J. (2002). Structure and mechanisms of South Indian Ocean climate variability. *J. Climate*, 15(8):864–878.

Yang, J., Liu, Q., Xie, S., Liu, Z., and Wu, L. (2007). Impact of the Indian Ocean SST basin mode on the Asian summer monsoon. *Geophys. Res. Lett.*, 34(2):L02708.

You, Y. (1997). Seasonal variations of thermocline circulation and ventilation in the Indian Ocean. *J. Geophys. Res.*, 102(C5):10391–10422.

Yu, J. and Lau, K. (2005). Contrasting Indian Ocean SST variability with and without ENSO influence: A coupled atmosphere-ocean GCM study. *Meteorology and Atmospheric Physics*, 90(3):179–191.

Zahn, R., Lutjeharms, J., Biastoch, A., Hall, I., Knorr, G., Park, W., and Reason, C. (2010). Investigating the Global Impacts of the Agulhas Current. *Eos Trans. AGU*, 91(12):109–116.

Zharkov, V. and Nof, D. (2008a). Agulhas ring injection into the South Atlantic during glacials and interglacials. *Ocean Sci. Discuss.*, 5(1):39–75.

Zharkov, V. and Nof, D. (2008b). Retroflection from slanted coastlines? circumventing the'vorticity paradox'. *Ocean Sci. Discuss.*, 5:1–37.

Zharkov, V., Nof, D., and Weijer, W. (2010). Retroflection from a double-slanted coastline: a model for the Agulhas leakage variability. *Ocean Sci. Discuss.*, 7:1209–1244.

Appendix1: publication abstracts

Chapter 5; Loveday, B. R., Durgadoo, J., Reason, C. J. C., Biastoch, A. and Penven, P. Decoupling of the Agulhas leakage from the Agulhas Current. *(accepted; J. Phys. Oceanogr.)*

The relationship between the Agulhas Current and the Agulhas leakage is not well understood. Here, this is investigated using two basin-scale and two global ocean models, of incrementally increasing resolution. The response of the Agulhas Current is evaluated under a series of sensitivity experiments, in which idealised anomalies, designed to geometrically modulate zonal trade wind stress, are applied across the Indian Ocean basin. The imposed wind stress changes exceed ± 2 standard deviations from the annual mean trade winds and, in the case of intensification, are partially representative of recently observed trends.

The Agulhas leakage is quantified using complimentary techniques based on Lagrangian virtual floats and Eulerian passive tracer flux. As resolution increases, model behavior converges and the sensitivity of the leakage to Agulhas Current transport is reduced. In the two eddy-resolving configurations tested, the leakage is insensitive to changes in Agulhas Current transport at 32^{o}S, though substantial eddy kinetic energy anomalies are evident. Consistent with observations, the position of the retroflection remains stable.

The decoupling of Agulhas Current variability from the Agulhas leakage suggests that, while correlations between the two may exist, they may not have a clear dynamical basis. It is suggested that present and future Agulhas leakage proxies be considered in the context of potentially transient forcing regimes.

Chapter 6; Durgadoo, J., Loveday, B. R., Reason, C. J. C., Penven, P., and Biastoch, A. (2013). Agulhas leakage predominantly responds to the Southern Hemisphere Westerlies. *J. Phys. Oceanogr.*, **43**, 2113-2131.

The Agulhas Current plays a crucial role in the thermohaline circulation through its leakage into the South Atlantic Ocean. Under both past and present climates, the trade winds and westerlies could have the ability to modulate the amount of IndianÐAtlantic inflow. Compelling arguments have been put forward suggesting that trade winds alone have little impact on the magnitude of Agulhas leakage. Here, employing three ocean models for robust analysis − a global coarse-resolution, a regional eddy-permitting, and a nested high- resolution eddy-resolving configuration−and systematically altering the position and intensity of the westerly wind belt in a series of sensitivity experiments, it is shown that the westerlies, in particular their intensity, control the leakage. Leakage responds proportionally to the intensity of westerlies up to a certain point. Beyond this, through the adjustment of the large-scale circulation, energetic interactions occur between the Agulhas Return Current and the Antarctic Circumpolar Current that result in a state where leakage no longer increases. This adjustment takes place within one or two decades. Contrary to previous assertions, these results further show that an equatorward (poleward) shift in westerlies increases (decreases) leakage. This occurs because of the redistribution of momentum input by the winds. It is concluded that the reported present-day leakage increase could therefore reflect an unadjusted oceanic response mainly to the strengthening westerlies over the last few decades.